Leibniz Institute for Baltic Sea Research Warnemünde

Universität Rostock Traditio et Innovatio

DOCTORAL THESIS

Diurnal Warm Layers in the Ocean: Dynamics, Turbulence and Atmospheric Feedbacks

Author:
Mira SCHMITT

Supervisor:
PD Dr. Lars UMLAUF

A cumulative thesis submitted in fulfillment of the requirements for the degree of Doctor rerum naturalium (Dr. rer. nat.)

in the

Faculty of Mathematics and Natural Sciences
at the University of Rostock

Rostock, September 2024

https://doi.org/10.18453/rosdok_id00005110

Reviewers:

1. Reviewer: PD Dr. Lars Umlauf
Leibniz-Institut für Ostseeforschung Warnemünde
2. Reviewer: Prof. Dr. Peter Brandt
GEOMAR Helmholtz-Zentrum für Ozeanforschung Kiel

Submission date: 30.09.2024
Defense date: 14.03.2025

"We demand rigidly defined areas of doubt and uncertainty!"

Douglas Adams, The Hitchhiker's Guide to the Galaxy

UNIVERSITY OF ROSTOCK

Faculty of Mathematics and Natural Sciences

Abstract

Diurnal Warm Layers in the Ocean: Dynamics, Turbulence and Atmospheric Feedbacks

by Mira SCHMITT

Small-scale physical processes in the ocean surface layer govern the energy exchange at the air-sea interface and play a crucial role in the distribution of momentum, energy and tracers in the ocean. However, they are usually not directly resolved in climate models due to limited computational resources. This dissertation investigates the influence of Diurnal Warm Layers (DWLs), which are thin, buoyant layers that form on the surface of the ocean on days with weak surface winds and waves due to heating by the sun, on oceanic mixing and flux exchange with the atmosphere.

Based on a second-moment turbulence model and Large Eddy Simulations, the interplay between DWLs and Langmuir Turbulence (LT) is investigated. LT introduces a Stokes shear mechanism that impacts DWL energy budgets, and reduces surface buoyancy and velocity significantly, even under weak wind and wave conditions. This impact is included in a parameterization for DWLs that is based on dimensional analysis and results in reliable estimates of DWL bulk properties over a large physical parameter space.

A combination of field measurements and second-moment turbulence modelling reveals a complex interplay caused by the coexistence of DWLs and submesoscale fronts. DWLs periodically decouple the deeper parts of the surface layer from direct atmospheric forcing. In the presence of a front, this effectively eliminates the modification of the surface-layer Ertel potential vorticity by the surface fluxes, with strong implications for the surface-layer stability properties. The underlying layer remains marginally unstable, making it susceptible to symmetric instability and turbulence from small disturbances.

A regional ocean model located in the trade-wind zone of the tropical North Atlantic, forced at the surface by a high-resolution atmospheric model, is used to investigate the impact of diurnal heating, local precipitation, cold pools and wind bursts, on air-sea exchange and the structure of the ocean surface layer. Results show that the oceanic heat loss is reduced by on average 30 W m^{-2} in the presence of cold pools. Moreover, the non-solar heat flux is dominated by the diurnal cycle of the trade winds rather than by diurnal heating. In the surface layer, rain layers and cloud shading induce a strong lateral variability in the strength and depth of DWLs. From a series of numerical tracer experiments, a new shear-dispersion mechanism is identified, induced by the Diurnal Jet, that is reflected in an extreme anisotropy of horizontal dispersion with diffusivities of order 10-100 m^2 s^{-1}.

A kilometer-scale global coupled simulation reveals the impact of DWLs on atmospheric convection in the tropics. DWLs cause an abrupt afternoon increase of atmospheric moisture due to enhanced latent heat flux, followed by an increase in cloud cover and cloud liquid water. However, this effect lasts only 5–6 hours and leads to an absolute difference of 1% in cloud cover, which is negligible in the tropical mean.

UNIVERSITÄT ROSTOCK
Mathematisch-Naturwissenschaftliche Fakultät

Zusammenfassung

Diurnal Warm Layers in the Ocean: Dynamics, Turbulence and Atmospheric Feedbacks

von Mira SCHMITT

Kleinskalige physikalische Prozesse in den oberflächennahen Schichten des Ozeans bestimmen den Energieaustausch zwischen Ozean und Atmosphäre und spielen eine essentielle Rolle bei der Verteilung von Impuls, Energie und gelösten Stoffen im Ozean. Aufgrund begrenzter Rechenkapazitäten werden sie jedoch in Klimamodellen meist nicht direkt aufgelöst. Diese Dissertation untersucht der Einfluss von Diurnal Warm Layers (DWLs), dünnen, leichten Schichten, die sich bei schwachem Wind und Wellengang an der Ozeanoberfläche aufgrund der Erwärmung durch die Sonne bilden, auf die Durchmischung der tieferen Schichten des Ozeans und den Austausch mit der Atmosphäre.

Auf der Grundlage eines Turbulenzmodells und einer Large Eddy Simulation wird das Zusammenspiel von DWLs und Langmuir Turbulenz (LT) untersucht. LT und Stokes-Scherung wirken sich auf das Energiebudget von DWLs aus und verringern Oberflächenauftrieb und -geschwindigkeit selbst unter schwachen Wind- und Wellenbedingungen erheblich. Die Auswirkungen von LT auf DWLs sind in einer Parametrisierung für DWLs enthalten, die auf einer Dimensionsanalyse basiert und zu zuverlässigen Schätzungen der DWL-Bulk-Eigenschaften über einen großen physikalischen Parameterraum führt.

Eine Kombination aus Feldmessungen und Turbulenzmodellierung offenbart ein komplexes Zusammenspiel verursacht durch die Koexistenz von DWLs und submesoskaligen Fronten. DWLs entkoppeln die tieferen Teile der Oberflächenschicht periodisch von direkten atmosphärischen Einflüssen. In Gegenwart einer Front wird dadurch die Änderung der Ertel Potential Vorticity wirksam beseitigt, was sich stark auf die Stabilität der Oberflächenschicht auswirkt. Die untere Schicht bleibt marginal instabil, was sie anfällig für symmetrische Instabilitäten und Turbulenz durch kleine Störungen macht.

Mit einem regionalen Ozeanmodell der Passatwindzone des tropischen Nordatlantiks, angetrieben durch ein hochauflösendes Atmosphärenodell, werden die Auswirkungen täglicher Erwärmung, lokaler Niederschläge, Cold Pools und Windböen auf den Energieaustausch mit der Atmosphäre und die Struktur der Oberflächenschicht untersucht. Die Ergebnisse zeigen, dass der Wärmeverlust des Ozeans in Regionen mit Cold Pools um durchschnittlich 30 W m^{-2} reduziert wird. Außerdem werden die nicht-solaren Wärmeflüsse durch den Tageszyklus der Passatwinde und nicht durch DWLs dominiert. Regen und Wolken bewirken eine starke laterale Variabilität in der Stärke und Tiefe der DWLs. Aus numerischen Tracer-Experimenten wird ein neuer, durch den Diurnal Jet induzierter, Scher-Dispersions-Mechanismus identifiziert, der sich in einer extremen Anisotropie der horizontalen Dispersion mit Diffusivitäten in der Größenordnung 10-100 m^2 s^{-1} widerspiegelt.

Eine globale gekoppelte Simulation mit Auflösung im Kilometer-Bereich zeigt den Einfluss von DWLs auf atmosphärische Konvektion in den Tropen. DWLs verursachen einen Anstieg der Feuchtigkeit in der Atmosphäre am Nachmittag aufgrund eines erhöhten latenten Wärmeflusses, gefolgt von einer Zunahme der Wolkenbedeckung und des flüssigen Wassers in den Wolken. Dieser Effekt hält jedoch nur 5-6 Stunden an und führt zu einer absoluten Differenz von 1% bei der Wolkenbedeckung, was im tropischen Mittel vernachlässigbar ist.

Acknowledgements

First and foremost, I would like to thank Lars. I don't think I would have wanted to do a PhD with anyone else as my supervisor. Thank you for always finding time to talk, for your advice, for understanding every single line of thought in everything I've done, and for repeating the basics of turbulence again and again and again... Above all, thank you for being a friend. Don't change (except maybe please be punctual to my defence).

Thank you to all my co-authors on the publications for making this dissertation possible, it's been a pleasure to work with you. In particular, I'd like to give a thank you to Knut, our model guru, for taking the time to do the model development (not just for me, but for anyone who needs help), and for patiently answering every GETM/GOTM question this universe can come up with. Thank you to the people in my PhD committee, Hans, Gregor, and Cathy, for listening to me say the words "diurnal warm layer" innumerous times, for your advice and for always making sure that I stay on track with this PhD.

The next big thank you goes to my office mates for most of the time here, Erika, Markus and Lev. It was nice to have you as allies from beginning to end and you are the main reason I enjoyed coming to the office every day. A big shout out to all my colleagues at IOW, especially to Peter, Martin, Kseniia, Anna, Lloyd, Leonie, Yannik and Caroline. Thank you for many coffee breaks (maybe initiated by me), beach visits (partly initiated by me) and pub evenings (definitely initiated by me). To Swen, for fixing my laptop over and over again, I don't know what's wrong with that thing, but I blame it on either infernal intervention or myself.

Thank you to the TRR-181 (funded by the Deutsche Forschungsgesellschaft, Project-ID 274762653) for providing the opportunity and resources for this work, to Lea and Jennifer for the organisation around it all, and to my fellow TRR PhDs for the support and nice memories during our many retreats and meetings. A big thank you to Jen-Ping and everyone in the working group of Nicole Jones in Perth for welcoming me during my research stay and for making sure that I had such a nice time there. I'll make sure I wear Quokka socks to the defence.

Danke an meine Familie, ohne deren stetige Unterstützung ich niemals so weit gekommen wäre, und deren Begeisterung für Warnemünde und Ozeanographie (vor allem vielleicht Forschungsschiffreisen) mich immer wieder daran erinnert hat, was für ein Glück ich hatte hier zu arbeiten. Und zu guter Letzt an Simon, danke, dass du an meiner Seite bist.

Contents

Declaration of Authorship

I, Mira SCHMITT, declare that this thesis titled, "Diurnal Warm Layers in the Ocean: Dynamics, Turbulence and Atmospheric Feedbacks" and the work presented in it are my own. I confirm that:

- This work was done wholly while in candidature for a research degree at this University.
- No part of this thesis has never been submitted for a degree or any other qualification at this University or any other institution.
- Where I have consulted the published work of others, this is always clearly attributed.
- Where I have quoted from the work of others, the source is always given. With the exception of such quotations, this thesis is entirely my own work.
- I have acknowledged all main sources of help.
- Where the thesis is based on work done by myself jointly with others, I have made clear exactly what was done by others and what I have contributed myself.

Signed: _____

Date: _____

List of Publications

PUBLICATIONS FOR THE CUMULATIVE DISSERTATION

1. Schmitt, M., H. T. Pham, S. Sarkar, K. Klingbeil, and L. Umlauf, 2024: Diurnal Warm Layers in the Ocean: Energetics, Nondimensional Scaling, and Parameterization. *Journal of Physical Oceanography*, **54**, 1037–1055, https://doi.org/10.1175/JPO-D-23-0129.1.

2. Peng, J.P., N. Jones, M. Rayson, M. Schmitt, L. Umlauf, C. Whitwell, S.R. Keating, C.J. Shakespeare, and G.N. Ivey: Interactions between diurnal warm layers and surface-layer fronts. *Journal of Geophysical Research: Oceans*. *submitted*.

3. Schmitt, M., K. Klingbeil, R. Shevchenko, and L. Umlauf: Three-dimensional Ocean Surface Layer Response to Rain, Wind bursts and Diurnal Heating. *Journal of Geophysical Research: Oceans*. *submitted*.

4. Shevchenko, R., C. Hohenegger, and M. Schmitt, 2023: Impact of Diurnal Warm Layers on Atmospheric Convection. *Journal of Geophysical Research: Atmospheres*, 128, e2022JD038473. https://doi.org/10.1029/2022JD038473.

List of Attended Conferences

1. European Geosciences Union (EGU) General Assembly, Vienna, Austria, 23.04.2023-28.04.2023, poster presentation: "Dynamics and impact of diurnal warm layers in the ocean"

2. International Union of Geodesy and Geophysics (IUGG) General Assembly, Berlin, Germany, 11.07.2023-15.07.2023, oral presentation: "Scaling of Diurnal Warm Layers in the Ocean"

3. Warnemuende Turbulence Days, Rostock, Germany, 17.09.2023-22.09.2023, oral presentation: "Diurnal Warm Layers in the ocean: How does the energy budget differ between equator and high latitudes?"

4. Gordon Research Conferences: Mixing, Boston, Massachusetts, USA, 09.06.2024-15.06.2024, poster presentation: "Diurnal Warm Layers"

List of Abbreviations

CC	**C**loud **C**over
CLW	**C**loud **L**iquid **W**ater
DSA	**D**iurnal **S**ST **A**mplitude
DWL	**D**iurnal **W**arm **L**ayer
GETM	**G**eneral **E**stuarine **T**ransport **M**odel
GOTM	**G**eneral **O**cean **T**urbulence **M**odel
ICON	**ICO**sahedral **N**onhydrostatic
LES	**L**arge **E**ddy **S**imulation
LHF	**L**atent **H**eat **F**lux
LT	**L**angmuir **T**urbulence
MOST	**M**onin-**O**bukhov **S**imilarity **T**heory
PV	**P**otential **V**orticity
RANS	**R**eynolds **A**veraged **N**avier-**S**tokes
RL	**R**ain **L**ayer
SI	**S**ymmetric **I**nstability
SST	**S**ea **S**urface **T**emperature
TKE	**T**urbulent **K**inetic **E**nergy
WVP	**W**ater **V**apour **P**ath

Chapter 1

Introduction

1.1 Motivation

The focus of this dissertation is the analysis of small-scale physical processes near the air-sea interface, which is the boundary between the atmosphere and the ocean and one of the most physically and chemically active regions on the planet.

Here, atmosphere and ocean exchange energy and momentum via radiative energy transfers and turbulent fluxes of heat and momentum. Changes in the atmospheric dynamics feed back to the turbulent fluxes, short- and longwave radiation, and precipitation, which all affect the ocean temperature, salinity and momentum, with the most immediate impact felt by the surface mixed layer. In return, changes in the energy input from the ocean to the atmosphere can affect the atmospheric state, the redistribution of energy within the atmosphere, and therefore the atmospheric circulation. Hence, atmosphere and ocean form a coupled system, in which a multitude of feedback mechanisms occur (Foltz, 2019).

Despite the importance of these energy transfers for climate studies, most climate models are unable to achieve the high horizontal and vertical scales required to resolve the small-scale processes involved. This dissertation contributes to the Collaborative Research Centre TRR 181, whose aim is to develop the necessary understanding of the energy transfers between the different dynamical regimes in the atmosphere and ocean, and develop, test and implement new and energetically consistent parameterizations in ocean, atmosphere and coupled models.

This work focuses mainly on the smallest spatial and temporal scales, where small-scale turbulence drives the dissipation of kinetic energy to internal energy, and on how these smallest scales are ultimately linked to and strongly influence the larger scales of the energy cycle through a variety of complex processes. More specifically, a large part of this dissertation focuses on modelling and understanding Diurnal Warm Layers, which are thin layers that form on the ocean surface due to the absorption of solar shortwave radiation during the day. Diurnal Warm Layers are able to impact mixing in the ocean and modify the strength of the radiative fluxes back to the atmosphere, yet they remain unresolved in most model studies, and universally applicable parameterizations are a topic of ongoing work. In this dissertation, several gaps in the study of Diurnal Warm Layers are investigated:

1. None of the previous attempts to parameterize Diurnal Warm Layers used a systematic and comprehensible non-dimensional approach to the problem, which led to a limited applicability of the results. Moreover, the effect of surface wave turbulence on Diurnal Warm Layers remained excluded from earlier parameterizations. The publication Schmitt et al. (2024), included in this dissertation, focuses on these topics with the use of a high resolution second-moment turbulence model, validated by a Large Eddy Simulation.

2. Interactions between Diurnal Warm Layers and submesoscale fronts are investigated for the first time in Peng et al. (submitted) by combining observations with idealized second-moment modelling.

3. The three-dimensional features of Diurnal Warm Layers, their transport of tracers, and interplay with Rain Layers and small-scale atmospheric processes involving the formation of cold pools, were never previously studied using a three dimensional ocean model. The publication Schmitt et al. (submitted), included here, is the first model study that resolves, and has a specific focus on, the impact of all of these processes.

4. The feedback that Diurnal Warm Layers have on the atmosphere had never been studied in a fully-coupled, global model configuration. In Shevchenko et al. (2023), a direct resolution of DWLs in such a set up was realized for the first time, allowing for an analysis of their impact on the atmosphere.

Working towards closing these gaps contributes to understanding air-sea interactions and reducing biases in climate predictions.

1.2 Fundamental Principles

To provide an overview of the physical principles that form the basis of the models used in this dissertation, this section briefly summarises the fundamental governing equations, turbulence closures, and basic concepts of turbulent boundary layer theory.

1.2.1 The Shallow-Water Equations

The basis for all atmosphere and ocean fluid dynamics are the Navier-Stokes Equations for momentum and buoyancy. This set of partial differential equations, derived from fundamental principles like the balance of momentum and the first law of thermodynamics, accurately describes the motions of Newtonian Fluids such as air and water. However, due to limited computational resources, a statistical approach is required when modelling the turbulent nature of atmosphere and oceans with its chaotic and unpredictable fluctuations and non-linear interactions. Osborne Reynolds was the first to propose a decomposition of the turbulent field quantities, e.g. the velocity, into mean (u_i) and fluctuating (u_i') components, which led to the Reynolds Averaged Navier-Stokes (RANS) Equations for momentum:

$$\frac{\partial u_i}{\partial t} + \frac{\partial}{\partial x_j}(u_i u_j + \langle u_i' u_j' \rangle - \nu \frac{\partial u_i}{\partial x_j}) + 2\epsilon_{ijk}\Omega_j u_k = -\frac{1}{\rho_0}\frac{\partial p}{\partial x_i} + \frac{g_i}{\rho_0}\rho \, . \tag{1.1}$$

Here, the indices denote zonal, meridional and vertical direction and $\langle \cdot \rangle$ the mean (Kundu et al., 2016). The first term on the left hand side represents the change with time, followed by three transport terms, namely the mean advective flux, the momentum flux supported by the turbulent motions and the diffusive flux with the kinematic viscosity ν. The fifth term represents the Coriolis acceleration with Ω denoting Earth's rotation. The terms on the right hand side consist of a pressure gradient force with pressure p and a gravitational force with the gravity vector g_i. For the ocean, the Boussinesq approximation is assumed, in which the fluid is incompressible and the density ρ_0 is constant except for the buoyancy term. The second-order tensor $\langle u_i' u_j' \rangle$ is physically equivalent to a stress and is therefore usually called the *Reynolds stress tensor*. The presence of this term makes it impossible to obtain a closed set of equations, since it requires solving new transport equations in which new, unknown, higher-order terms appear. This is known as the closure problem of turbulence

(Burchard, 2002), and can only be solved with the use of empirical modelling assumptions and parameterizations, as explained in more detail in Section 1.2.2.

Since geophysical fluid flows are very shallow, i.e. their vertical scale is much smaller than their horizontal scale, (1.1) can be simplified to what is known as the shallow-water equations for velocities u and v in zonal and meridional direction:

$$\frac{\partial u}{\partial t} + \frac{\partial u^2}{\partial x} + \frac{\partial uv}{\partial y} + \frac{\partial uw}{\partial z} + \frac{\partial \langle u'u' \rangle}{\partial x} + \frac{\partial \langle u'v' \rangle}{\partial y} + \frac{\partial}{\partial z}(\langle u'w' \rangle - \nu \frac{\partial u}{\partial z}) - fv = -\frac{1}{\rho_0}\frac{\partial p}{\partial x} , \quad (1.2)$$

$$\frac{\partial v}{\partial t} + \frac{\partial vu}{\partial x} + \frac{\partial v^2}{\partial y} + \frac{\partial vw}{\partial z} + \frac{\partial \langle v'u' \rangle}{\partial x} + \frac{\partial \langle v'v' \rangle}{\partial y} + \frac{\partial}{\partial z}(\langle v'w' \rangle - \nu \frac{\partial v}{\partial z}) + fu = -\frac{1}{\rho_0}\frac{\partial p}{\partial y} , \quad (1.3)$$

where the Coriolis frequency $f = 2\Omega \sin(\phi)$ at a latitude ϕ was introduced (Burchard, 2002). The vertical velocity w can be reduced to the hydrostatic relation, and the continuity equation becomes

$$\frac{\partial u}{\partial x} + \frac{\partial v}{\partial y} + \frac{\partial w}{\partial z} = 0 . \quad (1.4)$$

In ocean models, the potential density ρ of water is determined from an equation of state involving the potential temperature T, salinity S and pressure p. Assuming a simplified linear approximation, $\rho = \rho_0 + \alpha(T - T_0) + \beta(S - S_0)$, where α and β denote the thermal and haline volume expansion coefficients, and 0 a reference value (Olbers et al., 2012), the RANS transport equation for buoyancy $b = -g/\rho_0(\rho - \rho_0)$ can be derived from the transport equations for T and S as

$$\frac{\partial b}{\partial t} + \frac{\partial}{\partial x_i}(u_i b + \langle u_i' b' \rangle - \nu^b \frac{\partial b}{\partial z}) = r , \quad (1.5)$$

where r represents all possible sources and sinks of buoyancy, like e.g. heating due to absorption of solar radiation (Burchard, 2002).

The equations in (1.2)-(1.5) form the basis for all the models used in this dissertation.

1.2.2 Turbulence Closure

As already mentioned in Section 1.2.1, deriving expressions for the turbulent Reynolds stresses in (1.2), (1.3) and (1.5) requires numerical parameterizations and is one of the key elements of turbulence modelling. A simple starting point is the eddy viscosity assumption, in which, in analogy with the molecular transport, the Reynolds stresses are formulated in terms of a turbulent diffusivity (also called eddy viscosity) and the gradient of the mean quantities. The separation of horizontal and vertical scales in the shallow-water equations also implies different turbulent diffusivities in the horizontal and vertical direction, denoted here by K and ν_t, respectively (Klingbeil et al., 2022). Under these assumptions, one common formulation for the Reynolds stress tensor for momentum is

$$\begin{bmatrix} \langle u'u' \rangle & \langle u'v' \rangle & \langle u'w' \rangle \\ \langle v'u' \rangle & \langle v'v' \rangle & \langle v'w' \rangle \end{bmatrix} = \begin{bmatrix} -2K\partial_x u & -K(\partial_x v + \partial_y u) & -\nu_t \partial_z u \\ -K(\partial_x v + \partial_y u) & -2K\partial_y v & -\nu_t \partial_z v \end{bmatrix} . \quad (1.6)$$

Analogously, the buoyancy stress $\langle u_i' b' \rangle$ introduces additional diffusivities K^b and ν_t^b. The horizontal turbulent diffusivities K can be determined from a Smagorinsky-type closure that takes the horizontal model resolution and shear into account. Usually, K^b is then calculated in terms of a prescribed turbulent Prandtl number $K^b = K/\mathrm{Pr}_t$ (for more details see Klingbeil et al., 2022; Schmitt et al., submitted). The vertical turbulent diffusivities ν_t and ν_t^b are highly variable in time and space and, for high-Reynolds number flows as encountered in

this study, typically many orders of magnitude larger than the molecular viscosity. In the publications Schmitt et al. (2024), Peng et al. (submitted) and Schmitt et al. (submitted), the vertical turbulent diffusivities are computed by the General Ocean Turbulence Model (GOTM) with the use of a second-order turbulence closure. This type of closure calculates ν_t and ν_t^b based on the turbulent kinetic energy (TKE) k, a typical length scale, l, or, equivalently, a frequency or the dissipation ϵ, and a set of dimensionless stability functions that represent the effects of shear and stratification on the diffusivities. The two quantities k and l are computed by solving their corresponding transport equations. Only the TKE transport equation is shown here, for the length scale it is referred to the Appendix of Schmitt et al. (2024).

The TKE $k = \frac{1}{2}\langle u_i' u_i' \rangle$ is the kinetic energy of the turbulent velocity fluctuations and its transport equation can be written as

$$\frac{\partial k}{\partial t} = D + P + G - \varepsilon \, . \tag{1.7}$$

On the right hand side, the transport terms D describe transport of TKE by the mean flow, transport by turbulent motions, viscous transport, and pressure transport. The second term on the right is a shear-production term

$$P = -\langle u'w' \rangle \frac{\partial u}{\partial z} - \langle v'w' \rangle \frac{\partial v}{\partial z} = \nu_t S^2 \tag{1.8}$$

with the squared shear $S^2 = (\partial u/\partial z)^2 + (\partial v/\partial z)^2$. It represents the conversion from mean-flow energy to TKE, and vice-versa. The third term is the buoyancy production term

$$G = \langle w'b' \rangle = -\nu_t^b \frac{\partial b}{\partial z} = -\nu_t^b N^2 \tag{1.9}$$

that describes conversion between TKE and potential energy, with the introduction of the Brunt-Väisällä frequency N. Lastly, the final term is the rate of dissipation ε of TKE into internal energy (Burchard, 2002; Olbers et al., 2012).

1.2.3 Boundary Layer Turbulence

Close to a boundary, in this work represented by the air-sea interface, a steady state ($\mathrm{d}k/\mathrm{d}t \approx 0$) and lateral homogeneity can be assumed, which leads to a balance between TKE production and the dissipation rate. Under these assumptions, (1.7) becomes

$$P + G = \varepsilon \, . \tag{1.10}$$

Assuming a neutrally stable boundary layer, the buoyancy production only depends on the incoming or outgoing buoyancy flux B, and can therefore be approximated as $G \approx B$. Likewise, the Reynolds stresses in the shear production term are approximated by a constant friction velocity $u_*^2 = \tau/\rho_0$ that is proportional to the normalized wind stress τ. Very close to a boundary, the flow is dominated by shear production and from the logarithmic law of the wall follows $P = \epsilon = u_*^3/(\kappa z)$, where $\kappa = 0.4$ is known as the von Kármán constant and z describes the distance from the wall (Burchard, 2002). Further away from the boundary, shear production reduces and buoyancy production becomes the dominant term in the TKE production. The Monin-Obhukov length L_{MO} is defined as the distance from the wall, at which the two forces balance ($G = P$), from which follows

$$B = \frac{u_*^3}{\kappa L_{\mathrm{MO}}} \rightarrow L_{\mathrm{MO}} = \frac{u_*^3}{\kappa B} \, . \tag{1.11}$$

L_{MO} forms the basis of the Monin-Obukhov similarity theory (MOST), which is often used to describe the nonlinear turbulent exchange of momentum, heat, and mass between Earth's surface and the overlying atmosphere in weather, climate, and air pollution models (Monin and Obukhov, 1954). Based on dimensional analysis, MOST states that for high Reynolds number flows, in the absence of mean vertical flow, in steady state conditions, and over horizontally homogeneous and flat surfaces, a single nondimensional ratio $\zeta = z/L_{MO}$ fully characterizes the turbulent fluxes and vertical gradients (Stiperski and Calaf, 2023). According to MOST, any mean quantity χ (e.g. momentum, heat) in the surface layer, when properly non-dimensionalized with the respective turbulent scaling variable χ^*, formed from the key variables, can be expressed as a universal function F_χ of the scaling parameter ζ:

$$\frac{\chi}{\chi^*} = F_\chi(\zeta) \, . \tag{1.12}$$

The functional forms of the scaling relations F_χ have to be obtained experimentally, noteworthy is here the landmark 1968 Kansas field experiment by Businger et al. (1971), in which temperature and wind velocity were measured from a tower in the middle of a flat wheat field, leading to exceptional agreements with MOST. There are, however, various shortcomings: MOST assumes flat and horizontally homogeneous terrain, yet it is often applied to more complex topography. There is a lack of scaling of horizontal velocity variances under unstable thermal stratification, and its applicability to the ocean is unclear since the assumptions that lead to (1.10) really only apply to rigid walls. The presence of waves or ocean currents is therefore not properly considered. Hence, the processes introduced in the next sections complicate the exchange between ocean and atmosphere beyond the findings from MOST. The Monin-Obhukov length, however, remains a relevant length scale when parameterizing Diurnal Warm Layers, as shown later on in Section 2.1 which summarizes Schmitt et al. (2024).

1.3 Relevant Small-Scale Processes

As explained in Section 1.2.3, classical boundary layer theory has its limitation, and the small-scale processes investigated in this dissertation, which are all summarized in Fig. 1.1, complicate the energy exchange between ocean and atmosphere. This section therefore introduces the current state of research on Diurnal Warm Layers and Rain Layers, and explains the generation of Langmuir turbulence by surface waves. Next, submesoscale fronts and frontal instabilities are introduced. Lastly, atmospheric feedbacks and their influence the ocean through cold pools, wind bursts and precipitation is explained.

1.3.1 Diurnal Warm Layers

Diurnal Warm Layers (DWLs) form on the surface of the ocean on days with strong solar heating and weak to moderate wind and wave conditions. Lasting from late morning to the evening hours, the characteristic feature of DWLs is a strong temperature stratification down to depths on the order of meters (Price et al., 1986). In the oceanic mixed layer, DWLs lead to a modification of the turbulent motions by trapping the wind stress within the strong stratification. This causes strong turbulence within the DWL and a horizontal acceleration, termed the Diurnal Jet, that persists for as long as the DWL is present and reaches velocities on the order of 0.1 m s^{-1} (Hughes et al., 2020). At the same time, TKE and energy dissipation in the deeper mixed layer are reduced by several orders of magnitude in the presence of a DWL (Moulin et al., 2018).

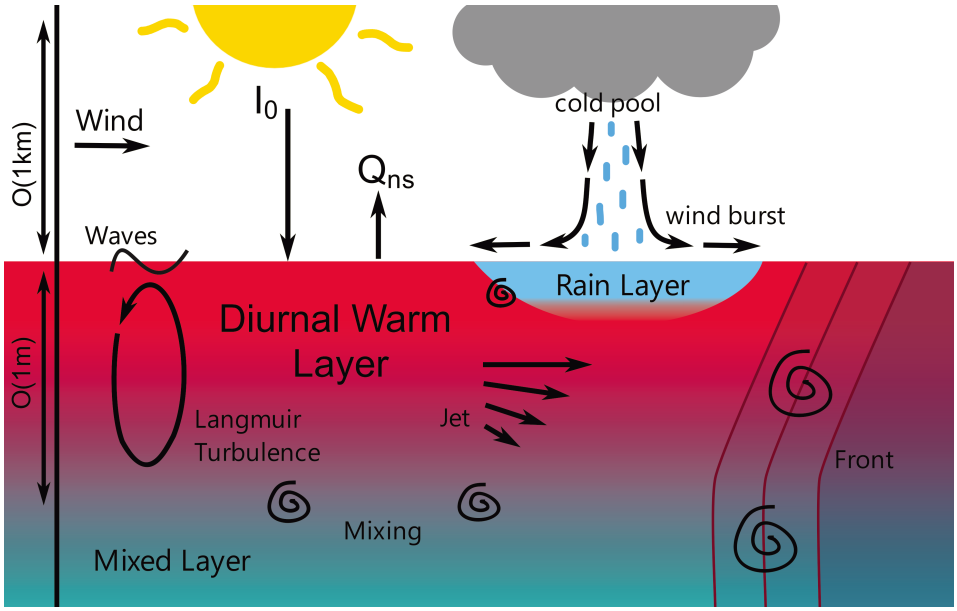

FIGURE 1.1: Process sketch depicting the coexistence of Diurnal Warm Layers, Rain Layers, surface wave turbulence, submesoscale fronts and the exchange of energy with the overlying atmosphere.

A typical DWL evolution at a latitude of 10°N, based on a high-resolution simulation with the model GOTM (see Section 1.2.2 and Section 1.4), is shown in Fig. 1.2. At the surface, the model is forced by a constant wind stress τ, equivalent to 3 m s^{-1} wind speed, and an idealized net heat flux Q_{net} that resembles the typical daily variation of cooling at night time and heating during the day with a maximum at midday. Shortly after Q_{net} becomes positive, a DWL starts to develop that reaches its maximum sea surface temperature (SST) anomaly of 1°C at around 15:00 (see Fig. 1.2b). At this tropical latitude, the inertial period from the Coriolis rotation is much longer than the lifetime of the DWL, which is why the diurnal jet in this simulation is only marginally influenced by the Coriolis force and constantly points in the direction of wind propagation (Fig. 1.2c). The rotation of the jet at higher latitudes with shorter Coriolis periods, and the resulting changes in DWL evolution, are part of the analysis in Schmitt et al. (2024). During the afternoon, the DWL depth starts to increase due to entrainment of colder water at the base of the DWL. This entrainment is the result of wind-driven shear instabilities, as also evident by the gradient Richardson number Ri being close to the critical value 0.25 (Fig. 1.2d). The non-dimensional number $\text{Ri} = N^2/S^2$ compares the destabilizing influence of the wind shear, S, and the stabilizing influence of stratification, represented by N. Large values of Ri indicate that mixing is suppressed, while $\text{Ri} = 0$ is indicative of a well-mixed, convective layer. From instability theory (Smyth and Carpenter, 2019), it was derived that a Richardson number of $\text{Ri} \approx 0.25$ is a necessary criterion for the development of shear instability. The suppression of turbulence below the DWL is evident in both $\text{Ri} > 1$, as well as the reduction in turbulent kinetic energy k (Fig. 1.2e).

DWLs are difficult to observe since they require undisturbed measurements of the ocean surface layer at a high temporal and spatial resolution. Successful measurements of temperature and velocity were obtained using surface following platforms (Hughes et al., 2020; Hughes et al., 2021), drifters (Hans et al., 2024) and autonomous gliders (Peng et al., submitted). Similarly, modelling of DWLs requires high vertical resolutions of ideally < 0.10 m near the surface and small time steps, which is why not only global, but also regional model studies usually do not resolve the surface warming and subsequent mixing suppression in

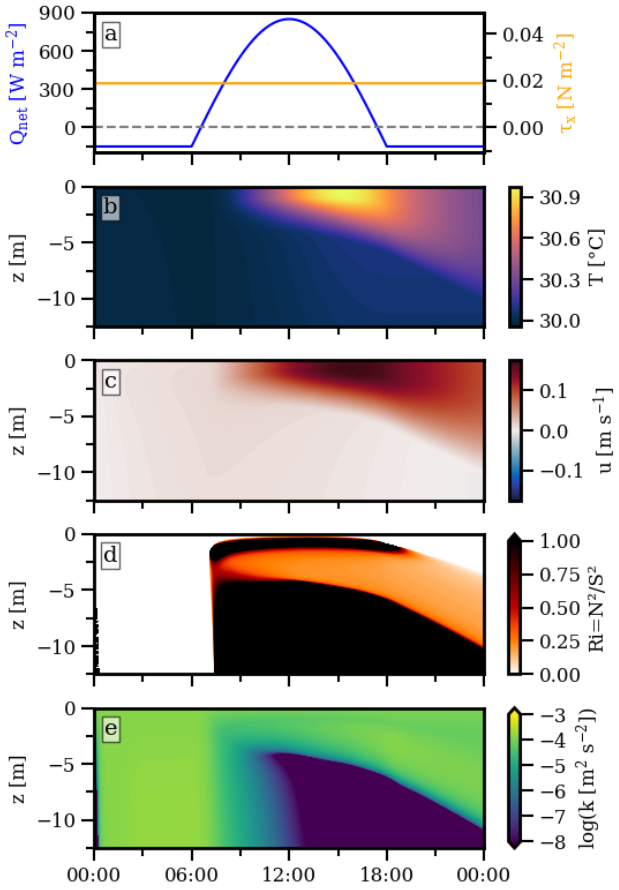

FIGURE 1.2: Time series of DWL evolution with (a) surface heat flux and wind stress, (b) temperature, (c) $u-$velocity in wind direction, (d) gradient Richardson number, and (e) turbulent kinetic energy.

the deeper layers correctly. For these reasons, a parameterization for DWLs is a topic of ongoing research.

The first publication that aimed at finding reliable scaling formulas for the most important DWL bulk properties was the study by Price et al. (1986). Their scaling model uses a critical Richardson number criterion applied to the momentum and heat transport equations to determine the DWL depth h, an average bulk temperature $\overline{T}$ and an average bulk velocity $\overline{V}$, all evaluated at the midday heat flux maximum. In comparisons with observations taken at around 30°N and results from a simple bulk mixing model, the derived scaling performed well. Shortcomings are the assumption that the DWL is noninteractive with the mixed layer below, the lack of a parameterization for different water types with varying shortwave absorption lengths, the lack of surface-wave effects, an uncertainty in the applicability of the scaling at higher latitudes, and missing information about the vertical structure and temporal evolution of DWL temperatures and velocities.

The Price et al. (1986) scaling was expanded upon in the publication by Fairall et al. (1996), in which the authors focused on deriving the evolution of temperature profiles over the course of the day. For this, they integrated the incoming surface fluxes in time and made the assumption that there is a linear gradient in temperature through the warm layer. A three-band spectral parameterization for the absorption of shortwave radiation was introduced, tuned to the water type found at their observational site. Unfortunately, Fairall's

model focuses only on temperature and neglects to derive expressions for the velocity profiles. Furthermore, the dependency of the profiles on latitude and Coriolis frequency f was neglected, and surface-wave effects are still missing. Gentemann et al. (2009) further refined Fairall's model by the use of a nine-band absorption model, again tuned to the clear waters found at their study site. In addition, they introduced reduction rates that are supposed to incorporate the effects of mixing and entrainment at the DWL base, and improved the shape of the temperature profiles from linear to exponential with a dependency on wind speed. These profiles are predicted at each time step in the model and provide an estimate of the vertical temperature structure within the diurnal thermocline that compared well to their observations. On the downside, due to the heavy tuning of the absorption model to fit the observations, the profiles predicted by the Gentemann et al. (2009) model are not universally applicable to all water types. Moreover, the introduced reduction rates are simply derived by fitting to the observations and lack physical reasoning.

All in all, none of the attempts at deriving a scaling for DWLs have been able to incorporate all possible atmospheric forcings, locations and water types. There is a lack of a non-dimensional approach to the problem, and existing proposed scalings were never thoroughly tested over large parameter spaces. Schmitt et al. (2024), included in this dissertation, aims to fill this gap.

1.3.2 Rain Layers

Precipitation on the ocean leads to the formation of thin Rain Layers (RLs), an accumulation of buoyant fresh water on the more saline surface mixed layer. RLs have similar characteristics as DWLs, in that they stably stratify the near ocean surface under low wind conditions and in doing so temporarily stall vertical mixing (Schlüssel et al., 1997; Shackelford et al., 2022). The trapping of momentum causes an acceleration of the fresh water lens, identical to the formation of the Diurnal Jet, which led to the term "slippery layer" (Kudryavtsev and Soloviev, 1990). Float experiments by Shcherbina et al. (2019) in the Eastern Pacific Fresh Pool showed an increased lateral advection of surface waters by 25 km compared to waters at 30 m depth due to this slippery layer effect. The acceleration of the surface current is further increased by the suppression of surface gravity waves under heavy rainfall (Laxague and Zappa, 2020).

Furthermore, RLs can have a significant effect on air-sea CO_2 exchange directly through increased transfer velocity and indirectly by chemical dilution and wet deposition, particularly in regions of low wind and high precipitation (Turk et al., 2010). Although rain was observed to also cool the surface waters, the stabilizing effect of rain freshening on surface buoyancy is reported to be larger than the destabilizing effect of rain cooling on surface buoyancy (Thompson et al., 2019).

1.3.3 Langmuir Turbulence

Langmuir Turbulence (LT), named after its discoverer Irving Langmuir, is a turbulent flow that is caused by the interaction of ocean surface waves with the mean current. Characteristic of LT is the formation of shallow, counter-rotating cells with bands of divergence and convergence at the surface that are aligned with the wind direction (see the schematic in Fig. 1.3). Most observations of LT consist of marine debris, seaweed or bubbles that accumulate at the surface along the convergence bands in long, straight lines. Below the convergence zones, downward facing jets transport surface waters to the base of the mixed layer and inject turbulent kinetic energy to depths well below the depth scale for the surface waves.

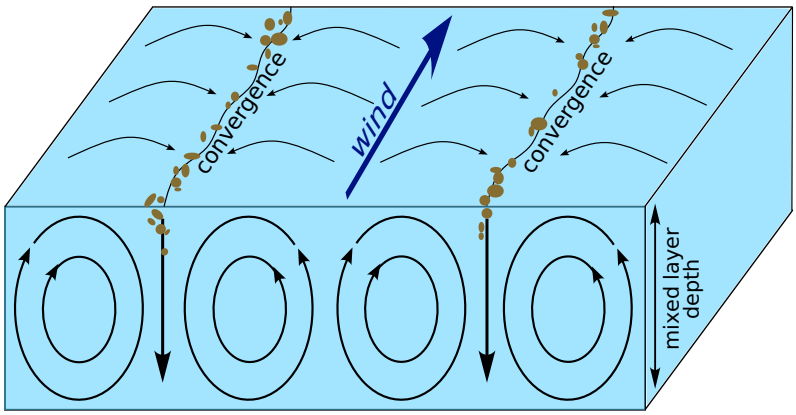

FIGURE 1.3: Schematic of counter-rotating Langmuir cells and resulting divergence and convergence zones with accumulated marine debris.

The generally accepted theoretical interpretation of Langmuir cells is as solutions of the equations derived by Craik and Leibovich (1976), which are a multi-scale theory for the phase-averaged dynamics of low-frequency motions in the presence of high-frequency surface gravity waves with Stokes velocity (McWilliams et al., 1997). The Stokes velocity $\mathbf{u_s}$ is a slow drift in the direction of wave propagation that fluid parcels undergo in the presence of nonlinear, finite amplitude waves, i.e waves whose amplitude can not be considered small in comparison with either the wavelength or the depth of water column (Kundu et al., 2016). In a fully developed sea, where wind and waves are in equilibrium, the Stokes drift can be derived from empirical wave spectra as in Li et al. (2017) which take into account the peak wave number, as well as effects like the directional spreading of wind-waves and the remotely generated swell which lead to the misalignment of wind and waves. The resulting Stokes drift profiles have a surface value u_s^0 that is proportional to the wind speed and decay exponentially with depth. In the theory of Craik and Leibovich (1976), the essential feature to represent the interaction between wave field and mean flow, is the addition of a "vortex force" $\mathbf{u_s} \times \boldsymbol{\omega}$ to the momentum transport equations. Here, $\boldsymbol{\omega} = \boldsymbol{\nabla} \times \mathbf{u}$ represents the curl of the Eulerian velocity $\mathbf{u}$.

Under equilibrium conditions, the turbulent Langmuir number, which is the relevant parameter measuring the competition between shear instability of the wind-driven currents and the vortex force,

$$\mathrm{La} = (u_* / u_s^0)^{\frac{1}{2}} , \tag{1.13}$$

is usually around 0.2 to 0.5 (McWilliams et al., 1997). Generally, LT is considered to be the dominant mixing process when $\mathrm{La} \leq 0.3$. Typical for this range are nonequilibrium swell conditions with low wind and large wave ages (Kukulka et al., 2013).

Overall, LT has the ability to homogenize and deepen the oceanic near surface boundary layer. In the presence of waves and LT, buoyant surface layers like DWLs and RLs are expected to be destabilized and mixed deeper than under wind-driven shear instabilities alone. The interplay between surface heating and LT has been the subject of several

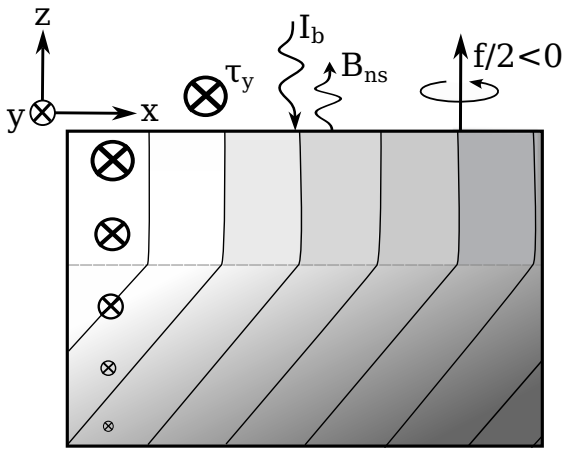

FIGURE 1.4: Schematic of an idealized front, identical to the model set up in Peng et al. (submitted). The gray scale represents density with horizontal and vertical buoyancy gradients M^2 and N^2 and a mixed layer down to a depth depicted by the gray dashed line. The inward pointing arrows show the direction of the thermal current v_g in the y-direction. From Peng et al. (submitted).

high-resolution Large Eddy Simulations (LES), which rely on the computationally expensive solving of the low-pass filtered Craik-Leibovich equations (Min and Noh, 2004; Pearson et al., 2015; Wang et al., 2023). A parameterization of LT was also included in the second-moment model GOTM specifically for the study presented in Schmitt et al. (2024), more on this in Section 1.4.

1.3.4 Submesoscale Fronts

Submesoscale fronts and filaments exist on temporal and spatial scales on the order of hours to days and 0.1–10 km (Peng et al., 2021) and have the ability to re-distribute water properties, including momentum, buoyancy, heat, freshwater, and biogeochemical tracers (Gula et al., 2022). Mesoscale straining leads to a sharpening of frontal gradients in a processes called frontogensis (Capet et al., 2008), which generates submesoscale fronts that are amenable to different types of instability. They are characterized by large horizontal density gradients, which in Fig. 1.4 is represented by a horizontal buoyancy gradient $M^2 = -\partial b/\partial x$ where x is in cross-front direction. Within geostrophically balanced fronts, the hydrostatic pressure gradient is in a balance with the Coriolis force, resulting in a meridional flow that is termed thermal jet or geostrophic current v_g with the thermal wind shear $\mathrm{d}v_g/\mathrm{d}z = M^2/f$ (Taylor and Ferrari, 2010).

Fronts are theorized to provide an energetic link between the large, energy-containing mesoscales and small-scale energy dissipating turbulence through various types of flow instabilities (McWilliams, 2016). Of particular relevance are two instabilities that are expected to occur if the Ertel potential vorticity (PV) q and the Coriolis frequency f attain opposite signs:

$$fq = f(f\mathbf{k} + \boldsymbol{\omega})\boldsymbol{\nabla} b < 0\,. \tag{1.14}$$

Here, $\mathbf{k}$ is the upward unit vector and $\boldsymbol{\omega}$ the vorticity (Haine and Marshall, 1998). If the front is straight ($\partial b/\partial y = 0$), has a constant M^2, a velocity in thermal wind balance and zero

relative vertical vorticity as assumed in the idealized simulations in Taylor and Ferrari (2010) and Peng et al. (submitted), the Ertel PV simplifies to $q = fN^2 - M^4/f$. The two possible types of instability are gravitational instability for $N^2 < 0$, and symmetric instability (SI) for stable stratification and a sufficiently large M^2. In the latter case, the condition in (1.14) is equivalent to a threshold of the balanced Richardson number, $Ri_b = N^2 f^2 / M^4 < 1$ (Taylor and Ferrari, 2010). The development of SI is closely tied to boundary forcing, which is capable of changing the surface layer PV. "Forced" SI refers to SI that develops in response to destabilizing surface forcing. The conditions required for destruction of PV by surface forcing are discussed in Thomas (2005), who showed that fq is reduced when the ocean surface is cooled by non-solar heat fluxes, or when the surface wind stress points in the direction of the geostrophic current, as depicted in Fig. 1.4. The latter process is called a "downfront wind", during which dense water is advected on top of lighter water by the cross-front Ekman flow acting on the horizontal density gradient at the front. Both cooling and downfront wind result in a decrease in surface buoyancy and PV, which triggers SI. Secondary shear instabilities evolve inside the SI structures, providing the final step towards energy dissipation (Taylor and Ferrari, 2009).

On the other hand, surface warming is expected to increase PV, leading to a restratification and stabilization of the surface boundary layer, and potentially also to the generation of DWLs. Diurnal variability in the atmospheric forcing therefore strongly affects the dynamics, stability, and turbulence of submesoscale structures, as previously investigated in Peng et al. (2021). Peng et al. (submitted), summarized in Section 2.2, is the first study in which fronts could be observed under a diurnal forcing that was strong enough to form DWLs.

1.3.5 Atmospheric Feedbacks

As introduced with the above processes, forcing from winds, heating, cooling, and rainfall has a profound influence on the distribution of mass, heat, and momentum in the ocean. In return, the atmosphere can respond to ocean surface conditions, particularly changes in temperature, salinity and currents, by adapting its patterns of cloudiness, rainfall, and winds. Thus, the oceans and atmosphere form a coupled system through the exchange of heat, mass and momentum.

The strength of the latent and sensible heat fluxes radiated by the ocean depend on the humidity and temperature differences between air and water. They are therefore directly influenced by the increase in SST in the presence of a DWL, with estimates for the flux increase ranging from 2-5 W m^{-2}, based on an observational study by Matthews et al. (2014), to up to 100 W m^{-2} in the modelling study of atmosphere-ocean interactions in the tropics by Brilouet et al. (2021). The global increase and effect that this increase has on atmospheric properties like humidity and cloud cover is the main subject of the publication Shevchenko et al. (2023) to which this dissertation contributed (see Section 2.4).

An atmospheric process that influences the mixed layer properties of the ocean through exchange of wind momentum, and in return triggers changes in the surface heat flux, is an atmospheric cold pool. A cold pool is a cold pocket of dense air that forms when rain evaporates during precipitation underneath a cloud. The cold air is denser than its surroundings and therefore sinks towards the air-sea interface. There, it generates a divergent flow that moves radially away from the location of the precipitation and can be felt in the form of strong wind bursts (see Fig. 1.5). As the wind burst spreads outwards, it increases the surface heat fluxes and creates entrainment and lifting of warmer air which may trigger new convection and influence wind patterns and cloud cover (Vogel et al., 2021). Cold pools exist both over land and ocean and are often observed underneath shallow clouds in the trade-wind region of the subtropics (Bony et al., 2017). The effects they have on mixing

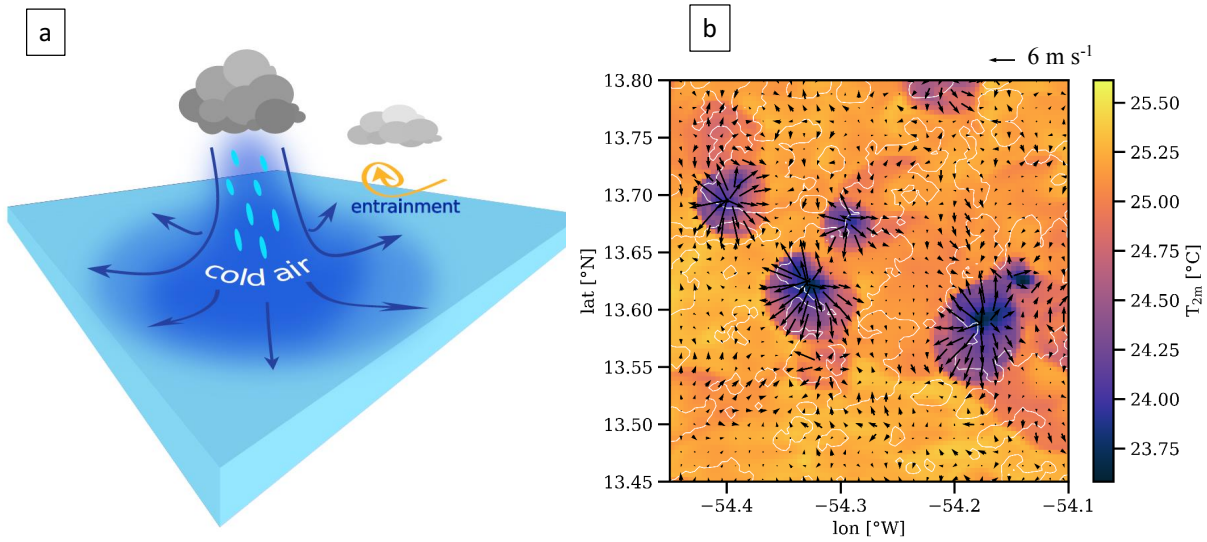

FIGURE 1.5: (a) Process sketch of a cold pool and (b) cold pools as seen in the atmospheric Large Eddy Simulation used as forcing in Schmitt et al. (submitted). Shown in (b) is the 2 m air temperature with the mean wind anomaly as arrows. Several cold pools are clearly visible as dark purple areas surrounded by circular wind bursts. The white contour marks areas with cloud cover $> 10\%$.

of the ocean surface and the influence on the surface fluxes is the main subject of Schmitt et al. (submitted), summarized in Section 2.3.

Last but not least, sharp SST gradients between RLs and the surrounding waters, especially in the presence of DWLs, have been hypothesized to generate horizontal pressure gradients in the atmospheric boundary layer, thus influencing the distribution of atmospheric convection (Lindzen and Nigam, 1987). In the same way, submesoscale fronts are hypothesized to influence air-sea fluxes and atmospheric convection patterns because of their sharp SST gradients, which are sustained even under high winds.

1.4 Methods

The publications included in this dissertation are based on different types of high-resolution models. The following is a brief summary:

- Schmitt et al. (2024) and Peng et al. (submitted) use the one-dimensional water column model GOTM (General Ocean Turbulence Model) that solves the one-dimensional versions of the transport equations in (1.2), (1.3) and (1.5) (Umlauf et al., 2005). Specifically for Schmitt et al. (2024), the increased mixing by waves and LT is included through additional terms in the transport equations. Firstly, the Stokes drift components u_s and v_s are added to the velocities in the Coriolis term in (1.2) and (1.3). Secondly, the vertical Reynolds stresses are modified to include an additional Stokes diffusivity ν_t^S and the vertical gradient of the Stokes velocity. For example, in (1.2), the modified stress becomes $\langle u'w' \rangle = -(\nu_t \partial u/\partial z + \nu_t^S \partial u_s/\partial z)$. The stability functions needed

to calculate ν_t and ν_t^S were also modified to include LT effects following the work in Harcourt (2015). Lastly, an additional Stokes shear production term P_S was added to the TKE transport equation in (1.7), as well as to the length scale transport equation. More details on the model modifications can be found in Schmitt et al. (2024) itself. To validate these new additions, GOTM was compared to a Large Eddy Simulation (LES), which is a high-resolution three-dimensional model that solves the low-pass filtered Craik-Leibovich equations and is often used for idealized process studies. The low-pass filtering can be viewed as a sufficiently fine time- and spatial-averaging such that the mean flow quantities still resolve the large energy-containing eddies down to the inertial subrange. Applying this filter reduces the computational cost of the simulations by ignoring the smallest length scales, which are the most computationally expensive to resolve. Still, the full momentum balance must be solved, including the vertical velocity transport equation and the nonhydrostatic pressure contribution. The unresolved subgrid scales are assumed to be isotropic and can therefore be included in the form of simple parameterizations. Details on the LES set up in Schmitt et al. (2024) can be found in Pham et al. (2023) and in the Appendix of Schmitt et al. (2024).

- In Peng et al. (submitted), constant horizontal density and pressure gradients, as well as a geostrophic current v_g, are prescribed to represent the presence of a front with infinite width, as inspired by the idealized model set up in Taylor and Ferrari (2010). This set up makes it possible to account for some of the key physical processes in two-dimensional fronts with the help of the one-dimensional (vertical) model GOTM.

- Schmitt et al. (submitted) uses the three-dimensional model GETM (General Estuarine Transport Model), which was designed to model the advective transport of water masses in highly dynamic estuaries and coastal oceans (Burchard and Bolding, 2002). In GETM, the transport equations in (1.2)-(1.5) are solved under the Boussinesq and hydrostatic approximations. GETM is coupled to GOTM for the computation of the vertical turbulent fluxes and uses the second-order turbulence closure explained in Section 1.2.2.

- Lastly, Shevchenko et al. (2023) is based on the fully coupled, global ICON (ICOsahedral Nonhydrostatic) climate model. Here, ocean and atmosphere are computed with state of the art 5 km scale resolution on an icosahedral–triangular grid (a detailed description of the configuration can be found in Hohenegger et al. (2023)). The ocean model again solves (1.2)-(1.5) and the vertical grid resolution was increased near the surface to capture diurnal warming. The main difference in this set up is that the parameterization of turbulent vertical mixing relies on the closure suggested by Gaspar et al. (1990). This closure, also based on the eddy viscosity assumption, is a simplified form of the second order closure explained in Section 1.2.2 as it relies on using a constant instead of the dimensionless stability functions.

Chapter 2

Results

This chapter summarizes the main results from the publications included in this dissertation. They are structured by increasing model complexity. Firstly, the publication Schmitt et al. (2024) introduces DWLs in an idealized, one-dimensional framework with a focus on the interplay with wave turbulence and the search for a global parameterization. Peng et al. (submitted) uses the same model, but combines it with observations of DWLs and fronts from a measurement campaign. This is followed by the results from Schmitt et al. (submitted), in which the three-dimensional structure of DWLs and the reaction of the surface layer to high-resolution forcing is investigated in a realistic setting. Lastly, Shevchenko et al. (2023) focuses on the atmospheric feedback caused by DWLs with the use of a global, fully coupled model configuration.

2.1 Idealized Beginnings: "Diurnal Warm Layers in the Ocean: Energetics, Non-dimensional Scaling, and Parameterization"

Schmitt et al. (2024) focused on DWLs with the intent to assess the relevance, implications, and parameterizations of different processes (in particular: Langmuir Turbulence (LT), rotational effects in high-latitude DWLs, and shortwave absorption) across the entire physically relevant parameter space. As already mentioned in Section 1.4, the results were obtained with the one-dimensional second-moment turbulence model GOTM, which was validated using a high-resolution LES.

GOTM solves the one-dimensional transport equations introduced in Section 1.2.1 for an infinitely deep water column and was forced at the upper boundary by idealized atmospheric fluxes. These idealized fluxes, depicted in Fig. 2.1, reflect typical atmospheric forcings and help to identify the key parameters that control DWL evolution. The solar radiative heat flux I, or its equivalent buoyancy flux I_b, is zero at night time and varies periodically during the day with a maximum at midday, a period of $T_p = 24$ h and a sunlight duration T_d during which $I_b > 0$. The non-solar heat or buoyancy loss B_0, representing long-wave, latent and sensible fluxes, is assumed constant. The resulting total surface buoyancy flux $B = I_b + B_0$ has a midday maximum $B_{\max}$ and a, for DWLs characteristic, heating time T_h during which $B > 0$. The penetration of short-wave radiation into the water column was computed from a simple model of the form

$$I(z) = I_0 \mathrm{e}^{\frac{z}{\eta}} , \tag{2.1}$$

where I_0 denotes the surface flux and η the shortwave absorption scale. In addition, all simulations were forced at the surface with a constant wind stress $\tau_x/\rho_0 = u_*^2$ in $x-$direction, introducing a constant friction velocity u_*. All in all, this forcing, although strongly idealized,

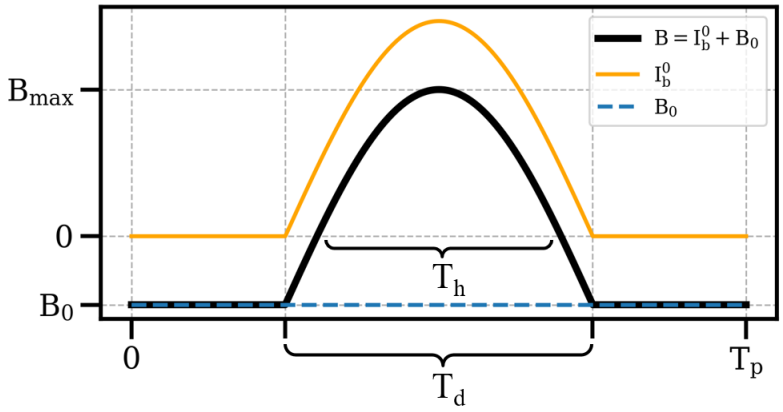

FIGURE 2.1: Idealized buoyancy forcing with the radiative buoyancy flux at the surface, I_b^0, the non-solar surface buoyancy flux, B_0, and their sum, the total surface buoyancy flux B for the special case with $T_d = T_p/2$. From Schmitt et al. (2024).

is able to realistically capture DWL evolution (Fig. 1.2 in Section 1.3.1 shows an example of a typical DWL evolution using this idealized forcing).

As explained in Section 1.4, specifically for this publication, it was decided to include a LT parameterization in GOTM, for which previous work by Li et al. (2017) and Harcourt (2013); Harcourt (2015) was used. The Stokes drift $\mathbf{u}_s$ was computed from a theoretical wave spectrum assuming equilibrium waves, which resulted in a constant turbulent Langmuir number $\mathrm{La} = (u_*/u_s^0)^{1/2} = 0.3$.

The results in Schmitt et al. (2024) are divided into three sections, beginning with the model validation. This is followed by an assessment of the influence of the Coriolis force on DWLs at high latitudes. Finally, the key-nondimensional parameters in DWL evolution are identified, before the existing parameterization by Price et al. (1986) is thoroughly tested in various parameter space studies. The following subsections summarize the findings.

2.1.1 Model Validation

To validate GOTM and its performance concerning LT and DWL evolution, it was compared to LES results for two selected scenarios, one including Stokes drift and LT, the other excluding those processes ($u_s = 0$). The horizontally averaged profiles from the three dimensional LES fields were compared to the second-moment model results. Both models used the same wave model for the computation of the Stokes drift, identical atmospheric forcing and the same vertical resolution of 0.05 m at the surface, gradually coarsening towards the bottom which was deep enough as to not influence the results.

Fig. 2.2 compares the DWL evolution of buoyancy b and zonal velocity u in the LES and GOTM for four selected points in time. Overall, the characteristics of the LES are well reproduced by GOTM, including DWL thicknesses and vertical structures of the profiles. The main differences are near the surface, where the LES shows a strong reduction of stratification and shear due to the mixing from surface waves. While GOTM captures this reduction well in case of the surface velocity (panels d,f), the reduction in buoyancy is existent but underestimated. Surprisingly, LT does not lead to a strong modification in DWL thicknesses or bulk values, but the reduction in surface temperature and velocity by almost 50% has important implications for air-sea coupling. Overall, the performance of the second-moment

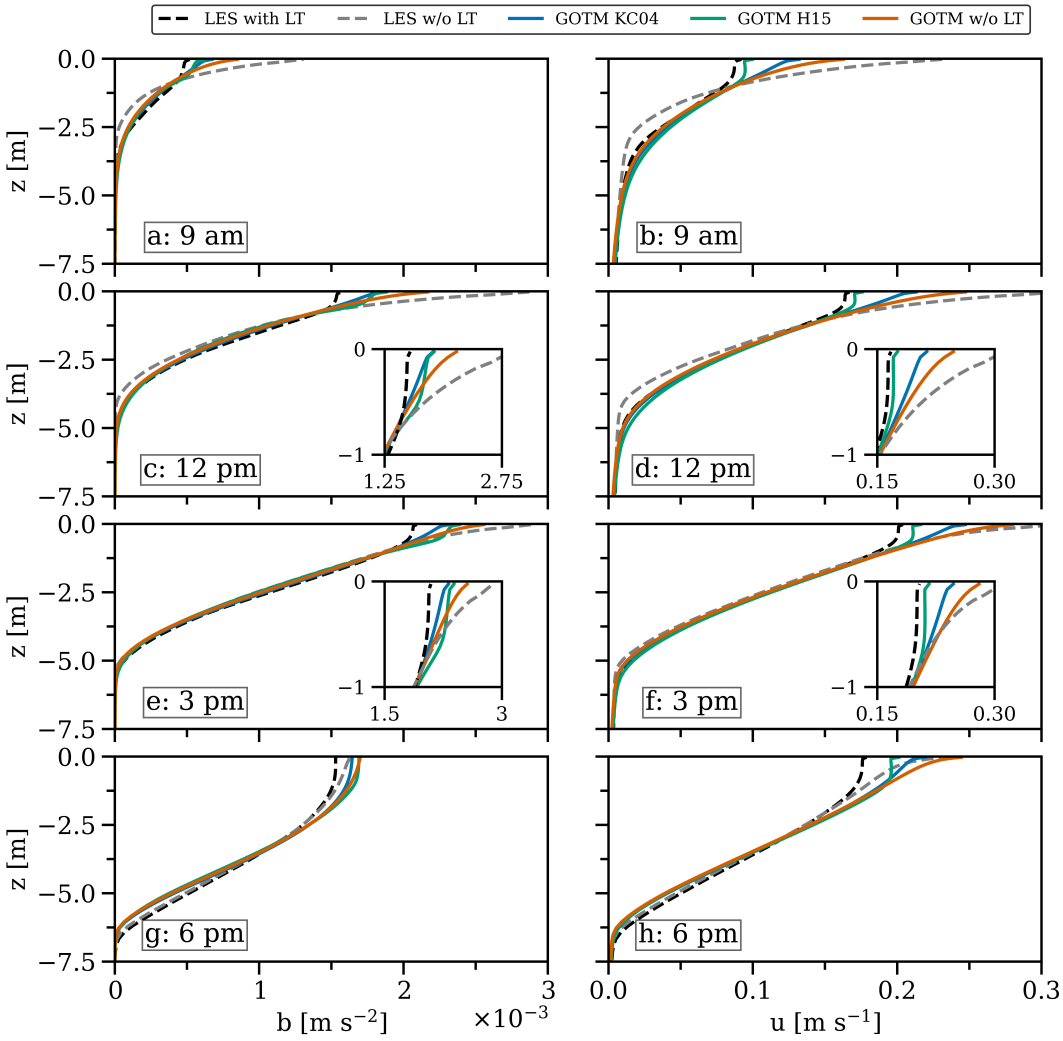

FIGURE 2.2: Comparison of LES and GOTM simulations for (a,c,e,g) buoyancy and (b,d,f,h) u-component of the velocity at four time points. Dashed lines show LES results with (black) and without (gray) LT. Colored lines correspond to different second-moment models as indicated in the legend. Inlays panels in (c-f) show enlarged views of the near-surface region. From Schmitt et al. (2024).

model is excellent and it was concluded that the more advanced Langmuir paramtererization by Harcourt (2015), denoted H15 in the figure legend, performed better than the previous parameterization by Kantha and Clayson (2004) (denoted KC04). It was therefore used in the remainder of Schmitt et al. (2024).

2.1.2 DWL Energy Budgets

To study the effects of rotation and heating time on high-latitude versus tropical DWLs, Schmitt et al. (2024) derived budgets for the kinetic and potential energy of DWLs, E_k and E_{pot}. The kinetic energy budget, derived from the equations in (1.2) and (1.3), results in:

$$\frac{\mathrm{d}}{\mathrm{d}t}E_k = \frac{\mathrm{d}}{\mathrm{d}t}\int_{z_{\text{ref}}}^{0}\frac{u^2+v^2}{2}\mathrm{d}z = \mathbf{u}^0\cdot\tau^0 + \int_{z_{\text{ref}}}^{0} f\mathbf{k}\cdot(\mathbf{u}\times\mathbf{u}_s)\,\mathrm{d}z - \int_{z_{\text{ref}}}^{0} P\mathrm{d}z\,. \tag{2.2}$$

Here, **k** is again the upward unit vector, P the shear production term, and subscript 0 denotes surface values. The terms on the right hand side are interpreted as (a) the work performed by the wind stress on the DWL, (b) the exchange of kinetic energy with the surface wave field due to the effect of rotation , and (c) the loss of kinetic energy to TKE k by turbulence shear production.

Similarly, the potential energy budget follows from (1.5) and can be rearranged to yield

$$\underbrace{\varphi h(B_0 + I_b^0 - \frac{\overline{I}_b}{\varphi})}_{\substack{\text{work required to}\\ \text{mix down buoyancy}\\ \text{added near surface}}} + \underbrace{\varphi h \overline{b} w_e}_{\substack{\text{work required}\\ \text{to mix up}\\ \text{entrained fluid}}} + \underbrace{\frac{\mathrm{d}\varphi}{\mathrm{d}t}\overline{b}h^2}_{\substack{\text{work required to}\\ \text{change the DWL}\\ \text{buoyancy structure}}} = \underbrace{-\int_{z_{\mathrm{ref}}}^{0} G \mathrm{d}z}_{\substack{\text{work done}\\ \text{by turbulence}}} , \tag{2.3}$$

where the profile shape factor φ, the DWL thickness h, the entrainment velocity $w_e = \mathrm{d}h/\mathrm{d}t$, the average bulk buoyancy $\overline{b}$, and $\overline{I}_b = h^{-1} \int_{z_{\mathrm{ref}}}^{0} I_b \mathrm{d}z$ is introduced. Schmitt et al. (2024) then continued with evaluating these budgets for two DWL scenarios. One was a typical tropical case at 10°N (Coriolis period T_f =69 hours) with a high peak radiative heat flux at midday and a day length of 12 hours. The other simulated high latitude DWLs at 70°N (T_f =12 hours) during the summer months with a weaker midday heat flux maximum, but a longer day length of 18 hours.

Comparing the kinetic energy budget for both scenarios, Schmitt et al. (2024) showed that the work performed by the wind stress is the main source of kinetic energy. In the tropics, this energy source is mainly used to accelerate the DWL over midday and increase kinetic energy. It is only in the late afternoon that entrainment at the bottom of the DWL starts to dominate, acceleration slows down and the shear production term becomes the main energy sink. At high latitudes, the Coriolis force veers the near surface velocity out of the wind direction in the early afternoon. This leads to a decrease in wind work and a decay of kinetic energy that is transferred to turbulence shear production instead. Overall, the energy turnover is reduced by the Coriolis rotation, which leads to a collaps of entrainment and an increased importance of the Stokes shear production and LT.

In the potential energy budget, Schmitt et al. (2024) showed that, for both tropical and high-latitude DWLs, during midday, the largest fraction of the work performed by turbulence is used to mix down buoyancy added neat the surface by the solar heating. For the tropical case, the work required to entrain dense bottom waters becomes the dominant term in the afternoon and evening, while the work required to change the buoyancy structure within the DWL remains negligible. This is in contrast to the high-latitude case, where entrainment never becomes an energetically relevant factor, but instead there is a stronger tendency to a well-mixed DWL towards the evening, shown by a dominance of the term representing the work required to change the DWL buoyancy structure.

2.1.3 Key Parameters and Parameterization

This chapter of Schmitt et al. (2024) started with the identification of all dimensional parameters that effect the strength and evolution of DWLs. For velocity scale, the constant friction velocity u_* was chosen, which, combined with the maximum total buoyancy flux at midday B_{max}, yields the relevant length scale $L = u_*^3/B_{\mathrm{max}}$ that it proportional to the Monin-Obukhov length evaluated at midday. Together with the heating period T_h (see Fig. 2.1), these parameters were used to scale the transport and boundary equations, as well as the surface forcing including the wave field, which resulted in the identification of the key non-dimensional parameters of the problem, namely a non-dimensional Coriolis parameter

$\hat{f} = fT_h = 2\pi T_h/T_f$, a forcing ratio $R = u_*^2/(T_h B_{\max})$, and a non-dimensional absorption scale $\hat{\eta} = \eta/L$. Additional non-dimensional parameters were introduced by the surface buoyancy forcing and the wave and turbulence model: a buoyancy flux ratio $B_0/B_{\max}$, a time ratio T_h/T_p, a non-dimensional surface roughness $\hat{z}_0$, and a non-dimensional peak wave number $\hat{k}_p$. However, as was shown in parameter space studies, these additional non-dimensional parameters have negligible impact on the bulk properties of the DWL. Therefore, the focus for the last part of Schmitt et al. (2024) was on the remaining parameters $\hat{f}$, R and $\hat{\eta}$ in the search for a universal parameterization.

As already mentioned in Section 1.3.1, the first and most often cited scaling relations for DWL bulk properties were formulated by Price et al. (1986) (PWP86 from here on), and included estimates for the DWL thickness h and the bulk anomalies for buoyancy $\overline{b}$ and velocity $\overline{V}$, all evaluated at midday. Non-dimensionalized and changed to the notation of Schmitt et al. (2024), these scaling relations can be written as

$$\hat{h} = \frac{h}{L} = a_1 \cdot R^{-1/2} F(\hat{f}) \,, \tag{2.4}$$

$$\hat{\overline{b}} = \frac{\overline{b}\, u_*}{B_{\max}} = a_2 \cdot R^{-1/2} F(\hat{f})^{-1} \,, \tag{2.5}$$

$$\hat{\overline{V}} = \frac{\overline{V}}{u_*} = a_3 \cdot R^{-1/2} \,, \tag{2.6}$$

with the non-dimensional model constants a_1, a_2, and a_3, and F a non-dimensional model function accounting for the effect of rotation:

$$F(\hat{f}) = \frac{1}{\hat{f}} \left[2 - 2\cos(\hat{f}/2)\right]^{\frac{1}{2}} \,. \tag{2.7}$$

To test these scaling relations for their accuracy over the entire physically relevant parameter space, a thorough parameter space study was performed in Schmitt et al. (2024) in which R and $\hat{f}$, or, equivalently, T_h/T_f, were varied while keeping all other non-dimensional parameters constant. The results, shown in Fig. 2.3, prove that the performance of the PWP86 scaling is generally excellent, even at high latitudes. Plotted here are simulations results for $\hat{h}$, $\hat{\overline{b}}$ and $\hat{\overline{V}}$, normalized by the scaling relations in (2.4), (2.5) and (2.6) to show any variability in scaling constants that would reveal errors in the scaling. The only region where the PWP86 scaling fails is the regime with $R < 7.7 \cdot 10^{-4}$, which corresponds to weak winds and strong buoyancy forcing. Here, DWLs remain very shallow, so that molecular transport becomes of comparable importance as turbulent transport. This, however, is not accounted for in the scaling and also the model performance becomes questionable under these circumstances due to the low Reynolds numbers involved here.

Nonetheless, for the regime $R > 7.7 \cdot 10^{-4}$, Schmitt et al. (2024) presents a set of new scaling constants that include the effects of Langmuir turbulence and result in reliable bulk parameters with maximum deviations being only on the order of 10%. In addition to the midday bulk values, it was possible to show that the scaling works equally well for the buoyancy peak in the afternoon, typically between 15:00 to 16:30, given the scaling coefficients are adjusted to the afternoon values presented in this paper.

The PWP86 scaling relations investigated up to here assumed only surface absorption, therefore $\hat{\eta}$ was set to zero during all these parameter runs. As this is not a sensible assumption in nature, lastly, Schmitt et al. (2024) investigated the impact of penetrating short-wave radiation on the bulk properties by carrying out a parameter space study with varying R

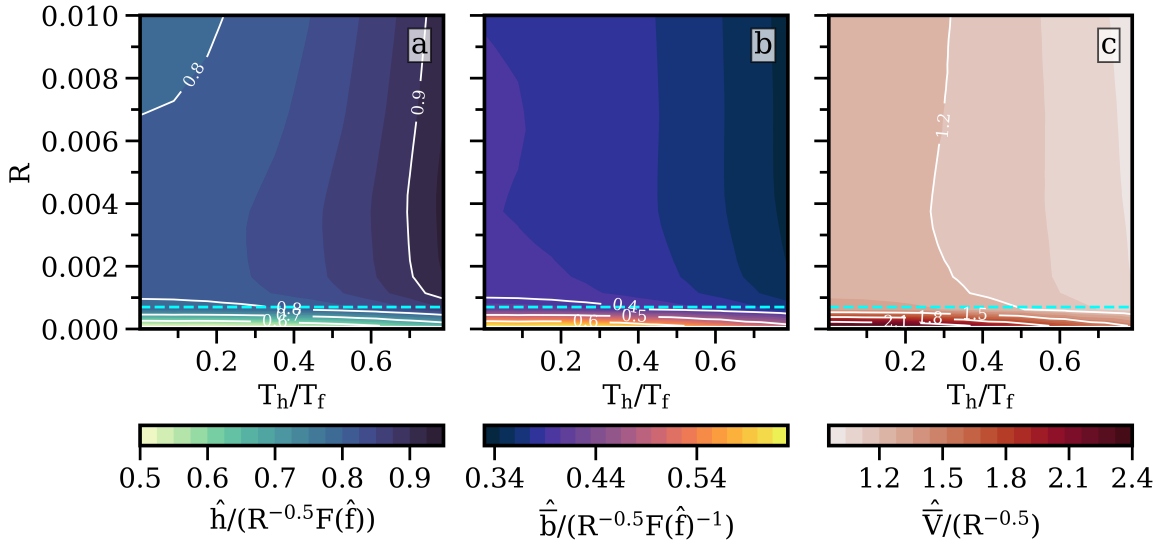

FIGURE 2.3: DWL properties as functions of $R = u_*^2/(B_{\max}T_h)$ and $T_h/T_f = \hat{f}/(2\pi)$. Shown are midday values of (a) DWL thickness, (b) DWL bulk buoyancy, and (c) DWL bulk velocity, normalized by the PWP86 scalings in (2.4), (2.5), and (2.6). This implies that the results shown in (a)-(c) correspond to PWP86 model constants a_i. The blue line shows the critical value of R below which DWL turbulence does not occur. From Schmitt et al. (2024).

and $\hat{\eta}$ at both a tropical and a high latitude. A non-dimensional function

$$J(\hat{h}/\hat{\eta}) = \left(1 - 6.9e^{-\hat{h}/\hat{\eta}}\right)^{-\frac{3}{2}} \tag{2.8}$$

was introduced to the scaling relations of PWP86 and results showed that this modified scaling captures the bulk properties well for the tropical case. For the high-latitude case, the agreement is moderate, which led to the conclusion that future work is needed for an accurate representation of different water types in a DWL parameterization. An additional interesting finding was that both LT and η affect the near surface structure of buoyancy and velocity profiles and surface values, which is of special relevance in coupled models.

2.2 Introducing Observations: "Interactions between diurnal warm layers and surface-layer fronts"

Peng et al. (submitted) focused on the interaction of DWLs and submesoscale fronts, which were introduced in Section 1.3.4, in a subtropical region. The basis of the study were measurements taken over the course of 6 days at a study area located on the Australian Northwest Shelf. Characteristic of this site is a strong tidal forcing and frequently occurring submesoscale eddies, fronts and filaments. In addition, Peng et al. (submitted) employed an idealized model to further analyse the findings from the observations.

Key to observing DWLs was an autonomous glider equipped with sensors to measure temperature and salinity. The glider slowly moved up and down the water column while following a track that crossed the front twice. In addition, a fixed mooring was deployed at a depth of around 200 m inside the frontal region. This mooring consisted of a chain of

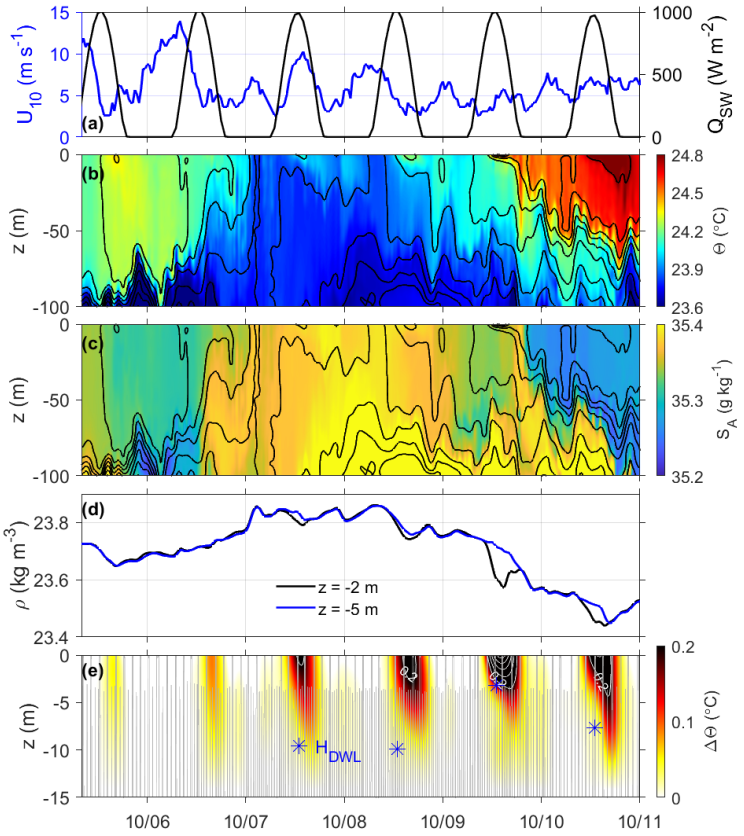

FIGURE 2.4: The evolution of (a) 10-m wind speed (blue) and shortwave radiation (black), (b) glider-based conservative temperature, (c) absolute salinity, (d) near-surface density, and (e) near-surface temperature anomaly, relative to the 15-m reference level. Black lines in panels (b) and (c) denote isopycnals (potential density) at intervals of 0.025 kg m^{-3}. Grey lines and white contours in panel (e) denote glider dive profiles and near-surface temperature anomaly at intervals of 0.2^{o}C, respectively, and blue stars indicate the scaling of diurnal warm layer depth (which is out of range on 6 October and thus not shown). From Peng et al. (submitted).

temperature sensors and an Acoustic Doppler Current Profiler that allowed for the measurement of currents between 19 and 155 m depth. Satellite data provided the SST distribution, which was used to determine the lateral buoyancy gradient M^2 (see Section 1.3.4). Meteorological data of surface wind and heat fluxes was taken from reanalysis. The vertical turbulent diffusivity was estimated from the mooring data and involves the measured shear S, the background temperature gradient and the turbulent temperature fluctuations based on Ivey et al. (2018); Ivey et al. (2021). Note that this paper uses the conservative temperature, which is denoted by the symbol Θ. More details on all of the instruments and data processing is found in Peng et al. (submitted).

The following is a brief summary of the observations.

2.2.1 Results from Observations

The glider data analysed in Peng et al. (submitted) is shown in Fig. 2.4. As evident from panel Fig. 2.4a, the surface forcing was favourable for the formation of DWLs with strong

midday peaks in short wave radiation and moderate to weak winds, staying below 10 m s^{-1} for the majority of the survey period. The temperature, salinity and near-surface density data clearly shows two crossings of the front, which extends down to 80 m, with strong horizontal temperature gradients and tilted isopycnals. Estimates of M^2 from satellite data showed a horizontal surface buoyancy gradient that fluctuated around $1.5 - 2 \cdot 10^{-7}$ s^{-2} during the survey period. The near surface temperature anomaly, shown in Fig. 2.4e, reveals that, from 7 October onwards, robust DWLs formed with temperature anomalies from 0.1 to 0.7°C, indicated by white contours in panel e. These observations agree closely with the midday DWL thicknesses calculated from the DWL scaling relation in (2.4), supporting the scaling derived in Schmitt et al. (2024).

Satellite SST showed that the frontal region was at the mooring location between 6-9 October, which could be confirmed by the temperature sensors at the mooring. Strong vertical shear $\mathcal{O}(10^{-5} - 10^{-4})$ s^{-2} was measured between 7-8 October throughout the entire surface boundary layer, even during daytime, when the glider data showed the presence of DWLs. Unfortunately, the upper 19 m were not measured by the instruments on the mooring, so information about the Diurnal Jet and associated shear is missing from the velocity data. Further analysis concluded that the high shear below the DWL can be associated with the thermal current or jet, v_g, that was already introduced in Section 1.3.4. Comparison with the strength of M^2 further confirmed this. This observation led to a more detailed investigation of the coexistence of DWLs and frontal instability, as will be summarized next.

2.2.2 DWL-Front Interactions

Peng et al. (submitted) continued with showing that, between 7 and 8 October, the entire surface boundary layer below the DWL exhibited gradient Richardson numbers Ri < 1 and, locally, even below 0.25, which indicates conditions favourable for shear instability and other types of frontal instability, such as SI. Furthermore, turbulent diffusivities were calculated to increase with depth, different from what would be expected for surface-driven turbulence, with peak values of around 10^{-3} m^2 s^{-1} at 55 m depth. The presence of a DWL without a front is expected to increase Ri and decrease diffusivity in the deeper surface layers (see Fig. 1.2d,e), hence the measurements indicated instabilities that were not directly driven by surface forcing. Possible drivers are local processes, including frontal instability (such as SI), local shear instability, or other local dynamics such as internal tides.

To further investigate this, Peng et al. (submitted) used an idealized GOTM set up (depicted in Fig. 1.4 and explained in Section 1.4) of an infinite front under idealized diurnal forcing. The boundary and initial conditions were chosen to closely match the observations, with a constant M^2 and a constant downfront wind. Three simulations are compared, one of a front without diurnal forcing, one of a DWL without a front ($M^2 = 0$), and one including both processes. Only the last one will be summarized here, for the other see Peng et al. (submitted). Note that the notation and definition for the buoyancy flux has changed between Schmitt et al. (2024) and Peng et al. (submitted). In Peng et al. (submitted), the total buoyancy flux, previously B, is denoted as B_0, and defined as negative for ocean heating (see Fig. 2.5a).

The simulation in Fig. 2.5 shows the typical diurnal variations in vertical stratification and shear associated with DWL dynamics near the surface, and the key features of vertical frontal stratification with according N^2 and S^2 in the subsurface layers below the DWL, closely matching the observations. Comparison with the DWL only simulation revealed a reduction in the near-surface magnitudes of N^2 and S^2 and a reduction of the day-night temperature variations when a front is present. This suggests that frontal dynamics can play an additional role in modulating the development of DWLs by mixing near-surface momentum and density through additional frontal turbulence. This additional turbulence

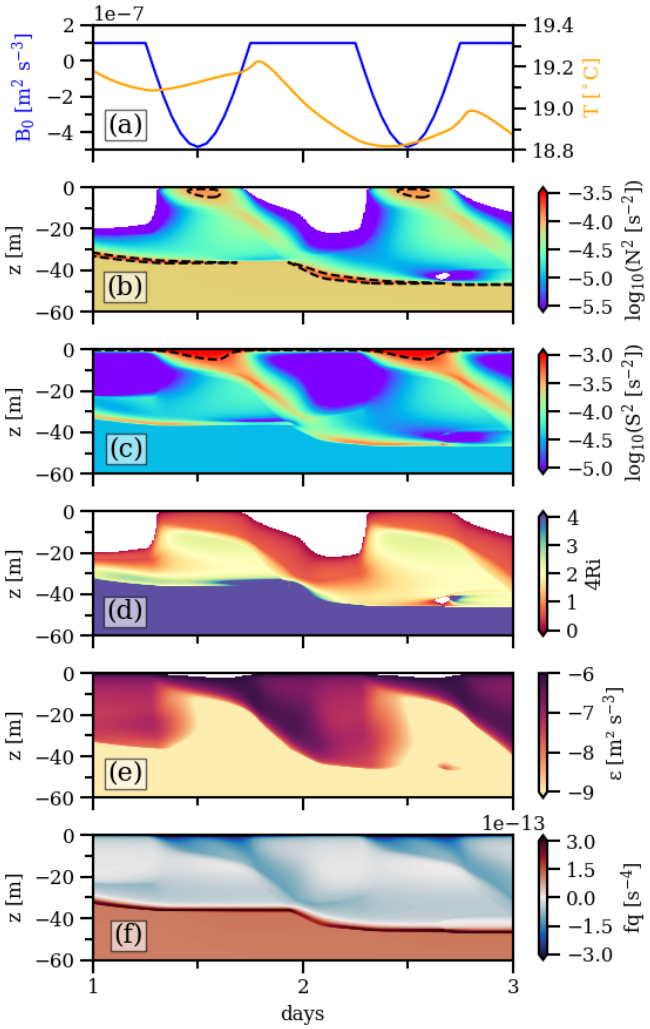

FIGURE 2.5: The GOTM simulation with DWLs and fronts: Evolution of (a) net surface buoyancy flux and temperature at $z = -5$ m, (b) vertical stratification, (c) vertical shear, (d) 4 times gradient Richardson number, (e) turbulence energy dissipation rate, and (f) Ertel potential vorticity. Dashed lines marked in (b) and (c) denote $N^2 = 10^{-4}$ s^{-2} and $S^2 = 10^{-3.5}$ s^{-2}. From Peng et al. (submitted).

is also the reason why, during the evening, the diurnal shear reaches deeper layers compared to conditions without a front. Moreover, the Ertel PV in Fig. 2.5f, calculated based on (1.14), shows negative regions within and below the DWL, suggesting instability with respect to a mix of shear instability and SI. The main conclusion from the GOTM simulations in Peng et al. (submitted) therefore was that even in the presence of a DWL, the underlying regions remain close to marginal instability and may become sporadically turbulent if an additional disturbance or energy source, e.g. due to internal tides, becomes available. This seems to be the case in the turbulence measurements at the mooring location.

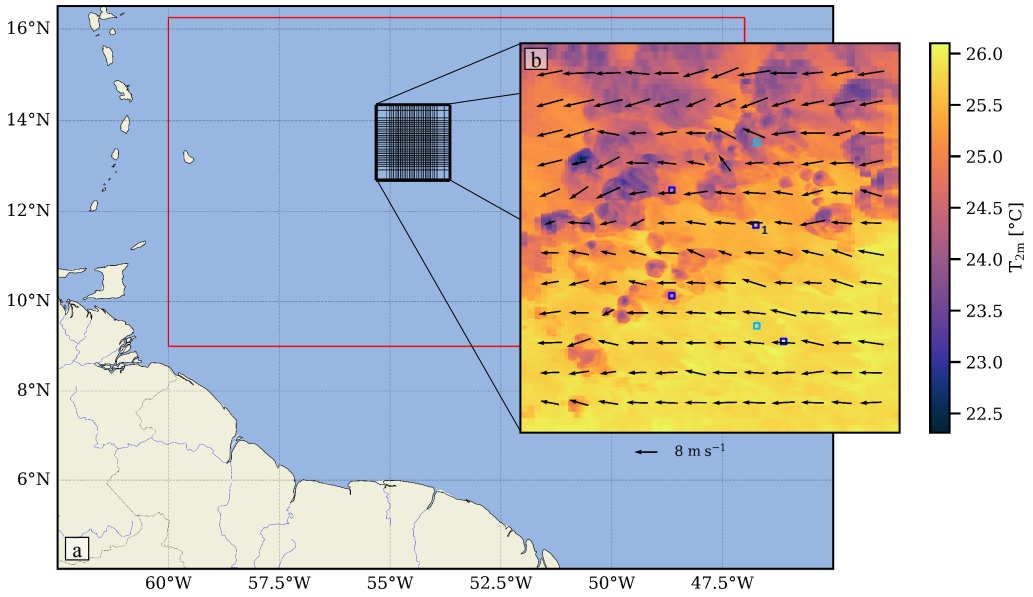

FIGURE 2.6: Overview map showing the size and location of the model domains off the coast of South America. The black box in (a) represents the ocean model grid with an increase in grid size towards the boundaries (only every 10th grid line shown). The red box marks the boundary of the ICON-LES with 312 m resolution. The inset (b) shows an enlarged view of the ocean model domain with an example snapshot of the air temperature at 2 m height on 8 February at 09:50 local time. Black arrows in (b) show the wind speed at 10 m above the surface, representative of the constant trade winds that were present during the entire simulation period. Dark and light blue squares in (b) mark the initial locations of the near-surface tracers discussed in 2.3.2. From Schmitt et al. (submitted).

2.3 Realistic Forcing: "Three-dimensional Ocean Surface Layer Response to Rain, Wind bursts and Diurnal Heating"

For Schmitt et al. (submitted), the idealized set up from the one-dimensional study in Schmitt et al. (2024) was expanded to three dimensions and the forcing was replaced by realistic, high-resolution atmosphere model output. The goal was to study the direct response of the oceanic mixed layer to small-scale atmospheric processes that remain unresolved in most regional and global model studies.

The forcing was provided from an ICON-LES of a region in the trade-wind zone of the tropical North Atlantic. The LES has a high horizontal resolution of 312 m and is able to directly resolve deep and shallow convection. It was designed to complement the EUREC^{4}A field campaign that took place in February 2020 and focused on the interplay between clouds and convection (Bony et al., 2017). Characteristic features of the LES are small, frequently occuring cold pools (as explained in Section 1.3.5) that are advected across the model domain by moderate easterly trade winds (see the inset in Fig. 2.6b for an example snap shot of the air temperature and winds).

The ocean was modelled using GETM for a period of 8 days and covers the area of

200x200 km from 12.65-14.35°N and 55.35-53.65°W (see black grid in Fig. 2.6a) with a high-resolution central area between 13-14°N and 55-54°W that is resolved by 430 m. As in Schmitt et al. (2024), the vertical resolution near the surface allowed for the resolution of DWLs and the bottom was sufficiently below the halocline as to not effect the results. Surface fluxes of wind stress and non-solar heat were computed from the bulk algorithms presented in Fairall et al. (2003).

The analysis of Schmitt et al. (submitted) focused on two gaps in the study of air-sea interactions. Firstly, it is known that the cold air, circular wind bursts and cloud cover in the presence of cold pools all have a direct influence on the strength of the non-solar surface heat fluxes. However, few model studies have so far been able to resolve these effects, a notable exception being the publication by Brilouet et al. (2023). However, Schmitt et al. (submitted) is the first study that is located in the trade-wind zone, uses a three-dimensional model, and has an area large enough to provide statistics on the change in surface fluxes in the presence of cold pools. Secondly, while the reduction of the vertical diffusivity in the presence of stabilizing DWLs and RLs has been the subject of various publications, there has been less focus on the three-dimensional structures and processes that affect mixing and dispersion in the ocean surface layer, such as increased transport due to the Diurnal Jet, and increased mixing by wind bursts surrounding cold pools. The high-resolution three-dimensional ocean model customized set up presented in Schmitt et al. (submitted) is the first that was designed with the study of these processes in mind. In the following, the results are briefly summarized.

2.3.1 Impact on Air-Sea Fluxes

Following Brilouet et al. (2023), cold pools in Schmitt et al. (submitted) were defined as areas in which the the air temperature anomaly exceeds the threshold

$$T'_{2\mathrm{m}} = T_{2\mathrm{m}} - \langle T_{2\mathrm{m}} \rangle < -0.3^{\circ}\mathrm{C}\ , \tag{2.9}$$

where $\langle \cdot \rangle$ indicates the mean over the high-resolution central model area between 13-14°N and 55-54°W, and primes the deviation from the mean (see an example in Fig. 2.7a). Due to the constant trade winds present in this study, all cold pools are moving from east to west, and wind anomalies within cold pools, U'_{cp}, are unequal on the western and eastern edges of the cold pools, termed "leading" and "trailing edges", due to the superposition of circular wind bursts and trade winds. On the leading edge, wind anomalies are positive, while the trailing edges are characterized by negative wind anomalies (see Fig. 2.7b). The wind, together with the cloud cover and air temperature, are the main factors in the strength of the surface heat fluxes. The analysis in Schmitt et al. (submitted) therefore began with an evaluation of the spatial variability of the total non-solar heat flux Q_{ns} and its components, the long-wave radiation Q_{lw}, latent heat Q_{lat} and sensible heat Q_{sen}, in the presence of cold pools for a selected in time point representative of the entire data set.

Focusing on the total non-solar heat flux first, Fig. 2.7c shows that the highest heat losses with the most negative Q_{ns} are found in areas without cold pools in the northern part of the high-resolution central model area, as well as at the leading edges of the cold pools, where trade winds and cold-pool wind bursts are aligned. Schmitt et al. (submitted) showed that the latent heat contributes approx 60% to the total Q_{ns} with same behaviour in the presence of cold pools. The long-wave heat flux, here depicted in Fig. 2.7d, has the second largest contribution to the total surface heat flux with approx. 35% and is reduced underneath cloud cover, which often coincides with cold pools, but is not strictly limited to the same areas. Lastly, the sensible heat flux was shown to have the most negligible contribution to the total heat flux with only 5%. It showed the largest heat loss inside cold pool areas due to a larger $T_a - \mathrm{SST}$ difference caused by the drop in air temperature. Overall, the net

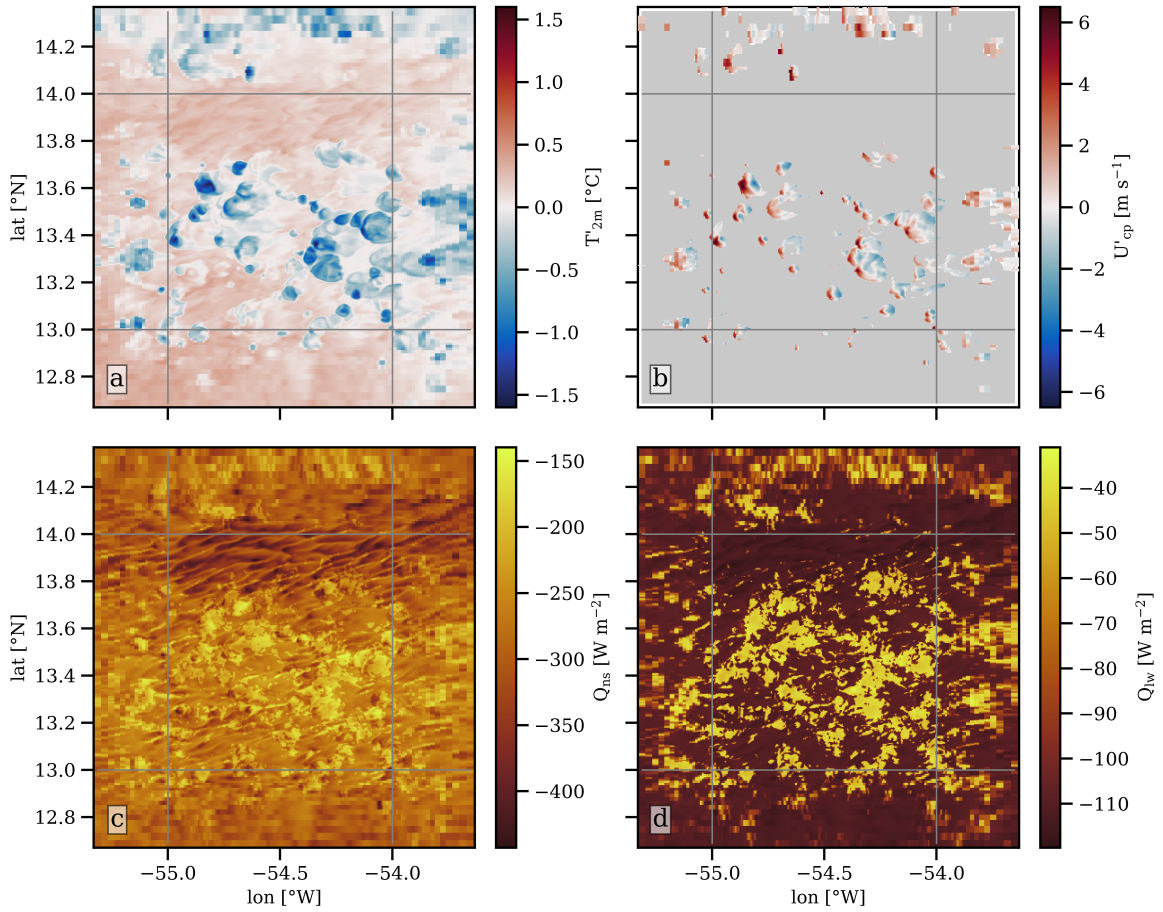

FIGURE 2.7: The model domain on 5 February, 23:00 local time with (a) air temperature anomaly T'_{2m}, (b) wind anomaly U'_{cp} within the cold pools, (c) the total non-solar heat flux and (d) net long-wave radiation. Gray areas in panel (b) show regions blocked by the cold pool mask. Gray vertical and horizontal lines mark the high-resolution part of the domain. Modified from Figures 3 and 4 in Schmitt et al. (submitted).

effect of these opposing trends inside cold pools remained unclear, therefore, Schmitt et al. (submitted) continued with an investigation of the temporal evolution.

The time series of the mean non-solar surface fluxes over the 8 days of the model run showed, first of all, that the fluxes' evolution was dominated by changes in the mean wind speed. Despite the presence of DWLs in the mean SST signal, which are known to lead to an increase in surface fluxes (Brilouet et al., 2021), there was instead a visible reduction of Q_{ns} during the day due to a concurrent reduction of the mean winds which over-compensated the impact of the DWLs. The diurnal reduction in trade winds is not fully understood, but the phenomenon is widely observed in the trade wind zone (Savazzi et al., 2022). Moreover, the time series showed that the Q_{ns} heat loss was larger on the leading edges of the cold pools than on the trailing edges, but, when averaged over the entire cold pool area, the heat loss was smaller than in the surrounding regions by on average 30 W m^{-2}. This could be explained by three factors: (i) areas with cold pools are characterized by higher humidity, (ii) the cold pool areas are typically characterized by lower mean wind speeds in our study (iii) areas with cold pools have higher cloud cover. (i) and (ii) both reduce the latent heat loss by on overage 15 W m^{-2}. (iii) increases the atmospheric long-wave back radiation,

and therefore reduces the net long-wave heat loss to the ocean by on average 24 W m^{-2}. Although there is an increase in sensible heat loss in the presence of cold pools by on average 9 W m^{-2} and an increase on the leading edges due to positive wind anomalies, both effects do not compensate the overall reduction of non-solar surface heat loss in the presence of cold pools.

2.3.2 Impact on Surface Layer Processes

Focusing on the ocean surface layer next, Schmitt et al. (submitted) investigated how the small-scale variability in winds and surface fluxes affected the three-dimensional structures and processes that are responsible for mixing and dispersion. The simulations showed an unexpected lateral variability in DWL temperature and thickness distribution, as evident in the meridional cross-section shown in Fig. 2.8a. This is mirrored in a variability of the horizontal and vertical mixing coefficients (Fig. 2.8c,d), with possible consequences for ecosystem processes. The stronger RLs also show a direct impact on the mixing coefficients (Fig. 2.8b,d) but, due to the weakness of the precipitation events in this study, this effect is small and transient.

To gain insights into these ocean processes that would be "sub-grid" in coarser-resolution models in terms of both atmospheric forcing fields and ocean surface-layer processes, Schmitt et al. (submitted) conducted several tracer release experiments. Four tracer patches were released in the surface layer at different locations of the model domain (dark blue squares in Fig. 2.6b) at the start of the simulation and their temporal evolution was tracked by fitting a 2D Gaussian distribution to the (normalized) depth-integrated tracer concentration C for each tracer patch at each time step.

Assuming that the normalized tracer concentration in each patch has a total mass M and a Dirac delta distribution at time $t = 0$, the two-dimensional anisotropic diffusion equation has a known solution of the form

$$C = \frac{M}{2\pi\sigma_{\hat{x}}\sigma_{\hat{y}}} \exp\left(-\frac{\hat{x}^2}{2\sigma_{\hat{x}}^2} - \frac{\hat{y}^2}{2\sigma_{\hat{y}}^2}\right) , \tag{2.10}$$

corresponding in shape to an anisotropic Gaussian distribution in $\hat{x}$ and $\hat{y}$ with variances $\sigma_{\hat{x}}^2 = 2K_{\hat{x}}t$ and $\sigma_{\hat{y}}^2 = 2K_{\hat{y}}t$, respectively. $K_{\hat{x}}$ and $K_{\hat{y}}$ are the spatially constant diffusivities in the time-dependent directions of $\hat{x}$ and $\hat{y}$ and can be computed from the observed spreading rates according to

$$K_{\hat{x},\hat{y}} = \frac{1}{2}\frac{\partial\sigma_{\hat{x},\hat{y}}^2}{\partial t} . \tag{2.11}$$

The time evolution of the fitted 2-σ confidence ellipses for Tracer 1 (marked with "1" in Fig. 2.6b) is shown in Fig. 2.9a as an example for all tracers. The Gaussian distribution fit starts off as a circle with equal standard deviations $\sigma_{\hat{x}} = \sigma_{\hat{y}}$, however, within the next days, the ellipses start to stretch and rotate out of the wind direction, while the entire tracer patch is advected north-west, clearly indicating the relevance of Ekman effects. Most interestingly, however, is that all tracer patches experienced a strongly anisotropic spreading in the horizontal with the largest spreading rates found along a direction oriented approximately 15-25 degrees to the right of the mean wind direction. The resulting variances (Fig. 2.9b) show very little growth in the $\hat{y}$-direction when compared to the strong spreading observed along the major $\hat{x}$-axis. The growth of $\sigma_{\hat{x}}$ occurs intermittently with the largest spreading rates observed each day during the afternoon and evening hours (see for example the yellow area), followed by a nighttime plateau with strongly reduced spreading rates (blue area).

Schmitt et al. (submitted) found the explanation for this strong anisotropy to be the presence of the Diurnal Jet. Over the course of the afternoon, the jet displaces the surface tracers

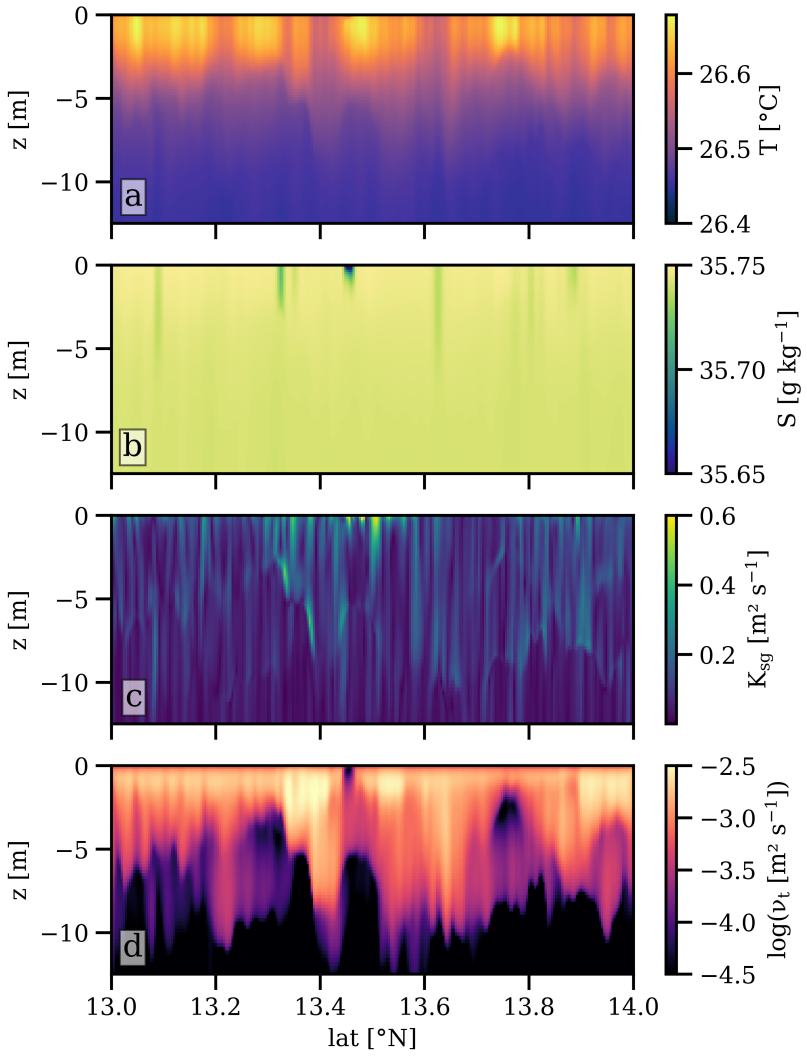

FIGURE 2.8: Cross section along 54.8°W with (a) temperature, (b) salinity, (c) horizontal subgrid diffusivity, (d) vertical turbulent diffusivity. From Schmitt et al. (submitted).

relative to the underlying waters by several kilometers. At the same time, vertical mixing is confined to the DWL, suggesting a decoupling of the laterally advected tracer inside the DWL from the underlying waters. This differential advection process is reflected in a stretching of the vertically integrated tracer patch in the direction of the Diurnal Jet, or, mathematically, in an increase in $\sigma_{\hat{x}}$, as observed in Fig. 2.9b. The angle of rotation of the major axis of the tracer patch to the right of the mean wind direction reflects the Ekman-induced veering of the diurnal jet out of the wind direction. In the evening hours, the tracer evolution is dominated by entrainment and DWL deepening, and increasing vertical diffusivity homogenizes the tracer the entire surface layer. Vertical mixing, however, does not change the horizontal distribution of the vertically integrated tracer concentrations, which explains the nighttime plateau. Overall, the anisotropic tracer spreading was found to be largely a result of a DWL-induced shear-dispersion mechanism, combining differential tracer advection due to the presence of DWLs during daytime, with nighttime vertical mixing. Calculated 24 h average diffusivities based on (2.11) showed that $K_{\hat{x}}$ is $\mathcal{O}(10)$ m^2 s^{-1}, and with that 10-30 times larger than $K_{\hat{y}}$.

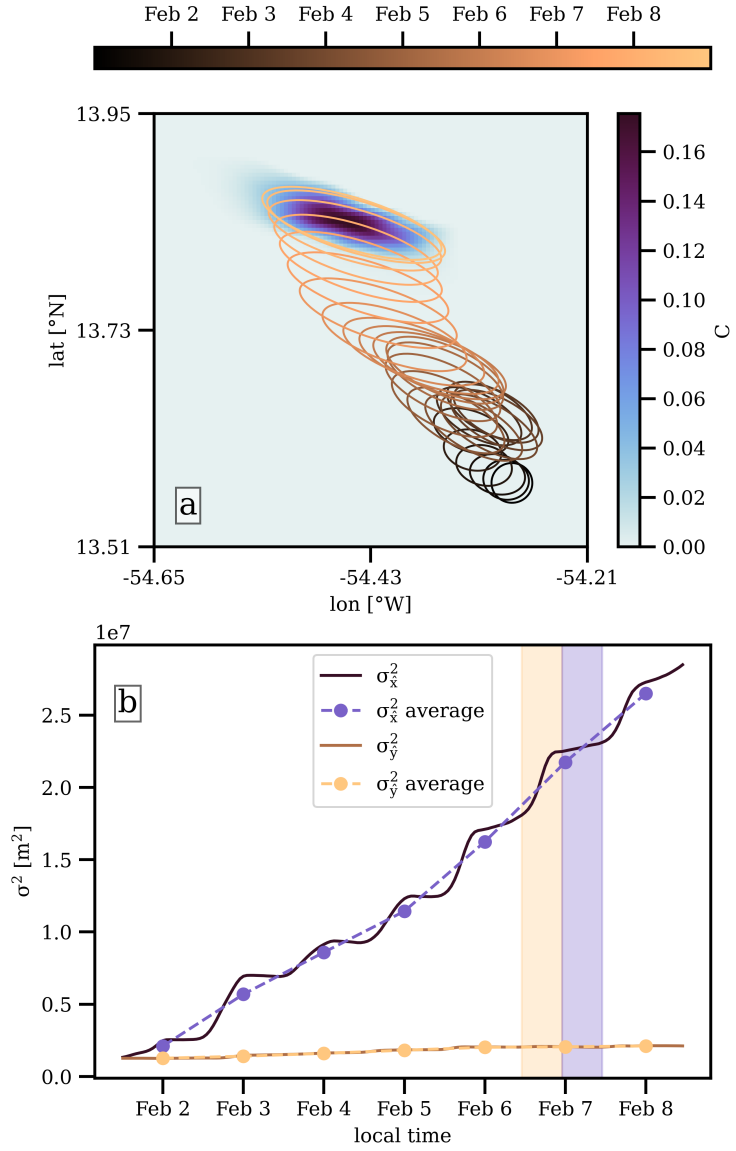

FIGURE 2.9: Evolution of Tracer 1 with (a) depth integrated normalized concentration on 8 February, 12:00 local time and evolution of fitted 2-σ tracer isocontours according to (2.10) over the entire time range, (b) time series of variances in major ($\hat{x}$) and minor ($\hat{y}$) axes directions with 24 h averages marked. Yellow and blue areas mark daytime and nighttime spreading periods discussed in the text. Modified from Fig. 9 in Schmitt et al. (submitted).

Schmitt et al. (submitted) also investigated the impact of the small-scale atmospheric variability (especially regarding the effect of cold pools and associated wind bursts and RLs) on horizontal tracer dispersion, but found it to be negligible. The reasons for this are the horizontal resolution of the model and the time scales of the relevant processes, which cause a transport that is not resolved. However, beyond the potential direct advective impact in even finer models, the wind burst-induced velocity anomalies were found to induce small-scale horizontal strain, which was mirrored in an increased subgrid-scale dispersion rate, although of a smaller magnitude than the DWL-induced diffusivities.

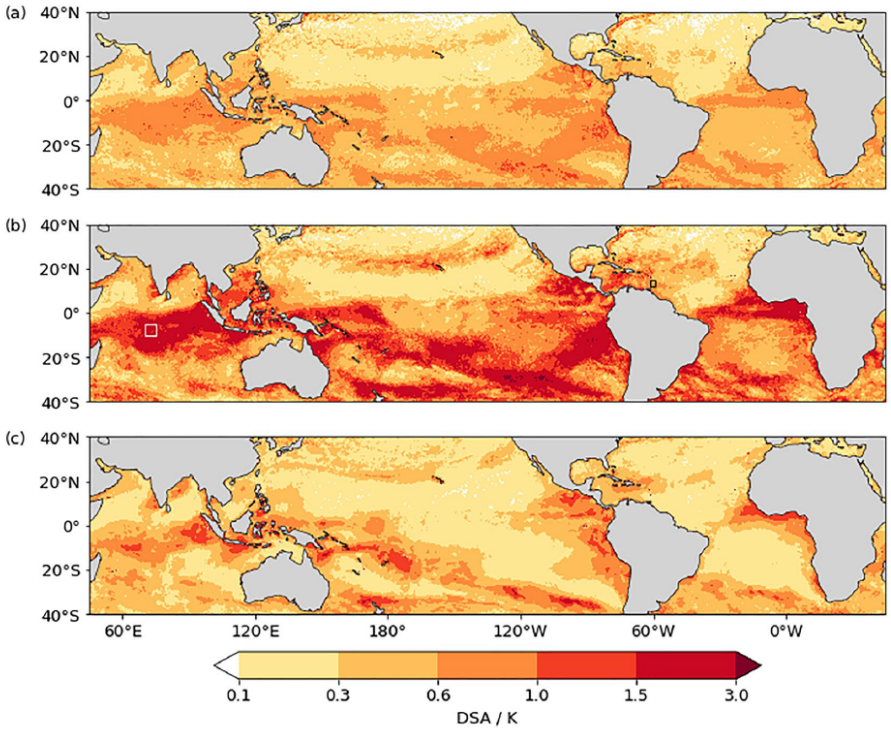

FIGURE 2.10: Magnitude of the diurnal SST amplitude (DSA), averaged between 22 and 30 January 2020 in (a) S_{control}, (b) $S_{+\text{DWL}}$, and (c) ERA5. The white rectangle in (b) designates an area in the Indian ocean that is analyzed later on, and the black rectangle designates the EUREC^{4}A campaign area. From Shevchenko et al. (2023).

2.4 Coupled Global Study: "Impact of Diurnal Warm Layers on Atmospheric Convection"

Shevchenko et al. (2023) was the first publication that extended the question of interactions between DWLs and atmospheric convection to a realistic, global framework with resolved convection and directly resolved DWLs by using a kilometer-scale global coupled simulation. Particular interest was on whether the presence of DWLs enhances cloud cover (CC) in a time frame of several days and if so, whether this happens through a direct moistening by the latent heat flux Q_{lat} (abbreviated by LHF in this study), or by enhancing the spatial gradient in SST and mesoscale circulations.

The analysis in Shevchenko et al. (2023) was based on two model simulations. The reference set up, named S_{control}, used the ICON model in its Sapphire configuration with a horizontal grid spacing of approximately 5 km, which is at the boundary of resolving convection (Hohenegger et al., 2023). The ocean component had 128 vertical levels, starting at 2 m at the surface and gradually growing with depth. The second simulation, $S_{+\text{DWL}}$, differed in only one setting: Here, the ocean was resolved with 139 vertical levels, allowing for an increase in resolution near the surface, starting here at 0.5 m. The layer thickness of the $S_{+\text{DWL}}$ simulation was determined using GOTM and it was ensured that it allows for the accurate modelling of DWL temperature evolution. The analysis then concentrated on the tropics, which is defined in Shevchenko et al. (2023) as the area comprised between 40°N and 40°S.

DWLs were defined as places with a diurnal SST amplitude (DSA) larger than 0.1°C. SST

in the simulation was defined as the temperature in the uppermost layer, which means that in $S_{+\mathrm{DWL}}$ it is the average temperature over 0.5 m and in S_{control} the average temperature over 2 m. This difference is not corrected for, since the main interest of Shevchenko et al. (2023) is the response of the atmosphere. Fig. 2.10 compares the DSA magnitude for both $S_{+\mathrm{DWL}}$ and $S_{+\mathrm{control}}$ to results from ERA5, a reanalysis that combines model data with observations (Hersbach et al., 2023). DWLs appear frequently and the spatial distribution is in moderately good agreement with ERA5. While for S_{control} the DSA field appears nearly homogeneous and the extremes are underestimated compared to ERA5, as expected from the use of thick ocean vertical layers, the amplitudes in $S_{+\mathrm{DWL}}$ are much larger than in the reanalysis, with values twice as high. The overestimation probably is because of insufficient vertical mixing in the upper layers of the ocean, an error that requires further future investigation. However, as this study concentrated on the atmospheric effect of the DWLs, this problem does not jeopardize the analysis, and if anything indicates that the simulated effects are too strong.

Apart from the overestimated amplitudes, the spatial organisation of DWLs was captured well in the model, with the strongest DWLs in areas with little cloud cover, high shortwave radiation and low wind speeds. The majority of DWLs had a small horizontal extend on the $\mathcal{O}(10)$ km^2, but there were also a few DWLs that extend to 10^6 km^2. They were not persistent, with 80% of all episodes lasting 5 days or less. The dependency of DSA on wind speed and heat flux was reproduced as expected and a comparison with Glider data from the EUREC^{4}A campaign showed good agreement in vertical structure and timing of maximum DSA despite the overestimation in heat anomaly.

The main analysis then focused on assessing the impact of DWLs on convective clouds by analyzing the differences between the simulations S_{control} and $S_{+\mathrm{DWL}}$ at places where DWLs of a certain magnitude are present in $S_{+\mathrm{DWL}}$. For this, the ocean was divided into squares and the hourly maximal SST difference between $S_{+\mathrm{DWL}}$ and S_{control} during a day, denoted by ΔSST, was computed. The analysis only included the first 4 days after the start of each simulation, during which the simulations remain highly correlated, before diverging due to the chaotic nature of the atmosphere. The following is a summary of the results.

2.4.1 Effects on Convection

Firstly, Shevchenko et al. (2023) investigated the effect of higher ΔSST on the latent heat flux (LHF) and the column water vapor path (WVP).

As shown in Fig. 2.11a, the LHF is increased when DWLs are present, with a peak around noon on every day. The increase of WVP (Fig. 2.11b) after 12 hr reflects the increase in moisture due to increased LHF. While LHF reacts immediately and is tied directly to differences in temperature, the effect on WVP is delayed by several hours and persists over the following days without losing its magnitude. The dip just before 12 h is likely caused by a weakening in convergence of moisture due to the weakening winds required for DWL formation. The analysis was accompanied by statistical t-tests for equality of means for independent samples with different variances. In Fig. 2.11c,d, p-values smaller than 0.005 indicate that the differences observed visually are highly significant even on the third day. Nonetheless, when compared to the global averages of the two quantities over the ocean, which are ca. 130 W m^{-2} for LHF and ca. 34.6 kg m^{-2} for WVP, the increase in the presence of DWLs is small. A plausible reason for this is that DWLs develop in wind still areas. LHF increases with higher SST, but it also scales linearly with wind, which means that the impact of DWLs on the LHF remains small.

For the impact of DWLs on clouds, Shevchenko et al. (2023) analysed the total CC and cloud liquid water (CLW) path. Both showed a similar behaviour: on midday of the first day, DWL regions exhibit dips whose magnitude is positively correlated with the ΔSST amplitude (see Fig. 2.12a,c). The reason for this is that stronger DWLs generally appear in areas

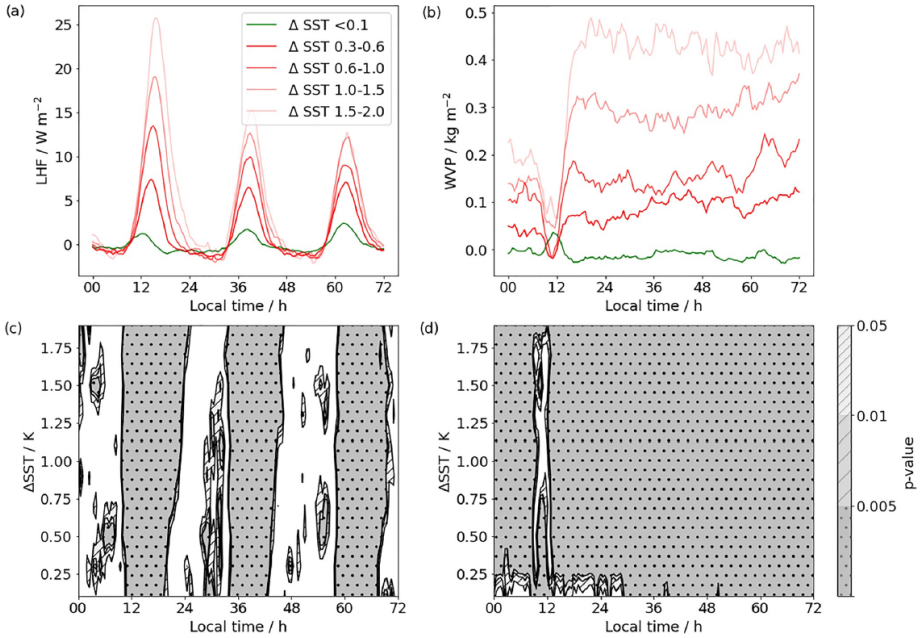

FIGURE 2.11: Time series of $S_{+\mathrm{DWL}} - S_{\mathrm{control}}$ and t-test significance levels in bins of 0.1 K for latent heat flux (a, c) and water vapor path (b, d). On panel c and d, white means not significant. From Shevchenko et al. (2023).

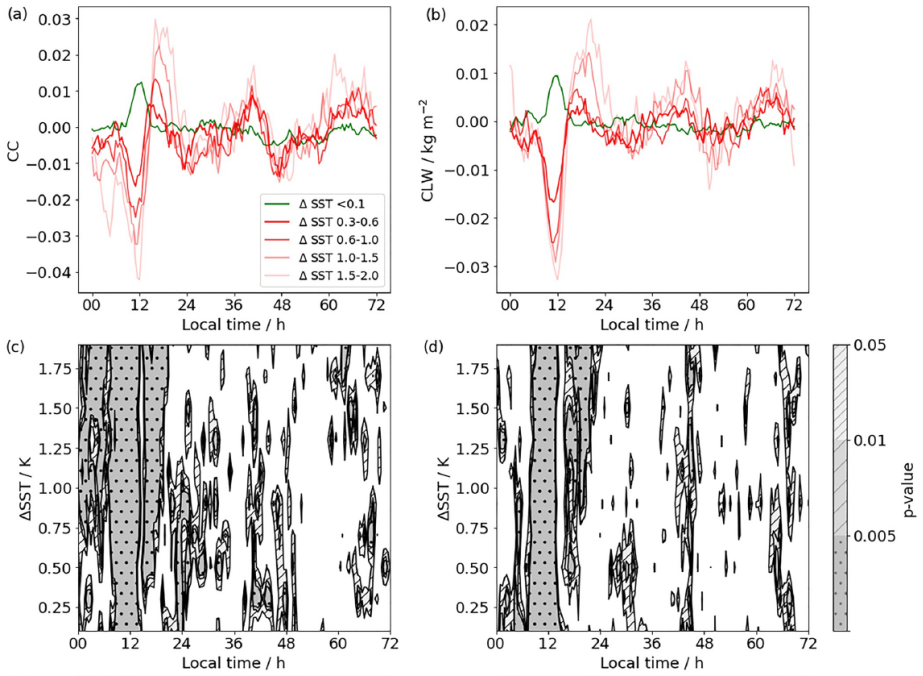

FIGURE 2.12: Time series of $S_{+\mathrm{DWL}} - S_{\mathrm{control}}$ and t-test significance levels in bins of 0.1 K for cloud cover (a, c) and cloud liquid water (b, d). On panel c and d, white means not significant. Modified from Shevchenko et al. (2023).

with low cloud amount. Shortly after midday, CC and CLW both show a growth that is statistically significant starting from an SST amplitude of 0.3 K and lasts for 5-6 h. The second and third day show the same behaviour, however here the deviation is barely significant. Overall, the average increase in CC is about 0.2% and the increase in CLW about 1% even for very large ΔSST, which remains a very small effect. Therefore, Shevchenko et al. (2023) concluded that DWLs do not significantly increase the global mean of CC or CLW path. Differentiating between shallow and deep clouds did not lead to relevant differences, and also fluctuations in precipitation did not show statistically significant dependence on ΔSST.

Lastly, Shevchenko et al. (2023) compared the diurnal cycle of shallow convection for areas with DWLs to areas without DWLs in the EUREC^{4}A region and found that an increase in CC from the appearance of DWLs occurred in the late afternoon, but overall there was a reduction in CC amplitude by about 10% due to reduced CC in the morning hours. This showed that in some specific locations, DWLs do play a role in the evolution of convection, however, this remains a local phenomenon.

Chapter 3

Summary and Discussion

The publication Schmitt et al. (2024) focused on the derivation of a universal scaling, including the influence of LT on DWL properties. It was shown that LT strongly impacts DWL energetics, mainly by reducing the work performed by the surface stress and partly compensating for this effect by Stokes shear production. In the presence of waves, surface buoyancy and surface velocity are strongly reduced, even under weak winds, which has important implications for air–sea exchange in coupled models.

The scaling presented in this publication provides reliable bulk properties at midday and the afternoon buoyancy maximum for a large range of possible forcings and settings. The most important non-dimensional parameters for the evolution of DWLs are the forcing ratio $R = u_*^2/(T_h B_{\max})$, the non-dimensional Coriolis parameter $\hat{f} = fT_h$ and the non-dimensional shortwave absorption length $\hat{\eta} = \eta/L$. Together with the set of scaling coefficients presented in Schmitt et al. (2024), the most important DWL bulk properties can be calculated based on these non-dimensional numbers.

Here, it needs to be mentioned that these scalings were derived with the use of an equilibrium wave model. Under equilibrium waves, LT only has a small effect on the bulk properties, while other studies focusing on swell effects (Kukulka et al., 2013) have shown a stronger impact of LT on DWL properties. The scaling coefficients may have to be adjusted for different wave conditions. Moreover, the effects of penetrating shortwave radiation with the inclusion of the function $J(\hat{h}/\hat{\eta})$ only yielded good agreement with our simulations for tropical DWLs, pointing at future work for a reliable description of high-latitude DWLs.

Peng et al. (submitted) focused on the interactions between DWLs and surface-layer fronts using field observations and a second-moment turbulence model. It is concluded that the presence of a DWL isolates the deeper layers of the front from diabatic and frictional surface forcing, which causes these layers to quickly become non-turbulent while remaining in a state of marginal stability. This condition suggests that small perturbations from local processes, such as internal tides and waves, can easily trigger instability and turbulence.

The model, although highly idealized, was able to reproduce the key features of frontal dynamics when compared to previous LES studies by Taylor and Ferrari (2010). Although the one-dimensional model cannot directly simulate SI, it does indicate conditions favourable for SI ($fq < 0$), and therefore predicts instability. The model results were largely consistent with the observations, which showed enhanced turbulence and shear especially in the lowest part of the surface boundary layer, where internal-tide motions were present at the field site. The complex dynamics in the interplay of DWLs and fronts deserves further analysis, either involving three-dimensional LES or dedicated measurement campaigns that can also capture the near-surface DWL shear, but Peng et al. (submitted) provides a first look into the combination of these two processes.

Schmitt et al. (submitted) continued the study of DWLs by introducing realistic atmospheric forcing and three-dimensional processes with the use of a regional ocean model for

the tropical north-east Atlantic. The atmospheric LES used as forcing explicitly resolves atmospheric convection, cold pools and associated local rain patches, wind bursts, and cloud shading effects.

Focusing on the surface fluxes first, results showed that DWLs were present throughout the simulated period of 8 days, but there was no increase in the ocean heat loss to the atmosphere as expected from the flux parameterizations of the latent and sensible heat. A more detailed analysis showed that the evolution of DWLs in the simulations co-occured with a slight reduction of the trade winds during daytime, which overcompensated the effects of DWLs and higher SST. This leads to the conclusion that the impact of DWLs on the air-sea fluxes may be overestimated in studies of the trade wind zone, where a diurnal reduction of wind has been reported frequently. The result stands in contrast to model studies of the Indian Ocean and points at regional differences in DWL impact.

The publication found a reduction of the oceanic heat loss underneath cold pools by 30 W m^{-2}, which contrasts a recent publication by Brilouet et al. (2023), who observe the opposite instead. The difference may be explained by the magnitude of the background wind field, which was much weaker in Brilouet et al. (2023). This result also suggests that the influence of cold pools on the surface heat fluxes is not universal.

The small-scale variability in the atmospheric forcing (cold pools, wind bursts, rain patches) induced a strong lateral variability in DWL properties, most notably a factor-3 variability in DWL thicknesses and a factor-2 variability in DWL temperature anomaly. The bulk parameter scaling from Schmitt et al. (2024) showed great accuracy when compared to average DWL properties over the entire model domain, but the variability under small-scale forcing reveals that the local applicability of bulk scalings is questionable. The three-dimensional high-resolution ocean model revealed a new shear-dispersion mechanism with an advective component associated with the Diurnal Jet and a mixing component associated with night time convection. This mechanism leads to extreme anisotropy of horizontal tracer spreading, with net horizontal diffusivities that are comparable in magnitude to diffusivities associated with baroclinic mixed layer instabilities in the vicinity of submesoscale surface layer fronts (Fox-Kemper et al., 2008). The mechanism has implications for the transport of particles like e.g. micro plastics, but is not resolved in most regional model studies and has not received much attention up to now.

Finally, Shevchenko et al. (2023) extended the study of DWLs to atmospheric effects with the use of a global coupled climate model. This model configuration represents the state of the art of high-resolution climate models, and it was the first time that DWLs were directly resolved in a coupled global model. The DWLs produced by the simulation reproduced the extent and evolution known from observations, but the magnitude of the diurnal SST fluctuations was exaggerated in comparison to reanalysis, by about a factor of two. A possible reason for this are complications with the simpler turbulence model by Gaspar et al. (1990) under strong heating.

In the atmosphere, the increase in SST led to a significant increase in LHF and WVP, but the overall values were small. Similarly, CC and CLW decreased around noon in areas with strong diurnal warming, before increasing in the afternoon. However, these effects were small and lost statistical significance within 5–6 hours of appearance. The impact of DWLs on convection remained small even for a strongly enhanced diurnal SST amplitude, possibly due to the low wind speeds that facilitated the presence of DWLs (this is supported by the findings in Voldoire et al. (2022)). Nonetheless, it needs to be differentiated between the local and the overall impact of DWLs, as also became clear in Schmitt et al. (submitted). The small impact of DWLs on convection due to weak winds leads to the conclusion that it is important to resolve (sub)mesoscale oceanic structures such as the fronts presented in Peng et al. (submitted), as they can result in large SST anomalies even under strong wind conditions. There are some limitations to the model set up in Shevchenko et al. (2023). Firstly,

the 5 km resolution distorts shallow convection in the subtropics, which is why model biases can not be excluded here. Moreover, the study only covers short-term effects of DWLs. DWLs may have a long-term influence on the energy budget that is not treated here.

Overall, the presence of DWLs results in a multitude of interesting physical processes and interactions with larger scales. The results presented in this dissertation are a contribution towards the understanding and modelling of DWLs, yet there is much more to learn. Advances in ocean and climate modelling with higher model resolution will allow for even more of these processes to be investigated in the future.

Bibliography

Bony, Sandrine et al. (2017). "EUREC4A: A Field Campaign to Elucidate the Couplings Between Clouds, Convection and Circulation". In: *Surveys in Geophysics* 38(6), pp. 1529–1568. ISSN: 1573-0956. DOI: 10.1007/s10712-017-9428-0.

Brilouet, Pierre-Etienne, Jean-Luc Redelsperger, Marie-Noëlle Bouin, Fleur Couvreux, and Cindy Lebeaupin Brossier (2021). "A Case-Study of the Coupled Ocean–Atmosphere Response to an Oceanic Diurnal Warm Layer". In: *Quarterly Journal of the Royal Meteorological Society* 147(736), pp. 2008–2032. ISSN: 1477-870X. DOI: 10.1002/qj.4007.

Brilouet, Pierre-Etienne, Jean-Luc Redelsperger, Marie-Noëlle Bouin, Fleur Couvreux, and Najda Villefranque (2023). "A Numerical Study of Ocean Surface-Layer Response to Atmospheric Shallow Convection: Impact of Cloud Shading, Rain, and Cold Pools". In: *Quarterly Journal of the Royal Meteorological Society* n/a(n/a). ISSN: 1477-870X. DOI: 10.1002/qj.4651.

Burchard, Hans (2002). *Applied Turbulence Modelling in Marine Waters*. Springer. ISBN: 978-3-540-43795-6. DOI: 10.1007/3-540-45419-5.

Burchard, Hans and Karsten Bolding (2002). *GETM: A General Estuarine Transport Model; Scientific Documentation*. EUR 20253 EN, JRC23237. European Commission, Joint Research Centre, Institute for Environment and Sustainability. URL: https://publications.jrc.ec.europa.eu/repository/handle/JRC23237.

Businger, J. A., J. C. Wyngaard, Y. Izumi, and E. F. Bradley (1971). "Flux-Profile Relationships in the Atmospheric Surface Layer". In: *Journal of the Atmospheric Sciences* 28(2), pp. 181–189. ISSN: 0022-4928, 1520-0469. DOI: 10.1175/1520-0469(1971)028<0181:FPRITA>2.0.CO;2.

Capet, X., J. C. McWilliams, M. J. Molemaker, and A. F. Shchepetkin (2008). "Mesoscale to Submesoscale Transition in the California Current System. Part II: Frontal Processes". In: *Journal of Physical Oceanography* 38(1), pp. 44–64. ISSN: 0022-3670. DOI: 10.1175/2007JPO3672.1.

Craik, A. D. D. and S. Leibovich (1976). "A Rational Model for Langmuir Circulations". In: *Journal of Fluid Mechanics* 73(3), pp. 401–426. ISSN: 1469-7645, 0022-1120. DOI: 10.1017/S0022112076001420.

Fairall, C. W., E. F. Bradley, J. E. Hare, A. A. Grachev, and J. B. Edson (2003). "Bulk Parameterization of Air–Sea Fluxes: Updates and Verification for the COARE Algorithm". In: *Journal of Climate* 16(4), pp. 571–591. ISSN: 0894-8755, 1520-0442. DOI: 10.1175/1520-0442(2003)016<0571:BPOASF>2.0.CO;2.

Fairall, C. W., E. F. Bradley, D. P. Rogers, J. B. Edson, and G. S. Young (1996). "Bulk Parameterization of Air-Sea Fluxes for Tropical Ocean-Global Atmosphere Coupled-Ocean Atmosphere Response Experiment". In: *Journal of Geophysical Research: Oceans* 101(C2), pp. 3747–3764. ISSN: 2156-2202. DOI: 10.1029/95JC03205.

Foltz, Gregory R. (2019). "Wind- and Buoyancy-Forced Upper Ocean". In: *Encyclopedia of Ocean Sciences*. Elsevier, pp. 113–121. ISBN: 978-0-12-813082-7. DOI: 10.1016/B978-0-12-409548-9.11336-3.

Fox-Kemper, Baylor, Raffaele Ferrari, and Robert Hallberg (2008). "Parameterization of Mixed Layer Eddies. Part I: Theory and Diagnosis". In: *Journal of Physical Oceanography* 38(6), pp. 1145–1165. ISSN: 0022-3670. DOI: 10.1175/2007JPO3792.1.

Gaspar, Philippe, Yves Grégoris, and Jean-Michel Lefevre (1990). "A Simple Eddy Kinetic Energy Model for Simulations of the Oceanic Vertical Mixing: Tests at Station Papa and Long-Term Upper Ocean Study Site". In: *Journal of Geophysical Research: Oceans* 95(C9), pp. 16179–16193. ISSN: 2156-2202. DOI: 10.1029/JC095iC09p16179.

Gentemann, Chelle L., Peter J. Minnett, and Brian Ward (2009). "Profiles of Ocean Surface Heating (POSH): A New Model of Upper Ocean Diurnal Warming". In: *Journal of Geophysical Research: Oceans* 114(C7). ISSN: 2156-2202. DOI: 10.1029/2008JC004825. (Visited on 09/25/2023).

Gula, Jonathan, John Taylor, Andrey Shcherbina, and Amala Mahadevan (2022). "Chapter 8 - Submesoscale processes and mixing". In: *Ocean Mixing*. Elsevier, pp. 181–214. ISBN: 978-0-12-821512-8. DOI: https://doi.org/10.1016/B978-0-12-821512-8.00015-3. URL: https://www.sciencedirect.com/science/article/pii/B9780128215128000153.

Haine, Thomas W. N. and John Marshall (Apr. 1998). "Gravitational, Symmetric, and Baroclinic Instability of the Ocean Mixed Layer". In: *Journal of Physical Oceanography* 28(4), pp. 634–658. ISSN: 0022-3670, 1520-0485. DOI: 10.1175/1520-0485(1998)028<0634:GSABIO>2.0.CO;2.

Hans, A. C., P. Brandt, F. Gasparin, M. Claus, S. Cravatte, J. Horstmann, and G. Reverdin (2024). "Observed Diurnal Cycles of Near-Surface Shear and Stratification in the Equatorial Atlantic and Their Wind Dependence". In: *Journal of Geophysical Research: Oceans* 129(8), e2023JC020870. ISSN: 2169-9291. DOI: 10.1029/2023JC020870.

Harcourt, Ramsey R. (2013). "A Second-Moment Closure Model of Langmuir Turbulence". In: *Journal of Physical Oceanography* 43(4), pp. 673–697. ISSN: 0022-3670, 1520-0485. DOI: 10.1175/JPO-D-12-0105.1.

Harcourt, Ramsey R. (2015). "An Improved Second-Moment Closure Model of Langmuir Turbulence". In: *Journal of Physical Oceanography* 45(1), pp. 84–103. ISSN: 0022-3670, 1520-0485. DOI: 10.1175/JPO-D-14-0046.1.

Hersbach, H. et al. (2023). "ERA5 hourly data on single levels from 1940 to present". In: DOI: 10.24381/cds.adbb2d47.

Hohenegger, C. et al. (2023). "ICON-Sapphire: simulating the components of the Earth system and their interactions at kilometer and subkilometer scales". In: *Geoscientific Model Development* 16(2), pp. 779–811. DOI: 10.5194/gmd-16-779-2023.

Hughes, Kenneth G., James N. Moum, and Emily L. Shroyer (2020). "Evolution of the Velocity Structure in the Diurnal Warm Layer". In: *Journal of Physical Oceanography* 50(3), pp. 615–631. ISSN: 0022-3670. DOI: 10.1175/JPO-D-19-0207.1.

Hughes, Kenneth G., James N. Moum, Emily L. Shroyer, and William D. Smyth (2021). "Stratified Shear Instabilities in Diurnal Warm Layers". In: *Journal of Physical Oceanography* 51(8), pp. 2583–2598. ISSN: 0022-3670, 1520-0485. DOI: 10.1175/JPO-D-20-0300.1.

Ivey, Gregory N, Cynthia E Bluteau, Bishakhdatta Gayen, Nicole L Jones, and Taimoor Sohail (2021). "Roles of shear and convection in driving mixing in the ocean". In: *Geophys. Res. Lett.* 48(3), e2020GL089455.

Ivey, Gregory N, Cynthia E Bluteau, and Nicole L Jones (2018). "Quantifying diapycnal mixing in an energetic ocean". In: *J. Geophys. Res.* 123(1), pp. 346–357.

Kantha, Lakshmi H. and Anne Carol Clayson (2004). "On the Effect of Surface Gravity Waves on Mixing in the Oceanic Mixed Layer". In: *Ocean Modelling* 6(2), pp. 101–124. ISSN: 1463-5003. DOI: 10.1016/S1463-5003(02)00062-8.

Klingbeil, Knut, Eric Deleersnijder, Oliver Fringer, and Lars Umlauf (2022). "Basic Equations of Marine Flows". In: *The Mathematics of Marine Modelling: Water, Solute and Particle Dynamics in Estuaries and Shallow Seas*. Springer International Publishing, pp. 1–9. ISBN: 978-3-031-09559-7. DOI: 10.1007/978-3-031-09559-7_1.

Kudryavtsev, Vladimir and Alexander Soloviev (1990). "Slippery Near-Surface Layer of the Ocean Arising Due to Daytime Solar Heating". In: *Journal of Physical Oceanography* 20(5), pp. 617–628. DOI: 10.1175/1520-0485(1990)020<0617:SNSLOT>2.0.CO;2.

Kukulka, T., A. J. Plueddemann, and P. P. Sullivan (2013). "Inhibited Upper Ocean Restratification in Nonequilibrium Swell Conditions". In: *Geophysical Research Letters* 40(14), pp. 3672–3676. ISSN: 1944-8007. DOI: 10.1002/grl.50708.

Kundu, Pijush K., Ira M. Cohen, and David R. Doling (2016). *Fluid Mechanics*. Elsevier. ISBN: 978-0-12-405935-1. DOI: 10.1016/C2012-0-00611-4.

Laxague, Nathan J. M. and Christopher J. Zappa (2020). "The Impact of Rain on Ocean Surface Waves and Currents". In: *Geophysical Research Letters* 47(7), e2020GL087287. ISSN: 1944-8007. DOI: 10.1029/2020GL087287.

Li, Qing, Baylor Fox-Kemper, Øyvind Breivik, and Adrean Webb (2017). "Statistical Models of Global Langmuir Mixing". In: *Ocean Modelling* 113, pp. 95–114. ISSN: 1463-5003. DOI: 10.1016/j.ocemod.2017.03.016. (Visited on 07/19/2022).

Lindzen, Richard S. and Sumant Nigam (Sept. 1987). "On the Role of Sea Surface Temperature Gradients in Forcing Low-Level Winds and Convergence in the Tropics". In: *Journal of the Atmospheric Sciences* 44(17), pp. 2418–2436. ISSN: 0022-4928, 1520-0469. DOI: 10.1175/1520-0469(1987)044<2418:OTROSS>2.0.CO;2.

Matthews, Adrian J., Dariusz B. Baranowski, Karen J. Heywood, Piotr J. Flatau, and Sunke Schmidtko (2014). "The Surface Diurnal Warm Layer in the Indian Ocean during CINDY/DYNAMO". In: *Journal of Climate* 27(24), pp. 9101–9122. ISSN: 0894-8755, 1520-0442. DOI: 10.1175/JCLI-D-14-00222.1.

McWilliams, James C. (May 2016). "Submesoscale Currents in the Ocean". In: *Proceedings of the Royal Society A: Mathematical, Physical and Engineering Sciences* 472(2189), p. 20160117. DOI: 10.1098/rspa.2016.0117.

McWilliams, James C., Peter P. Sullivan, and Chin-Hoh Moeng (1997). "Langmuir Turbulence in the Ocean". In: *Journal of Fluid Mechanics* 334, pp. 1–30. ISSN: 1469-7645, 0022-1120. DOI: 10.1017/S0022112096004375.

Min, Hong Sik and Yign Noh (2004). "Influence of the Surface Heating on Langmuir Circulation". In: *Journal of Physical Oceanography* 34(12), pp. 2630–2641. ISSN: 0022-3670, 1520-0485. DOI: 10.1175/JPOJPO-2654.1.

Monin, AS and AM Obukhov (1954). "Osnovnye zakonomernosti turbulentnogo peremeshivanija v prizemnom sloe atmosfery (Basic laws of turbulent mixing in the atmosphere near the ground)". In: *Trudy geofiz. inst. AN SSSR* 24(151), pp. 163–187.

Moulin, Aurélie J., James N. Moum, and Emily L. Shroyer (2018). "Evolution of Turbulence in the Diurnal Warm Layer". In: *Journal of Physical Oceanography* 48(2), pp. 383–396. ISSN: 0022-3670, 1520-0485. DOI: 10.1175/JPO-D-17-0170.1.

Olbers, Dirk, Jürgen Willebrand, and Carsten Eden (2012). *Ocean Dynamics*. Ed. by Dirk Olbers, Jürgen Willebrand, and Carsten Eden. Springer: Berlin, Heidelberg. ISBN: 978-3-642-23450-7. DOI: 10.1007/978-3-642-23450-7_1.

Pearson, Brodie C., Alan L. M. Grant, Jeff A. Polton, and Stephen E. Belcher (2015). "Langmuir Turbulence and Surface Heating in the Ocean Surface Boundary Layer". In: *Journal of Physical Oceanography* 45(12), pp. 2897–2911. ISSN: 0022-3670, 1520-0485. DOI: 10.1175/JPO-D-15-0018.1.

Peng, Jen-Ping, Julia Dräger-Dietel, Ryan P. North, and Lars Umlauf (2021). "Diurnal Variability of Frontal Dynamics, Instability, and Turbulence in a Submesoscale Upwelling Filament". In: *Journal of Physical Oceanography* 51(9), pp. 2825–2843. DOI: 10.1175/JPO-D-21-0033.1.

Peng, J.P., N. Jones, M. Rayson, M. Schmitt, L. Umlauf, C. Whitwell, S.R. Keating, C.J. Shakespeare, and G.N. Ivey (submitted). "Interactions between diurnal warm layers and surface-layer fronts". In: *Journal of Geophysical Research: Oceans*.

Pham, Hieu T., Sutanu Sarkar, Leah Johnson, Baylor Fox-Kemper, Peter P. Sullivan, and Qing Li (2023). "Multi-Scale Temporal Variability of Turbulent Mixing During a Monsoon Intra-Seasonal Oscillation in the Bay of Bengal: An LES Study". In: *Journal of Geophysical Research: Oceans* 128(1), e2022JC018959. ISSN: 2169-9291. DOI: 10.1029/2022JC018959.

Price, James F., Robert A. Weller, and Robert Pinkel (1986). "Diurnal Cycling: Observations and Models of the Upper Ocean Response to Diurnal Heating, Cooling, and Wind Mixing". In: *Journal of Geophysical Research: Oceans* 91(C7), pp. 8411–8427. DOI: 10.1029/JC091iC07p08411.

Savazzi, Alessandro Carlo Maria, Louise Nuijens, Irina Sandu, Geet George, and Peter Bechtold (2022). "The Representation of the Trade Winds in ECMWF Forecasts and Reanalyses during EUREC^{4}A". In: *Atmospheric Chemistry and Physics* 22(19), pp. 13049–13066. ISSN: 1680-7316. DOI: 10.5194/acp-22-13049-2022.

Schlüssel, Peter, Alexander V. Soloviev, and William J. Emery (1997). "COOL AND FRESHWATER SKIN OF THE OCEAN DURING RAINFALL". In: *Boundary-Layer Meteorology* 82(3), pp. 439–474. ISSN: 1573-1472. DOI: 10.1023/A:1000225700380.

Schmitt, M., K. Klingbeil, R. Shevchenko, and L. Umlauf (submitted). "Three-dimensional Ocean Surface Layer Response to Rain, Wind bursts and Diurnal Heating". In: *Journal of Geophysical Research: Oceans*.

Schmitt, M., H. T. Pham, S. Sarkar, K. Klingbeil, and L. Umlauf (2024). "Diurnal Warm Layers in the Ocean: Energetics, Nondimensional Scaling, and Parameterization". In: *Journal of Physical Oceanography* 54(4), pp. 1037–1055. ISSN: 0022-3670, 1520-0485. DOI: 10.1175/JPO-D-23-0129.1.

Shackelford, Kyle, Charlotte A. DeMott, Peter Jan van Leeuwen, Elizabeth Thompson, and Samson Hagos (2022). "Rain-Induced Stratification of the Equatorial Indian Ocean and Its Potential Feedback to the Atmosphere". In: *Journal of Geophysical Research: Oceans* 127(3), e2021JC018025. ISSN: 2169-9291. DOI: 10.1029/2021JC018025.

Shcherbina, Andrey, Eric D'Asaro, and Ramsey Harcourt (2019). "Rain and Sun Create Slippery Layers in the Eastern Pacific Fresh Pool". In: *Oceanography* 32(2), pp. 98–107. ISSN: 10428275. DOI: 10.5670/oceanog.2019.217.

Shevchenko, Radomyra, Cathy Hohenegger, and Mira Schmitt (2023). "Impact of Diurnal Warm Layers on Atmospheric Convection". In: *Journal of Geophysical Research: Atmospheres* 128(14), e2022JD038473. ISSN: 2169-8996. DOI: 10.1029/2022JD038473.

Smyth, William D. and Jeffrey R. Carpenter (2019). *Instability in Geophysical Flows*. Cambridge University Press: Cambridge. ISBN: 978-1-108-70301-7. DOI: 10.1017/9781108640084.

Stiperski, Ivana and Marc Calaf (2023). "Generalizing Monin-Obukhov Similarity Theory (1954) for Complex Atmospheric Turbulence". In: *Physical Review Letters* 130(12), p. 124001. DOI: 10.1103/PhysRevLett.130.124001.

Taylor, John R. and Raffaele Ferrari (2009). "On the Equilibration of a Symmetrically Unstable Front via a Secondary Shear Instability". In: *Journal of Fluid Mechanics* 622, pp. 103–113. ISSN: 0022-1120, 1469-7645. DOI: 10.1017/S0022112008005272.

Taylor, John R. and Raffaele Ferrari (June 2010). "Buoyancy and Wind-Driven Convection at Mixed Layer Density Fronts". In: *Journal of Physical Oceanography* 40(6), pp. 1222–1242. ISSN: 0022-3670, 1520-0485. DOI: 10.1175/2010JPO4365.1.

Thomas, Leif N. (2005). "Destruction of Potential Vorticity by Winds". In: *Journal of Physical Oceanography* 35(12), pp. 2457–2466. ISSN: 0022-3670, 1520-0485. DOI: 10.1175/JPO2830.1.

Thompson, Elizabeth J., James N. Moum, Christopher W. Fairall, and Steven A. Rutledge (2019). "Wind Limits on Rain Layers and Diurnal Warm Layers". In: *Journal of Geophysical Research: Oceans* 124(2), pp. 897–924. ISSN: 2169-9291. DOI: 10.1029/2018JC014130.

Turk, Daniela, Christopher J. Zappa, Christopher S. Meinen, James R. Christian, David T. Ho, Andrew G. Dickson, and Wade R. McGillis (2010). "Rain Impacts on CO2 Exchange

in the Western Equatorial Pacific Ocean". In: *Geophysical Research Letters* 37(23). ISSN: 1944-8007. DOI: 10.1029/2010GL045520.

Umlauf, Lars, Hans Burchard, and Karsten Bolding (2005). "GOTM - Scientic Documentation : Version 3.2". In: 63, p. 279. ISSN: 0939-396X. DOI: 10.12754/MSR-2005-0063.

Vogel, Raphaela, Heike Konow, Hauke Schulz, and Paquita Zuidema (2021). "A Climatology of Trade-Wind Cumulus Cold Pools and Their Link to Mesoscale Cloud Organization". In: *Atmospheric Chemistry and Physics* 21(21), pp. 16609–16630. ISSN: 1680-7316. DOI: 10.5194/acp-21-16609-2021.

Voldoire, Aurore, Romain Roehrig, Hervé Giordani, Robin Waldman, Yunyan Zhang, Shaocheng Xie, and Marie-Nöelle Bouin (2022). "Assessment of the Sea Surface Temperature Diurnal Cycle in CNRM-CM6-1 Based on Its 1D Coupled Configuration". In: *Geoscientific Model Development* 15(8), pp. 3347–3370. ISSN: 1991-959X. DOI: 10.5194/gmd-15-3347-2022.

Wang, Xingchi, Tobias Kukulka, J. Thomas Farrar, Albert J. Plueddemann, and Seth F. Zippel (2023). "Langmuir Turbulence Controls on Observed Diurnal Warm Layer Depths". In: *Geophysical Research Letters* 50(10), e2023GL103231. ISSN: 1944-8007. DOI: 10.1029/2023GL103231.

Appendix A

Declaration of my contributions

A.1 Diurnal Warm Layers in the Ocean: Energetics, Non-dimensional Scaling, and Parameterization

The concept for this study was derived by me and my supervisor, Lars Umlauf. The LES model results, as well as the LES description in the text, were provided by my co-authors Hieu Pham and Sutanu Sarkar. The Langmuir Turbulence parameterization in GOTM was realized by my co-author Knut Klingbeil. I evaluated the parameterization by testing different second-moment closures and by tuning the model coefficients. All GOTM runs were performed by me. The analysis, including the comparison with the LES results, was done by me with valuable input from my supervisor. The visualization and plotting in the manuscript was done entirely by me. I came up with the first draft, which was then refined with the help of all co-authors. The revisions were done by me with valuable input from my co-authors, especially Lars Umlauf.

A.2 Interactions between diurnal warm layers and surface-layer fronts

As a co-author, I helped with the set up and validation of the idealized model, and interpretation of the results regarding the behaviour of DWLs. I co-wrote Sections 2.4 and 2.5 about the DWL scaling and the numerical set up. The schematic in Fig. 2 was made by me and I provided a first draft of the script that runs GOTM and plots Figures 8-10. Lastly, I was involved in the editing of the final manuscript, especially of the sections that focused on the model simulations.

A.3 Three-dimensional Ocean Surface Layer Response to Rain, Wind bursts and Diurnal Heating

This manuscript was again conceptualized by my supervisor, Lars Umlauf, and me. All my co-authors were involved in the methodology. The atmospheric data for the forcing was curated by my co-author Radomyra Shevchenko, and the ocean model set up was developed by Knut Klingbeil with direct consultation by Lars Umlauf and myself. I validated the results and did all of the analysis with the help of my supervisor. All plotting was again done by me, as well as the writing of the first draft. The final submission was edited and refined with the help of all my co-authors.

A.4 Impact of Diurnal Warm Layers on Atmospheric Convection

As a co-author, I was involved in the development of the vertical grid of the S_{+DWL} model set up. To find a vertical resolution that is able to correctly resolve DWL evolution, while keeping the number of needed grid cells to a minimum for model performance, I performed several GOTM studies with varying resolutions. Fig. 1 and A1 in the publication were plotted by me. In addition, I helped with the interpretation of the ocean results and was involved in the editing of the final manuscript.

Mira Schmitt

Lars Umlauf

Appendix B

Publications

Diurnal Warm Layers in the Ocean: Energetics, Nondimensional Scaling, and Parameterization

M. SCHMITT[a], H. T. PHAM[b], S. SARKAR[b,c], K. KLINGBEIL[a], AND L. UMLAUF[a]

[a] *Leibniz-Institute for Baltic Sea Research, Warnemünde, Germany*
[b] *Mechanical and Aerospace Engineering, University of California, San Diego, La Jolla, California*
[c] *Scripps Institution of Oceanography, University of California, San Diego, La Jolla, California*

(Manuscript received 11 July 2023, in final form 26 January 2024, accepted 1 February 2024)

ABSTRACT: Diurnal warm layers (DWLs) form near the surface of the ocean on days with strong solar radiation, weak to moderate winds, and small surface-wave effects. Here, we use idealized second-moment turbulence modeling, validated with large-eddy simulations (LES), to study the properties, dynamics, and energetics of DWLs across the entire physically relevant parameter space. Both types of models include representations of Langmuir turbulence (LT). We find that LT only slightly modifies DWL thicknesses and other bulk parameters under equilibrium wave conditions, but leads to a strong reduction in surface temperature and velocity with possible implications for air–sea coupling. Comparing tropical and the less frequently studied high-latitude DWLs, we find that LT has a strong impact on the energy budget and that rotation at high latitudes strongly modifies the DWL energetics, suppressing net energy turnover and entrainment. We identify the key nondimensional parameters for DWL evolution and find that the scaling relations of Price et al. provide a reliable representation of the DWL bulk properties across a wide parameter space, including high-latitude DWLs. We present different sets of revised model coefficients that include the deepening of the DWL due to LT and other aspects of our more advanced turbulence model to describe DWL properties at midday and during the DWL temperature peak in the afternoon, which we find to occur around 1500–1630 local time for a broad range of parameters.

KEYWORDS: Atmosphere-ocean interaction; Diurnal effects; Langmuir circulation; Sea surface temperature; Model evaluation/performance; Parameterization

1. Introduction

Diurnal warm layers (DWLs) form near the surface of the ocean on days with strong solar radiation, weak to moderate winds, and weak surface-wave activity. Reviewing existing literature, Kawai and Wada (2007) noted that DWLs are a widespread feature, found at all latitudes and characterized by typical sea surface temperature (SST) anomalies of $\mathcal{O}(0.1–1)$°C and typical thicknesses of $\mathcal{O}(1–10)$ m. DWLs isolate the deeper parts of the surface layer from atmospheric forcing (Wijesekera et al. 2020), provide a niche for marine microorganisms (Kahru et al. 1993), modify air–sea fluxes (Matthews et al. 2014), and feed back to the atmosphere in ways that are just beginning to be understood (Brilouet et al. 2021).

Recent field investigations with specialized instrumentation (Matthews et al. 2014; Sutherland et al. 2016; Moulin et al. 2018; Hughes et al. 2020) and numerical modeling studies (Sarkar and Pham 2019; Large and Caron 2015) have provided a consistent picture of the physical processes determining the evolution of DWLs in the ocean: strong surface buoyancy forcing tends to suppress turbulence below the DWL and induce a near-surface trapping of momentum, reflected in the evolution of a near-surface diurnal jet with speeds $\mathcal{O}(0.1)\,\mathrm{m\,s^{-1}}$. The strong shear at the lower edge of the diurnal jet generates a marginally stable stratified shear layer, triggering strong DWL turbulence and entrainment (Hughes et al. 2020).

This detailed understanding of the DWL dynamics was, however, almost exclusively gained based on investigations and long-term studies at tropical latitudes (e.g., Matthews et al. 2014; Bellenger and Duvel 2009), despite the observation that during the summer months diurnal SST anomalies at high latitudes may be as large as those found in tropical regions (Kawai and Wada 2007). The few available studies of high-latitude DWLs (e.g., Eastwood et al. 2011; Jia et al. 2023) found a widespread occurrence also in the Arctic Ocean. Jia et al. (2023) reported a repeated occurrence of DWLs with significant warming amplitudes > 2°C, including extreme events with amplitudes > 5°C, during the two summer months of their measurement campaign at latitudes of up to 80°N. A recent evaluation of turbulence models, including their performance under strong diurnal warming (Johnson et al. 2023), was for a low-latitude DWL. Due to the lack of detailed observations and numerical studies of high-latitude DWLs, our understanding of the energetics and parameterization of these features is limited at the moment.

A few recent studies focusing on the impact of surface-wave effects on DWLs (Kukulka et al. 2013; Pham et al. 2023; Wang et al. 2023) underlined the importance of Langmuir turbulence (LT) for the evolution of diurnal near-surface stratification, typically identifying a reduction of the diurnal SST

Denotes content that is immediately available upon publication as open access.

Supplemental information related to this paper is available at the Journals Online website: https://doi.org/10.1175/JPO-D-23-0129.s1.

Corresponding author: Mira Schmitt, mira.schmitt@io-warnemuende.de

DOI: 10.1175/JPO-D-23-0129.1

amplitude and an increase of the DWL thickness due to stronger mixing. The ability of existing parameterizations (Price et al. 1986, hereafter PWP86; Fairall et al. 1996) and ocean turbulence models to reproduce these effects has not been systematically evaluated so far.

The goal of this paper is to investigate the relevance, implications, and parameterizations of different processes (in particular: LT and rotation effects in high-latitude DWLs) across the entire physically relevant parameter space. Section 2 introduces the models used in this study. Most of the analysis is based on a second-moment turbulence model that includes the effects of LT. To validate this model and evaluate its performance concerning the effects of LT, we use section 3 to compare it to our LES results for a typical DWL scenario. After that, in section 4, we use our validated second-moment model to investigate DWL energy budgets in a typical tropical versus a high-latitude DWL, thereby focusing especially on the effects of rotation and day length that have so far received only little attention. Last, in section 5, we attempt to provide a unified description of DWLs in the ocean by first identifying the key nondimensional parameters that govern their structure and evolution, and then evaluating the influence of these parameters across a large parameter space. Here, we also test the applicability of the frequently used bulk parameter model by PWP86 for high latitudes and DWLs influenced by LT.

2. Model formulation

a. Momentum and buoyancy equations

Our analysis will be based on the one-dimensional transport equations for momentum and buoyancy for an infinitely deep water column,

$$\frac{\partial u}{\partial t} - f(v + v_s) = \frac{\partial}{\partial z}\left(\nu \frac{\partial u}{\partial z}\right) - \frac{\partial \tau_x}{\partial z}, \tag{1}$$

$$\frac{\partial v}{\partial t} + f(u + u_s) = \frac{\partial}{\partial z}\left(\nu \frac{\partial v}{\partial z}\right) - \frac{\partial \tau_y}{\partial z}, \tag{2}$$

$$\frac{\partial b}{\partial t} = \frac{\partial}{\partial z}\left(\nu^b \frac{\partial b}{\partial z}\right) - \frac{\partial G}{\partial z} + \frac{\partial I_b}{\partial z}, \tag{3}$$

where u and v are the Reynolds-averaged velocities in the x and y directions, u_s and v_s are the corresponding Stokes drift velocities, f is the Coriolis parameter, and ν and ν^b are the molecular diffusivities of momentum and buoyancy (or heat), respectively. The vertical turbulent momentum fluxes (normalized here with a constant reference density $\rho_0 = 1027$ kg m^{-3}) are denoted by τ_x and τ_y. The evolution of the Reynolds-averaged buoyancy b is determined by the vertical turbulent buoyancy flux G and the radiative buoyancy flux I_b due to penetrating shortwave radiation. We use the conventions that z points vertically upward with $z = 0$ at the surface, that all turbulent fluxes are positive upward, and that the radiative buoyancy flux I_b is positive downward.

As boundary conditions for the momentum equations in (1) and (2), we describe the components of the (normalized) wind stress, τ_x^0 and τ_y^0, at the surface. Similarly, for the buoyancy equation in (3), we prescribe the nonsolar surface buoyancy flux $B_0 = \alpha g Q_{ns}/(\rho_0 c_p)$ at $z = 0$, where Q_{ns} (positive downward) is the nonsolar heat flux, accounting for the longwave, latent, and sensible heat fluxes. Here, g is the acceleration of gravity, c_p the specific heat capacity, and α the thermal expansion coefficient. Note that Q_{ns} and B_0 will generally be negative (surface heat loss) in our study. Zero-flux conditions for the turbulent fluxes of momentum and buoyancy are applied at $z \to -\infty$ (practically, the lower boundary conditions are imposed at some finite value of z that is sufficiently far below the surface to not affect the results).

b. Surface forcing

To identify the key parameters controlling the DWL evolution and structure, the following analysis will be based on idealized atmospheric fluxes that reflect the essential characteristics of the atmospheric forcing under conditions favorable for DWLs. This forcing consists of a constant nonsolar heat (or buoyancy) loss at the surface ($B_0 < 0$), and a periodic diurnal variability induced by the radiative heat flux according to

$$I_0(t) = \max\left\{0, I_{\max}\cos\left[\frac{\pi}{T_d}\left(t - \frac{T_p}{2}\right)\right]\right\}, \tag{4}$$

where T_p is the period of the prescribed forcing (24 h), T_d the duration of the daylight period with $I_0 > 0$, and $I_{\max}$ the maximum radiative heat flux reached at $T_p/2$ (midday). We performed numerical tests in which we compared this simplified solar radiation model with a more realistic radiation expression based on Stull (1988) and found only small differences in the DWL evolution that did not affect any of our conclusions. For our idealized study focusing on the basic mechanisms of DWL formation, the downward shortwave radiation I will be computed from a simple absorption model of the form

$$I(z) = I_0 e^{z/\eta}, \tag{5}$$

where η is the shortwave absorption scale. Note that in section 3 (model validation), and in some parts of the parameter space study in section 5, we will make the additional simplifying assumption that $\eta = 0$, i.e., that all radiation is absorbed at the surface. The radiative buoyancy flux I_b in (3) follows from

$$I_b = \frac{\alpha g}{\rho_0 c_p} I. \tag{6}$$

The temporal evolution of the surface buoyancy flux B_0, the radiative buoyancy flux at the surface $I_b(z = 0) = I_b^0$, and their sum (the total surface buoyancy flux B), are shown in Fig. 1.

The surface buoyancy forcing defined this way is completely described by four dimensional parameters: the two time scales T_p and T_d, the maximum total surface buoyancy flux at midday $B_{\max}$, and the surface buoyancy loss B_0. Rather than T_d, the more sensible parameter to describe the formation of DWLs is the heating period T_h during which the total surface buoyancy flux B is positive (see Fig. 1). From (4), it is clear that these two time scales are related according to

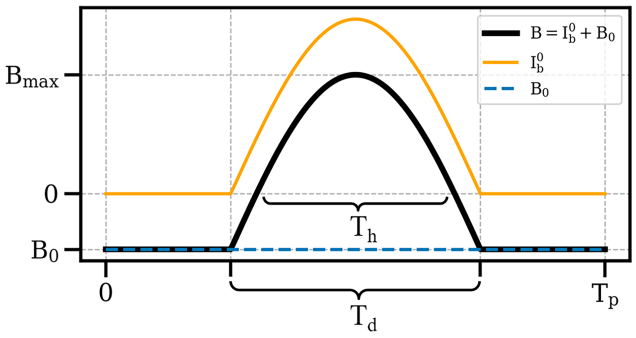

FIG. 1. Idealized buoyancy forcing with the radiative buoyancy flux at the surface I_b^0 , the nonsolar surface buoyancy flux B_0, and their sum, the total surface buoyancy flux B. Note that here we show the special case for which $T_d = T_p/2$.

$$T_h = \frac{2T_d}{\pi}\arccos\left(\frac{B_0}{B_0 - B_{\max}}\right). \tag{7}$$

All our simulations will be forced by a constant wind stress in the x direction, $\tau_x^0 = C_d(\rho_a/\rho_0)U_{10}^2$, where $\rho_a = 1.23$ kg m^{-3} is the air density, U_{10} is the 10-m wind speed, and $C_d = 1.7 \times 10^{-3}$ is a constant drag coefficient. Introducing the friction velocity, $u_* = \sqrt{|\tau_x^0|}$, as another key dimensional parameter of the problem, the quadratic drag law can also be expressed as $u_*^2 = C_d(\rho_a/\rho_0)U_{10}^2$.

Finally, surface wave parameters used to calculate the Stokes drift in our study are computed from the "Theory Wave" approach of Li et al. (2017). In brief, this model accounts for contributions to the Stokes drift profile from the entire frequency band of the theoretical wave spectrum of Phillips (1958), ignoring swell but including the effects of directional spreading. The surface Stokes drift velocity u_s^0 and the Stokes transport V_s are estimated from expressions of the form

$$u_s^0 = c_s U_{10}, \quad V_s = C_s g U_{10}^3, \tag{8}$$

where $c_s = 0.016$ and $C_s = 2.67 \times 10^{-5}$ s^4 m^{-2} are model constants. From these expressions, and the quadratic drag law mentioned above, the turbulent Langmuir number $\mathrm{La} = (u_*/u_s^0)^{1/2}$, defined by McWilliams et al. (1997), can also be expressed as $\mathrm{La} = (\rho_a C_d)^{1/4}/(\rho_0 c_s^2)^{1/4}$. Note that this yields a constant La = 0.3, as typical for equilibrium wave fields.

As shown by Li et al. (2017), the profile of the Stokes velocity u_s predicted by their model is a function of the surface Stokes velocity u_s^0 and the spectral peak wavenumber defined as

$$k_p = 0.176\frac{u_s^0}{V_s}. \tag{9}$$

For the exact expressions of the Stokes velocity profile, $u_s(z, u_s^0, k_p)$, which we use to compute the Stokes shear in our model, please refer to Li et al. (2017) or to section 1 in the online supplemental material.

c. *Second-moment turbulence modeling approach*

In our second-moment turbulence modeling approach, which is validated in section 3 and then used for all of the analyses in sections 4 and 5, the turbulent momentum fluxes appearing in (1) and (2) are computed from downgradient expressions of the form

$$\tau_x = \langle u'w'\rangle = -\left(\nu_t\frac{\partial u}{\partial z} + \nu_t^S\frac{\partial u_s}{\partial z}\right),$$
$$\tau_y = \langle v'w'\rangle = -\left(\nu_t\frac{\partial v}{\partial z} + \nu_t^S\frac{\partial v_s}{\partial z}\right), \tag{10}$$

where primes and angle brackets denote turbulent fluctuations and ensemble averages, respectively, and ν_t and ν_t^S the vertical turbulent diffusivities of momentum related to the Eulerian and Stokes velocities, respectively (Harcourt 2013; Harcourt 2015, hereafter H15). Similarly, the vertical turbulent buoyancy flux in (3) is computed from

$$G = \langle w'b'\rangle = -\nu_t^b\frac{\partial b}{\partial z} = -\nu_t^b N^2, \tag{11}$$

with the vertical turbulent diffusivity ν_t^b and the squared buoyancy frequency $N^2 = \partial b/\partial z$.

As discussed in more detail in appendix A, the turbulent diffusivities are assumed to be proportional to a turbulence length scale l and a turbulent velocity scale $k^{1/2}$, where $k = \overline{u_i'u_i'}/2$ is the turbulence kinetic energy (TKE) computed from a transport equation of the form

$$\frac{\partial k}{\partial t} = D_k + P + P_s + G - \varepsilon, \tag{12}$$

generalized here to also account for the effects of LT. Here, D_k denotes the vertical transport of TKE and ε the turbulence dissipation rate. The terms P and P_s are the Eulerian and Stokes shear production terms defined as (Harcourt 2013; H15):

$$P = -\langle u'w'\rangle\frac{\partial u}{\partial z} - \langle v'w'\rangle\frac{\partial v}{\partial z} = \nu_t S^2 + \nu_t^S S_c^2, \tag{13}$$

$$P_s = -\langle u'w'\rangle\frac{\partial u_s}{\partial z} - \langle v'w'\rangle\frac{\partial v_s}{\partial z} = \nu_t S_c^2 + \nu_t^S S_s^2, \tag{14}$$

where

$$S^2 = \left(\frac{\partial u}{\partial z}\right)^2 + \left(\frac{\partial v}{\partial z}\right)^2,\ S_c^2 = \frac{\partial u}{\partial z}\frac{\partial u_s}{\partial z} + \frac{\partial v}{\partial z}\frac{\partial v_s}{\partial z},\ S_s^2 = \left(\frac{\partial u_s}{\partial z}\right)^2 + \left(\frac{\partial v_s}{\partial z}\right)^2. \tag{15}$$

Finally, the turbulent length scale l, required for the computation of the turbulent diffusivities, is inferred from the solution of a Mellor–Yamada-type transport equation for the product kl in (A2) or, alternatively for comparison, from a transport equation for the inverse turbulence time scale $\omega \propto k^{1/2}l^{-1}$ in (A4). All relevant details of the turbulence closure models used in our study are summarized in appendix A.

d. *LES modeling approach*

The LES approach is used to validate the second-moment models in section 3. The approach is based on the Craik–Leibovich

equations to produce the Eulerian velocity, pressure, and buoyancy fields in a temporally evolving three-dimensional computational domain. Readers are referred to appendix B for the numerical implementation of the LES and the model setup.

From the LES, horizontally averaged profiles of velocities $\langle U_i \rangle$, buoyancy $\langle B \rangle$, and turbulent fluxes $\langle U_i' U_j' \rangle$ are obtained and used to compare with the second-moment turbulence model outputs (e.g., u, v, and b) in (1)–(3), as elaborated in section 3. Here, we use angle brackets to denote the horizontal average of the LES fields and primes to denote the fluctuations.

3. Comparison of LES and second-moment models

In this section, we compare the second-moment turbulence closure models to our LES results for a typical tropical DWL scenario both with and without the effects of LT, focusing especially on the performance of the second-moment model for this newly included process. Both LES and second-moment models are driven with identical atmospheric and buoyancy forcing and use the same parametric surface-wave model by Li et al. (2017) to compute the Stokes velocities. Note that the effects of surface-wave breaking are not taken into account in our simulations.

The three different second-moment models that we want to test are described in detail in section 2c and appendix A. They include (i) the full model of H15, which represents LT effects in both the stability functions and the transport equations for k and kl in Eqs. (12) and (A2) through the additional Stokes production term P_s; (ii) the model of Kantha and Clayson (2004, hereafter KC04), which only considers the additional Stokes production terms in the transport equations but ignores the impact of LT on the stability functions; and (iii) the model of Kantha and Clayson (1994), which ignores LT effects entirely. Both the models of H15 and KC04 converge to the model of Kantha and Clayson (1994) for the special case of zero Stokes drift ($u_s = 0$), which allows for a clear separation of LT effects from other modeling components. To compute the turbulent length scale l, we used an extended version of the Mellor–Yamada equation for kl in (A2) for all of the following simulations but we will also include a short comparison with a modified version of the k–ω model in section 2 of the supplemental material.

All second-order moment model simulations were conducted with a modified version of the General Ocean Turbulence Model (GOTM), described in Umlauf et al. (2005). The time step for these simulations was set to 6 s, and the domain depth and grid size match those of the LES grid with a resolution of 0.05 m at the surface, gradually coarsening toward the bottom (see appendix B). These parameters were found to ensure numerical convergence and exclude any impact of the lower edge of the domain on the DWL properties.

For all the simulations in this section, we use a peak solar buoyancy flux of $I_b = 2.3 \times 10^{-7}\ \mathrm{m^2\ s^{-3}}$ at noon at the surface (see Fig. 1), which, for comparison, would correspond to a peak solar heat flux of $I_{\max} = 400\ \mathrm{W\ m^{-2}}$ for a thermal expansion coefficient $\alpha = 2.4 \times 10^{-4}\ \mathrm{K^{-1}}$. To keep the setup for this model comparison as simple as possible, we also assume that the nonsolar surface buoyancy flux vanishes ($B_0 = 0$) and that all short wave radiation is absorbed at the surface ($\eta = 0$). The heating period is $T_h = T_d = 12$ h at a tropical latitude of 10°N (corresponding to $f = 2.53 \times 10^{-5}\ \mathrm{s^{-1}}$ and a local inertial period of $T_f = 69.1$ h). A constant friction velocity of $u_* = 4.4 \times 10^{-3}\ \mathrm{m\,s^{-1}}$ is applied, equivalent to a wind speed of $U_{10} = 3.1\ \mathrm{m\ s^{-1}}$. This results in a Monin–Obukhov length $L_{\mathrm{MO}} = u_*^3/(\kappa B) = 0.93$ m at midday (with $\kappa = 0.4$), which is more than an order of magnitude larger than the numerical grid spacing near the surface. For all GOTM runs in this section, the surface roughness length z_0 that appears in the boundary condition (A9) for the turbulence length scale l was set to $z_0 = 0.01$ m. This model parameter is not well constrained. Our parameter studies in section 5 show, however, that the impact of z_0 is negligible.

To save computational resources for the LES, all simulations in this section start at 0500 local time (1 h before the start of the radiative buoyancy forcing) rather than at midnight. Note, however, that in all the following sections, the beginning of the simulations is at midnight.

The horizontally averaged LES results are shown in Fig. 2, comparing simulations without ($u_s = 0$) and with LT. In both cases, the buoyancy structure (Figs. 2a,b) shows the evolution of DWLs with similar characteristics. LT effects are clearly noticeable especially in the reduced near-surface buoyancy in the simulation with wave forcing, which is consistent with the reduced near-surface stratification due to LT-enhanced mixing (Figs. 2c,d). The Eulerian shear (Figs. 2e,f) in the simulation with LT deviates from its counterpart with $u_s = 0$ significantly in the upper 2 m, where the Stokes shear production P_s becomes the dominant source of turbulence (u_s decays to approximately 10% of its surface value within the uppermost 0.65 m). This effect is also clearly evident in the Richardson number, $\mathrm{Ri} = N^2 S^{-2}$, which does not account for Stokes shear (Figs. 2g,h).

Figures 3 and 4 compare the DWL evolution in the LES (with and without LT) and the second-moment models for four selected points in time (marked in Fig. 2). This comparison shows that the overall characteristics of the LES are well reproduced by all models: both the DWL thicknesses and the vertical structures of buoyancy, velocity, and the turbulent momentum flux closely correspond to those predicted by the LES. Significant differences are largely confined to the upper 1–2 m, where the LES suggest a strong reduction of stratification and shear due to the effects of LT. For the period between 1200 and 1500 local time, when DWL anomalies are most distinct, the inlay plots in Figs. 3d and 3f show that the inclusion of LT effects leads to a significant reduction of the near-surface velocity. Only the model of H15 is in close agreement with the LES, while the model of KC04 clearly underestimates the additional mixing of momentum due to LT effects, underlining the importance of the Stokes shear term in (10). For the near-surface buoyancy profiles (see inlay plots in Figs. 3c,e), differences between the second-moment models are less pronounced, and all tend to underestimate the reduction of near-surface stratification due to LT. Differences between the simulations with and without LT become especially clear in the gradient Richardson number shown in Figs. 4b, 4d, 4f, and 4h. The pronounced near-surface peak in Ri is captured only by the most advanced model of H15 as shown in Fig. 4.

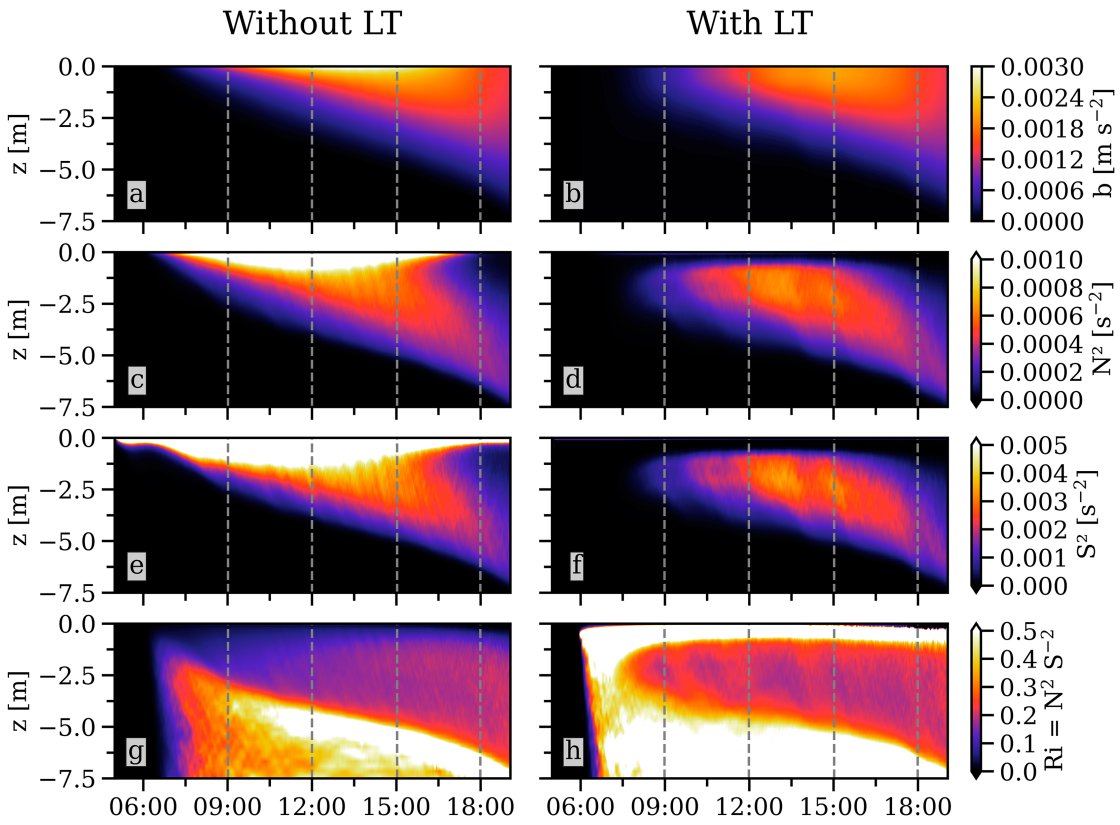

FIG. 2. Evolution of (a),(b) buoyancy, (c),(d) buoyancy frequency squared, (e),(f) total Eulerian shear squared, and (g),(h) gradient Richardson number for a typical DWL scenario (left) without and (right) with LT forcing, respectively. Shown are horizontally averaged LES results for the forcing parameters discussed in section 3. Dashed vertical lines mark the profiles shown in Figs. 3 and 4.

It is worth noting that all second-moment models predict virtually identical profiles underneath the thin near-surface region directly affected by Stokes production. For the LES, the negligible effect of LT below the thin-surface layer is the case only for the late-stage DWLs (Figs. 3e–g), while the DWL evolution in the morning and around noon (Figs. 3a–d) shows weak but significant LT effects also below the Stokes layer. These LT effects on the mean fields are accompanied by inflectional shear, similar to observations of inflectional shear by Hughes et al. (2021) when convective cooling commenced at sundown, as well as by enhanced TKE transport from the Stokes layer toward the layer underneath (Li and Fox-Kemper 2020).

Overall, we conclude that the performance of the model of H15 is most satisfying, and we will therefore use this model for all of the following numerical investigations. As shown in section 2 of the supplemental material, simulations conducted with a modified version of the k–ω model (see appendix A), using the same stability functions of H15, yield very similar results, providing support for the robustness of our results.

4. DWL energy budgets at low and high latitudes

In this section, we derive energy budgets for DWLs and use these to investigate the effects of rotation and heating time on high-latitude DWLs.

a. Theory

For the analysis of the DWL energetics, it is convenient to define a DWL-averaged buoyancy $\overline{b}$ and a DWL thickness h based on expressions of the form

$$\overline{b}h = \int_{z_{\mathrm{ref}}}^{0} \tilde{b}\,dz \quad \text{and} \tag{16}$$

$$\varphi \overline{b} h^2 = -\int_{z_{\mathrm{ref}}}^{0} \tilde{b} z\,dz, \tag{17}$$

where $\tilde{b} = b - b_{\mathrm{ref}}$ is the DWL buoyancy anomaly, referenced with respect to the buoyancy b_{ref} at some reference level z_{ref} below the DWL, and φ a shape factor that depends on the vertical structure of the buoyancy profile. For example, it can be shown that $\varphi = 1/2$ and $\varphi = 1/3$ correspond to the cases of well-mixed and linearly stratified DWLs, respectively. For comparison, it is worth noting that Fairall et al. (1996) assumed DWLs with linear stratification ($\varphi = 1/3$), whereas applying (16) and (17) to the empirical DWL profiles in expression (17) of Gentemann et al. (2009) yields $\varphi \approx 0.2$–0.4 with a transition from exponential to more well-mixed profiles depending on wind speed. In our model, φ changes in time during the evolution of the DWL.

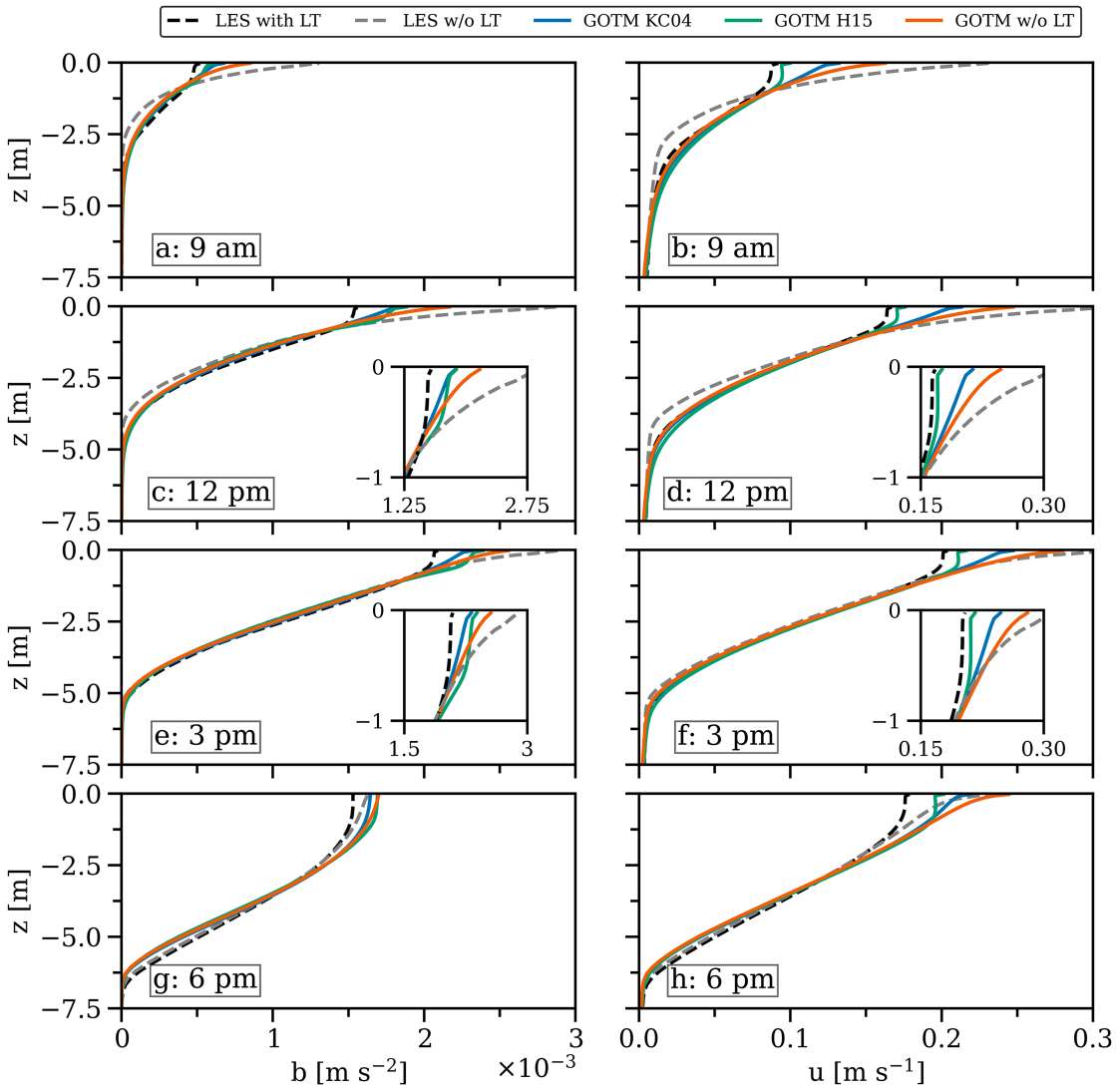

FIG. 3. Comparison of LES and GOTM simulations for (a),(c),(e),(g) buoyancy and (b),(d),(f),(h) u component of the velocity at the times indicated in Fig. 2. Dashed lines show LES results with (black) and without (gray) LT. Colored lines correspond to different second-moment models as indicated in the legend. Inset panels in (c)–(f) show enlarged views of the near-surface region.

Reformulating (3) in terms of $\tilde{b}$, ignoring the molecular fluxes, and integrating the resulting equation vertically between z_{ref} and the surface, the time derivative of the relation in (16) can be expressed as

$$\frac{d(\bar{b}h)}{dt} = \frac{d}{dt}\int_{z_{\mathrm{ref}}}^{0} \tilde{b}\,dz = B_0 + I_b^0, \tag{18}$$

which reflects the heat budget of the DWL, expressed in terms of buoyancy. In the derivation of (18), we have assumed that the temporal variability of the reference buoyancy b_{ref} has a negligible effect. Our idealized simulations show that the variability of b_{ref} indeed becomes negligible shortly after the DWL has formed, isolating the reference level from surface buoyancy forcing.

The expression in (17) is recognized as the potential energy anomaly E_{pot} induced by the presence of the DWL. Reformulating (3) in terms of $\tilde{b}$, multiplying the result by z, and integrating by parts, yields an equation for the evolution of the potential energy anomaly:

$$\frac{d}{dt}E_{\mathrm{pot}} = \frac{d(\varphi\bar{b}h^2)}{dt} = -\frac{d}{dt}\int_{z_{\mathrm{ref}}}^{0} \tilde{b}z\,dz = -\int_{z_{\mathrm{ref}}}^{0} G\,dz + h\bar{I}_b, \tag{19}$$

where we again ignored the molecular fluxes and introduced $\bar{I}_b = h^{-1}\int_{z_{\mathrm{ref}}}^{0} I_b\,dz$. In the derivation of (19), we have assumed $I_b(z_{\mathrm{ref}}) \ll I_b^0$ to ensure that our analysis includes the entire near-surface region with significant radiative heating. Similar to (18), the effect of the temporal variability of b_{ref} is found to be negligible in our simulations and has therefore been neglected in (19).

Using (18), the energy budget in (19) can thus be rearranged in the form

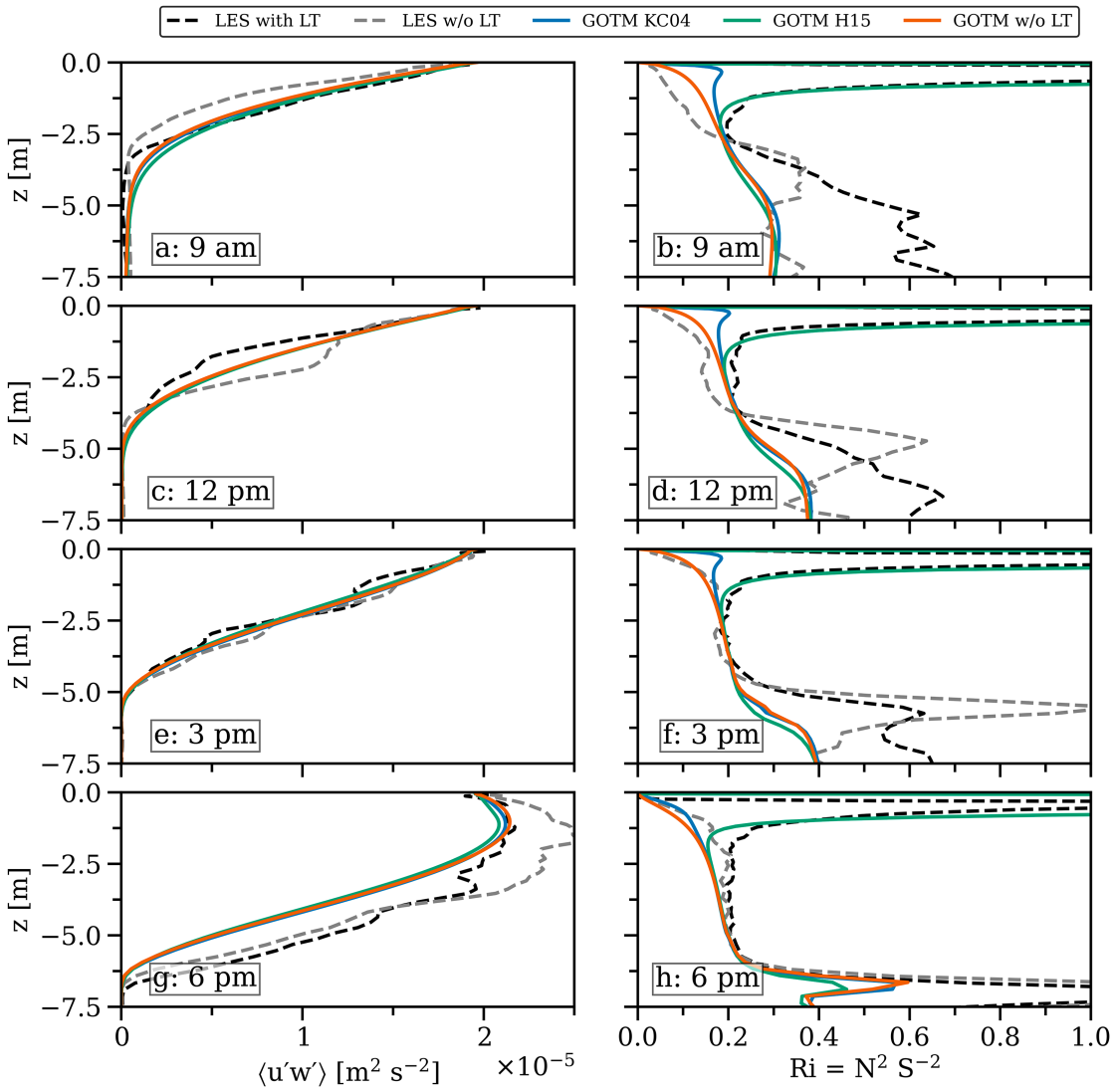

FIG. 4. As in Fig. 3, but for (a),(c),(e),(g) total (resolved plus subgrid-scale) turbulent momentum flux $\langle u'w' \rangle$ and (b),(d),(f),(h) gradient Richardson number Ri.

$$\underbrace{\varphi h\left(B_0 + I_b^0 - \frac{\overline{I}_b}{\varphi}\right)}_{\substack{\text{work required to}\\ \text{mix down buoyancy}\\ \text{added near surface}}} + \underbrace{\varphi h \overline{b} w_e}_{\substack{\text{work required}\\ \text{to mix up}\\ \text{entrained fluid}}} + \underbrace{\frac{d\varphi}{dt}\overline{b}h^2}_{\substack{\text{work required to}\\ \text{change the DWL}\\ \text{buoyancy structure}}}$$

$$= \underbrace{-\int_{z_{\text{ref}}}^{0} G dz}_{\substack{\text{work done}\\ \text{by turbulence}}}, \tag{20}$$

where we introduced the entrainment velocity $w_e = dh/dt$.

Similarly, an equation for the DWL kinetic energy can be obtained by multiplying the momentum equations in (1) and (2) with u and v, respectively, adding the results, and integrating from z_{ref} to the surface. Ignoring again the molecular flux terms for simplicity, this yields an energy budget of the form:

$$\frac{d}{dt}E_k = \frac{d}{dt}\int_{z_{\text{ref}}}^{0} \frac{u^2 + v^2}{2} dz = \mathbf{u}^0 \cdot \boldsymbol{\tau}^0 + \int_{z_{\text{ref}}}^{0} f\mathbf{k} \cdot (\mathbf{u} \times \mathbf{u}_s) dz - \int_{z_{\text{ref}}}^{0} P dz, \tag{21}$$

where $\mathbf{k}$ is the upward unit vector and $\mathbf{u}^0$ the velocity at the surface. The terms on the right hand side of (21) can be interpreted as (i) the work performed by the wind stress on the DWL, (ii) the exchange of kinetic energy with the surface wave field due to the effect of rotation (see, e.g., Suzuki and Fox-Kemper 2016), and (iii) the loss of kinetic energy to TKE by turbulence shear production. Similar to the negligible effect of temporal variations of b_{ref} in (18) and (19), we also find that the temporal variability of the reference kinetic energy, $(u_{\text{ref}}^2 + v_{\text{ref}}^2)/2$, has a negligible effect on the energy budget in (21) shortly after the DWL has formed. Therefore, this term has been omitted in (21).

The shear production term in (21) connects the DWL kinetic energy to the vertically integrated TKE equation,

TABLE 1. Atmospheric forcing and model parameters used for the analysis of the DWL energetics.

	B_{max} (m^2 s^{-3})	B_0 (m^2 s^{-3})	U_{10} (m s^{-1})	L_{MO} (m)	T_f (h)	T_h (h)	z_0 (m)	η (m)	k_p (m^{-1})
10°N	5.5×10^{-7}	-2.6×10^{-7}	3.1	0.39	69.1	9.5	0.01	0.87	1.13
70°N	1.4×10^{-7}	-1.2×10^{-7}	3.1	1.53	12.6	12.2	0.01	0.87	1.13

$$-\int_{z_{ref}}^{0} G dz = -\frac{d}{dt}\int_{z_{ref}}^{0} k dz + \int_{z_{ref}}^{0} (P + P_s) dz - \int_{z_{ref}}^{0} \varepsilon dz, \quad (22)$$

which is easily derived from (12). The left-hand side of (22) and the right-hand side of the potential energy budget in (20) are identical, showing that the energy available for mixing within the DWL corresponds to the fraction of the (mean flow and Stokes) shear production that is neither dissipated nor used to change the DWL integrated TKE. The relative importance of the various terms in the DWL energy budgets in (20)–(22) will be investigated in the following discussion.

b. Results

To investigate the DWL energy budgets derived above, we compare a typical tropical case at 10°N with a high-latitude DWL at 70°N. The results were obtained using GOTM with the turbulence closure model of H15 that was shown to compare favorably to the LES in the previous section. We used a time step of 6 s and a grid spacing of 0.015 m at the surface, gradually coarsening toward the lower end of the numerical domain at 50-m depth. The atmospheric forcing and model parameters are summarized in Table 1. For both cases, we assumed that the surface buoyancy loss B_0 due to cooling exactly compensates for the radiative buoyancy supply over the course of a day. The buoyancy forcing parameters in Table 1 were chosen to yield realistic summertime values for the peak radiative heat flux I_{max} for the corresponding latitudes, water temperatures, and thermal expansion coefficients. For the tropical case, the values in Table 1 correspond to $I_{max} = 1000$ W m^{-2}, using $\alpha = 3.4 \times 10^{-4}$ K^{-1} for tropical 30°C water temperatures. Analogously, the parameters for the high-latitude case yield $I_{max} = 680$ W m^{-2} with $\alpha = 1.6 \times 10^{-4}$ K^{-1} for 10°C water temperatures. Since the buoyancy flux is linearly proportional to α, it can correspond to different heat fluxes, depending on water temperature. To make our model more generally applicable, we have therefore formulated it in terms of buoyancy rather than temperature.

For the tropical case, as before, the period with nonzero solar radiation was chosen as $T_d = 12$ h (between 0600 and 1800 local time), whereas we assume $T_d = 18$ h (between 0300 and 2100 local time) for the high-latitude case. The resulting effective heating periods T_h, computed from (7), can be found in Table 1, together with all other model parameters that were kept constant. To determine the shortwave absorption length η in (5), we varied η and compared our GOTM results for the tropical scenario against a plot of the parametric temperature profile from Eq. (17) of Gentemann et al. (2009), who used a more complex nine-band absorption model for clear tropical waters. We find that our simple one-band model results in a very similar vertical DWL structure for $\eta = 0.87$ m, which is the value we used for all simulations in this section (Table 1).

The evolution of the near-surface buoyancy for the two cases is shown in Figs. 5a and 6a. The DWL thickness h, one of the most important bulk parameters, is defined here by a simple density threshold, identifying the lower edge of the DWL with the vertical position where the buoyancy has decayed to 5% of its maximum value. Figures 5a and 6a show that this definition provides a plausible representation of the vertical extent of the DWL for both cases.

The reference level z_{ref} is chosen to coincide with the location of the minimum buoyancy in the water column, and $\tilde{b} = b - b_{ref}$ is defined based on the reference buoyancy b_{ref} found at this depth. This definition guarantees that the entire near-surface region affected by radiative heating is included in our analysis.

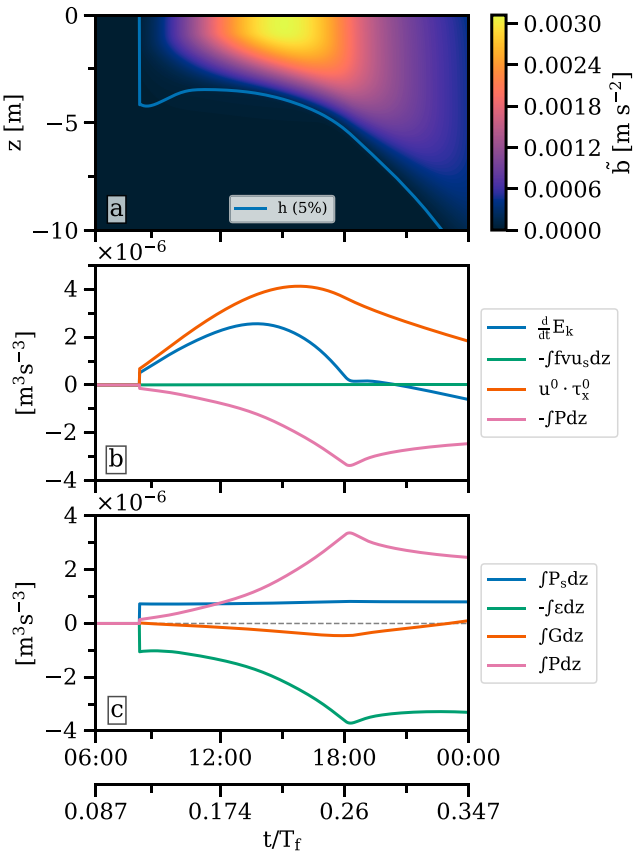

FIG. 5. Evolution of (a) DWL buoyancy anomaly, (b) DWL kinetic energy budget in (21), and (c) turbulent kinetic energy budget in (22) for the tropical case at 10°N (Table 1). The blue line in (a) shows the DWL thickness h computed from the depth at which the buoyancy has dropped to 5% of its maximum value. Note that the simulation starts at midnight ($t/T_f = 0$), and that both the wind stress and Stokes drift point into the x direction ($\tau_y^0 = 0$ and $v_s = 0$).

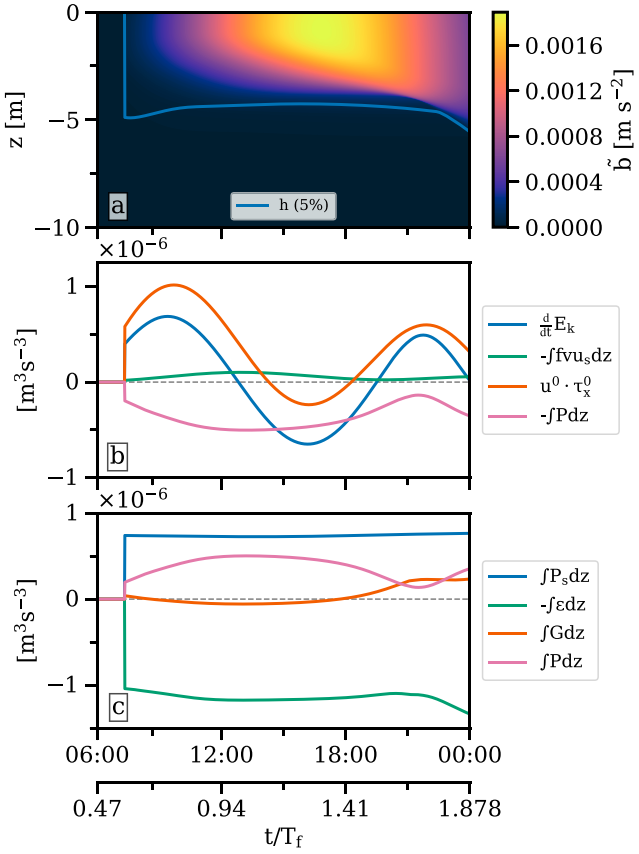

FIG. 6. As in Fig. 5, but now for the high-latitude case at 70°N (Table 1). Note the different scales with respect to Fig. 5.

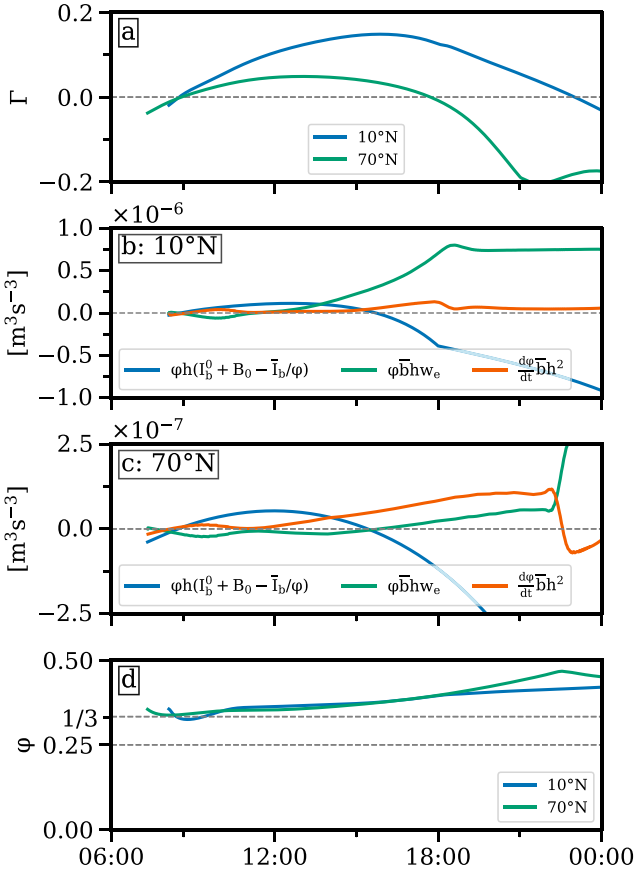

FIG. 7. Evolution of (a) bulk mixing efficiency Γ, the left-hand side terms in (20) at (b) 10°N and (c) 70°N, and (d) shape factor ϕ computed from (16) based on h from the 5% density threshold with the values of Fairall et al. (1996) and Gentemann et al. (2009) as dashed gray lines. Note the different axes scales in (b) and (c).

Figure 5b shows the evolution of the kinetic energy budget in (21) for the tropical case. During the initial DWL formation phase until approximately early afternoon, the work performed by the wind, $u^0\tau_x^0$, is largely used to accelerate the DWL [cf. to $(d/dt)E_k$] with a significantly smaller contribution used for turbulence shear production $\int Pdz$. In the afternoon, entrainment starts to become increasingly important (Fig. 5a), and additional energy is thus required to accelerate entrained fluid. As a consequence, the DWL kinetic energy increases at a slower rate while shear production becomes the dominant energy sink. After the surface buoyancy forcing collapses in the late afternoon and evening, the entrainment rate further increases as no more work is required to mix down buoyant fluid from the surface (see more detailed discussion below). This point is marked by a sharp transition in the energy budget at approximately 1800 local time, after which $(d/dt)E_k$ becomes insignificant, and the wind work is largely used for turbulence shear production that in turn becomes available for entrainment. Stokes shear production (Fig. 5c) dominates turbulence production during the initial DWL formation phase until approximately noon, while the exchange of mean kinetic energy with the wave field (marked in green in Fig. 5b) is negligible throughout the simulations.

For the high-latitude case shown in Fig. 6, the work performed by the surface stress, $u^0\tau_x^0$, starts to be suppressed by the veering of the near-surface velocity out of the wind direction shortly after the formation of the DWL. This is reflected in a late-morning peak of the wind energy input, and a subsequent monotonic decay down to negative values (energy loss) around 1400 local time (Fig. 6b). Therefore, starting from the early afternoon, the pool of DWL kinetic energy built up during the initial DWL formation in the morning becomes an increasingly important energy source $[(d/dt)E_k < 0]$ to feed turbulence shear production in the afternoon. Comparison with Fig. 5 shows that due to these effects, the integrated wind work is approximately a factor of 5 smaller compared to the tropical case. Due to the overall strongly reduced energy turnover, the extraction of energy from the wave field due to Coriolis effects (green line in Fig. 6b) becomes significant in the mean kinetic energy budget, and Stokes shear production P_s exceeds Eulerian shear production P in the TKE budget. The net effect of the reduced turbulence production due to rotation is a complete collapse of entrainment after the initial DWL shoaling in the morning (blue curve in Fig. 6a).

To investigate the extent to which the strong surface buoyancy forcing and the stratification inside the DWL affect the energetics of turbulence, we computed the bulk flux coefficient, $\Gamma = -\int_{z_{ref}}^{0} Gdz / \int_{z_{ref}}^{0} \varepsilon dz$, and find strong differences between tropical and high latitudes. As shown in Fig. 7a, for the

tropical case we find $\Gamma \approx 0.15$ during the late afternoon and evening, close to the popularly used value of $\Gamma = 0.2$. At high latitudes, however, Γ only reaches positive values during the time of strongest buoyancy forcing and the values are small compared to the tropical case. At later times, convection near the surface dominates the integral of the buoyancy production, causing it to change signs.

The different contributions to the potential energy budget in (20) for the tropical and high-latitude cases are compared in Figs. 7b and 7c, respectively. During midday, in both cases, the largest fraction of the work performed by turbulence against gravity is used to mix down near-surface buoyant fluid generated by solar heating. According to (20), the ratio $\overline{I}_b/(I_b^0\varphi)$ determines to what extent the work required for this process is reduced by the penetration of shortwave radiation. If all shortwave radiation is absorbed at the surface ($\eta = 0$), this ratio is zero. We find $\overline{I}_b/(I_b^0\varphi) = 0.53$ and $\overline{I}_b/(I_b^0\varphi) = 0.44$ at midday for the tropical and high-latitude cases, respectively, suggesting that penetrating shortwave radiation strongly impacts the DWL potential energy budget.

Figures 7b and 7c also show that the first hours after the initial generation of the DWLs are characterized by "detrainment" ($w_e < 0$) due to the restratifying effect of the increasing solar radiation. For the tropical case, w_e changes sign in the late morning, and around 1400 local time the work required for the entrainment of dense fluid at the DWL base finally becomes the dominating term in the potential energy budget. This is in strong contrast to the high-latitude case, in which entrainment never becomes an energetically relevant factor.

Beyond the work required for DWL deepening, turbulent mixing may also act to change the vertical DWL buoyancy structure. The energetic implications of this third type of energy conversion in (20) can be quantified by considering changes in the shape parameter φ, which is easily computed from (16) and (17) after determining the DWL thickness h from the 5% buoyancy threshold discussed above (see blue lines in Figs. 5a and 6a). Figure 7d shows that during the morning and early afternoon, this parameter starts close to $\varphi = 1/3$, but increases to larger values over the course of the day, reflecting the tendency toward a more well-mixed DWL especially in the evening due to the decreasing solar buoyancy forcing. For comparison, the parametric temperature profiles in Gentemann et al. (2009) for this wind speed yield a constant $\varphi \approx 0.25$, whereas the model of Fairall et al. (1996) corresponds to a constant $\varphi = 1/3$. These differences in φ between our model and the models of Fairall et al. (1996) and Gentemann et al. (2009) can be largely attributed to the thin near-surface convective layer generated by penetrating shortwave radiation in our simulations, which is not represented in the models of Fairall et al. (1996) and Gentemann et al. (2009). Figures 7b and 7c show that the work required for this partial homogenization of late-stage DWLs becomes significant only for the high-latitude case, where it dominates the potential energy balance during the afternoon.

5. Key parameters and DWL parameterization

a. *Identification of dimensional and nondimensional parameters*

The evolution and physical properties of the DWLs in our idealized simulations are affected by a number of independent dimensional parameters, imposed by the atmospheric forcing and the properties of the surface wave field. The former includes the constant wind stress, quantified here with the help of the friction velocity u_* (or, equivalently, the wind speed U_{10}), and the parameters describing the idealized buoyancy forcing shown in Fig. 1: the maximum total buoyancy flux at midday $B_{\max}$, the (constant) buoyancy loss at the surface B_0, the heating period T_h, and the period of the periodic forcing T_p. For penetrating shortwave radiation, the vertical absorption scale η in (5) has to be considered as an additional parameter.

The surface wave field affects the problem through the surface Stokes velocity u_s^0 and a vertical decay scale that is determined by the peak wavenumber k_p. Note that the same two dimensional parameters would also appear for the simpler case of monochromatic waves (Kukulka et al. 2013). However, in the equilibrium wave model of Li et al. (2017) used in our study, both u_s^0 and k_p depend on the wind speed through (8) and (9), and therefore do not constitute independent dimensional parameters.

Finally, as all model parameters of the turbulence model are nondimensional, no additional dimensional parameters are introduced, with a single exception: the upper boundary condition for the turbulent length scale l in (A9) involves the surface roughness length z_0 that we consider in the following as an additional independent parameter.

The most relevant velocity scale in our problem is the friction velocity u_*, which can be used to define the relevant length scale, $L = u_*^3/B_{\max}$ [note that this length scale is directly proportional to the Monin–Obukhov scale, $L_{\mathrm{MO}} = u_*^3/(\kappa B)$, evaluated at midday]. If we chose, in addition to u_* and L, the heating period T_h shown in Fig. 1 as the relevant time scale, we can nondimensionalize the key variables of our problem (Table 2), and derive nondimensional versions of the transport equations of momentum and buoyancy in (1)–(3). From these nondimensional transport equations, it is straightforward to identify two key nondimensional parameters of the problem. The first is the nondimensional Coriolis parameter, $\hat{f} = fT_h = 2\pi T_h/T_f$, which measures the ratio of the heating period and the inertial period T_f. The second parameter,

$$R = \frac{u_*^2}{T_h B_{\max}}, \tag{23}$$

compares the destabilizing effect of the wind stress u_*^2 to the stabilizing effect of the total buoyancy supply during the heating period (which is proportional to $T_h B_{\max}$). For simplicity, we ignore the molecular transport terms in (1)–(3) for our dimensional analysis, as their effect is only marginal in our simulations.

TABLE 2. Definition of nondimensional variables denoted by the hat (ˆ) symbol.

$z = \frac{u_*^3}{B_{\max}}\hat{z}$	$t = T_h\hat{t}$	$u, v = u_*\hat{u}, u_*\hat{v}$	$u_s, v_s = u_*\hat{u}_s, u_*\hat{v}_s$	$b = \frac{B_{\max}}{u_*}\hat{b}$	$k = u_*^2\hat{k}$
$l = \frac{u_*^3}{B_{\max}}\hat{l}$	$\varepsilon = B_{\max}\hat{\varepsilon}$	$\nu_t = \frac{u_*^4}{B_{\max}}\hat{\nu}_t$	$\nu_t^b = \frac{u_*^4}{B_{\max}}\hat{\nu}_t^b$	$I_b = B_{\max}\hat{I}_b$	$f = \frac{\hat{f}}{T_h}$

Additionally, the buoyancy flux ratio $B_0/B_{\max}$ and the time scale ratio T_h/T_p appear as independent nondimensional parameters in our model for the buoyancy forcing in Fig. 1. To reduce the number of free parameters and allow for quasi-periodic solutions, we will assume in most of the parameter studies that the daily average of the total buoyancy flux is zero, i.e., that the incoming solar radiation is exactly compensated by the net surface buoyancy loss B_0T_p. With this constraint, B_0 and $B_{\max}$ are no longer independent:

$$-\frac{B_{\max}}{B_0} = \frac{\pi}{2}\frac{T_p}{T_d} - 1, \tag{24}$$

and combining (7) and (24) thus yields

$$\frac{T_h}{T_p} = \frac{2}{\pi}\frac{T_d}{T_p}\arccos\left(\frac{2}{\pi}\frac{T_d}{T_p}\right), \tag{25}$$

revealing a direct one-to-one relation between the time scale ratios T_h/T_p and T_d/T_p. The final nondimensional parameter associated with the buoyancy forcing is the nondimensional absorption scale, $\hat{\eta} = \eta/L$.

Finally, as pointed out in the context of (8) above, the wave model of Li et al. (2017) predicts a constant value of the Langmuir number $\mathrm{La} = (u_*/u_s^0)^{1/2} = 0.3$. The second nondimensional product in this wave model is the nondimensional peak wavenumber, $\hat{k}_p = k_pL$, which, from (8) and (9), can be rewritten as $\hat{k}_p \propto u_*/(C_sgB_{\max})$, suggesting $u_*/(C_sgB_{\max})$ as the only independent nondimensional parameter arising from the surface wave model.

The surface roughness length, z_0, which represents the length scale of turbulence at the surface, transforms into the nondimensional roughness parameter $\hat{z}_0 = z_0/L$.

All nondimensional parameters present in this study are summarized in Table 3. We carefully checked that different numerical solutions indeed collapse if all nondimensional parameters are kept constant and all variables are nondimensionalized as in Table 2.

b. *Nondimensional PWP86 model*

A frequently used model to describe DWL bulk parameters has been formulated by PWP86. These authors used a vertically integrated mixed layer model with a simple parameterization for entrainment (Pollard et al. 1973), forced, as in our study, with a constant wind stress and a surface buoyancy forcing identical to that shown in Fig. 1. Based on a scale analysis of their model equations, PWP86 suggested simple scaling relations for the DWL thickness h, buoyancy anomaly $\overline{b}$ [as defined in (16)], and velocity anomaly, $\overline{V} = \sqrt{(\overline{u}^2 + \overline{v}^2)}$, with

$$\overline{u} = \frac{1}{h}\int_{z_{\mathrm{ref}}}^{0}\tilde{u}\,dz, \quad \overline{v} = \frac{1}{h}\int_{z_{\mathrm{ref}}}^{0}\tilde{v}\,dz \tag{26}$$

and $\tilde{u} = u - u_{\mathrm{ref}}$, $\tilde{v} = v - v_{\mathrm{ref}}$, all evaluated at the peak buoyancy flux (i.e., at noon). Converted to the notation used in our study, and expressed in nondimensional form, these scaling relations can be written as

$$\hat{h} = \frac{h}{L} = a_1R^{-1/2}F(\hat{f}), \tag{27}$$

$$\hat{\overline{b}} = \frac{\overline{b}\,u_*}{B_{\max}} = a_2R^{-1/2}F(\hat{f})^{-1}, \tag{28}$$

$$\hat{\overline{V}} = \frac{\overline{V}}{u_*} = a_3R^{-1/2}, \tag{29}$$

where a_1, a_2, and a_3 denote nondimensional model constants, and F is a nondimensional model function accounting for the effect of rotation:

$$F(\hat{f}) = \frac{1}{\hat{f}}[2 - 2\cos(\hat{f}/2)]^{1/2}. \tag{30}$$

Note that only two of the nondimensional parameters identified in the previous section, $R = u_*^2/(B_{\max}T_h)$ and $\hat{f}$, appear in the PWP86 model. The expressions in (27)–(29) apply only for the special case $\eta = 0$, i.e., if all shortwave radiation is absorbed at the surface. In section 5d, we will suggest a possible generalization for the case of penetrating shortwave radiation.

TABLE 3. The nondimensional parameters. Note that the variability of some parameters appearing in parentheses is restricted on our model.

$R = \frac{u_*^2}{T_hB_{\max}}$	$\hat{f} = fT_h$	$\frac{T_h}{T_p}$	$\frac{B_0}{B_{\max}}$
$\hat{z}_0 = \frac{z_0}{L}$	$\hat{\eta} = \frac{\eta}{L}$	(La = 0.3)	$\hat{k}_p \propto \frac{u_*}{C_sgB_{\max}}$

c. *Parameter space studies*

Before we tested the scaling relations by PWP86 over a wide parameter range, we performed parameter space studies for the nondimensional parameters T_h/T_p, $B_0/B_{\max}$, $\hat{z}_0$, and $\hat{k}_p$ that are not included in the PWP86 scaling. Here, we set $\hat{\eta} = 0$ for simplicity, varied R over the physically relevant range from $R = 10^{-4}$ to 10^{-2}, and individually tested the impact of the above nondimensional parameters. For this parameter space study, we again used the closure model of H15 with the same time step and the same number of grid cells as in section 4. However, the depth of the water column was now automatically adjusted to 10 times the DWL thickness at

midday to ensure that the lower edge of the numerical domain had no significant impact on the results.

As shown in Fig. 8, we find that the nondimensional parameters T_h/T_p, B_0/B_{max}, $\hat{z}_0$, and $\hat{k}_p$ have a negligible impact on the nondimensional DWL thickness $\hat{h}$ (and also on the other DWL bulk properties not shown here for brevity but included in section 2 of the supplemental material). We note, however, that the parameters T_h/T_p and B_0/B_{max} may have a larger impact for longer simulation periods of several days, where they may affect the nighttime DWL reset and thus the quasi-periodic evolution of the surface layer structure. Similarly, the peak wavenumber $\hat{k}_p$ may become relevant for nonequilibrium wave fields, especially for conditions when long-wave swell induces a larger penetration depth of the Stokes shear (Kukulka et al. 2013).

To test the scaling relations by PWP86, we performed a parameter space study using H15, consisting of 200 model runs, in which we varied R from 10^{-4} to 10^{-2} and $\hat{f}$ from 0 to 4.95 (or, equivalently, T_h/T_f from 0 to 0.79).

We especially focused on the model performance in high-latitude regions ($T_h/T_f > 0.5$), which are not well explored at the moment and for which the model assumptions of PWP86 are uncertain. We again assume surface absorption ($\hat{\eta} = 0$), and that the daily average of the total buoyancy flux is zero ($B_0/B_{max} = -0.466$, $T_h/T_p = 0.4$). The roughness length is set to $\hat{z}_0 = 0.01$.

In Fig. 9, we show simulation results for the nondimensional DWL thickness $\hat{h}$, bulk buoyancy $\hat{\bar{b}}$, and bulk velocity $\hat{\bar{V}}$ at $t = T_p/2$, i.e., at midday. These quantities are normalized by the PWP86 scaling relations in (27), (28), and (29), respectively, to reveal the variability of the model parameters a_1, a_2, and a_3. Figure 9 shows that the performance of the PWP86 scaling is generally excellent, except for a weakly forced regime with $R \lessapprox 7 \times 10^{-4}$ (weak winds and strong buoyancy forcing), where a strong variability in the PWP86 model parameters suggests that their scaling fails (blue dashed line in Fig. 9).

A more detailed analysis showed that turbulent and molecular diffusivities become comparable in this regime, and that Ri at the DWL base becomes much larger than the critical value for shear instability, indicating an absence of turbulent entrainment. It is worth noting that Hughes et al. (2020) studied this regime in more detail, based on high-resolution observations and a 1D model with a simpler turbulence closure without LT but similar radiative and atmospheric forcing parameters. From their simulations, these authors identified a critical wind speed of $U_{10} = 2$ m s^{-1} below which turbulent mixing does not occur. This is equivalent to $R = 6.6 \times 10^{-4}$ for the buoyancy forcing used in their study, and therefore consistent with the more generally applicable nondimensional threshold suggested by our simulations with a more advanced turbulence model that also included Langmuir effects. Overall, this indicates that molecular effects become significant in this regime, suggesting that the Reynolds and Prandtl numbers are additional relevant nondimensional parameters that have to be considered. As the effects of these parameters are not accounted for in any of the high-Re models used in our study, we do not investigate this regime any further here.

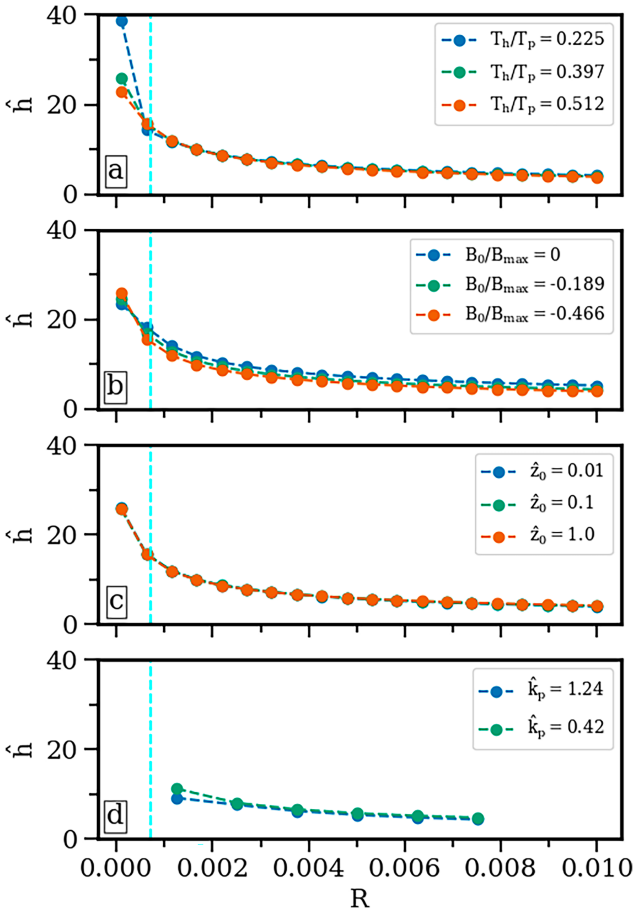

FIG. 8. Nondimensional thickness $\hat{h}$ for constant $T_h/T_f = 0.14$ as a function of $R = u_*^2/(B_{max}T_h)$ for different values of (a) the time scale ratio T_h/T_p, (b) the flux ratio B_0/B_{max}, (c) the nondimensional surface roughness $\hat{z}_0$, and (d) the nondimensional peak wavenumber $\hat{k}_p$. All other nondimensional parameters are kept fixed at $T_h/T_p = 0.4$, $B_0/B_{max} = 0.466$, and $\hat{z}_0 = 0.01$, respectively. The blue dashed line shows the critical threshold for the collapse of DWL turbulence, $R = 7 \times 10^{-4}$, which is discussed in detail further below.

We determined the model constants a_1, a_2, and a_3 by calculating the mean of the PWP86-scaled model results shown in Fig. 9, excluding regions with $R < 7 \times 10^{-4}$. Table 4 shows that the revised constants suggest a more than 30% increase in the DWL thickness (and a correspondingly smaller buoyancy/temperature anomaly) compared to the original values by PWP86, which is significant for many applications. Most importantly, differences between DWL bulk parameters from our GOTM simulations and those predicted by the (revised) PWP86 model rarely exceed 10% (with largest deviations observed at large T_h/T_f) across the entire parameter range. Table 4 also shows that simulations without LT (not discussed in detail here) result in DWLs that are approximately 10% shallower and have a correspondingly larger buoyancy contrast.

The PWP86 scaling relations were originally proposed to predict DWL properties at the solar radiation peak ($t = T_p/2$). More relevant for many applications, including the interpretation of SST snapshots from satellite data, atmosphere–ocean

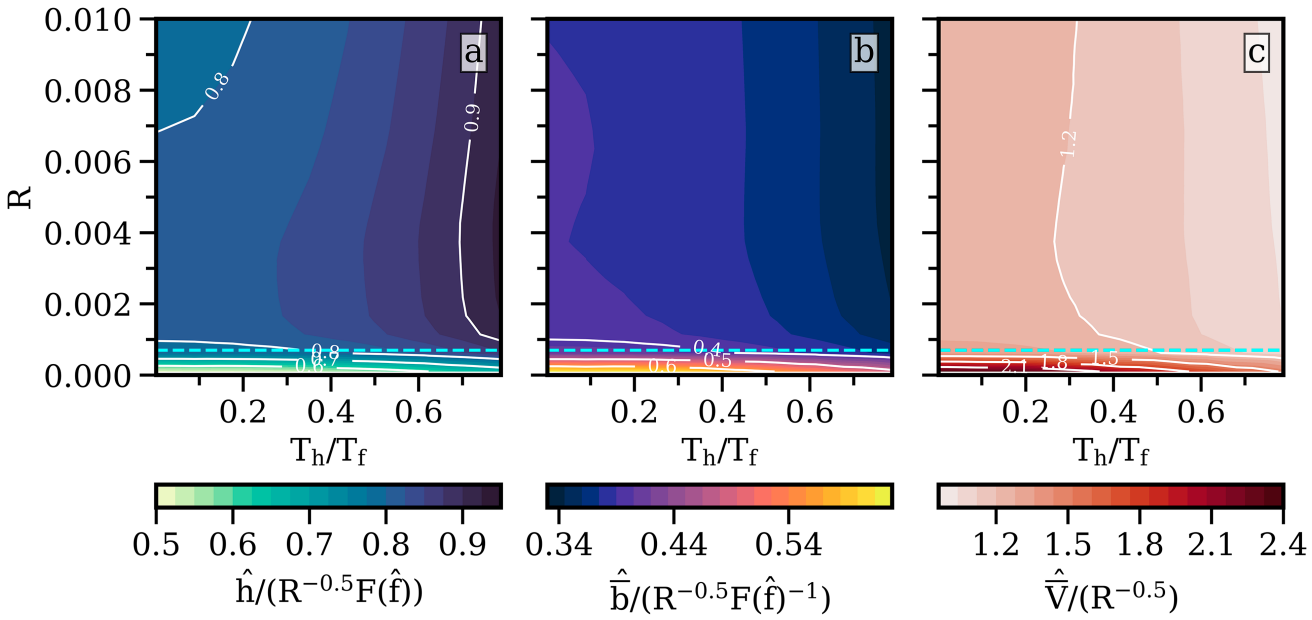

FIG. 9. DWL properties as functions of $R = u_*^2/(B_{max}T_h)$ and $T_h/T_f = \hat{f}/(2\pi)$. Shown are midday values of (a) DWL thickness, (b) DWL bulk buoyancy, and (c) DWL bulk velocity, normalized by the PWP86 scalings in (27)–(29). This implies that the results shown in (a)–(c) correspond to PWP86 model constants a_i. The blue line shows the critical value of R below which DWL turbulence does not occur.

coupling, and ecosystem applications, are, however, often the DWL properties at the peak of the DWL buoyancy or temperature anomaly in the afternoon. The timing of this peak cannot be determined from the PWP86 scaling. We therefore identified the (nondimensional) time t_{max}/T_p of the maximum buoyancy anomaly numerically from our simulations.

Scaling our simulations at $t = t_{max}$ with the expressions of PWP86 (see section 2 of the supplemental material) suggests that the PWP86 scaling also provides an excellent representation of the DWL bulk properties during the buoyancy peak in the afternoon, provided the model coefficients a_1, a_2, and a_3 are appropriately adjusted. The values in Table 4 show that the DWL thickness and the buoyancy anomaly have increased by 29% and 47%, respectively, compared to midday, illustrating a strong modification of the DWL during the early afternoon. The small variability of the model coefficients in Table 4 supports the applicability of the PWP86 scaling also for this case, except for the diurnal jet, which shows a strong dependency on T_h/T_f especially for large values of this parameter. We attribute this to the effect of the pronounced inertial oscillations at high latitudes that are not well represented by the scaling of PWP86. The good performance of the scaling of PWP86 for the depth and bulk buoyancy at this point in time is a surprising result, as we found that the model assumption of a constant bulk Richardson number $\mathrm{Ri}_b = \overline{b}h/\overline{V}^2 = 0.65$, which is the basis of PWP86, is not valid any more at high latitudes due to the decrease of $\overline{V}$ in the afternoon.

TABLE 4. Model constants a_1, a_2, and a_3 of the PWP86 model appearing in (27)–(29). The original constants of PWP86 were converted to our notation according to: $a_1 = 0.45 \times 2^{1/2} = 0.63$, $a_2 = 1.5 \times 2^{-3/2} = 0.53$, and $a_3 = 1.5 \times 2^{-1/2} = 1.06$. The factor 1/2 arises from the relation $T_h = 2P_Q$, where P_Q is the heating period in the notation of PWP86. The ranges given in the table correspond to the *maximum* deviations across the entire parameter range. Standard deviations (not shown) are considerably smaller. Here, t_{max} is the time of maximum buoyancy anomaly. All simulations were conducted for the case $\hat{\eta} = 0$.

	$t = T_p/2$			$t = t_{max}$	
	PWP86	With LT	Without LT	With LT	Without LT
a_1	0.63	0.84 ± 0.07	0.75 ± 0.1	1.08 ± 0.03	1.01 ± 0.05
a_2	0.53	0.38 ± 0.03	0.42 ± 0.05	0.56 ± 0.05	0.59 ± 0.05
a_3	1.06	1.15 ± 0.15	1.30 ± 0.2	1.3 ± 0.5	1.3 ± 0.5

Figure 10a shows that the timing of the afternoon buoyancy peak is relatively robust, generally observed between 1500 and 1630 local time with a shift toward later times for larger T_h/T_f. We attribute this shift to the suppression of entrainment of colder bottom waters due to stronger rotation effects at higher latitudes and/or a larger total buoyancy flux for larger T_h. A similar shift toward later times is observed if the shortwave absorption scale $\hat{\eta}$ is increased (Figs. 10b,c), which results in a larger DWL thickness and therefore more time required to heat up the DWL to its maximum temperature. Overall, however, the buoyancy/temperature peak is observed in the same range 1500–1630 local time for all absorption scales we investigated.

d. *Effect of penetrating shortwave radiation*

To investigate the first-order impacts of penetrating shortwave radiation in the scaling of PWP86, we carried out a parameter space study similar to that shown in Fig. 9. Now, however, we varied R and $\hat{\eta}$ over the physically relevant ranges $R = 10^{-4}$–10^{-2} and $\hat{\eta} = 0$–5 at two different latitudes. We chose $T_h/T_f = 0.14$ and 0.74, corresponding to our standard tropical and high-latitude cases from section 4, while

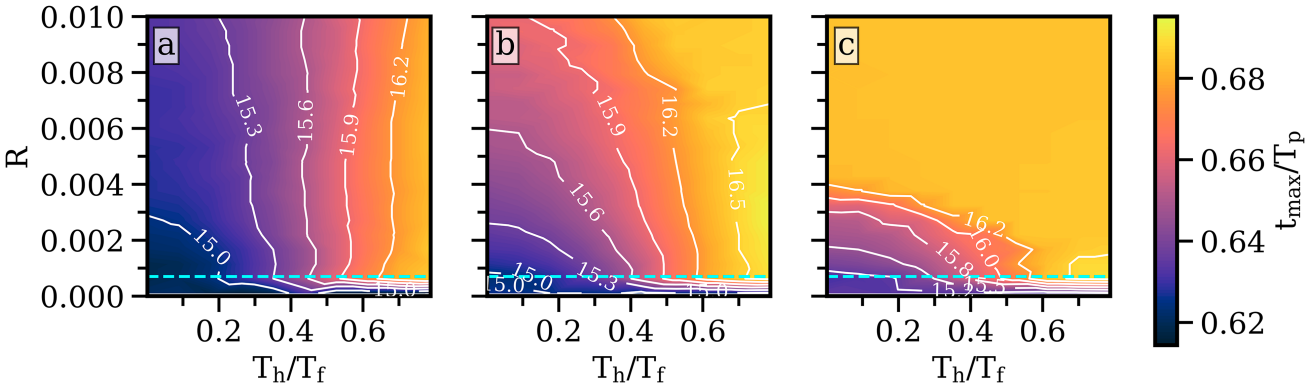

FIG. 10. Nondimensional time $t = t_{max}/T_p$ for varying R and T_h/T_f (the contour line labels show the time in hours of the day) for (a) $\hat{\eta} = 0$, (b) $\hat{\eta} = 2$, and (c) $\hat{\eta} = 4$.

keeping the other nondimensional parameters constant at $T_h/T_p = 0.4$, $B_0/B_{max} = -0.466$, and $\hat{z}_0 = 0.01$.

For the scaling, it appears physically more intuitive to relate the shortwave penetration depth η to the DWL thickness h, which yields η/h (rather than $\hat{\eta} = \eta/L$) as the key nondimensional parameter. Figure 11c shows that η/h always stays well below 1 for the range of $\hat{\eta}$ chosen in this study, which means that all the heat from the surface buoyancy flux is absorbed well within our definition of the DWL depth. Following the suggestion of PWP86, we parameterize the increase in thickness $\hat{h}$ due to an increase in η by multiplying the corresponding PWP86 expression in (27) with a function J that depends on $\hat{h}/\hat{\eta}$. We suggest

$$J(\hat{h}/\hat{\eta}) = (1 - A_\eta e^{-\hat{h}/\hat{\eta}})^{-(3/2)}, \tag{31}$$

where $A_\eta = 6.9$ was obtained from fitting [the original prefactor of PWP86, $(I_b^0 - B_0)/I_b^0$, did not yield acceptable results].

The modified PWP86 scaling that includes the effects of absorption is then given as

$$\hat{h} = a_1 R^{-1/2} F(\hat{f}) J(\hat{h}/\hat{\eta}), \tag{32}$$

$$\hat{\overline{b}} = a_2 R^{-1/2} F(\hat{f})^{-1} J(\hat{h}/\hat{\eta})^{-1}, \tag{33}$$

$$\hat{\overline{V}} = a_3 R^{-1/2} J(\hat{h}/\hat{\eta})^{-1/3}, \tag{34}$$

where the model constants a_i remain unchanged for consistency with (27)–(29). As $\hat{h}$ is unknown, (32) forms an implicit nonlinear equation that needs to be solved numerically. Alternatively, $\hat{h}$ appearing on the right-hand side could be approximated by the original expression in (27). Table 5 shows the maximum deviations from the standard model constants a_i, and thus the model uncertainties, based on (32)–(34). The variability of the parameters in Table 5 suggests that the modified PWP86 scaling captures the effect of penetrating shortwave radiation with good accuracy for the tropical case. For the high-latitude case, however, the agreement is only moderate, suggesting the need for a more detailed analysis of the effect of penetrating radiation in high-latitude DWLs. For the according plots, please see section 2 of the supplemental material.

Beyond its impact on the bulk DWL properties, our simulations also showed that penetrating shortwave radiation strongly affects the near-surface structure of the DWL buoyancy and velocity profiles. If $\eta > 0$, many of our simulations showed the evolution of a thin convective layer immediately below the surface. The overall effect of this additional mixing is a reduction of the surface buoyancy, similarly to the observed reduction caused by LT (see Fig. 3), suggesting that the two processes interact. In the following, we therefore investigate the combined effects of penetrating shortwave radiation and LT on the surface buoyancy b^0 and surface velocity V^0, both nondimensionalized here by the corresponding bulk values $\overline{b}$ and $\overline{V}$.

Figures 11a and 11b shows the variability of these variables as a function of the stability parameter R for a tropical $T_h/T_f = 0.14$ and different combinations of simulations with and without LT and various values of $\hat{\eta}$. As before, the other nondimensional parameters are kept fixed at $T_h/T_p = 0.4$, $B_0/B_{max} = 0.466$, and $\hat{z}_0 = 0.01$. While the bulk values show a change of only 10% resulting from LT (see Table 4), the surface values are influenced much more strongly by LT across the entire parameter range. The ratio $V^0/\overline{V}$ is reduced to roughly half when LT is included (Fig. 11b), which is in line with the strong reduction of the surface velocity visible in both the LES and the model of H15 in Fig. 3. The additional mixing due to LT results in a related reduction of the surface buoyancy only for the case with $\eta = 0$ (Fig. 11a), while, surprisingly, LT *increases* the surface buoyancy for the cases with $\eta > 0$. In these cases, the near-surface buoyancy is characterized by unstable thermal stratification (convection) such that the additional mixing associated with LT now brings *warmer* (less buoyant) fluid to the surface. For comparison, the linear DWL buoyancy profile assumed in Fairall et al. (1996) yields a constant $b^0/\overline{b} = 2$, while the parametric profiles of Gentemann et al. (2009) predict $b^0/\overline{b} = 3.4$–1.3 for increasing wind speeds (similar to our results with moderate absorption coefficient $\hat{\eta} = 2$ and LT).

6. Discussion and conclusions

Based on state-of-the-art second-moment turbulence modeling, and supported by turbulence-resolving LES, we have shown

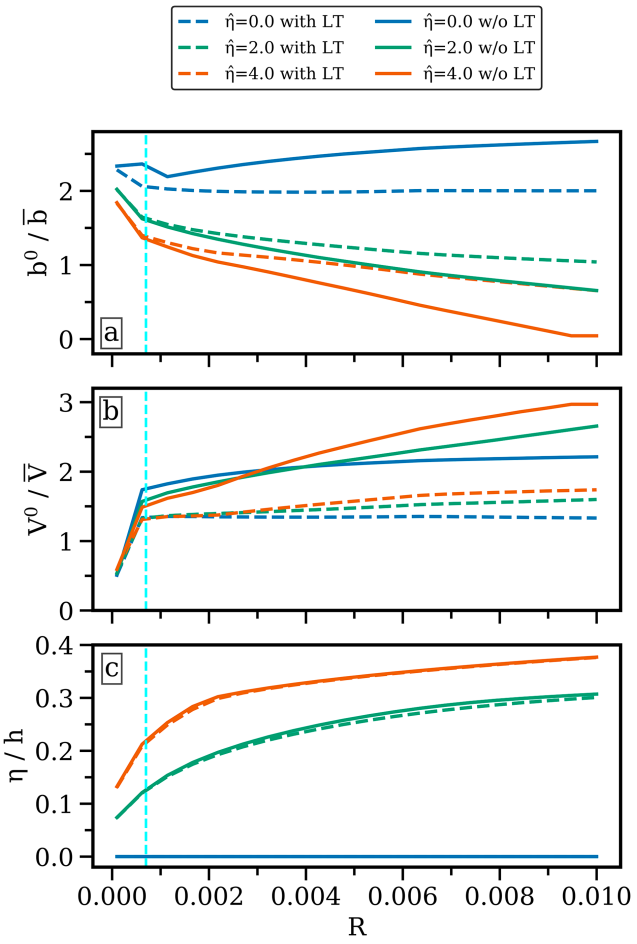

FIG. 11. Nondimensional DWL surface properties as functions of $R = u_*^2/(B_{\max} T_h)$ for different $\hat{\eta}$ with and without LT. Shown are midday values of (a) surface buoyancy scaled by bulk buoyancy, (b) surface velocity scaled by bulk velocity, and (c) absorption coefficient scaled by DWL depth. The cyan dashed line shows the critical value of R below which our DWL models are no longer applicable due to molecular effects.

that LT strongly impacts the DWL energetics, mainly by reducing the work performed by the surface stress and partly compensating this effect by Stokes shear production. Surface buoyancy and surface velocity are strongly reduced under LT, even under weak winds, which has important implications for air–sea exchange in coupled models. With an average increase in DWL thicknesses of only around 10%, the impact of LT on DWL bulk parameters, however, turned out to be moderate. We attribute this largely to the equilibrium wave model used in our study. Although equilibrium wave fields are typical in many situations, it is worth noting that previous LES studies with monochromatic nonequilibrium waves, focusing on swell effects (Kukulka et al. 2013), have shown a stronger impact of LT on DWL properties. Under nonequilibrium wind and wave conditions and deviations from a fixed La = 0.3, the scaling coefficients that were derived in section 5 may have to be adjusted.

Dimensional analysis and the parameter space studies in section 5 showed that the most relevant nondimensional

TABLE 5. Model constants a_1, a_2, and a_3 at $t = T_p/2$ of the modified PWP86 scaling relations in (32)–(34), evaluated for two different latitudes.

	10°N	70°N
a_1	0.83 ± 0.14	0.83 ± 0.3
a_2	0.38 ± 0.05	0.38 ± 0.2
a_3	1.20 ± 0.3	1.20 ± 0.4

parameters among those compiled in Table 3 are the following three: the stability parameter $R = u_*^2/(B_{\max} T_h)$, the time scale ratio T_h/T_f, and the shortwave radiation absorption scale $\hat{\eta} = \eta/L$. Parameterizations that do not independently account for these parameters are unlikely to be generally applicable. For example, the recent DWL model of Wang et al. (2023) only considers a single nondimensional parameter, $\hat{B}_0 \propto (\hat{f}R)^{-1}$, and is therefore not applicable outside the range of latitudes and optical water properties for which it was calibrated. Similarly, Gentemann et al. (2009) suggested a parametric temperature profile with a direct dependency on the wind speed, but neglected the changes in entrainment at high latitudes. An interesting topic of future research might therefore be the development of parametric DWL profiles with a dependency on the relevant nondimensional parameters R, T_h/T_f, and $\hat{\eta}$.

As shown in section 5, however, the three key parameters identified above do appear independently in the frequently used DWL scaling relations of PWP86. We showed that their model reliably predicts the most important DWL bulk parameters across a wide parameter range with our different sets of revised model coefficients that include the deepening of the DWL due to LT and other aspects of our more advanced turbulence model. We suggest a simple model extension to also account for the effects of penetrating shortwave radiation, which, however only yielded good agreement with our simulations for tropical DWLs, pointing at future work for a reliable description of high-latitude DWLs. One caveat of PWP86 applies to the low-energy regime with $R = u_*^2/(B_{\max} T_h) < 7 \times 10^{-4}$, where molecular effects become important, and the high-Reynolds number models and parameterizations used in this study are no longer applicable. Direct numerical simulations appear to be the only viable approach to explore this parameter range, which is relevant especially for very thin DWLs with weak wind forcing and strong buoyancy forcing.

The excellent performance of the simple PWP86 scaling relations was a somewhat unexpected result as our parameter space also included high-latitude DWLs for which the PWP86 modeling assumption of a constant bulk Richardson number formally breaks down. In view of increasing ice-free areas at high latitudes and strong DWL temperature anomalies already observed at high latitudes (Jia et al. 2023; Eastwood et al. 2011), it is likely that the physics of these DWLs (e.g., Sutherland et al. 2016) will receive increased attention in the future.

Acknowledgments. This paper is a contribution to the project L4 (Energy-Consistent Ocean-Atmosphere Coupling) of

the Collaborative Research Centre TRR 181 "Energy Transfers in Atmosphere and Ocean," funded by the German Research Foundation (DFG) under Grant 274762653 to L. Umlauf. H. T. Pham and S. Sarkar are pleased to acknowledge funding by NSF Grant OCE-1851390. We thank Kenneth Hughes and an anonymous reviewer for their valuable contributions. Qing Li and Ramsey Harcourt provided expert input on Langmuir turbulence in GOTM.

Data availability statement. Simulations in this manuscript were carried out with a modified version of the General Ocean Turbulence Model (GOTM). The used source code is archived at https://doi.org/10.5281/zenodo.8103884 (Klingbeil and Umlauf 2023). The LES data as well as the scripts that run GOTM and plot the figures shown in this article are archived at https://doi.org/10.5281/zenodo.10223915 (Schmitt 2023).

APPENDIX A

Second-Moment Turbulence Models

The turbulent diffusivities ν_t, ν_t^S, and ν_t^b appearing in (10) and (11) are assumed to be related to the turbulent kinetic energy k and a turbulence length scale l according to

$$\nu_t = c_\mu k^{1/2} l, \quad \nu_t^S = c_\mu^S k^{1/2} l, \quad \nu_t^b = c_\mu^b k^{1/2} l. \tag{A1}$$

The stability functions c_μ, c_μ^S, and c_μ^b are essential for the representation of the effects of shear, stratification, and LT on the anisotropy of turbulence.

Our analysis in sections 4 and 5 is based on the stability functions of H15 that constitute an improved version of an earlier model by Harcourt (2013) and are considered state of the art for the integration of LT effects in second-moment closure models. Note that the stability functions in (A1) are presented using the notation of the generic length scale (GLS) framework (Umlauf and Burchard 2003). They are related to their equivalents in Mellor–Yamada notation (see H15) as $c_\mu = 2^{1/2} S_M$, $c_\mu^S = 2^{1/2} S_M^S$, and $c_\mu^b = 2^{1/2} S_H$.

H15 showed that if LT effects are included, c_μ, c_μ^S, and c_μ^b are polynomial functions of the nondimensional time-scale ratios Nk/ε, Sk/ε, $S_c k/\varepsilon$, and $S_s k/\varepsilon$, where S_c and S_s defined in (15) represent the direct impact of Stokes shear on the stability functions that was ignored in earlier models of LT [the full expressions for the stability functions are shown in (33) of H15]. One example of these earlier models is the one of KC04 that is based on the original stability functions of Kantha and Clayson (1994), ignoring LT effects. In this case, we have $\nu_t^S = 0$, and the expressions for the shear production terms in P and P_s in (13) and (14) simplify accordingly.

Following work by KC04 and H15 on the parameterization of LT effects on the turbulent length scale l, we compute this quantity from a modified Mellor–Yamada-type transport equation for the variable kl. These authors suggested to include an extra Stokes production term, analogous to the TKE budget in (12), in the original k–l equation of Mellor and Yamada (1982), leading to an expression of the form:

$$\frac{\partial kl}{\partial t} = D_l + l(c_{l1} P + c_{l4} P_s + c_{l3} G - c_{l2} F \varepsilon), \tag{A2}$$

where the wall function $F = 1 + c_F [l/(\kappa L_z)]^2$ (here, κ is the von Kármán constant and L_z the distance from the surface) is required to reproduce the logarithmic wall layer distribution close to the surface. D_l summarizes the vertical transport terms, and c_{l1}–c_{l4} and c_F denote nondimensional model constants (or functions) discussed in more detail below. The conversion relations between our notation and that originally used by KC04 and H15 are summarized in Table A1.

The dissipation rate ε follows from the cascading relation

$$\varepsilon = (c_\mu^0)^3 \frac{k^{3/2}}{l}, \tag{A3}$$

with c_μ^0 denoting the value of c_μ in the logarithmic wall layer (Umlauf and Burchard 2005).

As an alternative to the transport equation for kl in (A2), we also computed some of the solutions based on the k–ω model by Umlauf et al. (2003), solving (12) combined with an equation of the form

$$\frac{\partial \omega}{\partial t} = D_\omega + \frac{\omega}{k}(c_{\omega 1} P + c_{\omega 4} P_s + c_{\omega 3} G - c_{\omega 2} \varepsilon), \tag{A4}$$

where ω denotes an inverse turbulence time scale defined as

$$\omega = (c_\mu^0)^{-4} \varepsilon k^{-1}. \tag{A5}$$

Similar to (A2), the transport equation for ω in (A4) includes a Stokes production term recently suggested by Yu et al. (2022) to account for LT effects. The term D_ω denotes again the turbulent transport terms, and $c_{\omega 1}$–$c_{\omega 4}$ are nondimensional model constants (see Table A1).

The transport terms D_k, D_l, and D_ω appearing in (12), (A2), and (A4), respectively, are modeled by downgradient expressions:

$$D_k = \frac{\partial}{\partial z}\left(\nu_t^k \frac{\partial k}{\partial z}\right), \quad D_l = \frac{\partial}{\partial z}\left(\nu_t^l \frac{\partial kl}{\partial z}\right), \quad D_\omega = \frac{\partial}{\partial z}\left(\nu_t^\omega \frac{\partial \omega}{\partial z}\right), \tag{A6}$$

TABLE A1. Nondimensional model constants as in (12), (A2), and (A4). The asterisk is only for KC04; for H15, these change according to (A7). The dagger symbol indicates $c_\mu^{k,\omega} = c_\mu/\sigma_{k,\omega}$ with $\sigma_{k,\omega} = 2.0$.

GLS notation		KC04 and H15 notation		ω	
c_{l1}	0.9	$E_1 = 2c_1$	1.8	$c_{\omega 1}$	0.55
c_{l2}	0.5	$E_2 = 2c_2$	1.0	$c_{\omega 2}$	0.83
c_{l3}	2.4	$E_3 = 2c_3$	4.8	$c_{\omega 3^-}$	−0.52
c_{l4}	3.0	$E_6 = 2c_4$	6.0	$c_{\omega 4}$	0.15
c_F	1.45	$E_4 = 2c_F$	2.9	—	—
c_μ^k	0.28	$S_q = 2^{-1/2} c_\mu^k$	0.2*		†
c_μ^l	0.28	$S_l = 2^{-1/2} c_\mu^l$	0.2*		†
c_μ^0	0.55	$B_1 = 2^{3/2}(c_\mu^0)^{-3}$	16.6	c_μ^0	0.55

where $\nu_t^k = c_\mu^k k^{1/2} l$, $\nu_t^l = c_\mu^l k^{1/2} l$ and $\nu_t^\omega = c_\mu^\omega k^{1/2} l$ are turbulent diffusivities, and c_μ^k, c_μ^l, and c_μ^ω the corresponding stability functions.

The model parameters c_{l1} and c_{l2}, and similarly $c_{\omega1}$ and $c_{\omega2}$ for the k–ω model (all compiled in Table A1) are well constrained by classical data for unstratified shear layers and decaying turbulence (e.g., Umlauf and Burchard 2003). The parameters c_{l3} and $c_{\omega3}$ determine the entrainment rate in stratified turbulent boundary layers. Their values follow from a condition on the so-called steady-state Richardson number, $\mathrm{Ri}_{\mathrm{st}} = 0.23$, corresponding to the value of the Richardson number Ri in the entrainment layer at the base of the turbulent surface layer (Umlauf and Burchard 2005). Note that $c_{l3} = 2.4$ is close to the value $c_{l3} = 2.5$ used by H15. We also follow the suggestion by H15 to limit the vertical length scale by the Ozmidov scale, $L_O = (\varepsilon N^{-3})^{1/2}$. Likewise, we use $E_4 = 1.33(1 + 0.5\mathrm{La}^{-2})^{1/3} = 2.9$ with a Langmuir number of La = 0.3 to account for the modified near-surface slope of the turbulent length scale due to LT. For our simulations without LT effects, this expression reduces to the traditional value $E_4 = 1.33$.

The most important model parameters in (A2) and (A4) in the context of LT are those multiplying the Stokes shear production terms, respectively. For the k–l equation, we adopt H15's value $E_6 = 6$, corresponding to $c_{l4} = 3$ in GLS notation. Note that this value is close to the revised $E_6 = 7.2$ obtained from comparison to field measurements (see Kantha et al. 2010) of KC04. For the k–ω model, we follow Yu et al. (2022) and choose $c_{\omega4} = 0.15$.

For H15, the stability functions for the transport terms in (A6) are defined as

$$S_q = S_l = [0.2^2 + (0.41 S_H)^2]^{1/2}, \tag{A7}$$

to account for the enhanced transport due to LT (here, S_H is the stability function for the turbulent diffusivity of heat, c_μ^b in our notation). In the original model of Kantha and Clayson (1994) without LT effects, and in KC04, the stability functions reduce to constants. KC04 suggested $S_l/S_q = 3.7$ but, similar to Harcourt (2013), we find that $S_l = S_q = 0.2$ is more in line with the LES results. For the k–ω model, the stability functions c_μ^k and c_μ^ω are chosen proportional to c_μ (see Umlauf et al. 2003) with constant proportionality factors expressed in terms of the turbulent Schmidt numbers σ_k and σ_ω (see Table A1).

Finally, we use the following boundary conditions for (12) and (A2):

$$k = \frac{u^{*2}}{(c_\mu^0)^2} \text{ at } z = 0, \quad \frac{\partial k}{\partial z} = 0 \text{ at } z = -\infty, \tag{A8}$$

$$l = \kappa z_0 \text{ at } z = 0, \quad \frac{\partial kl}{\partial z} = 0 \text{ at } z = -\infty, \tag{A9}$$

where z_0 is the surface roughness length. For the upper boundary, these boundary conditions follow from the classical law-of-the-wall relations (see Umlauf and Burchard 2005). Please note that we do not consider the injection of TKE by breaking surface waves. A more detailed discussion of how z_0 affects the class of models used in our study with and without wave breaking can be found in Umlauf and Burchard (2003).

APPENDIX B

Large-Eddy Simulations

The three-dimensional Craik–Leibovich equations for the grid-filtered Eulerian velocity components U_i and buoyancy B are numerically solved in the LES as follows:

$$\begin{aligned}
&\frac{\partial U_i}{\partial x_i} = 0,\\
&\frac{DU_i}{Dt} = \epsilon_{ijk}(U_j + u_j^s) f_k + \epsilon_{ijk} u_j^s \omega_k - \frac{\partial \Pi}{\partial x_i} + B\delta_{i3} + \nu \frac{\partial^2 U_i}{\partial x_j^2}\\
&\qquad\qquad - \frac{\partial \tau_{ij}^{\mathrm{sgs}}}{\partial x_j},\\
&\frac{DB}{Dt} = -u_j^s \frac{\partial B}{\partial x_j} + \nu^b \frac{\partial^2 B}{\partial x_j^2} - \frac{\partial Q_j^{\mathrm{sgs}}}{\partial x_j}.
\end{aligned} \tag{B1}$$

Here, ω_k is the vorticity and $D/Dt = \partial/\partial t + U_j \partial/\partial x_j$. The generalized pressure (Π) is defined as

$$\Pi = \frac{p}{\rho_0} + \frac{2e}{3} + \frac{1}{2}(|U_i + u_i^s|^2 - |U_i|^2),$$

where p is the dynamic pressure and e is the subgrid turbulent kinetic energy. A Poisson equation derived by taking the divergence of the momentum equation in (B1) is solved to obtain the modified pressure ($p/\rho_0 + 2e/3$) using a multigrid method.

To compute the subgrid stresses $\tau_{ij}^{\mathrm{sgs}} = -\nu_{\mathrm{sgs}}(\partial U_i/\partial x_j + \partial U_j/\partial x_i)$ in (B1), we use the subgrid parameterization in Ducros et al. (1996) to obtain the subgrid viscosity ν_{sgs}:

$$\nu_{\mathrm{sgs}} = 0.0014 C_K^{-3/2} \Delta_f \left(\tilde{F}_2^{(3)}\right)^{1/2} \tag{B2}$$

where the Kolmogorov constant C_K is set to be 0.5 and Δ_f is the grid filter width. Here, $\tilde{F}_2^{(3)}$ is the second-order structure filtered function obtained after applying a high-pass filter in the horizontal directions to eliminate the larger scales of the field as follows. First, the high-pass filter is applied three times sequentially to the LES velocity to obtain an explicitly filtered velocity, denoted by $\tilde{U}$. Then, the second-order structure function $\tilde{F}_2^{(3)}$ is calculated from the filtered velocity field $\tilde{U}$ using the four neighboring points in the horizontal directions as follows:

$$\begin{aligned}
\left(\tilde{F}_2^{(3)}\right)_{i,j,k} = \frac{1}{4}(&\|\tilde{U}_{i+1,j,k} - \tilde{U}_{i,j,k}\|^2 + \|\tilde{U}_{i-1,j,k} - \tilde{U}_{i,j,k}\|^2 + \cdots\\
&+ \|\tilde{U}_{i,j+1,k} - \tilde{U}_{i,j,k}\|^2 + \|\tilde{U}_{i,j-1,k} - \tilde{U}_{i,j,k}\|^2).
\end{aligned} \tag{B3}$$

The subscripts i, j, and k in the equation above indicate the grid indices in the x, y, and z, directions, respectively. A unity subgrid Prandtl number is used to calculate the subgrid

buoyancy flux Q_j^{sgs}. Further details of the numerical method used in the LES can be found in VanDine et al. (2020) and Pham et al. (2023).

The computational domain is a rectangular box with dimensions of 64 × 64 × 72 m in the x, y, and z directions, respectively, using a grid size of 256^3. The grid is uniform in the horizontal directions with a spacing of 0.25 m. We use a fine vertical grid spacing of 0.05 m at the surface, and mildly stretch the grid at a rate of 3% in the region below.

The LES is initialized with zero velocity and a fixed buoyancy value throughout the domain. Periodicity is enforced at the horizontal boundaries. The wind stress components, τ_x^0 and τ_y^0, and the surface buoyancy flux B_0 are applied at the top surface as implemented in the second-moment turbulence modeling approach. Homogeneous Neumann boundary conditions (zero gradients) are used at the bottom boundary for the horizontal velocity components and buoyancy while the vertical velocity component is set to zero at the bottom. A sponge layer is set up in the bottom 20 m to absorb possible fluctuations excited by turbulence in the surface layer.

REFERENCES

Bellenger, H., and J.-P. Duvel, 2009: An analysis of tropical ocean diurnal warm layers. *J. Climate*, **22**, 3629–3646, https://doi.org/10.1175/2008JCLI2598.1.

Brilouet, P.-E., J.-L. Redelsperger, M.-N. Bouin, F. Couvreux, and C. Lebeaupin Brossier, 2021: A case-study of the coupled ocean–atmosphere response to an oceanic diurnal warm layer. *Quart. J. Roy. Meteor. Soc.*, **147**, 2008–2032, https://doi.org/10.1002/qj.4007.

Ducros, F., P. Comte, and M. Lesieur, 1996: Large-eddy simulation of transition to turbulence in a boundary layer developing spatially over a flat plate. *J. Fluid Mech.*, **326**, 1–36, https://doi.org/10.1017/S0022112096008221.

Eastwood, S., P. Le Borgne, S. Péré, and D. Poulter, 2011: Diurnal variability in sea surface temperature in the Arctic. *Remote Sens. Environ.*, **115**, 2594–2602, https://doi.org/10.1016/j.rse.2011.05.015.

Fairall, C. W., E. F. Bradley, D. P. Rogers, J. B. Edson, and G. S. Young, 1996: Bulk parameterization of air-sea fluxes for tropical ocean-global atmosphere coupled-ocean atmosphere response experiment. *J. Geophys. Res.*, **101**, 3747–3764, https://doi.org/10.1029/95JC03205.

Gentemann, C. L., P. J. Minnett, and B. Ward, 2009: Profiles of Ocean Surface Heating (POSH): A new model of upper ocean diurnal warming. *J. Geophys. Res.*, **114**, C07017, https://doi.org/10.1029/2008JC004825.

Harcourt, R. R., 2013: A second-moment closure model of Langmuir turbulence. *J. Phys. Oceanogr.*, **43**, 673–697, https://doi.org/10.1175/JPO-D-12-0105.1.

——, 2015: An improved second-moment closure model of Langmuir turbulence. *J. Phys. Oceanogr.*, **45**, 84–103, https://doi.org/10.1175/JPO-D-14-0046.1.

Hughes, K. G., J. N. Moum, and E. L. Shroyer, 2020: Evolution of the velocity structure in the diurnal warm layer. *J. Phys. Oceanogr.*, **50**, 615–631, https://doi.org/10.1175/JPO-D-19-0207.1.

——, ——, ——, and W. D. Smyth, 2021: Stratified shear instabilities in diurnal warm layers. *J. Phys. Oceanogr.*, **51**, 2583–2598, https://doi.org/10.1175/JPO-D-20-0300.1.

Jia, C., P. J. Minnett, and B. Luo, 2023: Significant diurnal warming events observed by Saildrone at high latitudes. *J. Geophys. Res. Oceans*, **128**, e2022JC019368, https://doi.org/10.1029/2022JC019368.

Johnson, L., B. Fox-Kemper, Q. Li, H. T. Pham, and S. Sarkar, 2023: A finite-time ensemble method for mixed layer model comparison. *J. Phys. Oceanogr.*, **53**, 2211–2230, https://doi.org/10.1175/JPO-D-22-0107.1.

Kahru, M., J.-M. Leppanen, and O. Rud, 1993: Cyanobacterial blooms cause heating of the sea surface. *Mar. Ecol. Prog. Ser.*, **101** (1/2), 1–7, https://doi.org/10.3354/meps101001.

Kantha, L. H., and C. A. Clayson, 1994: An improved mixed layer model for geophysical applications. *J. Geophys. Res.*, **99**, 25 235–25 266, https://doi.org/10.1029/94JC02257.

——, and ——, 2004: On the effect of surface gravity waves on mixing in the oceanic mixed layer. *Ocean Modell.*, **6**, 101–124, https://doi.org/10.1016/S1463-5003(02)00062-8.

——, H. U. Lass, and H. Prandke, 2010: A note on Stokes production of turbulence kinetic energy in the oceanic mixed layer: Observations in the Baltic Sea. *Ocean Dyn.*, **60**, 171–180, https://doi.org/10.1007/s10236-009-0257-7.

Kawai, Y., and A. Wada, 2007: Diurnal sea surface temperature variation and its impact on the atmosphere and ocean: A review. *J. Oceanogr.*, **63**, 721–744, https://doi.org/10.1007/s10872-007-0063-0.

Klingbeil, K., and L. Umlauf, 2023: GOTM source code with Langmuir turbulence closure, version 1. Zenodo, https://doi.org/10.5281/zenodo.8103884.

Kukulka, T., A. J. Plueddemann, and P. P. Sullivan, 2013: Inhibited upper ocean restratification in nonequilibrium swell conditions. *Geophys. Res. Lett.*, **40**, 3672–3676, https://doi.org/10.1002/grl.50708.

Large, W. G., and J. M. Caron, 2015: Diurnal cycling of sea surface temperature, salinity, and current in the CESM coupled climate model. *J. Geophys. Res. Oceans*, **120**, 3711–3729, https://doi.org/10.1002/2014JC010691.

Li, Q., and B. Fox-Kemper, 2020: Anisotropy of Langmuir turbulence and the Langmuir-enhanced mixed layer entrainment. *Phys. Rev. Fluids*, **5**, 013803, https://doi.org/10.1103/PhysRevFluids.5.013803.

——, ——, Ø. Breivik, and A. Webb, 2017: Statistical models of global Langmuir mixing. *Ocean Modell.*, **113**, 95–114, https://doi.org/10.1016/j.ocemod.2017.03.016.

Matthews, A. J., D. B. Baranowski, K. J. Heywood, P. J. Flatau, and S. Schmidtko, 2014: The surface diurnal warm layer in the Indian Ocean during CINDY/DYNAMO. *J. Climate*, **27**, 9101–9122, https://doi.org/10.1175/JCLI-D-14-00222.1.

McWilliams, J. C., P. P. Sullivan, and C.-H. Moeng, 1997: Langmuir turbulence in the ocean. *J. Fluid Mech.*, **334**, 1–30, https://doi.org/10.1017/S0022112096004375.

Mellor, G. L., and T. Yamada, 1982: Development of a turbulence closure model for geophysical fluid problems. *Rev. Geophys.*, **20**, 851–875, https://doi.org/10.1029/RG020i004p00851.

Moulin, A. J., J. N. Moum, and E. L. Shroyer, 2018: Evolution of turbulence in the diurnal warm layer. *J. Phys. Oceanogr.*, **48**, 383–396, https://doi.org/10.1175/JPO-D-17-0170.1.

Pham, H. T., S. Sarkar, L. Johnson, B. Fox-Kemper, P. P. Sullivan, and Q. Li, 2023: Multi-scale temporal variability of turbulent mixing during a monsoon intra-seasonal oscillation in the Bay of Bengal: An LES study. *J. Geophys. Res. Oceans*, **128**, e2022JC018959, https://doi.org/10.1029/2022JC018959.

Phillips, O. M., 1958: The equilibrium range in the spectrum of wind-generated waves. *J. Fluid Mech.*, **4**, 426–434, https://doi.org/10.1017/S0022112058000550.

Pollard, R. T., P. B. Rhines, and R. O. R. Y. Thompson, 1973: The deepening of the wind-mixed layer. *Geophys. Fluid Dyn.*, **4**, 381–404, https://doi.org/10.1080/03091927208236105.

Price, J. F., R. A. Weller, and R. Pinkel, 1986: Diurnal cycling: Observations and models of the upper ocean response to diurnal heating, cooling, and wind mixing. *J. Geophys. Res.*, **91**, 8411–8427, https://doi.org/10.1029/JC091iC07p08411.

Sarkar, S., and H. T. Pham, 2019: Turbulence and thermal structure in the upper ocean: Turbulence-resolving simulations. *Flow Turbul. Combus.*, **103**, 985–1009, https://doi.org/10.1007/s10494-019-00065-5.

Schmitt, M., 2023: Scripts for 'diurnal warm layers in the ocean: Energetics, non-dimensional scaling, and parameterization', version 2. Zenodo, https://doi.org/10.5281/zenodo.10223915.

Stull, R. B., 1988: *An Introduction to Boundary Layer Meteorology*. Atmospheric and Oceanographic Sciences Library, Vol. 13, Springer, 670 pp.

Sutherland, G., L. Marié, G. Reverdin, K. H. Christensen, G. Broström, and B. Ward, 2016: Enhanced turbulence associated with the diurnal jet in the ocean surface boundary layer. *J. Phys. Oceanogr.*, **46**, 3051–3067, https://doi.org/10.1175/JPO-D-15-0172.1.

Suzuki, N., and B. Fox-Kemper, 2016: Understanding Stokes forces in the wave-averaged equations. *J. Geophys. Res. Oceans*, **121**, 3579–3596, https://doi.org/10.1002/2015JC011566.

Umlauf, L., and H. Burchard, 2003: A generic length-scale equation for geophysical turbulence models. *J. Mar. Res.*, **61**, 235–265, https://doi.org/10.1357/002224003322005087.

——, and ——, 2005: Second-order turbulence closure models for geophysical boundary layers. A review of recent work. *Cont. Shelf Res.*, **25**, 795–827, https://doi.org/10.1016/j.csr.2004.08.004.

——, ——, and K. Hutter, 2003: Extending the k–ω turbulence model towards oceanic applications. *Ocean Modell.*, **5**, 195–218, https://doi.org/10.1016/S1463-5003(02)00039-2.

——, ——, and K. Bolding, 2005: GOTM—Scientific documentation: Version 3.2. Marine Science Rep. 63, 279 pp., https://doi.org/10.12754/MSR-2005-0063.

VanDine, A., H. T. Pham, and S. Sarkar, 2020: Investigation of LES models for a stratified shear layer. *Comput. Fluids*, **198**, 104405, https://doi.org/10.1016/j.compfluid.2019.104405.

Wang, X., T. Kukulka, J. T. Farrar, A. J. Plueddemann, and S. F. Zippel, 2023: Langmuir turbulence controls on observed diurnal warm layer depths. *Geophys. Res. Lett.*, **50**, e2023GL103231, https://doi.org/10.1029/2023GL103231.

Wijesekera, H. W., D. W. Wang, and E. Jarosz, 2020: Dynamics of the diurnal warm layer: Surface jet, high-frequency internal waves, and mixing. *J. Phys. Oceanogr.*, **50**, 2053–2070, https://doi.org/10.1175/JPO-D-19-0285.1.

Yu, C., J. Song, S. Li, and S. Li, 2022: On an improved second-moment closure model for Langmuir turbulence conditions and its application. *J. Geophys. Res. Oceans*, **127**, e2021JC018217, https://doi.org/10.1029/2021JC018217.

Supplemental Material
Diurnal Warm Layers in the ocean: Energetics, non-dimensional scaling, and parameterization

M. Schmitt[1], H. T. Pham[2], S. Sarkar[2,3], K. Klingbeil[1], and L. Umlauf[1]

[1]Leibniz-Institute for Baltic Sea Research, Warnemünde, Germany

[2]Mechanical and Aerospace Engineering, University of California at San Diego, USA

[3]Scripps Institution of Oceanography, University of California at San Diego, USA

M. Schmitt: mira.schmitt@io-warnemuende.de

1 Empirical Wave Model

Based on a simple model spectrum, Li et al. (2017) showed that the vertically averaged Stokes velocity,

$$\overline{u}_s = \frac{1}{z}\int_z^0 u_s \mathrm{d}z^* \ , \tag{1}$$

can be described in the following form:

$$\begin{aligned}\overline{u}_s \approx u_s^0 \Bigg\{ & 0.715 + \left(\frac{0.151}{k_p z} - 0.840\right)\left[1 - T_1(k_p, z)\right] - \left(0.840 + \frac{0.0591}{k_p z}\right) T_2(k_p, z) \\ & + \left(\frac{0.0632}{k_p^* z} + 0.125\right)\left[1 - T_1(k_p^*, z)\right] + \left(0.125 + \frac{0.0946}{k_p^* z}\right) T_2(k_p^*, z) \Bigg\}\end{aligned} \tag{2}$$

where

$$T_1(k_p, z) = 2\mathrm{e}^{k_p z} \tag{3}$$

$$T_2(k_p, z) = \sqrt{2\pi k_p |z|}\,\mathrm{erfc}\left(\sqrt{2k_p|z|}\right) \tag{4}$$

and $k_p^* = 2.56 k_p$ describes the peak wave number including wave spreading effects. From (1), it is clear that the local Stokes velocity follows from

$$u_s = -\frac{\partial \overline{u}_s z}{\partial z} \ , \tag{5}$$

which we use to compute the Stokes shear in the Stokes shear production term of the k and kl transport equations.

2 Additional Figures

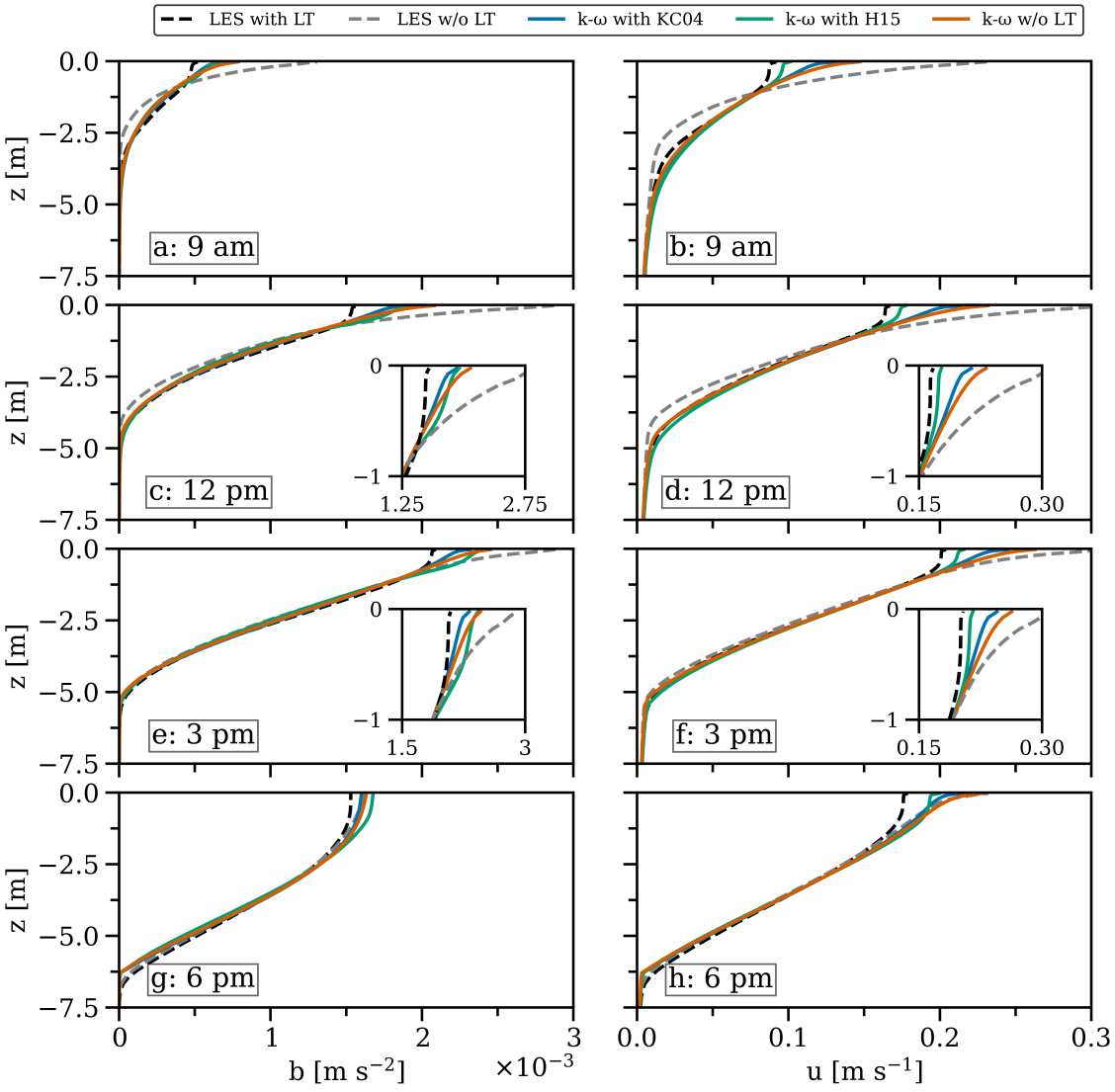

Figure 1: Same as Fig. 3 in the main paper but using the $k-\omega$ model. Comparison of LES and GOTM simulations for (a,c,e,g) buoyancy and (b,d,f,h) u-component of the velocity at the times indicated in Fig. 2 of the main paper. Dashed lines show LES results with (black) and without (gray) LT. Colored lines correspond to different second-moment models as indicated in the legend. Inlays panels in (c-f) show enlarged views of the near-surface region.

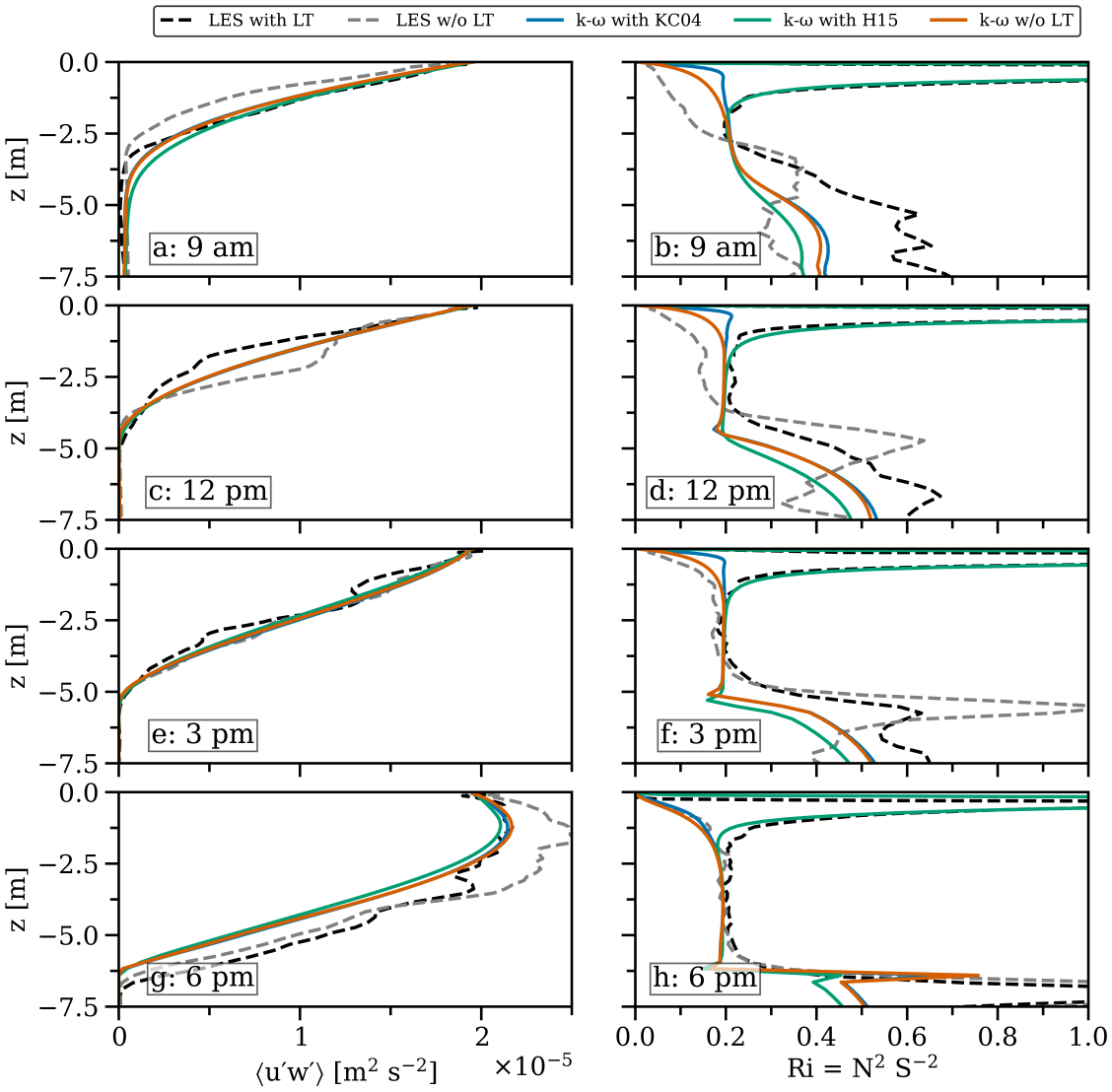

Figure 2: As in Fig. 1 but for (a,c,e,g) total (resolved plus subgrid-scale) turbulent momentum flux $\langle u'w' \rangle$ and (b,d,f,h) gradient Richardson number Ri.

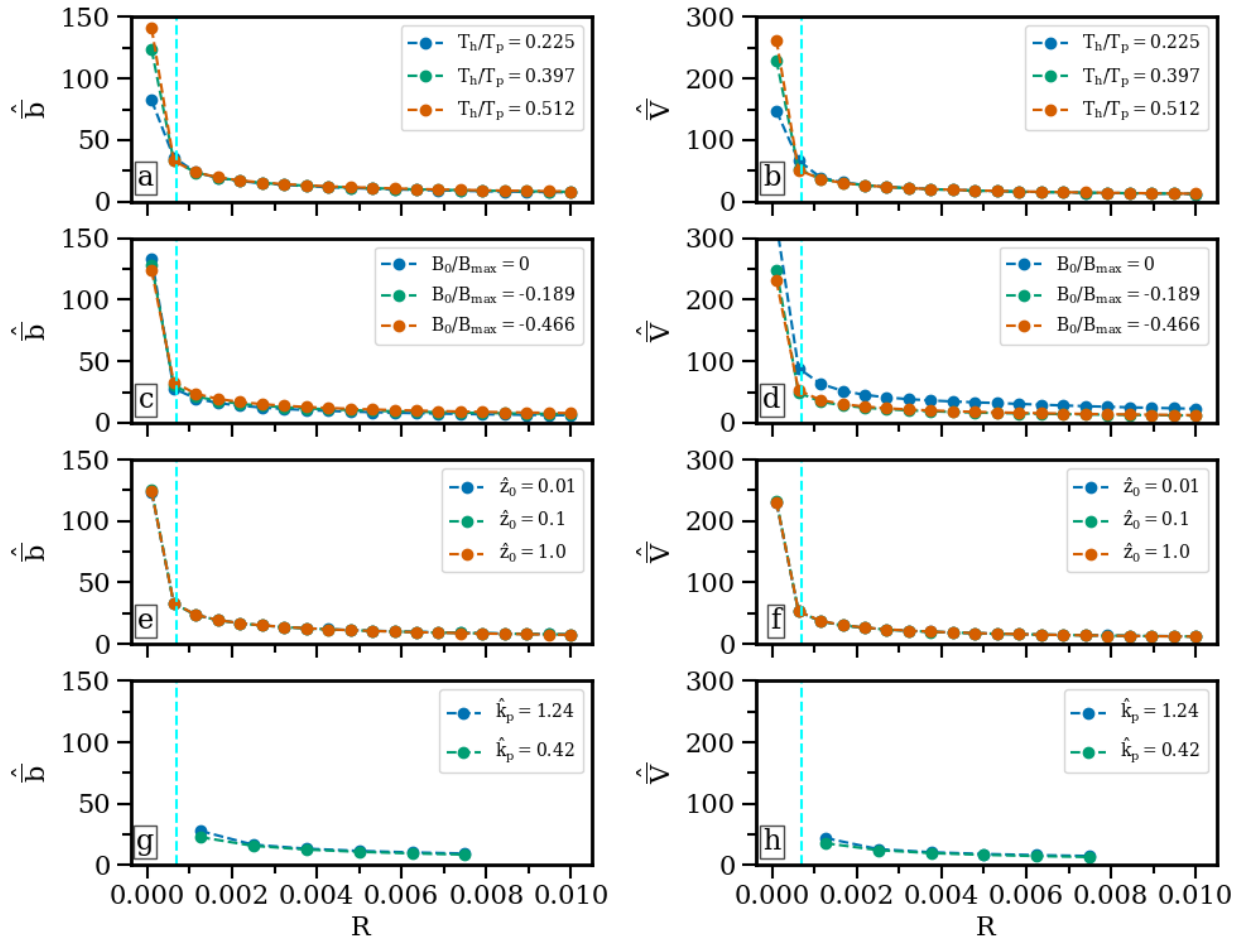

Figure 3: Non-dimensional bulk buoyancy $\hat{\bar{b}}$ and velocity $\hat{\bar{V}}$ as a function of $R = u_*^2/(B_{max}T_h)$ for different values of (a,b) the time scale ratio T_h/T_p, (c,d) the flux ratio B_0/B_{max}, (e,f) the non-dimensional surface roughness $\hat{z}_0$, and (g,h) the non-dimensional peak wave number $\hat{k}_p$. Parameters not varied are kept fixed at $T_h/T_p = 0.397$, $B_0/B_{max} = 0.466$ and $\hat{z}_0 = 0.01$, respectively. The blue line shows the critical threshold for the collapse of DWL turbulence, $R = 7 \cdot 10^{-4}$.

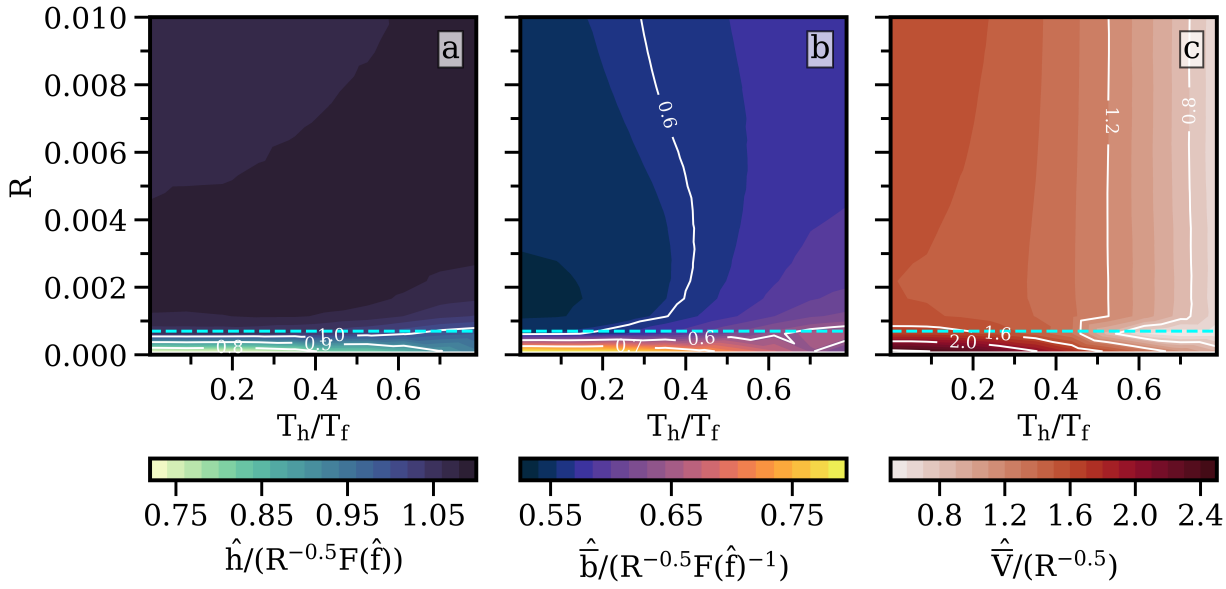

Figure 4: Parameter space for varying $R = u_*^2/(B_{\text{max}}T_h)$ and T_h/T_f at $t = t_{\text{max}}$, i.e. the time of the maximum buoyancy anomaly in the afternoon. Shown are midday values for (a) $\hat{h}$, (b) $\hat{\bar{b}}$, and (c) $\hat{\bar{V}}$ divided by the proposed scaling. For these runs, $T_h/T_p = 0.4$, $B_0/B_{\text{max}} = -0.466$ and $\hat{z}_0 = 0.01$ are kept constant. The blue line again shows $R = 7 \cdot 10^{-4}$.

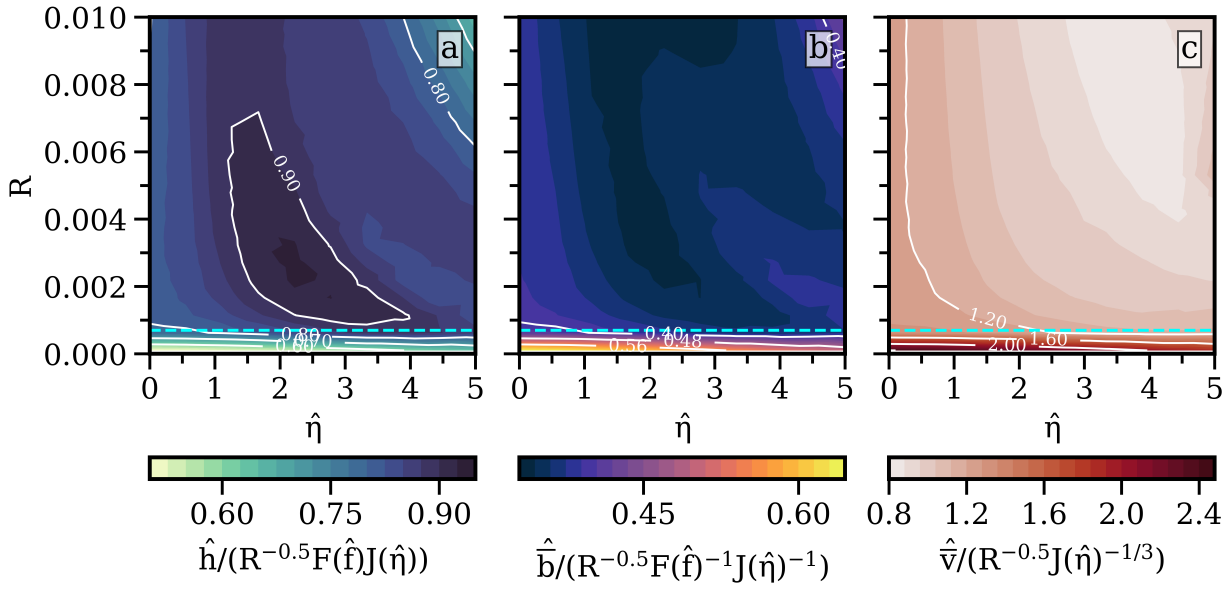

Figure 5: Parameter space for varying $R = u_*^2/(B_{\text{max}}T_h)$ and $\hat{\eta}$ at 10°N ($T_h/T_f = 0.14$). Shown are midday values for (a) $\hat{h}$, (b) $\hat{\bar{b}}$, and (c) $\hat{\bar{V}}$ divided by the proposed scaling. For these runs, $T_h/T_p = 0.4$, $B_0/B_{\text{max}} = -0.466$ and $\hat{z}_0 = 0.01$ are kept constant. The blue line again shows $R = 7 \cdot 10^{-4}$.

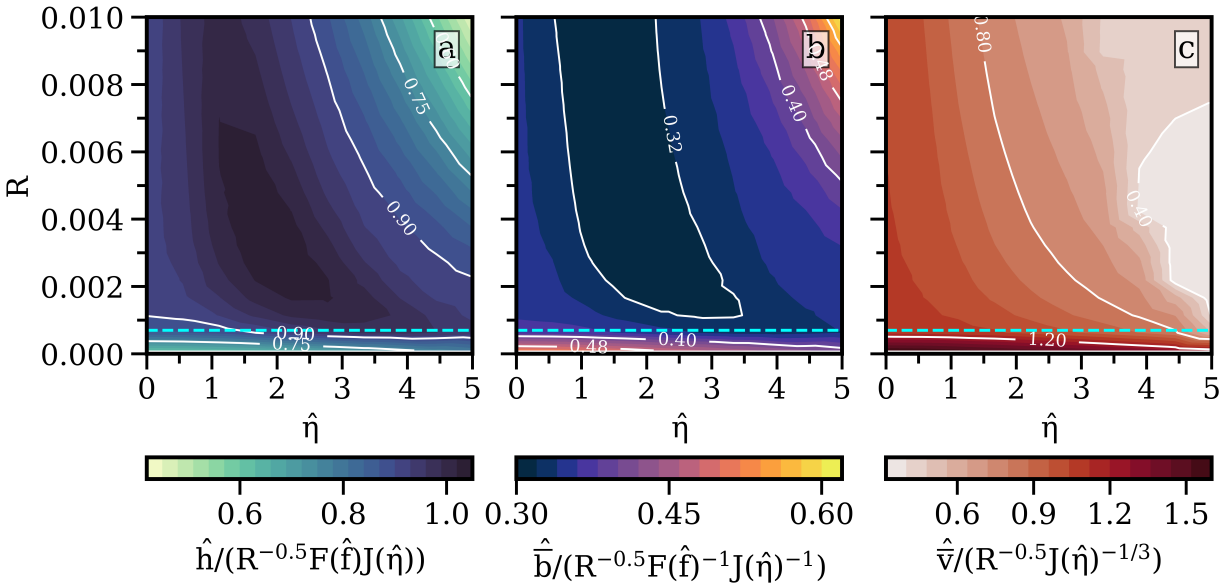

Figure 6: Parameter space for varying $R = u_*^2/(B_{\text{max}} T_h)$ and $\hat{\eta}$ at 70°N ($T_h/T_f = 0.74$). Shown are midday values for (a) $\hat{h}$, (b) $\hat{\bar{b}}$, and (c) $\hat{\bar{V}}$ divided by the proposed scaling. For these runs, $T_h/T_p = 0.4$, $B_0/B_{\text{max}} = -0.466$ and $\hat{z}_0 = 0.01$ are kept constant. The blue line again shows $R = 7 \cdot 10^{-4}$.

Interactions between diurnal warm layers and surface-layer fronts

Jen-Ping Peng[1], Nicole L. Jones[1], Matthew D. Rayson[1], Mira Schmitt[2], Lars Umlauf[2], Christopher Whitwell[1], Shane R. Keating[3], Callum J. Shakespeare[4], and Gregory N. Ivey[1]

[1]Ocean Graduate School and UWA Oceans Institute, University of Western Australia, Crawley, Australia
[2]Leibniz-Institute for Baltic Sea Research Warnemünde (IOW), Rostock, Germany
[3]School of Mathematics and Statistics, UNSW Sydney, Sydney, NSW, Australia
[4]Research School of Earth Sciences, Australian National University, Canberra, ACT, Australia

Key Points:

- Field observations reveal both diurnal warm layers and surface-layer fronts in the mixed layer under intense solar heating and weak winds.
- The layer below diurnal warm layers within a front remains marginally unstable, making it prone to turbulence from small disturbances.
- Frontal dynamics deepen the mixed layer, allowing diurnal shear to reach greater depths at night compared to conditions without a front.

Corresponding author: Jen-Ping Peng, jen-ping.peng@uwa.edu.au

Abstract

Previous studies have highlighted the individual importance of diurnal warm layers (DWLs) and surface-layer fronts within the surface boundary layer (SBL) in regulating energy, momentum, and gas exchange between the atmosphere and the ocean. This study investigates the interactions between DWLs and surface-layer fronts using field observations and numerical turbulence models. Our study provides the real-ocean relevance of the coexistence of DWLs and surface-layer fronts in the SBL in an eddy-rich tropical ocean subjected to intense solar heating and weak winds. We found that the presence of a DWL isolates the deeper layers of the SBL from diabatic and frictional surface forcing, causing these layers to quickly become non-turbulent while remaining in a state of marginal stability. This condition suggests that small perturbations from local processes, such as internal tides and waves, can easily trigger instability and turbulence. Additionally, frontal dynamics were observed to deepen the SBL, allowing near-surface diurnal shear associated with DWL dynamics to penetrate to greater depths during nighttime, compared to conditions without a front, thereby facilitating the vertical transport of heat and tracers. Our findings underscore the necessity of accurately representing the interactions between DWLs and surface-layer fronts to enhance the precision of ocean circulation and climate models.

Plain Language Summary

The oceanic mixed layer, the uppermost part of the ocean, plays a crucial role in regulating the exchange of heat, momentum, and gases between the ocean and atmosphere. Within this layer, surface fronts — areas of rapid temperature and salinity changes in space — can generate strong currents and enhance mixing. Diurnal warm layers (DWLs) also form at the surface during the day due to solar heating, creating a thin and stable layer that produces turbulence near the surface but suppresses it in the waters below. Although both surface fronts and DWLs are key to ocean dynamics, they have often been studied independently. Our study is the first to observe the coexistence of DWLs and surface-layer fronts in the mixed layer under intense solar heating and weak winds in a tropical ocean. Field observations and numerical models show that the layer beneath DWLs within a front can become turbulent from only small perturbations. Additionally, frontal dynamics deepen the mixed layer, allowing nighttime turbulence to reach greater depths. These findings underscore the need to incorporate surface fronts and DWLs in models to improve predictions of ocean circulation and heat and nutrient transport, crucial for understanding climate dynamics.

1 Introduction

Submesoscale fronts and filaments — i.e. horizontal scales of 0.1–10 km and temporal scales of hours–days — are frequently observed in the surface boundary layer (SBL) and have been extensively studied due to their significance in oceanographic processes. From a physical perspective, submesoscale fronts and filaments play crucial roles in energy transfer and dissipation. They act as intermediaries between larger mesoscale eddies and small-scale dissipative motions by breaking the constraint of large-scale quasigeostrophic dynamics through submesoscale frontogenesis (Gula et al., 2022; Taylor & Thompson, 2022). Additionally, they facilitate rapid SBL restratification by creating overturning circulations that flatten the isopycnal structure through mixed layer instabilities (Boccaletti et al., 2007; Fox-Kemper & Ferrari, 2008; Johnson et al., 2020). From a biological perspective, these features significantly impact the vertical transport of tracers. Strong ageostrophic motions associated with submesoscale fronts and filaments induce large vertical velocities, redistributing water properties such as momentum, buoyancy, heat, and biogeochemical tracers. This redistribution profoundly influences marine ecosystems (Lévy et al., 2018; Yu et al., 2019; Qu et al., 2022).

Frontogenesis is a key process that develops and intensifies submesoscale features by rapidly sharpening horizontal density gradients and their associated horizontal velocity shear (McWilliams, 2021). This process involves mesoscale straining (Hoskins, 1982; Capet et al., 2008; Shakespeare & Taylor, 2013; Gula et al., 2014) and ageostrophic secondary circulation (Gula et al., 2014; McWilliams et al., 2015). Submesoscale frontogenesis breaks the constraint of large-scale quasigeostrophic dynamics (Gula et al., 2022), making submesoscale flows prone to flow instabilities such as inertial instabilities (Grisouard, 2018; Peng et al., 2020) and symmetric instabilities (D'Asaro et al., 2011; Thomas et al., 2016), which promote a downscale transfer of mesoscale energy toward dissipation scales (Taylor & Thompson, 2022).

Both numerical and observational studies have shown that submesoscale processes in the SBL are influenced by atmospheric forcing (Thomas, 2005; Dong et al., 2022). These processes include cooling, evaporation, and downfront winds inducing destabilizing Ekman transport (Thomas & Lee, 2005), thereby sustaining frontal instabilities. Recent studies have highlighted the significant impact of diurnal forcing on submesoscale kinematics, including changes in vorticity, divergence, and strain (Dauhajre et al., 2017; Dauhajre & McWilliams, 2018; Sun et al., 2020), as well as on submesoscale dynamics, instability, and turbulence (Peng et al., 2021; Shang et al., 2023; Zheng & Jing, 2024). This underscores the important role of diurnal forcing in controlling submesoscale features within the SBL.

An important process in the SBL is the formation of diurnal warm layers (DWLs) that introduce a complex interplay of processes within the SBL. DWLs form in the top few meters below the sea surface by absorption of penetrative solar radiation under mild to moderate winds, and weak surface-wave activity (Spigel et al., 1986; Thompson et al., 2019; Wijesekera et al., 2020). DWLs have been shown to cover a large fraction of the tropical ocean, and exhibit temperature contrasts of up to several degrees Celsius compared to the deeper parts of the surface layer (Kawai & Wada, 2007). These layers enhance near-surface stratification, suppressing mixing while trapping wind-induced momentum and forming "diurnal jets." These jets, in turn, generate turbulence through shear instability, leading to substantial modifications of upper ocean and sea surface temperatures and instantaneous air-sea turbulent heat fluxes (Moulin et al., 2018; Hughes et al., 2020).

While both DWLs and submesoscale fronts in the SBL are important elements of ocean systems, these two processes have been investigated and understood largely independently of each other. The interaction between DWLs and submesoscale fronts remains mostly unexplored to date. To address this gap, we investigate the variability and interaction of submesoscale fronts and DWLs using both in-situ observations and a turbulence closure model at resolution sufficient to resolve DWLs and submesoscale motions in the SBL. Our study region is the tropical Australian Northwest Shelf (Figure 1), a region of high solar radiation and strong submesoscale fronts, and hence an ideal site to study the coupling between submesoscale processes and DWLs.

The paper is structured as follows: Section 2 describes the data and methods employed in our study, followed by an overview of DWLs and fronts in Section 3. Sections 4 and 5 include a detailed analysis of frontal dynamics, instability, and turbulence using observational and modeling datasets. Finally, our main findings are summarized in Section 6.

2 Study area and methods

2.1 Study area

Our study area is located approximately 50 km off Barrow Island on the Australian Northwest Shelf (approximately 114.7°E, 20.7°S, time zone: UTC + 8, see Figure 1a). The local inertial frequency is f = -5.1 $\times$ 10^{-5} rad s^{-1}, corresponding to a local inertial period of $T_f = 2\pi/|f| = 34.0$ h. This site is energized by tidal forcing and frequently exhibits a rich tapestry of interwoven submesoscale eddies, filaments, and fronts (Brink et al., 2007). The

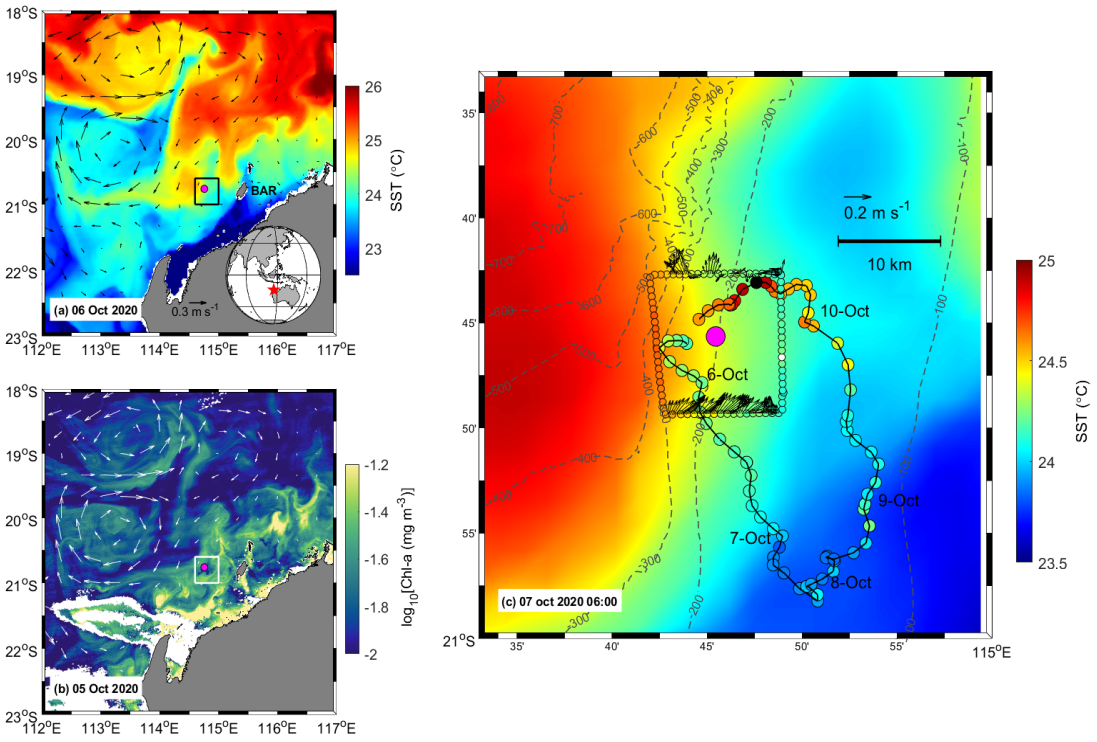

Figure 1. (a) Map of the Australian Northwest shelf sea and deeper Indian Ocean with satellite SST (in color) and surface geostrophic currents (arrows) from 6 October 2020 at 20:00 LT; (b) same as (a) but with satellite chlorophyll-a (in color) from 5 October 2020; (c) expanded view of the study area marked in (a) and (b) with satellite SST from 7 October 2020 at 06:00 LT (in color). Colored markers show the glider-based SST along the glider track (black line) from 5 October at 12:00 LT to 11 October 2020 at 00:00 LT. Ship-based SST (color markers) and near-surface velocity at 14-m depth (arrows) on 7 October at 05:00 – 11:20 LT are shown along the box-shaped ship track. Isobaths (dashed lines) are indicated in meters. The magenta point shown in all panels indicates the location of the mooring. BAR in (a) denotes Barrow Island.

data used in this study covered several diurnal cycles from 5 October 2020 at 12:00 LT to 11 October 2020 at 00:00 LT (time will be expressed in local time, LT, throughout). We used data from an autonomous underwater glider and a long-term mooring both of the Australian Integrated Marine Observing System, complemented by ship-based measurements on the R/V Solander (Figure 1a,b).

2.2 Field measurements

Underwater glider observations. A Slocum glider, equipped with a Sea-Bird SBE41 CTD and WETLabs optical sensors sampling at 0.5 Hz, transited across the frontal region (Figure 1c), providing dive profiles of temperature, salinity, and chlorophyll-a, including the thin near-surface region affected by DWL activity. The irregular glider-based CTD data were optimally interpolated onto a two-dimensional (depth-time) grid, using 12-minute time intervals for the period of 5–11 October, and 0.5 m vertical bins between depths of 0 and 100 m. A Gaussian weighting function was used to compute the weighting of each salinity and temperature data contribution to the gridded values, which were then converted into conservative temperature, Θ, and absolute salinity, S_A, according to the international TEOS-

10 standard for seawater (Millero et al., 2008; Feistel et al., 2010). The glider operations were managed by Australia's Integrated Marine Observing System (IMOS).

Mooring observations. One mooring was deployed initially, and, on October 7, replaced by a second mooring at the same location at a local depth of around 200 m inside the frontal region on 5–10 October, as indicated by the pink dot in Figure 1c. The moorings were consisted of instrument chains equipped with a combination of two temperature sensors (BlueZone Group AQUAloggerP, Australia or Seabird SBE 39, United States), one CTD sensor mounted at 30 m depth (Seabird SBE 37, United States), and three fast-response thermistors (Seabird SBE 56, United States, with 0.1-Hz sampling rate), distributed at intervals of 7–10 meters from 23.5 m depth down to a depth of approximately 200 m (the mounting depths are shown in Figure 5b). Data from the moored temperature loggers were converted to potential density using a Θ-S_A relationship based on CTD data from the glider in the vicinity of the mooring (see details in Appendix A). An upward-looking 150-kHz ADCP (Ocean Surveyor, RDI Workhorse) provided velocity estimates between 19 m and 155 m depth at an average ping interval of 2 s in 8 m vertical bins. All sensors on the moorings, including the ADCP and temperature loggers, were operated and quality-controlled by IMOS, ensuring the reliability and consistency of the data used in this study.

To ensure consistent effective resolution in both time and the vertical direction, both velocity and temperature data were 1-hour low-pass filtered and interpolated to common time steps t_i at 1-hour intervals. Velocity data were then vertically interpolated onto the positions z_i of the moored temperature loggers, spaced at 10 meters interval. We used centered finite differencing to compute the square of the buoyancy frequency, $N^2 = \partial b/\partial z$, where $b = -g(\rho_\theta - \rho_0)/\rho_0$ is the buoyancy based on the potential density ρ_θ and the constant reference density $\rho_0 = 1023$ kg m^{-3}. Similarly, the (squared) vertical shear, $S^2 = (\partial u/\partial z)^2 + (\partial v/\partial z)^2$, was derived from the horizontal velocity components u and v by vertical finite differencing.

Ship-based measurements. Velocity data were obtained from a ship-based 150-kHz ADCP (Ocean Surveyor from RDI Workhorse) on 7 October along the ship track shown in Figure 1c. The ADCP sampled the water column in 8 m vertical bins at 0.5 Hz, with the uppermost bin located at approximately 14 m depth. For noise reduction, these data were averaged over intervals of 3 s before further processing. Underway near-surface temperatures were obtained from an SBE21 thermosalinograph (water inlet at 2 m depth) at 10 s intervals, yielding a horizontal resolution of approximately 50 m.

Satellite data. The large-scale distributions of SST and chlorophyll-a in our study area were derived from the geostationary satellite Himawari-8 and MODIS satellite products at 2 km and 1 km spatial resolution, respectively. In addition, we used surface velocity data at 25 km resolution from OSCAR (Dohan, 2021). Hourly Himawari-8 SST data (also available at the 10-minute resolution, albeit noisier) are used to derive the lateral buoyancy gradient $M^2 = [(db/dx)^2 + (db/dy)^2]^{1/2}$, where b is the buoyancy as defined above, and x and y are the east and north directions, respectively. This complements the one-dimensional mooring data by providing high-resolution snapshots of the SST lateral structure in both space and time.

Meteorological data. We used hourly air-sea reanalysis data (Hersbach et al., 2020), provided by the German Weather Service, except for the wind data that were collected every 30 minutes from a weather station on Barrow island (Figure 1a), approximately 50 km from our experimental site. This station, operated by the Australian Bureau of Meteorology, allowed us to capture the rapid variability of the local winds. As described in more detail in Section 2b of Peng et al. (2020), the magnitude τ^w of the surface wind stress and the net surface heat flux Q_{net} were computed based on these data using the COARE 3.5 routines (Fairall et al., 2003; Edson et al., 2013). From this, the surface buoyancy flux B_0 (positive for buoyancy loss) was computed.

2.3 Estimation of turbulent diffusivity

To estimate mixing parameters from our mooring data, we used a fine-structure mixing length model for the turbulent vertical diffusivity, $K_\rho = 0.09\, L_E^2\, S$, where S is the total vertical shear and $L_E = \tilde{\theta}/(d\bar{\theta}/dz)$ the Ellison length scale, which we interpret as a measure of the scale of the vertical turbulent overturns (Ivey et al., 2018, 2021). Here, $\tilde{\theta}$ is the root-mean-square of the turbulent temperature fluctuations and $d\bar{\theta}/dz$ is the background temperature gradient, computed based on the 1-minute low-pass-filtered temperature $\bar{\theta}$ (sufficient to remove turbulent fluctuations in temperature signals). Estimates of S were derived from 10-minute averaged ADCP data which was additionally smoothed using a three-point rolling time average. We used a wavelet decomposition (Jones et al., 2020; Percival & Walden, 2000) to remove internal-wave contributions to $\tilde{\theta}$. We calculated the gradients for S and $d\bar{\theta}/dz$ with second-order central differencing with first-order differencing at the edges of the data ranges. The model assumes that turbulence is generated by mean shear S only, and that the fluid has a background stable density stratification characterized by N. Finally, we rejected the model results during periods when the local stratification was very weak ($N^2 < 3 \times 10^{-6} s^{-2}$) and estimates of L_E were unreliable.

2.4 Scaling of diurnal warm layers

Following Schmitt et al. (2024), we used a revised version of the classical DWL scaling relations by Price et al. (1986), estimating the DWL bulk buoyancy anomaly $\overline{b}$ and thickness H at midday as functions of the peak radiative buoyancy flux $B_{\max}$, the surface friction velocity $u_* = \sqrt{|\tau^w|/\rho_0}$, the heating period T_h during which $B_0 < 0$, and water clarity represented by the short-wave absorption scale η:

$$H = 0.85 R^{-1/2} F(\hat{f}) J(H/\eta) \frac{u_*^3}{B_{\max}} \tag{1}$$

$$\overline{b} = 0.38 R^{-1/2} F(\hat{f}) J(H/\eta) \frac{B_{\max}}{u_*}\ . \tag{2}$$

Here $R = u_*^2/(B_{\max} T_h)$ is a non-dimensional forcing ratio and $F(\hat{f})$ and $J(H/\eta)$ are functions of the non-dimensional products $\hat{f} = f T_h$ and H/η. For the scaling estimates discussed later on, we assume $\eta = 1$ m, which is consistent with the clear waters found at the study site. For more details refer to Schmitt et al. (2024).

2.5 Numerical model

We complemented the field observations with one-dimensional vertical model simulations using the General Ocean Turbulence Model (GOTM) (Umlauf et al., 2005), here extended to include background horizontal density and pressure gradients to represent the presence of a front with infinite width (see Figure 2). This idealized geometry makes it possible to account for some of the key physical processes in two-dimensional fronts with the help of a one-dimensional (vertical) model.

Here, $\tilde{x}$ is the cross-front direction (pointing towards denser water), $\tilde{y}$ the along-front direction, and z the vertical coordinate pointing upwards with $z = 0$ at the surface. The model solves the one-dimensional transport equations for momentum and buoyancy for an infinitely deep water column,

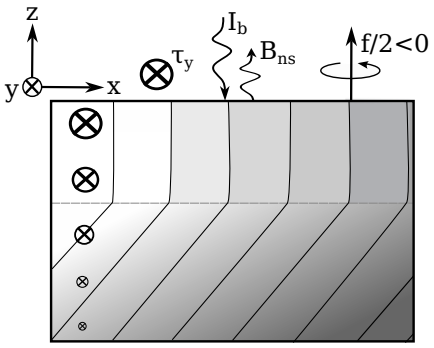

Figure 2. Schematic of the model set up. The gray scale represents density and the inward pointing arrows show the direction of the frontal jet $\tilde{v}_g$ in the $\tilde{y}$-direction.

$$\frac{\partial \tilde{u}}{\partial t} - f\tilde{v} = -g\frac{\partial \zeta}{\partial \tilde{x}} + zM^2 + \frac{\partial}{\partial z}\left(\nu \frac{\partial \tilde{u}}{\partial z}\right) - \frac{\partial \tau_x}{\partial z}\,, \tag{3}$$

$$\frac{\partial \tilde{v}}{\partial t} + f\tilde{u} = \frac{\partial}{\partial z}\left(\nu \frac{\partial \tilde{v}}{\partial z}\right) - \frac{\partial \tau_y}{\partial z}\,, \tag{4}$$

$$\frac{\partial b}{\partial t} - M^2\tilde{u} = \frac{\partial}{\partial z}\left(\nu^b \frac{\partial b}{\partial z}\right) - \frac{\partial G}{\partial z} + \frac{\partial I_b}{\partial z}\,. \tag{5}$$

where $\tilde{u}$ and $\tilde{v}$ are the Reynolds-averaged velocities in the $\tilde{x}$- and $\tilde{y}$-directions, b the buoyancy (defined above), g the gravitational constant, ζ the surface elevation, and ν and ν^b the (negligibly small) molecular diffusivities of momentum and buoyancy, respectively. G denotes the vertical turbulent buoyancy flux, I_b the radiative buoyancy flux (positive downward) due to penetrating shortwave radiation, and τ_x and τ_y the vertical turbulent momentum fluxes (normalized here with ρ_0). The horizontal buoyancy frequency, a measure for the strength of the front, is defined as

$$M^2 = -\frac{\partial b}{\partial \tilde{x}} = -f\frac{\partial \tilde{v}_g}{\partial z} > 0\,, \tag{6}$$

where v_g denotes the geostrophically balanced velocity of the frontal jet (Figure 2). The penetration of shortwave radiation is treated with a 2-band absorption assuming Jerlov type 1a for clear waters (Paulson & Simpson, 1977).

As boundary conditions for the momentum equations in (3) and (4), we prescribe the components of the wind stress, τ_x^w and τ_y^w, at the surface. Similarly, for the surface boundary condition in (5), we prescribe a constant non-solar surface buoyancy flux, $B_{\rm ns}$, and a sinusoidal variability in the daytime penetrating shortwave surface buoyancy flux, $B_{\rm sw} = -I_{\rm b}(z=0)$, with a peak at noon and zero fluxes before 06:00 and after 18:00 local time, as in Schmitt et al. (2024). Here, $Q_{\rm ns}$ accounts for the long-wave, latent, and sensible heat fluxes. $B_{\rm ns}$ is defined as positive for surface buoyancy loss (cooling) while $B_{\rm sw}$ is negative for surface buoyancy gain (heating) in our study. The net surface buoyancy flux is the sum of these two components: $B_0 = B_{\rm ns} + B_{\rm sw}$. At $z \to -\infty$, zero-flux conditions for the turbulent fluxes of momentum and buoyancy are applied (practically, the lower boundary conditions are imposed at some finite value of z that is sufficiently far below the surface to

not affect the results). The surface forcing, though strongly idealized, is able to realistically capture the DWL evolution (see Schmitt et al., 2024).

The turbulent momentum fluxes are computed from down-gradient expressions of the form

$$\tau_x = \langle \tilde{u}' w' \rangle = -\nu_t \frac{\partial \tilde{u}}{\partial z} , \quad \tau_y = \langle \tilde{v}' w' \rangle = -\nu_t \frac{\partial \tilde{v}}{\partial z} . \tag{7}$$

where primes and brackets denote turbulent fluctuations and ensemble averages, respectively, and ν_t the vertical turbulent diffusivity of momentum. The vertical turbulent buoyancy flux is computed from

$$G = \langle w' b' \rangle = -\nu_t^b \frac{\partial b}{\partial z} = -\nu_t^b N^2 , \tag{8}$$

with the vertical turbulent diffusivity ν_t^b and the squared buoyancy frequency $N^2 = \partial b/\partial z$. The turbulent diffusivities ν_t and ν_t^b are calculated within GOTM using the turbulent kinetic energy k, a turbulent length scale l, and so-called stability functions that depend on non-dimensional parameters describing the stability of the flow. These quantities are computed from a Mellor-Yamada-type (Kantha & Clayson, 1994) two-equation turbulence model described in detail in a recent study by Schmitt et al. (2024). These authors showed that the model described above provides an excellent representation of DWLs by comparing the output to Large Eddy Simulation (LES) results.

3 Frontal structure and dynamics

3.1 Background conditions and atmospheric forcing

A high-resolution map of the satellite altimetry-derived geostrophic currents from 6 October shows that, at the time of our measurements, the study area was characterized by several mesoscale eddies with horizontal scales of 100-200 km interacting with the shelf and the surface temperature field (Figure 1a). The strain field associated with these eddies formed frontal features with substantial lateral SST gradients along their edges, consistent with the classical view of frontogenesis due to mesoscale straining (Hoskins, 1982; Capet et al., 2008; Shakespeare & Taylor, 2013; Gula et al., 2014). Elevated concentrations of near-surface chlorophyll-a (Figure 1b) appear to be correlated with the position of these frontal features, indicative of the important role of fronts in local primary productivity (Lévy et al., 2012; Mahadevan, 2016).

Our survey was conducted in the proximity of one of these fronts near Barrow Island (black box in Figure 1a). The regional SST structure on 7 October is depicted in Figure 1c, showing that our research vessel followed a box-shaped track which crossed the front several times. Near-surface measurements across the front revealed a cross-front density contrast of 0.13-0.22 kg m^{-3} and a cross-front buoyancy gradient of $M^2 = 1.5\text{-}2.1 \times 10^{-7}$ s^{-2} (Figure 3c). These values might slightly underestimate the precise frontal buoyancy gradient as the ship track wasn't always perfectly normal to the front.

The temporal evolution of the cross-front buoyancy gradient becomes clearer using estimates of M^2 based on satellite SST gradients at the mooring location, using the same fixed T-S relationship described above (Figure 3c). The front started to intensify on 5 October, and peaked in strength close to $M^2 = 2 \times 10^{-7}$ s^{-2} shortly after the start of 6 October. The value of M^2 fluctuated around 1.5×10^{-7} s^{-2} over the following days until it began to decay late on 8 October. The SST-based values of M^2 were comparable to those of our ship-based near-surface measurements (blue stars in Figure 3c). It is worth noting that while the M^2 from SST shows the shape and temporal variability of the front, it may underestimate the frontal gradients in the deeper layers, as discussed below. For a more

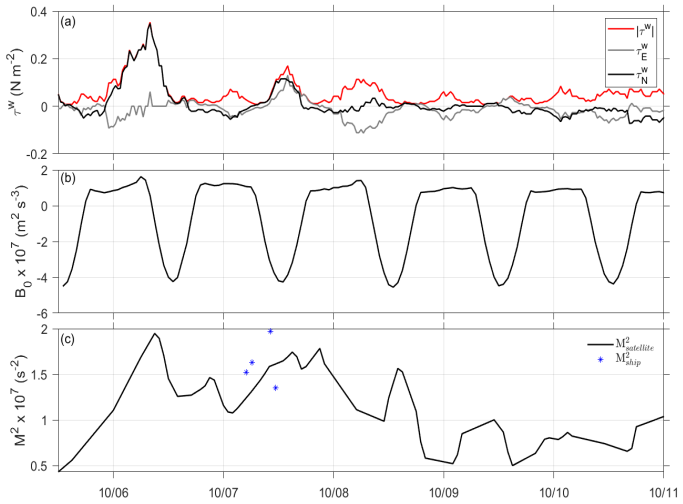

Figure 3. Time series of (a) wind stress magnitude and meridional, τ_N^w, and zonal, τ_E^w, components, (b) surface buoyancy flux (positive for buoyancy loss), and (c) surface buoyancy gradient, derived from satellite (line) and ship-based (stars) data. Time axis corresponds to local time.

detailed view of the evolution of the front during this 5-day period, please refer to the SST animation (Movie S1 in the supplemental material).

Throughout the 5-day survey period, the total surface buoyancy flux B_0 (positive for buoyancy loss) exhibited a distinct diurnal pattern: typically at a minimum near $B_0 = -4 \times 10^{-7}$ m^2 s^{-3} around midday due to the strong solar heating (Figure 3b), while the nighttime buoyancy loss induced by atmospheric cooling typically fell within the range $B_0 = 0.9 - 1.6 \times 10^{-7}$ m^2 s^{-3}. The wind stress was variable during this period, with the largest values observed early on 6 October with wind speeds around $U_{10} = 14$ m s^{-1}, subsequently decaying to moderate to weak values ($U_{10} = 2 - 10$ m s^{-1}) for the remaining days (Figure 3a).

3.2 Spatial structure

Glider observations on 5–10 October (trajectory in Figure 1c) provide a detailed view of the spatial structure of the frontal region and the near-surface DWL activity (Figure 4b,c,e). From two (strongly oblique) crossings of the frontal region, the glider data show that the front extends down to a depth of approximately 80 m with a lateral density contrast of 0.1-0.25 kg m^{-3}, largely controlled by temperature differences (Figure 4d). These findings are consistent with the ship-based near-surface measurements described above.

Of particular interest is the formation of stably stratified DWLs over the frontal region, observed near the surface at high vertical resolution (Figure 4e). These observations indicate that strong morning winds interrupted the formation of DWLs on 5 and 6 October, respectively. On these days, weak near-surface thermal stratification was only identified in the afternoon as the winds weakened. From 7 October onwards, more robust DWLs formed. We compared our observations to the DWL scaling relations recently suggested by Schmitt et al. (2024), as detailed in Section 2.4. Based on this scaling, the expected midday DWL thicknesses ranged from 19 m on 6 October to 3 m on 9 October, corresponding to bulk DWL temperature anomalies of 0.1 and 0.7°C, respectively. These estimates agree closely with the glider observations (Figure 4e), providing further support for the predictive capabilities of the DWL scaling model proposed by Schmitt et al. (2024).

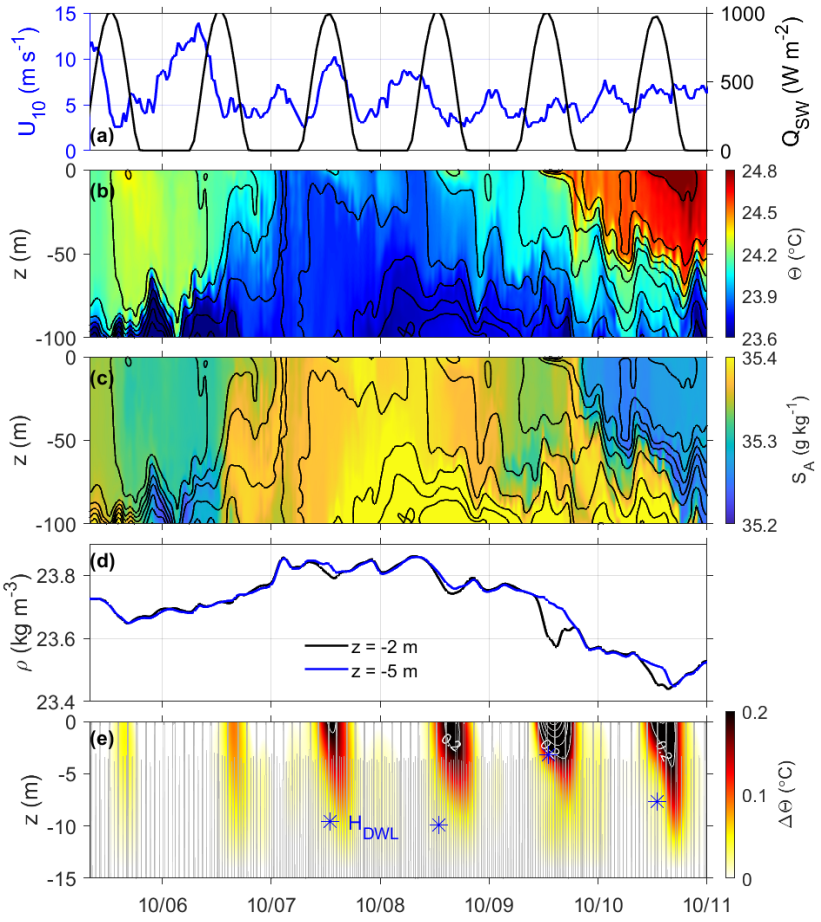

Figure 4. The evolution of (a) 10-m wind speed (blue) and shortwave radiation (black), (b) glider-based conservative temperature, (c) absolute salinity, (d) near-surface density, and (e) near-surface temperature anomaly, relative to the 15-m reference level. Black lines in panels (b) and (c) denote isopycnals (potential density) at intervals of 0.025 kg m^{-3}. Grey lines and white contours in panel (e) denote glider dive profiles and near-surface temperature anomaly at intervals of 0.2°C, respectively, and blue stars indicate the scaling of diurnal warm layer depth (which is out of range on 6 October and thus not shown). Local time applied.

DWLs enhance near-surface ocean stratification, thus acting as a barrier to the direct transfer of momentum from surface forcing down to greater depths. The implications of these DWL-related effects will be explored in more detail below.

3.3 Temporal evolution

The satellite-derived SST shows that the moving frontal region reached the mooring location from the west on 6 October, intensified on 7 October, and then gradually weakened and lost contact with the mooring by 9 October (see the animation of the temporal evolution in the supplementary material and the projection of the cross-front buoyancy gradient, M^2, onto the mooring location in Figure 5a). The temperature and vertical stratification in the near-surface region, inferred from the moored temperature loggers (Figure 5b,c),

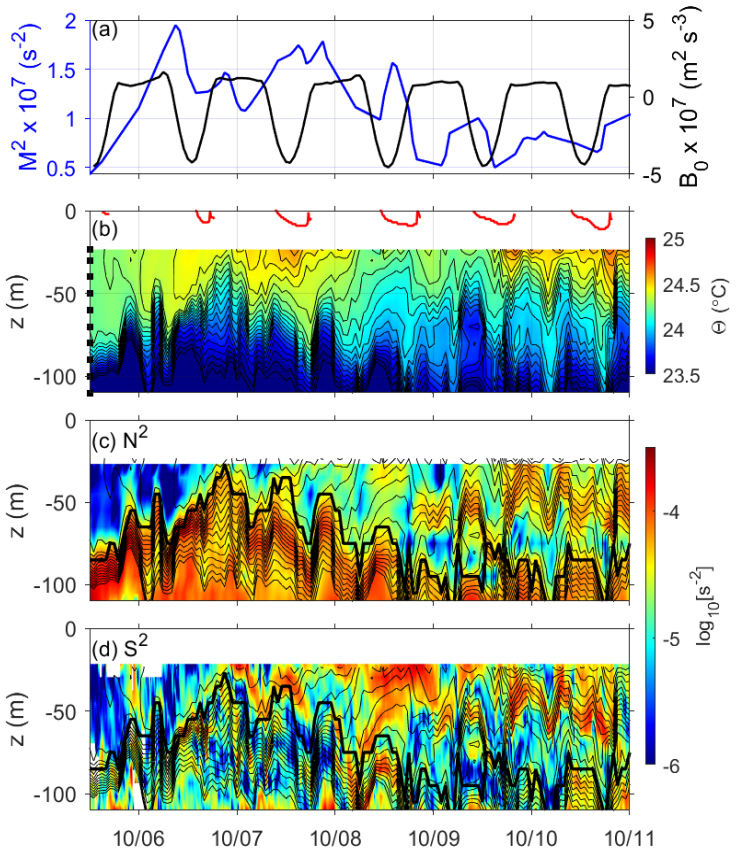

Figure 5. Mooring data showing the evolution of (a) lateral buoyancy gradient (based on satellite SST) and net surface buoyancy flux, (b) temperature, (c) square of the buoyancy frequency, (d) square of the total shear. Thick black lines in (c) and (d) indicate the depth of the SBL based on a density threshold of $\Delta\rho > 0.04$ kg m^{-3}. Red lines in (b) mark the lower edge of the DWLs based on the glider data, which is defined as the depth at which the near-surface temperature anomaly $\Delta\Theta$ has reduced to 0.05 °C. Thin black lines in (b)-(e) denote isopycnals (potential density) at intervals of 0.025 kg m^{-3}. Nominal depths of the moored temperature and CTD loggers are indicated by black squares in (b). Time axis corresponds to local time.

revealed a deep, well-mixed, and relatively cold surface layer on 5 October and the first half of 6 October, consistent with the nearly collocated glider observations during this period (Figure 4b). Strong winds in the first half of 6 October (Figure 3a) kept the water column well mixed despite strong diurnal heating and the increasing horizontal density gradient induced by the front (Figure 5a).

With increasing solar heating towards midday on 6 October and a decreased wind stress in the afternoon (Figure 3a) a weak DWL with a thickness of 7 m developed (Figure 4e), sheltering the deeper part of the SBL from atmospheric forcing. As a result, the SBL quickly shoaled and restratified while the front propagated across the mooring site (Figure 5). A continued surface-layer warming trend until approximately noon of 7 October, followed by a subsequent cooling and SBL deepening, indicated the advance and subsequent gradual retreat of the frontal region at the mooring location, consistent with the animated SST patterns in the supplementary material. After 9 October, as the influence of frontal dynamics diminished (reduced values of M^2), the SBL returned to its original depth.

The dynamical impact of the front becomes especially evident from an analysis of the development of the vertical shear at the mooring location (Figure 5d). Strong vertical shear $S^2 = \mathcal{O}(10^{-5} - 10^{-4})$ s^{-2} was present almost throughout the entire SBL during 7-8 October, when the SBL was characterized by stable stratification and pronounced lateral buoyancy gradients. Especially interesting were two periods with strong vertical shear in the SBL: in the first half of 7 October and in the second half of 8 October (shown in more detail in Figure 6a). This shear persisted even during daytime, when most of the SBL was isolated from direct wind forcing due to DWL-induced near-surface stratification, indicating that processes other than the surface stress maintained the high vertical shear levels at depth. Figure 6a-c shows that most of the shear was contributed by the v-component of the velocity, consistent with the direction of a frontal jet oriented in the along-front (south-north) direction (Figure 1c). Similarly, on late 8 October, when the front gradually rotated by about 45 degrees to a southeast-northwest alignment (see supplementary material), the u-component of the vertical shear became increasingly important. In both cases, the frontal jet and the associated shear (Figure 6) were in the along-front direction, consistent with what would be expected for a frontal jet in the Southern hemisphere, suggesting that thermal wind shear was the likely source of the observed vertical shear.

This is further supported by the following observation: to explain the observed time- and SBL-averaged shear, $\overline{S}^2 = 3.1 \times 10^{-5}$ s^{-2}, by the presence of a thermal wind shear, $S^2_{\mathrm{th}} = M^4/f^2$, a lateral buoyancy gradient of approximately $M^2 = 3 \times 10^{-7}$ s^{-2} would be required. This value is indeed of the same order of magnitude as the satellite-derived $M^2 = 1.4 \times 10^{-7}$ s^{-2}, although the latter seems to slightly underestimate the relevant lateral buoyancy gradient at depth. In view of the complex structure of the frontal region with locally sharpened density gradients (see Fig. 4b,c), it is, however, likely that our satellite-derived values of M^2 are not a reliable proxy for the horizontal density gradients in the deeper parts of the front, indicating the limitations of satellite derived M^2 to fully capture the dynamic nature of the subsurface frontal region.

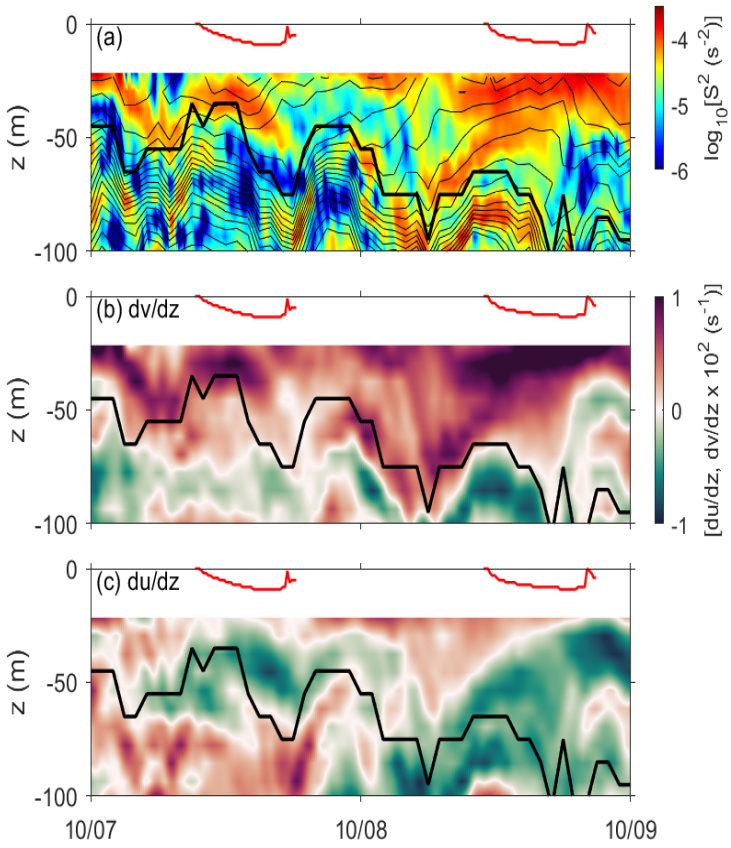

Figure 6. Evolution of (a) square of the total vertical shear, and (b,c) the squares of u and v components of the total vertical shear. Red lines in (a-c) mark the lower edge of the DWLs based on the glider data. Time axis corresponds to local time.

4 Interactions of diurnal warm layers and surface-layer fronts

4.1 Observations: frontal stability and mixing under diurnal warm layers

The frontal dynamics on 7-8 October detailed in Section 3.3 provide a unique opportunity to explore frontal stability and mixing in the presence of DWLs. During 7-8 October, when the frontal shear was most pronounced, the SBL exhibited gradient Richardson numbers $\mathrm{Ri} = N^2/S^2 < 1$ and, locally, even below $\mathrm{Ri} < 0.25$ (cyan line in Figure 7d). This indicates conditions favorable for shear instability and, in view of the relevance of thermal wind shear discussed above, other types of frontal instability, such as symmetric instability.

To ensure the robustness of our Ri estimates, we first cross-validated the N^2 estimates from the mooring data (which involved numerous assumptions) against an independent glider data set, as detailed in the appendix. This comparison yielded a correlation coefficient of $r = 0.91$, suggesting that our mooring-based estimates of N^2, used to compute Ri, are reliable, with minimal impact on Ri. Second, on a more qualitative level, the observed trends in Ri followed the variability of the lateral buoyancy gradients M^2 (Figure 7a,d) and the presence of DWLs, indicating that the Ri estimates reflect actual frontal conditions and are not dominated by measurement artifacts. Lastly, higher vertical resolution velocity measurements would likely result in larger frontal shear values, leading to even smaller Ri. We thus believe the relatively low values of Ri we observed are reliable, providing robust evidence for the presence of shear instability.

Quality-controlled turbulence data from 7-8 October, obtained from the moored instrumentation at 35 m and 55 m depth, showed that turbulent diffusivities increase with depth, different from what would be expected for surface-driven turbulence, with peak values exceeding $\kappa_\rho = 10^{-3}$ m^{2}s^{-1}. These higher diffusivity values at 55 m depth were associated with the lower values of Ri (Figure 7d), indicative of the importance of locally evolving instabilities that were not directly driven by surface forcing.

Increased turbulence at 55 m depth was observed during the daytime on 7 and 8 October, when this layer was within a weakly stratified SBL, but isolated from direct atmospheric influences by the development of DWLs. The data from 7 October shows that the variability of turbulence was strongly influenced by the 12-hour vertical excursion of the SBL base, likely associated with semidiurnal internal tides (Figure 7b). On 8 October, the SBL was deeper and less affected by tidal excursions of the SBL base, indicating two distinct dynamical regimes: One occurs in the central part of the SBL, where turbulence is suppressed by near-surface stratification due to the DWL. The other occurs in the deeper layer of the SBL, where frontal density gradients and strong vertical shear are sufficient to trigger instability and turbulence, which, if sustained, can result in weaker local vertical stratification.

The relatively low gradient Ri and enhanced turbulence in the upper ocean over this period with strong frontal shear cannot be attributed to the surface forcing due to the strong diurnal stratification (details in Section 3.3), suggesting that the turbulence was likely driven by a variety of local processes, including frontal instability (such as symmetric and inertial instability), local shear instability, or other local dynamics such as internal tides. However, the limitations of our data set preclude further in-depth investigation, hence we undertake an idealized simulation considering only DWLs, fronts and conditions in the near-surface layers.

4.2 Simulations: Interactions of frontal and diurnal warm layer dynamics

To obtain a better understanding of the frontal dynamics affected by the presence of DWLs observed on 7-8 October under conditions of intense solar heating and weak winds, we used the numerical model described in Section 2.5. Three simulations were carried out for this study: DWL only (S_D), front only (S_F), and DWL and front (S_{DF}). The simulations utilized a 60-second time step and resolved an 80 m deep water column with 500 grid cells,

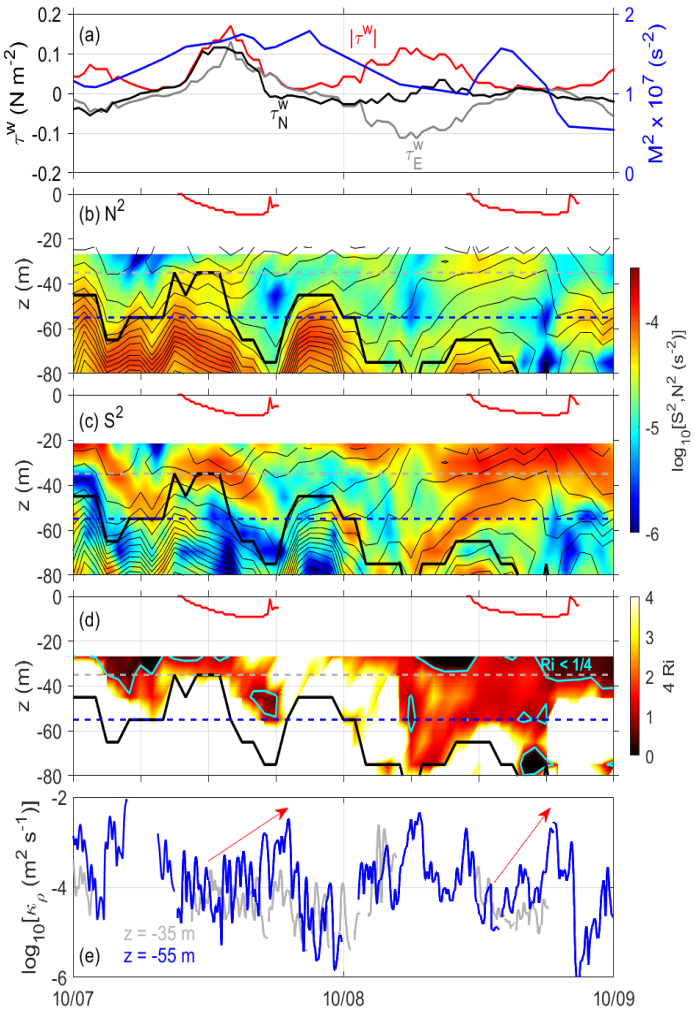

Figure 7. Time series at the mooring location of (a) wind stress magnitude $|\tau^w|$ and its meridional, τ_N, and zonal, τ_E, components and surface buoyancy flux B_0; (b) vertical stratification; (c) square of the total vertical shear; (d) gradient Richardson number; (e) the estimated turbulent diffusivity using a turbulence model based on the fine-scale temperature and shear data. During periods when the local stratification was very weak, estimates of L_E are unreliable and hence no estimates of eddy diffusivity can be made. Note that Ri has been multiplied by a factor of 4 to ease comparison with the critical gradient Richardson number (blue), namely Ri = 1/4 or equivalently, $N^2 = S^2/4$. Black lines in (b) - (d) are the depth of the surface boundary layer (as in Figure 5). Red lines in (b) - (d) mark the lower edge of the DWLs based on the glider data. Time axis corresponds to local time.

thus achieving a vertical resolution of 0.16 m. Each simulation ran for 3 days, with the first day as spin up time. The results shown in Figure 8, Figure 9, and Figure 10, show days 2 and 3 of the model runs. All simulations were initialized with constant vertical stratification, $N^2 = 7.5 \times 10^{-5}$ s^{-2}, chosen to match the observed environmental conditions (Figure 7b), and forced by a constant downfront wind stress of 0.05 N m^{-2}, corresponding to wind speeds of approximately 5 m s^{-1}. This wind forcing provides an idealized representation of the periods with stronger winds with a clear downfront component on 7-8 October (Figure 7a).

Table 1. Simulations and parameters for S_{DF}, S_F, and S_D, including the cross-front buoyancy gradient M^2, diurnal forcing, downfront wind stress τ_y^w, vertical stratification N^2, and balanced Richardson number Ri_b

-	M^2 (s^{-2})	Diurnal forcing	τ_y^w (N m^{-2})	N^2 (s^{-2})	Ri_b
S_{DF}	3.0×10^{-7}	on	0.05	7.5×10^{-5}	2.2
S_F	3.0×10^{-7}	off	0.05	7.5×10^{-5}	2.2
S_D	0	on	0.05	7.5×10^{-5}	-

Depending on the scenario, an additional surface buoyancy forcing (simulations S_D and S_{DF}) and/or a horizontal buoyancy gradient (simulations S_F and S_{DF}) were applied as summarized in Table 1.

For the interpretation of the following simulations, it is helpful to recall that a non-zero cross-front buoyancy gradient introduces a new energy source for turbulence in the form of a frontal jet, and the possibility of different frontal instabilities (Thomas et al., 2013; Taylor & Ferrari, 2010). Frontal instability is expected to occur in baroclinic fronts if the Ertel potential vorticity (EPV), q, and the Coriolis parameter, f, attain opposite signs (Thomas et al., 2013). In our simulations with zero relative vertical vorticity and a straight geostrophically-balanced front (Figure 2), this condition reads:

$$fq = f\left(f\hat{\mathbf{k}} + \nabla \times \mathbf{u}\right) \cdot \nabla b = f^2 N^2 + \frac{\partial \tilde{v}}{\partial z} M^2 < 0 \,, \tag{9}$$

were $\mathbf{u}$ is the three-dimensional velocity vector, $\hat{\mathbf{k}}$ the upward unit vector, and b the buoyancy (defined as above). Two types of instability can develop in this case: gravitational instability for $N^2 < 0$ and symmetric instability (SI) for stable stratification and a sufficiently large M^2 provided $\partial\tilde{v}/\partial z > 1$. The latter is the case especially in balanced fronts, where $\partial\tilde{v}/\partial z = -M^2/f$ according to (6). In this case, the condition in (9) is equivalent to a threshold of the balanced Richardson number, $Ri_b = N^2 f^2/M^4 < 1$. It is important to note that, similar to all other existing turbulence models of this type, the second-moment closure model used in our study does not represent SI. As shown in the following, in situations where SI is expected, the modeled shear will therefore increase until the threshold for shear instability is reached (modeled $Ri \approx 1/4$). This also implies that the model may predict non-turbulent regions with $fq < 0$ that would otherwise be amenable to SI.

Our first example, simulation S_D, incorporates a time-dependent surface buoyancy flux to simulate the diurnal heating cycle without the presence of a front. As shown in Figure 8a, the net surface buoyancy flux, B_0, is the sum of a daytime penetrating shortwave flux, $B_{\mathrm{sw}} < 0$, with a sinusoidal variability, and a constant non-solar surface flux, $B_{\mathrm{ns}} > 0$. Similar to the data shown in Figure 3a and Figure 5, the net surface buoyancy flux was chosen to peak at B_0 = -4.5 $\times$ 10^{-7} $m^2 s^{-3}$, while the constant non-solar buoyancy flux is $B_{\mathrm{ns}} = 1 \times 10^{-7}$ $m^2 s^{-3}$ (corresponding to the total flux at nighttime). The heating period with a negative net buoyancy flux spans T_h = 10 hours at a tropical latitude of 20.7°S. During the day, strong near-surface stratification develops (Figure 8b), inducing a night-day temperature contrast of approximately 0.3-0.4°C (Figure 8a). The evolution of the DWL is accompanied by the formation of diurnal shear at the lower flank of the diurnal jet, generating turbulence driven by shear instability (Figure 8c-e). In the late afternoon and at nighttime, the SBL is additionally forced by convection, and the diurnal shear bands gradually propagate downward, reaching the base of the SBL at a depth of approximately 20 m around midnight. Note that the model predicts a state of marginal instability ($Ri \approx 1/4$) inside these downward-propagating shear bands, in agreement with

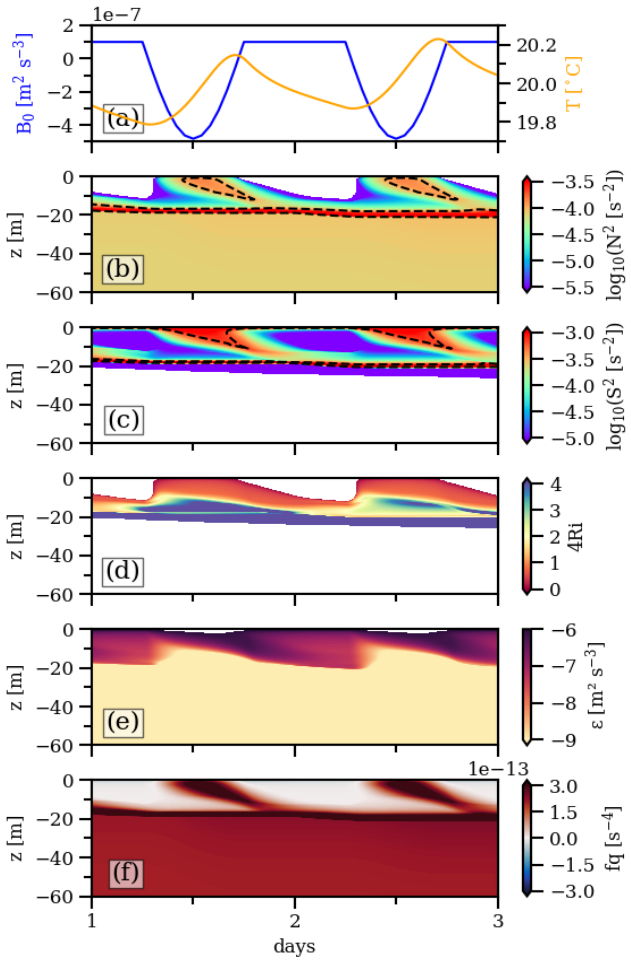

Figure 8. The GOTM simulation S_D: Evolution of (a) net surface buoyancy flux and temperature at z = -5 m, (b) vertical stratification, (c) vertical shear, (d) 4 times gradient Richardson number, (e) turbulence energy dissipation rate, and (f) Ertel potential vorticity. Dashed lines marked in (b) and (c) denote $N^2 = 10^{-4}$ s^{-2} and $S^2 = 10^{-3.5}$ s^{-2}, respectively, as reference for comparison with GOTM simulation S_D. White areas in (b) and (d) indicate regions with negative stratification.

recent LES discussed in Schmitt et al. (2024). EPV is extracted from the SBL by the buoyancy loss at the surface during nighttime conditions (Taylor & Ferrari, 2010), bringing the EPV close to the instability threshold of $fq = 0$ (Figure 8f). In regions with $fq < 0$, or, equivalently, $N^2 < 0$, gravitational instability develops.

For the front-only simulation S_F, no surface buoyancy flux was applied but the setup now included a horizontal buoyancy gradient and was initialized with a velocity field in thermal wind balance, as depicted in Figure 2. The lateral buoyancy gradient we selected is $M^2 = 3 \times 10^{-7}$s^{-2}, consistent with the discussion of the thermal wind shear at the end of Section 3.3. These parameters correspond to a balanced Richardson number of $Ri_b = N^2 f^2 / M^4 = 2.2$, which is stable with respect to SI (see above). With a downfront wind forcing, a cross-front Ekman transport is triggered, advecting colder waters laterally on top of warmer waters and inducing a persistent cooling trend near the surface (Figure 10a). This results in the formation of a thin convective layer near the surface and a turbulent

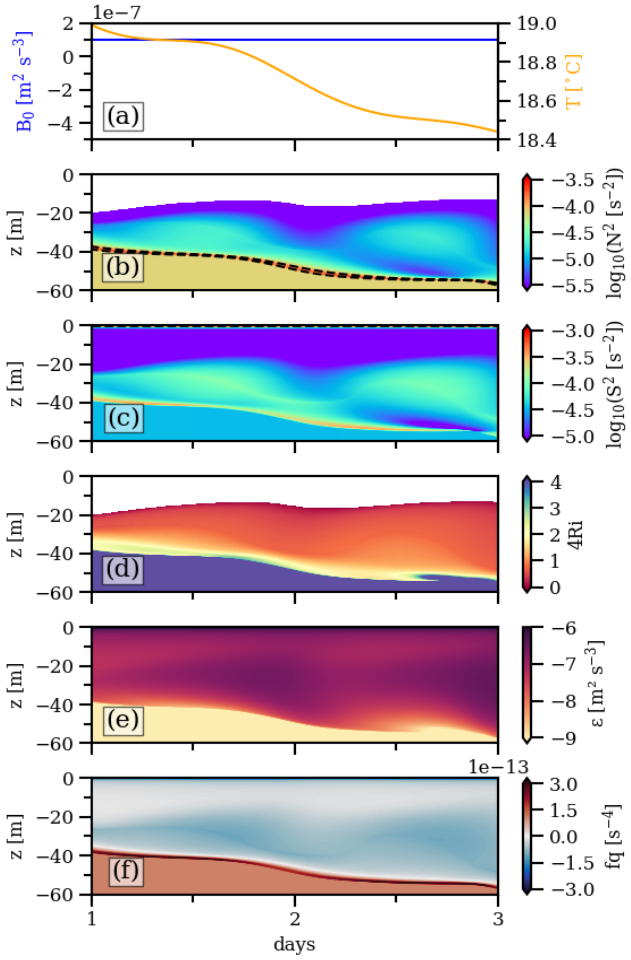

Figure 9. Same as Figure 8 but for the GOTM simulation S_F.

layer associated with weak but nonzero vertical stratification in the lower part of the SBL (Figure 9b,e), where fq decreases to below zero for this simulation (Figure 9f). This two-layer frontal structure, characterized by an upper convective layer and a marginally stable lower layer with negative EPV, is reminiscent of the results from Taylor and Ferrari (2010) based on LES. This confirms the suitability of the model setup for this study, however, with the caveat that our model cannot produce SI but instead generates turbulence through shear instability in the layer below the convectively unstable surface layer. As discussed above, this is reflected in Richardson numbers around $Ri = 1/4$, consistent with shear instability, rather than $Ri = 1$ that would be expected for SI in the deeper region below the convectively unstable surface layer (Figure 10d). For this reason, we also find persistent negative fq in this region (Figure 10f). The step-wise entrainment processes visible in Figure 10 reflects the effect of inertial oscillations with a period of $T_f = 34$ h (see Thomas et al., 2016).

Of particular interest in this study is simulation S_{DF}, which integrates the setups of both simulations S_D and S_F. Despite the idealized nature of the simulations, the model demonstrates strong alignment with our observations. Simulation S_{DF} replicates diurnal variations in vertical stratification and shear associated with DWL dynamics near the surface, and the key features of vertical frontal stratification [$N^2 = \mathcal{O}(10^{-5} - 10^{-4.5})$ s^{-2}] and vertical shear [$S^2 = \mathcal{O}(10^{-4.5} - 10^{-4})$ s^{-2}] in the subsurface layers of the SBL (Figure 10b,c), closely matching our observations (Figure 7b,c). The first insight gained from

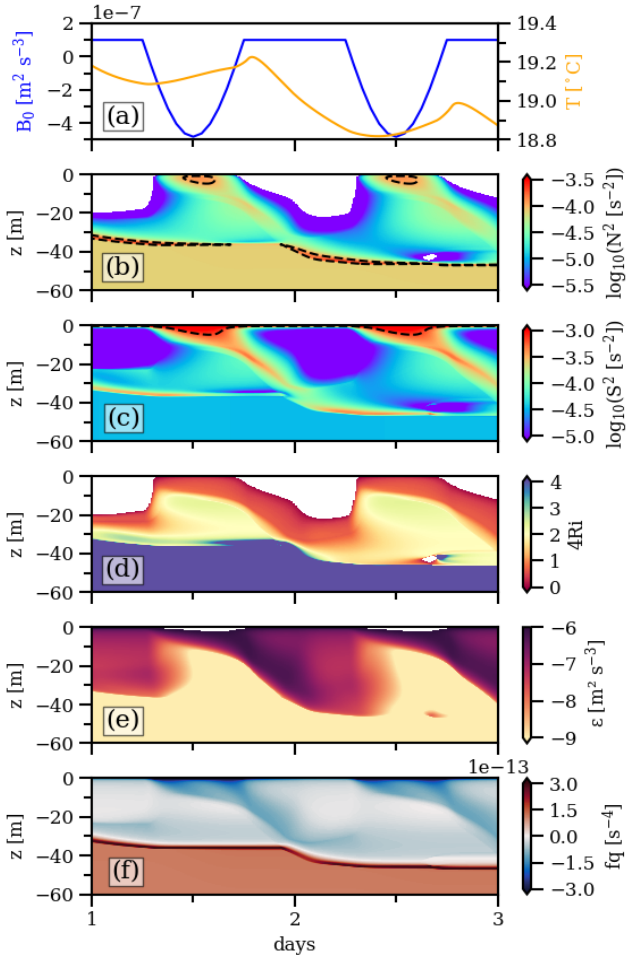

Figure 10. Same as Figure 8 but for the GOTM simulation S_{DF}.

this simulation is that the presence of the DWL shields the subsurface layer from direct wind forcing, leading to restratification. This is evident from the reduction in SBL depth to 50 m on day 3 and the suppression of SBL turbulence below the DWL (Figure 10) compared the simulation S_F without surface heating. This underlines the role of DWLs in shaping frontal SBL turbulence.

Closer inspection of differences in DWL properties between simulations S_{DF} and S_D reveals a reduction in the near-surface magnitudes of N^2 and S^2 (dashed lines in Figure 10b,c and Figure 8b,c) and a reduction of the day-night temperature variations (Figure 10a and Figure 8a) when a front is present. This suggests that frontal dynamics can play an additional role in modulating the development of DWLs by mixing near-surface momentum and density through additional frontal turbulence. Despite the lower near-surface S^2, diurnal shear persists, with the Richardson number remaining below $Ri = 1/4$ at the base of DWLs.

Interestingly, the DWLs in this simulation are characterized by extended regions with $fq < 0$ (Figure 10f), which, according to (9), can be traced back to the strongly ageostrophic downfront shear, $\partial\tilde{v}/\partial z \gg -M^2/f$, associated with the diurnal jet. This suggests that DWLs in frontal regions may be unstable with respect to a mix of shear instability and SI. The marginally unstable and strongly turbulent shear layer at the DWL base propagates towards the base of the SBL during the afternoon and evening hours (Figure 10c,d,e),

consistent with the typical view of the diurnal cycle of DWLs (Price et al., 1986; Wijesekera et al., 2020). It is noteworthy that simulation S_{DF} indicates that a deeper SBL, created by frontal dynamics, allows diurnal shear to reach deeper layers compared to conditions without a front (Figure 8).

Simulation S_{DF} shows a region with negative potential vorticity in the deepest part of the SBL even during daytime conditions, when these regions are isolated from direct atmospheric forcing by the presence of DWLs (Figure 10f). The temporal evolution suggests that these conditions are remnants of the downward propagating negative-PV regions at the DWL base during nighttime (see above). These regions, characterized by Richardson numbers in the range $Ri = 0.25 - 1$, remain unstable to SI and would be, in the real world, prone to turbulence and mixing from small perturbations. This may provide an explanation for the enhanced turbulence in the lower part of the SBL seen in our mooring data (Figure 7d). However, in our idealized simulations, there is no clear evidence of frontal turbulence arising from frontal instability (Figure 10e) due to the sheltering effects of DWLs. One of the main conclusions from the GOTM simulations therefore is that even in the presence of a DWL, the underlying regions of the SBL remain close to marginal instability and may become sporadically turbulent if an additional disturbance or energy source, e.g. due to internal tides, becomes available. This seems to be the case in our moored turbulence measurements discussed in Section 4.1.

5 Discussion and conclusion

In this study, we combined high-resolution near-surface glider data and mooring data in a frontal region to study the impact of diurnal forcing (DWLs) on frontal dynamics and mixing. To help interpret these data, we included the effect of an idealized front in a vertical ocean turbulence model. Test simulations with diurnal buoyancy forcing (and no fronts) and purely wind-forced fronts showed that the model, although highly idealized, was able to reproduce the key features of DWL and frontal dynamics. More specifically, our simulations with a front forced by downfront winds (but no surface buoyancy forcing) predicted a vertical SBL structure in good qualitative agreement with previous LES studies (Taylor & Ferrari, 2010). This structure consists of a weakly stratified, convective upper layer and a significantly stratified, vigorously turbulent lower layer (Figure 9), which has been shown to host symmetric instability (SI) and associated turbulence (Taylor & Ferrari, 2010; Thomas et al., 2016). Although our model cannot directly simulate SI, it does indicate conditions favorable for SI ($fq < 0$), and predicts strong turbulence in this lower layer (Figure 9e,f).

Adding diurnal buoyancy forcing to this setup showed that the presence of a DWL isolates the deeper layers of the SBL from diabatic and frictional surface forcing, and thus from the most relevant sink of EPV (Taylor & Ferrari, 2010). As a result, the deeper regions of the SBL quickly become non-turbulent (Figure 10e), different from our simulation without diurnal buoyancy forcing (Figure 9e). However, as one of our most important findings, our results show that the deeper regions of the SBL remain in a state of marginal stability ($fq \approx 0$, Figure 10f), suggesting that small perturbations from other local processes (e.g., internal tides and waves) can easily trigger instability and turbulence. Once triggered, this type of turbulence can feed on the frontal jet as an additional energy source.

These model results are largely consistent with our observations, showing that the thermal wind shear in the frontal region creates conditions favorable for SI and shear instability ($Ri < 1$) in the lower part of the SBL also during daytime when DWLs are present (Figure 7d). These deeper SBL regions, however, only show sporadic turbulence (Figure 7e), suggesting that they are often close to marginal stability, similar to our simulations. Enhanced turbulence is visible especially in the lowest part of the SBL, where the significant internal-tide motions present at the field site may trigger frontal turbulence.

Another important insight gained from the simulations is that frontal dynamics deepen the SBL, allowing diurnal shear associated with DWL dynamics to reach greater depths compared to conditions without a front (Figure 8e and Figure 10e). This process exhibits some analogy with the triggering of deep-cycle turbulence in the equatorial ocean by the downward-propagation of shear bands induced by the presence of DWLs (Moum et al., 2022), with the caveat that rotation effects play a more important role in our case. Our simulations also show that both DWLs and the downward propagating shear bands are characterized by strongly negative EPV ($fq < 0$) due to the strong ageostrophic shear associated with the diurnal jet. This finding suggests that DWLs located in frontal regions may be hotspots of SI, which deserved further investigation. This mechanism may contribute to the redistribution of heat and nutrients within the ocean. Vice-versa, our simulations also showed that frontal turbulence may feed back on DWLs by reducing near-surface vertical shear and stratification through additional turbulence (Figure 8a, Figure 10a), resulting in an overall reduction of DWL amplitudes. Field observations to substantiate this effect are so far lacking, however.

Our study highlights the complex interactions between DWL and frontal dynamics in the SBL. These processes, which are often not fully resolved in current ocean and climate modeling systems, can play a critical role in the SBL dynamics and turbulence, as well as the vertical transport of tracers. The cross-front density gradients, solar heating rates, and wind speeds observed in our study are representative of many tropical regions (Figure 3a,b), suggesting that the processes by which they interact may be common in tropical oceans that experience strong solar heating and weak winds, particularly in eddy-rich environments. Our study represents a first step in this direction, providing essential insights for developing more accurate turbulence parameterizations in ocean and climate models that do not resolve both DWLs and fronts (e.g., Fox-Kemper et al., 2008; Bodner et al., 2023).

References

Boccaletti, G., Ferrari, R., & Fox-Kemper, B. (2007). Mixed layer instabilities and restratification. *J. Phys. Oceanogr.*, *37*(9), 2228–2250.

Bodner, A. S., Fox-Kemper, B., Johnson, L., Van Roekel, L. P., McWilliams, J. C., Sullivan, P. P., ... Dong, J. (2023). Modifying the mixed layer eddy parameterization to include frontogenesis arrest by boundary layer turbulence. *J. Phys. Oceanogr.*, *53*(1), 323–339.

Brink, K., Bahr, F., & Shearman, R. K. (2007). Alongshore currents and mesoscale variability near the shelf edge off northwestern australia. *J. Geophys. Res.*, *112*(C5).

Capet, X., McWilliams, J. C., Molemaker, M. J., & Shchepetkin, A. (2008). Mesoscale to submesoscale transition in the California Current System. Part II: Frontal processes. *J. Phys. Oceanogr.*, *38*(1), 44–64.

D'Asaro, E., Lee, C., Rainville, L., Harcourt, R., & Thomas, L. (2011). Enhanced turbulence and energy dissipation at ocean fronts. *Science*, *332*(6027), 318–322.

Dauhajre, D. P., & McWilliams, J. C. (2018). Diurnal evolution of submesoscale front and filament circulations. *J. Phys. Oceanogr.*, *48*(10), 2343–2361.

Dauhajre, D. P., McWilliams, J. C., & Uchiyama, Y. (2017). Submesoscale coherent structures on the continental shelf. *J. Phys. Oceanogr.*, *47*(12), 2949–2976.

Dohan, K. (2021). *Ocean surface current analyses real-time (oscar) surface currents - interim 0.25 degree (version 2.0).* NASA Physical Oceanography Distributed Active Archive Center. Retrieved from `https://podaac.jpl.nasa.gov/dataset/OSCAR_L4_OC_INTERIM_V2.0` doi: 10.5067/OSCAR-25I20

Dong, J., Fox-Kemper, B., Jing, Z., Yang, Q., Tian, J., & Dong, C. (2022). Turbulent dissipation in the surface mixed layer of an anticyclonic mesoscale eddy in the south china sea. *Geophys. Res. Lett.*, *49*(16), e2022GL100016.

Edson, J. B., Jampana, V., Weller, R. A., Bigorre, S. P., Plueddemann, A. J., Fairall, C. W., ... Hersbach, H. (2013). On the exchange of momentum over the open ocean. *J. Phys.*

Oceanogr., *43*(8), 1589–1610.

Fairall, C., Bradley, E. F., Hare, J., Grachev, A., & Edson, J. (2003). Bulk parameterization of air-sea fluxes: Updates and verification for the COARE algorithm. *J. Climate*, *16*(4), 571–591.

Feistel, R., Weinreben, S., Wolf, H., Seitz, S., Spitzer, P., Adel, B., ... Wright, D. (2010). Density and absolute salinity of the Baltic Sea 2006–2009. *Ocean Sci.*, *6*(1), 3–24.

Fox-Kemper, B., & Ferrari, R. (2008). Parameterization of mixed layer eddies. part ii: Prognosis and impact. *J. Phys. Oceanogr.*, *38*(6), 1166–1179.

Fox-Kemper, B., Ferrari, R., & Hallberg, R. (2008). Parameterization of mixed layer eddies. part i: Theory and diagnosis. *J. Phys. Oceanogr.*, *38*(6), 1145–1165.

Grisouard, N. (2018). Extraction of potential energy from geostrophic fronts by inertial–symmetric instabilities. *J. Phys. Oceanogr.*, *48*(5), 1033–1051.

Gula, J., Molemaker, M. J., & McWilliams, J. C. (2014). Submesoscale cold filaments in the Gulf Stream. *J. Phys. Oceanogr.*, *44*(10), 2617–2643.

Gula, J., Taylor, J., Shcherbina, A., & Mahadevan, A. (2022). Submesoscale processes and mixing. In *Ocean mixing* (pp. 181–214). Elsevier.

Hersbach, H., Bell, B., Berrisford, P., Hirahara, S., Horányi, A., Muñoz-Sabater, J., ... others (2020). The era5 global reanalysis. *Quarterly Journal of the Royal Meteorological Society*, *146*(730), 1999–2049.

Hoskins, B. J. (1982). The mathematical theory of frontogenesis. *Annu. Rev. Fluid Mech.*, *14*(1), 131–151.

Hughes, K. G., Moum, J. N., & Shroyer, E. L. (2020). Evolution of the velocity structure in the diurnal warm layer. *J. Phys. Oceanogr.*, *50*(3), 615–631.

Inc, M. (2022). *Matlab version: 9.13. 0 (r2022b).* The MathWorks Inc Natick, Massachusetts.

Ivey, G. N., Bluteau, C. E., Gayen, B., Jones, N. L., & Sohail, T. (2021). Roles of shear and convection in driving mixing in the ocean. *Geophys. Res. Lett.*, *48*(3), e2020GL089455.

Ivey, G. N., Bluteau, C. E., & Jones, N. L. (2018). Quantifying diapycnal mixing in an energetic ocean. *J. Geophys. Res.*, *123*(1), 346–357.

Johnson, L., Lee, C. M., D'Asaro, E. A., Thomas, L., & Shcherbina, A. (2020). Restratification at a california current upwelling front. part i: Observations. *J. Phys. Oceanogr.*, *50*(5), 1455–1472.

Jones, N., Ivey, G., Rayson, M., & Kelly, S. (2020). Mixing driven by breaking nonlinear internal waves. *Geophys. Res. Lett.*, *47*(19), e2020GL089591.

Kantha, L. H., & Clayson, C. A. (1994). An improved mixed layer model for geophysical applications. *J. Geophys. Res.*, *99*(C12), 25235–25266.

Kawai, Y., & Wada, A. (2007). Diurnal sea surface temperature variation and its impact on the atmosphere and ocean: A review. *J. Oceanogr.aphy*, *63*, 721–744.

Klingbeil, K., & Umlauf, L. (2023). *GOTM source code with langmuir turbulence closure* [Software]. Zenodo. Retrieved from `https://doi.org/10.5281/zenodo.8103884`

Lévy, M., Ferrari, R., Franks, P. J., Martin, A. P., & Rivière, P. (2012). Bringing physics to life at the submesoscale. *Geophys. Res. Lett.*, *39*(14).

Lévy, M., Franks, P. J., & Smith, K. S. (2018). The role of submesoscale currents in structuring marine ecosystems. *Nat. Commun.*, *9*(1), 1–16.

Mahadevan, A. (2016). The impact of submesoscale physics on primary productivity of plankton. *Ann. Rev. Mar. Sci.*, *8*, 161–184.

McWilliams, J. C. (2021). Oceanic frontogenesis. *Annual Review of Marine Science*, *13*, 227–253.

McWilliams, J. C., Gula, J., Molemaker, M. J., Renault, L., & Shchepetkin, A. F. (2015). Filament frontogenesis by boundary layer turbulence. *J. Phys. Oceanogr.*, *45*(8), 1988–2005.

Millero, F. J., Feistel, R., Wright, D. G., & McDougall, T. J. (2008). The composition of standard seawater and the definition of the reference-composition salinity scale. *Deep Sea Res. Part I*, *55*(1), 50–72.

Moulin, A. J., Moum, J. N., & Shroyer, E. L. (2018). Evolution of turbulence in the diurnal warm layer. *J. Phys. Oceanogr.*, *48*(2), 383–396.

Moum, J. N., Hughes, K. G., Shroyer, E. L., Smyth, W. D., Cherian, D., Warner, S. J., ... Dengler, M. (2022). Deep cycle turbulence in atlantic and pacific cold tongues. *Geophys. Res. Lett.*, *49*(8), e2021GL097345.

NASA/JPL. (2020). *Ghrsst noaa/star himawari-08 ahi l2p pacific ocean region sst v2.70 dataset in gds2.* NASA Physical Oceanography Distributed Active Archive Center. Retrieved from `https://podaac.jpl.nasa.gov/dataset/AHI_H08-STAR-L2P-v2.70` doi: 10.5067/GHH08-2PO27

NASA/LARC/SD/ASDC. (2005, 5 31). *Ceres clouds and radiative swath terra fm2 modis edition2b.* NASA Langley Atmospheric Science Data Center DAAC. Retrieved from `https://doi.org/10.5067/TERRA/CERES/CRS_TERRA-FM2_L2.002B`

Paulson, C. A., & Simpson, J. J. (1977). Irradiance measurements in the upper ocean. *J. Phys. Oceanogr.*, *7*(6), 952 - 956.

Peng, J.-P. (2023a). *Grl peng et al 2023.* The University of Western Australia. Retrieved from `https://research-repository.uwa.edu.au/en/datasets/grlpengetal2023` doi: 10.26182/8c5d-6525

Peng, J.-P. (2023b). *Solander adcp data 2020.* The University of Western Australia. Retrieved from `https://research-repository.uwa.edu.au/en/datasets/solanderadcpdata2020` doi: 10.26182/dwyc-s149

Peng, J.-P., Dräger-Dietel, J., North, R. P., & Umlauf, L. (2021). Diurnal variability of frontal dynamics, instability, and turbulence in a submesoscale upwelling filament. *J. Phys. Oceanogr.*, *51*(9), 2825–2843.

Peng, J.-P., Holtermann, P., & Umlauf, L. (2020). Frontal instability and energy dissipation in a submesoscale upwelling filament. *J. Phys. Oceanogr.*, *50*(7), 2017–2035.

Percival, D. B., & Walden, A. T. (2000). *Wavelet methods for time series analysis* (Vol. 4). Cambridge university press.

Price, J. F., Weller, R. A., & Pinkel, R. (1986). Diurnal cycling: Observations and models of the upper ocean response to diurnal heating, cooling, and wind mixing. *J. Geophys. Res. Oceans*, *91*(C7), 8411–8427.

Qu, L., Thomas, L. N., Wienkers, A. F., Hetland, R. D., Kobashi, D., Taylor, J. R., ... Nash, J. D. (2022). Rapid vertical exchange at fronts in the northern gulf of mexico. *Nature Communications*, *13*(1), 5624.

Schmitt, M., Pham, H. T., Sarkar, S., Klingbeil, K., & Umlauf, L. (2024). Diurnal warm layers in the ocean: Energetics, nondimensional scaling, and parameterization. *J. Phys. Oceanogr.*, *54*(4), 1037 - 1055.

Shakespeare, C. J., & Taylor, J. R. (2013). A generalized mathematical model of geostrophic adjustment and frontogenesis: uniform potential vorticity. *J. Fluid Mech.*, *736*, 366–413.

Shang, X., Shu, Y., Wang, D., Yu, J., Mao, H., Liu, D., ... Tang, H. (2023). Submesoscale motions driven by down-front wind around an anticyclonic eddy with a cold core. *J. Geophys. Res.*, *128*(8), e2022JC019173.

Spigel, R. H., Imberger, J., & Rayner, K. N. (1986). Modeling the diurnal mixed layer. *Limnology and oceanography*, *31*(3), 533–556.

Sun, D., Bracco, A., Barkan, R., Berta, M., Dauhajre, D., Molemaker, M. J., ... McWilliams, J. C. (2020). Diurnal cycling of submesoscale dynamics: Lagrangian implications in drifter observations and model simulations of the northern gulf of mexico. *J. Phys. Oceanogr.*, *50*(6), 1605–1623.

Taylor, J. R., & Ferrari, R. (2010). Buoyancy and wind-driven convection at mixed layer density fronts. *J. Phys. Oceanogr.*, *40*(6), 1222–1242.

Taylor, J. R., & Thompson, A. F. (2022). Submesoscale dynamics in the upper ocean. *Annual Review of Fluid Mechanics*, *55*.

Thomas, L. N. (2005). Destruction of potential vorticity by winds. *J. Phys. Oceanogr.*, *35*(12), 2457–2466.

Thomas, L. N., & Lee, C. M. (2005). Intensification of ocean fronts by down-front winds. *J. Phys. Oceanogr.*, *35*(6), 1086–1102.

Thomas, L. N., Taylor, J. R., D'Asaro, E. A., Lee, C. M., Klymak, J. M., & Shcherbina, A. (2016). Symmetric instability, inertial oscillations, and turbulence at the Gulf Stream front. *J. Phys. Oceanogr.*, *46*(1), 197–217.

Thomas, L. N., Taylor, J. R., Ferrari, R., & Joyce, T. M. (2013). Symmetric instability in the Gulf Stream. *Deep Sea Res. Part II*, *91*, 96–110.

Thompson, E. J., Moum, J. N., Fairall, C. W., & Rutledge, S. A. (2019). Wind limits on rain layers and diurnal warm layers. *J. Geophys. Res.*, *124*(2), 897–924.

Umlauf, L., Burchard, H., & Bolding, K. (2005). GOTM - Scientic Documentation : Version 3.2. , *63*, 279. doi: 10.12754/MSR-2005-0063

Wijesekera, H. W., Wang, D. W., & Jarosz, E. (2020). Dynamics of the diurnal warm layer: Surface jet, high-frequency internal waves, and mixing. *J. Phys. Oceanogr.*, *50*(7), 2053–2070.

Yu, X., Naveira Garabato, A. C., Martin, A. P., Gwyn Evans, D., & Su, Z. (2019). Wind-forced symmetric instability at a transient mid-ocean front. *Geophys. Res. Lett.*, *46*(20), 11281–11291.

Zheng, R., & Jing, Z. (2024). Diurnal variability of mixed layer overturning instabilities from glider array observations in the south china sea. *Geophys. Res. Lett.*, *51*(11), e2023GL107694.

Acknowledgments

The Australian Research Council Discovery Project (DP210102745) funded this work. We thank the captain and crew on R/V Solander from the Australian Institute of Marine Science (AIMS) for data collection at sea. The glider and mooring data was sourced from Australia's Integrated Marine Observing System (IMOS) – IMOS is enabled by the National Collaborative Research Infrastructure Strategy (NCRIS).

6 Open Research

The data used in this study include mooring and glider data, which are accessible through the UWA library repository (Peng, 2023a), and ship-based ADCP data (Peng, 2023b). The GOTM source code utilized in the analysis is archived (Klingbeil & Umlauf, 2023), and all data processing was conducted using MATLAB (Inc, 2022). Seawater properties were standardized according to the International TEOS-10 standard (Millero et al., 2008; Feistel et al., 2010). Satellite products from Himawari-8 and MODIS are also included (NASA/JPL, 2020; NASA/LARC/SD/ASDC, 2005), along with surface velocity data from OSCAR (Dohan, 2021). Hourly air-sea reanalysis data were obtained from ERA5 (Hersbach et al., 2020), and the COARE 3.5 routines were employed to compute surface stress and fluxes (Fairall et al., 2003; Edson et al., 2013).

Appendix A Reconstruction of $\Theta - S_A$ relationship and its assessment

Due to the lack of full-depth salinity measurements from the mooring data, we reconstructed the conservative temperature-absolute salinity ($\Theta - S_A$) relationship using CTD data obtained from a glider operating near the mooring site. The reconstruction was based on glider data collected within the depth range of -32 m to -28 m (Figure A1a), carefully selected to closely match the depth of the mooring's available CTD data at -30 m. This alignment was critical for ensuring a robust comparison and validation of the reconstructed $\Theta - S_A$ relationship. The validation of this relationship was carried out through two independent processes using both mooring and glider data.

First, a comparison between the estimated and observed $\Theta - S_A$ values at the 30-m depth was performed (Figure A1b,c). This comparison resulted in a mean RMSE of 0.034

753 g kg^{-1} and a standard deviation of 0.007 g kg^{-1}, indicating strong concordance between the
754 estimated and observed salinity values. Second, to evaluate the applicability of the $\Theta - S_A$
755 relationship across different depths, it was applied to the upper 60 m of CTD data collected
756 by the glider to compute the square of the buoyancy frequency, N^2, across the entire SBL
757 (Figure A1d). To ensure the robustness of our Ri estimates, we first cross-validated the N^2
758 estimates derived from the mooring data against an independent glider dataset, as detailed
759 in the appendix. This comparison yielded a correlation coefficient of $r = 0.91$, indicating
760 that our mooring-based N^2 estimates, which are used to compute Ri, are reliable and have
761 minimal impact on the accuracy of the Ri values. This underscores the precision of the
762 method.

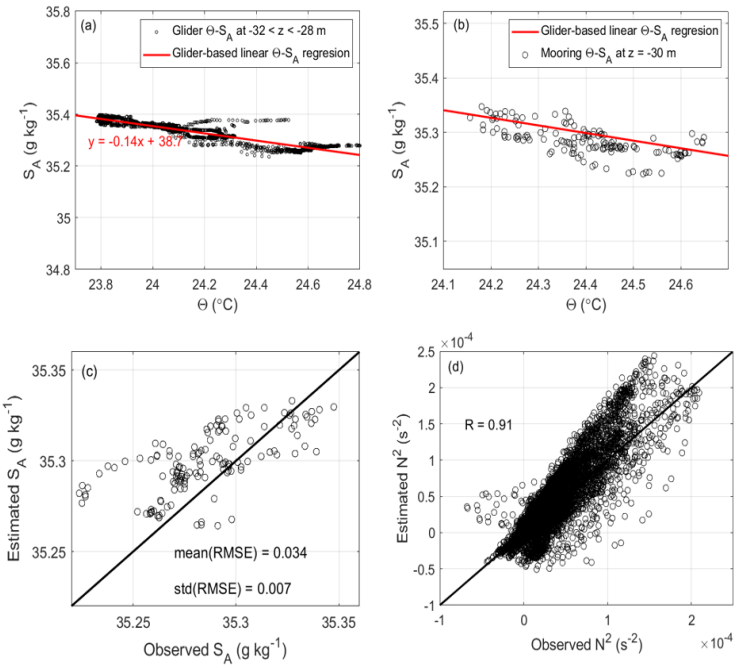

Figure A1. (a) Glider data collected at depths between -32 m and -28 m (black circles) and the corresponding derived linear $\Theta - S_A$ relationship (red line); (b) cross-validation of the glider-derived linear $\Theta - S_A$ relationship against mooring Θ and S_A data at a depth of -30 m; (c) comparison between the estimated S_A derived from moored temperature data at -30 m using the $\Theta - S_A$ relationship and the observed mooring S_A data at the same depth; and (d) extended comparison of the estimated square of the buoyancy frequency N^2 based on glider temperature data of upper 60 m against observed N^2 from glider CTD measurements at corresponding depths.

Three-dimensional Ocean Surface Layer Response to Rain, Wind bursts and Diurnal Heating

M. Schmitt[1], K. Klingbeil[1], R. Shevchenko[2,3], and L. Umlauf[1]

[1]Leibniz-Institute for Baltic Sea Research, Warnemuende, Germany
[2]Université Côte d'Azur, Nice, France
[3]Centrale Méditerannée, Nice, France
=[1]=Seestraße 15, 18119 Rostock, Germany=
=[2]=Laboratoire J.A. Dieudonné, UMR CNRS 7351, Nice, 06108, France=
=[3]=61/63 avenue Simone Veil, Nice, 06200, France=

Key Points:

- Based on high-resolution atmosphere and ocean models, we observe a decrease in surface heat loss underneath atmospheric cold pools.
- Despite the presence of diurnal warm layers, the simulated surface fluxes are dominated by a diurnal reduction of the mean trade winds.
- A shear-dispersion mechanism induced by the diurnal jet causes anisotropic horizontal dispersion with diffusivities of order 10-100 $m^2\ s^{-1}$.

Corresponding author: Mira Schmitt, `mira.schmitt@io-warnemuende.de`

Abstract

In the tropical ocean, diurnal heating and the formation of atmospheric convection cells associated with local precipitation events, cold pools and wind bursts, have been shown to impact air-sea exchange and the structure of the ocean surface layer. Here, we use a high-resolution regional ocean model, forced by an atmospheric Large Eddy Simulation (LES) that explicitly resolves these processes in a realistic scenario in the tropical north-east Atlantic Ocean, to study their impact on the ocean surface layer and parameterized air-sea fluxes. We find that the oceanic heat loss is, unexpectedly, reduced in the presence of cold pools by on average 30 W m^{-2} due to the higher air humidity, weaker mean winds, and increased cloud cover. Our results also show that the total non-solar heat flux is dominated by the diurnal cycle of the trade winds, rather than by diurnal heating. In the ocean surface layer, local wind bursts, rain layers, and cloud shading induce a strong lateral variability in the strength and depth of Diurnal Warm Layers, questioning the local applicability of available bulk parameterizations. From a series of numerical tracer experiments, we identify a new shear-dispersion mechanism, induced by the Diurnal jet, that is reflected in an extreme anisotropy of horizontal dispersion with diffusivities of order 10-100 m^2 s^{-1}.

Plain Language Summary

We investigate the response of the ocean surface layer to heating by the sun and the presence of cold pools, which are cold pockets of dense air that form when rain evaporates underneath a precipitating cloud, sink and cause wind burst at the ocean surface. To study these processes in a model, high vertical and horizontal resolutions are needed. Our ocean model simulates an area of 200x200 km situated in the trade wind zone, forced at the surface by a high resolution atmospheric simulation. We study the surface fluxes at the air-sea interface and find that the ocean loses less heat underneath cold pools because of higher air humidity, weaker mean winds, and increased cloud cover. Furthermore, we find that the diurnal decrease in mean wind is the most important factor in the strength of the total surface flux. In the ocean surface layer, the diurnal jet, an increase in surface velocity due to the daily heating of the near ocean surface, causes strong horizontal dispersion in a preferred direction. Wind bursts, rain layers, and cloud shading also alter the structure and mixing of the surface layer, but on small time scales and of overall less importance for oceanic transport.

1 Introduction

Forcing from winds, heating, cooling and rainfall have an immediate impact on the oceanic surface layer, controlling the distributions of energy and momentum, and modifying the exchange with the atmosphere. Under weak wind and wave conditions, solar radiation heats up the uppermost layers of the ocean, generating Diurnal Warm Layers (DWLs) with a typical thickness of a few meters (Price et al., 1986; Fairall et al., 1996). Similarly, high precipitation rates change the mixed layer salinity and lead to the formation of thin Rain Layers (RLs) on top of more saline waters.

Both processes, DWLs and RLs, trap momentum through the generation of stable near-surface stratification. This results in an acceleration of these uppermost layers, referred to as "Diurnal jet" or "slippery layer" (Shcherbina et al., 2019). It also isolates the layers underneath this energetic region from surface forcing, thereby suppressing vertical mixing (Hughes et al., 2021; Moulin et al., 2018; Drushka et al., 2014; ten Doeschate et al., 2019). While the impact of these processes on the vertical mixing of the surface layer has been measured and modeled quite extensively, the three-dimensional structure of DWLs and RLs induced by small-scale atmospheric forcing and the consequences for

surface-layer dynamics and horizontal transport have rarely been investigated so far. This will therefore be a central topic of our work.

Vice-versa, the atmosphere may respond to the surface layer conditions, in particular changes in sea surface temperature (SST) (Shevchenko et al., 2023), sea surface salinity (SSS) (Lee & Hong, 2019) and surface velocity (Renault & Marchesiello, 2022). E.g, some studies have found an increase of the heat flux from the ocean to the atmosphere associated with the presence of DWLs, ranging from 2-5 W m^{-2}, estimated from an observational study byMatthews et al. (2014), to 5-25 W m^{-2} on global average from coupled high-resolution global simulations (Shevchenko et al., 2023). Brilouet et al. (2021) find diurnal signals of up to 100 W m^{-2} in their modeling study of atmosphere-ocean interactions in the tropics.

A similar change in surface flux is predicted during rain layer formation due to the presence of atmospheric cold pools (Shackelford et al., 2022). The evaporation of rain drops inside atmospheric convection cells induces a downward motion of cold air, generating atmospheric cold pools with a lateral scale of $\mathcal{O}(10)$ km. These regions of cold air spread out radially when reaching the ocean surface, thereby triggering wind bursts. There is evidence that both wind bursts and cold air lead to an increase in latent and sensible heat fluxes towards the atmosphere (Brilouet et al., 2023). However, most model studies lack the resolution needed in both atmosphere and ocean to resolve these small-scale processes. It therefore remains unclear how the complex patterns associated with atmospheric convection impact the ocean surface layer and affect ocean surface fluxes under realistic conditions.

Here, we use a ultra high-resolution, realistic atmospheric Large Eddy Simulation that explicitly resolves shallow atmospheric convection in a tropical region that was the focus of the recent EUREC^{4}A field campaign (Bony et al., 2017; Stevens et al., 2021). From this simulation, we derive the surface forcing fields to run a high-resolution regional ocean model, which we use to investigate the imprint of small-scale atmospheric features on the three-dimensional structure of the ocean surface layer and atmosphere-ocean fluxes. This is the first study that can quantitatively evaluate these small-scale processes, typically not resolved, in a realistic setting over a large area. Section 2 introduces the atmospheric simulations and the ocean model. Section 3 then focuses on the influence of the above mentioned processes on the exchange between ocean and atmosphere. In Section 4, we discuss the influence of DWLs, RLs and wind bursts on vertical mixing and horizontal dispersion in the surface layer, before we draw some conclusions in Section 5.

2 Model Formulation

2.1 The Atmospheric Forcing

The atmospheric forcing fields were derived from a Large Eddy Simulation (LES) for the tropical North-West Atlantic Ocean (Fig. 1a), based on the ICOsahedral Non-hydrostatic (ICON) model (Schulz & Stevens, 2023; EUREC4A community, 2023). The model follows the setup described in detail in Dipankar et al. (2015) and was initially validated through a set of nested simulations over Germany in Heinze et al. (2017). It runs on an icosahedral grid with a very high resolution of 312 m, therefore requiring neither deep nor shallow convection to be parameterized. Also, no subgrid-scale cloud fraction parameterization is necessary. The 312 m simulation is one-way nested into a 624 m ICON LES, with the SST interpolated continuously from hourly ERA5 SKT data (see Schulz and Stevens (2023)). The 624 m simulation is initialized and forced hourly by a storm-resolving simulation (ICON-SRM) with 1.25 km horizontal resolution. More details on the models can be found in Schulz and Stevens (2023).

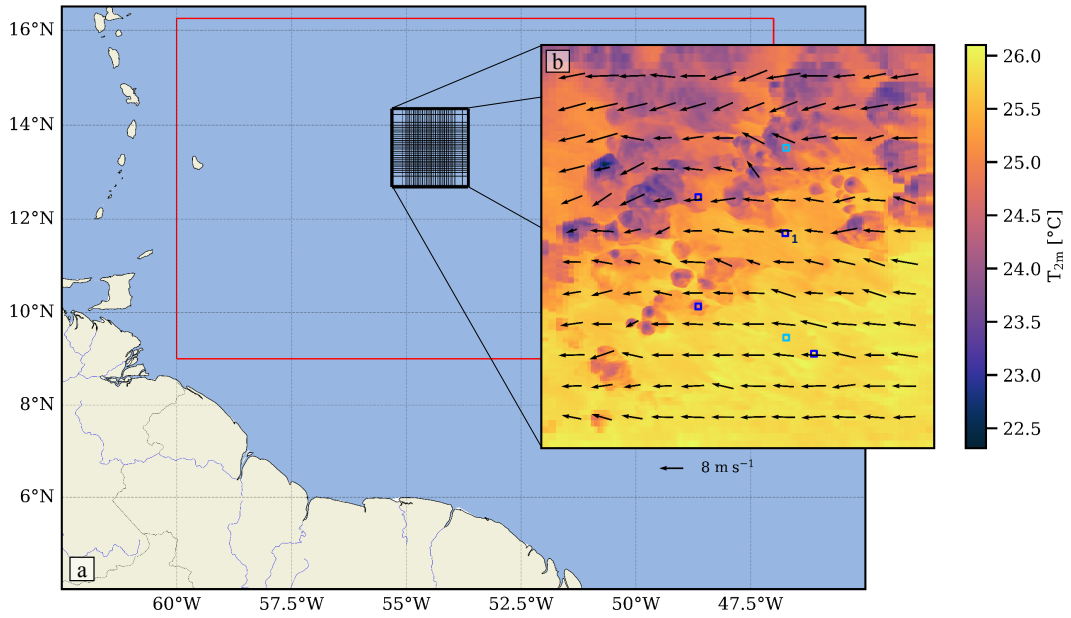

Figure 1. Overview map showing the size and location of the model domains off the coast of South America. The black box in (a) represents the ocean model grid with an increase in grid size towards the boundaries (only every 10th grid line shown). The red box marks the boundary of the ICON-LES with 312 m resolution. The inset (b) shows an enlarged view of the ocean model domain with an example snapshot of the air temperature at 2 m height on 8 February at 09:50 local time. Black arrows in (b) show the wind speed at 10 m above the surface, representative of the constant trade winds that were present during the entire simulation period. Dark and light blue squares in (b) mark the initial locations of the near-surface tracers discussed in Section 4.

The LES was designed to complement the EUREC^{4}A field campaign (Bony et al., 2017; Stevens et al., 2021), focusing on the interplay between clouds and convection in the downstream winter trades of the tropical North Atlantic during January-February 2020. Comparisons to observations in Schulz and Stevens (2023) showed that the 312 m ICON-LES only slightly underestimates the observed average cloud amount and reliably captures the variability and the diurnal cycle of the clouds. Precipitation was found to be overestimated, but the variability was in good agreement with the observations. For the study presented here, a sub-region of the 312 m LES with a size of ∼200x200 km (see black square in Fig. 1a) was selected to force a high-resolution numerical ocean model for the 8-day period from 1 February 2020 00:00 UTC to 8 February 2020 00:00 UTC.

Local time corresponds to UTC-4 h with the solar maximum at 11:30 local time. Characteristic of this time frame are solar radiation maxima of 800 W m^{-2}, constant easterly trade winds ranging typically from 4 to 10 m s^{-1} (the arrows in Fig. 1b show an example of the wind field), and small, frequently occurring atmospheric cold pools associated with sporadic wind bursts and precipitation events with rain rates of 4-18 mm h^{-1}, lasting for an hour or less.

2.2 The Ocean Model

In order to efficiently simulate the response of the ocean surface layer to the high-resolution atmospheric forcing, a custom configuration for the open-source General Estuarine Transport Model GETM (`www.getm.eu`) was designed. GETM solves the shallow-water Boussinesq equations with an explicit free surface, coupled to transport equations for temperature and salinity, on a surface-following high-resolution numerical grid. The model domain covers the area 12.65-14.35°N and 55.35-53.65°W (see Fig. 1a). Inertial periods in this area range from 54.6 h ($f = 0.32{\cdot}10^{-4}$ s^{-1}) to 48.4 h ($f = 0.36{\cdot}10^{-4}$ s^{-1}). The central part between 55-54°W and 13-14°N is resolved by 430 m. Towards the lateral boundaries, the resolution is linearly coarsened to 3.9 km. Since high-resolution boundary data were not available, double periodic boundary conditions are applied. This type of boundary conditions, combined with the gradually coarsening numerical grid, turned out to be sufficient to exclude any significant impact of spurious boundary effects on air-sea fluxes and small-scale processes in the ocean surface layer that were the focus of our study. To reliably resolve the complex vertical structure of DWLs and RLs (Schmitt et al., 2024), the upper 200 m of the ocean are simulated by 300 layers with the vertical resolution gradually increasing from 0.13 m at the surface to 1.43 m at depth. The lower boundary is sufficiently below the surface mixed layer and the pycnocline to not have a significant effect. In this study, the model time step is 1 min and the temporal resolution of atmospheric data 5 min. Details of the numerical implementation can be found in Burchard and Bolding (2002) and Klingbeil et al. (2018).

We follow the usual convention that u and v denote the velocity components in the zonal and meridional directions, respectively, and that z is the vertical coordinate (positive upward) with $z = 0$ at the surface. The model is initialized with horizontally uniform temperature and salinity profiles based on the horizontal average of the HYCOM + NCODA Global 1/12° analysis data (HYCOM Consortium, 2024) between 13-14°N and 55-53°W on 1 February 2020 at 00:00 UTC. Fig. 2 shows the initial conditions, suggesting a mixed layer of approximately 40 m depth, capped by a shallow halocline. The rationale behind these horizontally homogeneous initial conditions is that they allow us to exclusively focus on the imprint of the small-scale atmospheric forcing on the atmosphere-ocean fluxes and small-scale processes in the ocean surface layer. These effects would have been more difficult to identify from a model initialized with more complex hydrographic fields, including, e.g., mesoscale and submesoscale features.

The vertical turbulent diffusivities of momentum, ν_t, and tracers, ν_t^Θ, are computed from an algebraic second-moment turbulence closure, based on the turbulence kinetic

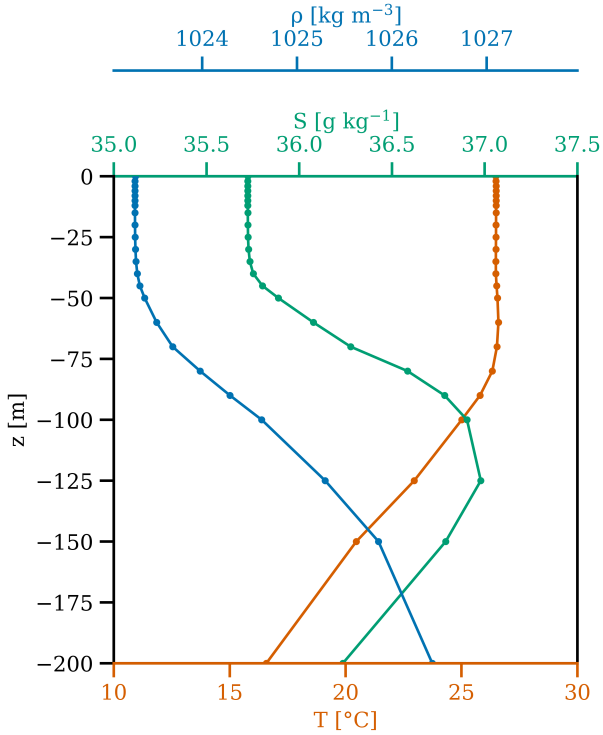

Figure 2. The initial profiles of temperature, salinity and density.

energy, k, and dissipation rate, ε, from a $k-\varepsilon$ two-equation turbulence model (Umlauf & Burchard, 2005; Canuto et al., 2001). Technically, GETM is coupled to the General Ocean Turbulence Model (GOTM; `http://www.gotm.net`) that is described in detail in Umlauf et al. (2005). In the context of this work, it is worth pointing out that a recent high-resolution numerical study of Schmitt et al. (2024) showed, by comparison with LES of the ocean surface layer, that this type of turbulence model provides an excellent representation of the vertical structure and dynamics of DWLs.

The horizontal diffusivity of momentum, K_{sg}, is determined from a Smagorinsky-type model of the form

$$K_{\mathrm{sg}} = C_{\mathrm{M}} \Delta x \Delta y \sqrt{(\partial_x u)^2 + 0.5(\partial_y u + \partial_x v)^2 + (\partial_y v)^2} \tag{1}$$

where Δx and Δy are the horizontal grid resolutions in the zonal and meridional directions, respectively. The constant $C_{\mathrm{M}} = 0.11$ is related to the constant Sm in Tab. 1 of Fox-Kemper et al. (2008) via $C_{\mathrm{M}}/\sqrt{2} = (Sm/\pi)^2$ and thus equivalent to $Sm = 0.88$, which is close to their selected $Sm = 1$. Based on the horizontal momentum diffusivity in (1), we computed the horizontal diffusivities of heat and tracers by assuming a constant horizontal Prandtl number, $Pr_t = 2$, as in Holt and James (2006). Simulations with $Pr_t = 1$ showed no significant differences.

2.3 Computation of the Air-Sea Fluxes

The wind stress components, τ_x^w and τ_y^w, and the non-solar heat flux, Q_{ns}, are computed from the Coupled Ocean–Atmosphere Response Experiment (COARE) version 3.0 bulk algorithm (Fairall et al., 2003; Kara et al., 2005). Although these parameterizations are a standard in most ocean modeling applications, they are briefly summarized in the following to support the interpretation of the results presented below.

The non-solar surface heat flux Q_{ns} is defined as pointing downwards (positive values indicate ocean heating). Q_{ns} is the sum of the sensible heat flux Q_{sen}, the latent heat flux Q_{lat}, and the net long-wave radiation Q_{lw}:

$$Q_{\mathrm{ns}} = Q_{\mathrm{sen}} + Q_{\mathrm{lat}} + Q_{\mathrm{lw}} \, . \tag{2}$$

The sensible heat flux acts to reduce the gradient between the SST and the 10-m air temperature T_a:

$$Q_{\mathrm{sen}} = \rho_a c_{pa} C_H U_{10} (T_a - \mathrm{SST}) \, , \tag{3}$$

where ρ_a is the air density, c_{pa} the specific heat of air, C_H the transfer coefficient of sensible heat and $U_{10} = (u_{10}^2 + v_{10}^2)^{1/2}$ the wind speed (relative to the ocean surface currents) at 10 m above sea surface with $x-$ and $y-$components u_{10} and v_{10} (Fairall et al., 2003; Kara et al., 2005).

Similarly, the latent heat flux has a tendency to reduce the gradient in humidity between the ocean surface and the atmosphere via moisture evaporation:

$$Q_{\mathrm{lat}} = -L \rho_{\mathrm{fw}} E \, , \tag{4}$$

where L is the latent heat of evaporation, ρ_{fw} the density of fresh water, and E the rate of evaporation. Expressed in bulk parameters, this becomes

$$Q_{\mathrm{lat}} = \rho_a L C_L U_{10} (q_a - q_s) \tag{5}$$

with the transfer coefficient of latent heat C_L, the specific humidity q_a at T_a, and the saturated humidity q_s at SST (Fairall et al., 2003; Kara et al., 2005). Lastly, the net long-wave radiation is the combination of the outgoing and incoming long-wave radiation. It typically tends to cool the ocean and is assumed proportional to $\mathrm{SST}^4 - T_{\mathrm{rad}}^4$. Here, T_{rad} refers to the effective radiative temperature of the atmosphere, which includes adjustments for the effects of cloud cover, atmospheric humidity and dew point depression on T_a (Josey et al., 2003).

The surface short-wave net radiation Q_s^0 is calculated based on the fractional cloud cover C (here derived from the atmospheric LES), following the model by Rosati and Miyakoda (1988):

$$Q_s^0 = Q_{\mathrm{tot}} (1 - 0.62C + 0.0019\beta)(1 - \alpha) \, , \tag{6}$$

with the total radiation, Q_{tot}, reaching the surface under clear skies, the solar noon altitude, β, and the albedo, α. For the penetration of short wave radiation into the ocean, we use the two-band absorption model of Paulson and Simpson (1977),

$$Q_s(z) = Q_s^0 \left[A e^{z/\eta_1} + (1 - A) e^{z/\eta_2} \right] \, , \tag{7}$$

where η_1 and η_2 are attenuation lengths representing the long-wave and short-wave bands, respectively, while A describes the relative amount of red light incident on the sea surface. In this work, we prescribed $A = 0.65$, $\eta_1 = 0.8$ m and $\eta_2 = 19$ m to approximate a 1% light level at 25 m depth, shown to be characteristic of the region (Pitarch et al., 2021).

3 Impact on Air-Sea Fluxes

The flux formulas presented in the previous section show that all non-solar heat flux components are directly influenced by changes in temperature caused by DWLs, RLs and cold pools. In addition, both latent and sensible heat fluxes depend on the wind speed and are therefore modified by the wind bursts surrounding cold pools. However, most model studies, even regional ones, do not use an atmospheric forcing with a resolution high enough to include these processes, which is why their effect on the air-sea energy exchange remains unclear. Here, we will therefore analyze the effects of cold pools, DWLs, RLs and wind bursts on the components of the non-solar surface heat flux Q_{ns} over the 8 days modelled in this high-resolution study.

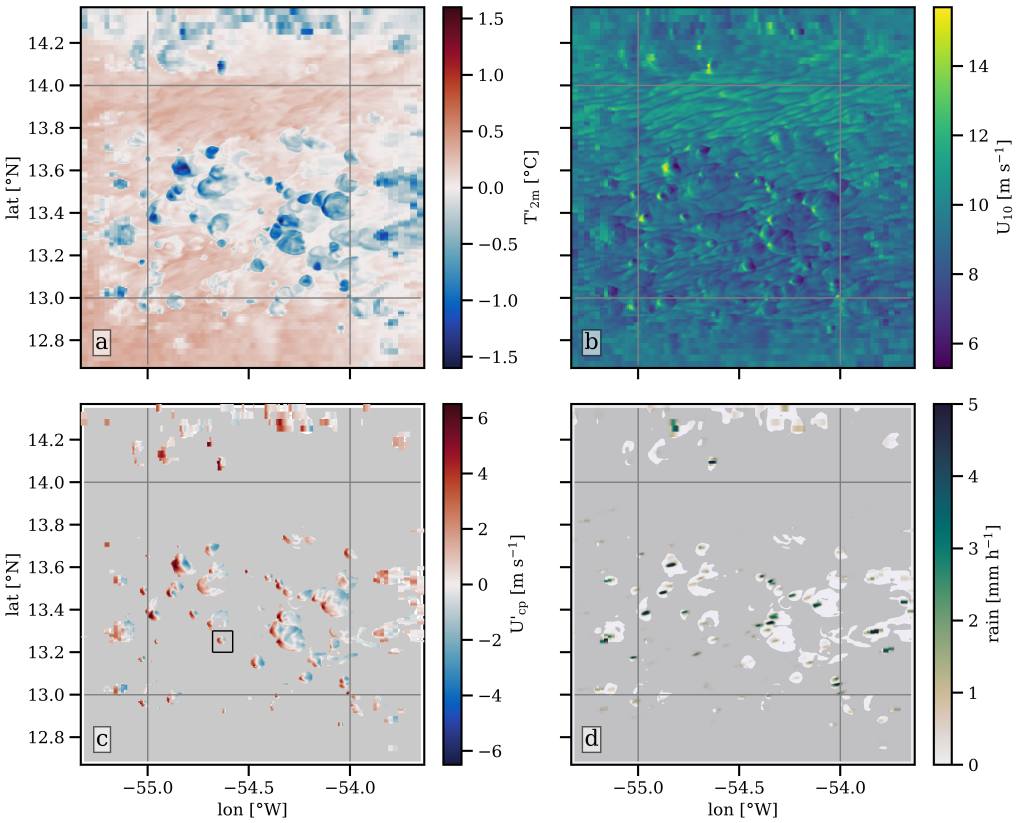

Figure 3. The model domain on 5 February, 23:00 local time with (a) air temperature anomaly T'_{2m}, (b) 10-m wind field, (c) wind anomaly U'_{cp} within the cold pools, and (d) precipitation. Gray areas in panel (c) and (d) show regions blocked by the cold pool mask. Gray vertical and horizontal lines mark the high-resolution part of the domain. The black box in (c) marks the region shown in Fig. 5.

3.1 Spatial Variability

For the definition of cold pool areas, we follow the approach in Brilouet et al. (2023) based on the temperature anomaly,

$$T'_{2m} = T_{2m} - \langle T_{2m} \rangle \ , \tag{8}$$

where $\langle \cdot \rangle$ indicates the mean over the high-resolution central model area between 13-14°N and 55-54°W marked in Fig. 3, and primes the deviation from the mean. Cold pool areas are defined as regions where

$$T'_{2m} < -0.3°C \ . \tag{9}$$

Fig. 3a shows an example snapshot of T'_{2m} on February 5 at 23:00 local time. This example shows a typical situation found at any time in our data set, and represents all the relevant processes we want to discuss. The cold pools are clearly visible as negative temperature anomalies and, if they are in their earlier formation stages, coincide with significant wind bursts and weak rainfall (see Fig. 3b and d).

Considering only the wind in regions with cold pools, we define the cold-pool wind anomaly,

$$U'_{cp} = U_{10} - \langle U_{10} \rangle_{cp} \ , \tag{10}$$

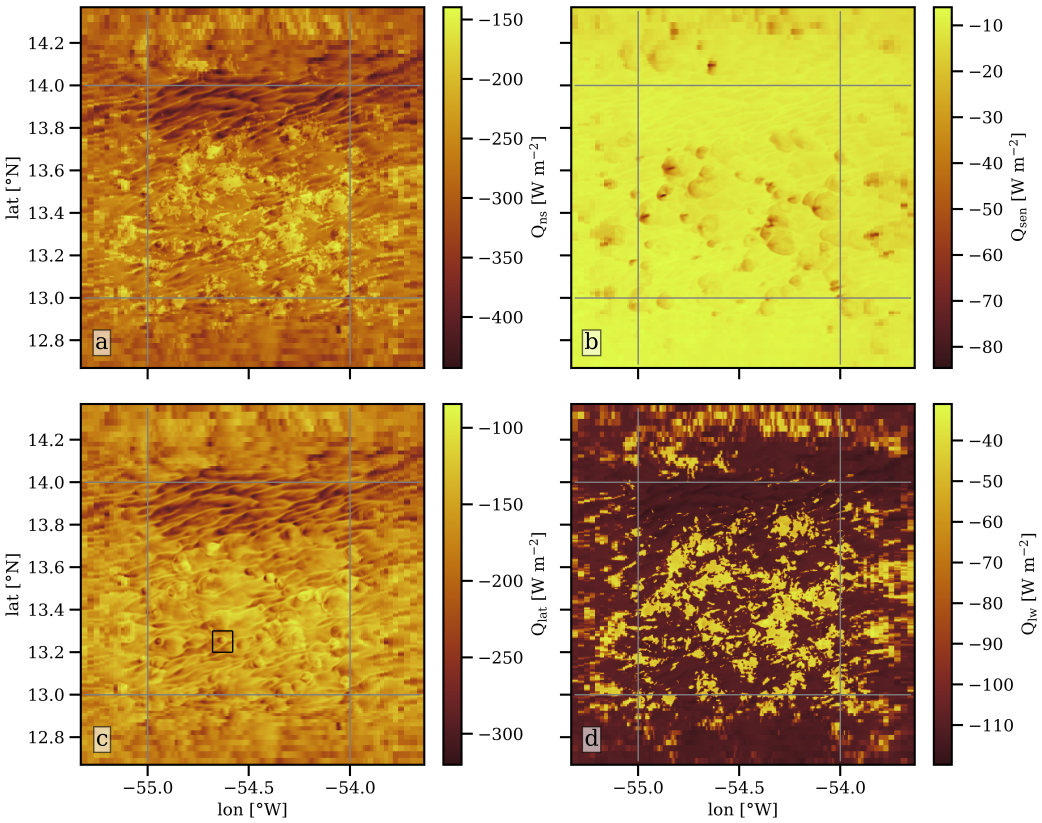

Figure 4. The model domain on 5 February, 23:00 local time with (a) the total non-solar heat flux, (b) sensible heat flux, (c) latent heat flux, and (d) net long-wave radiation. Gray lines mark the center area of high model resolution. The black box in (c) marks the region shown in Fig. 5.

where $\langle U_{10}\rangle_{\mathrm{cp}} = (\langle u_{10}\rangle^2_{\mathrm{cp}} + \langle v_{10}\rangle^2_{\mathrm{cp}})^{1/2}$ is the magnitude of the winds averaged across all cold pool areas. This definition highlights areas of positive and negative wind anomalies within cold pools, which influence the strength of the non-solar heat fluxes underneath cold pools as discussed in more detail in the following. Due to the constant trade winds present in this study, all cold pools are moving from east to west. In the following, we will therefore refer to the western edges as the "leading edges" of the cold pools, and similarly to the eastern edges as the "trailing edges". The largest positive wind anomalies, visible as red areas in Fig. 3c, are located on the leading edges of the cold pools, whereas negative wind anomalies are observed on their trailing edges. This is in line with findings of Brilouet et al. (2023), and can be explained by the superposition of radially expanding wind burst and (nearly) constant easterly trade winds.

The impact of the small-scale atmospheric variability on the surface heat fluxes becomes clearer from Fig. 4, showing Q_{ns} and its components for the same time step. Here, more negative values indicate a stronger oceanic heat loss (cooling). Interestingly, the highest heat losses with the most negative Q_{ns} are found in areas without cold pools in the northern part of the high-resolution central model area, as well as at the leading edges of the cold pools, where trade winds and cold-pool wind bursts are aligned ($U'_{\mathrm{cp}} > 0$ in Fig. 3c).

The largest contribution to Q_{ns} with approximately 60% of the total heat flux comes from the latent heat flux Q_{lat} shown in Fig. 4c. The behaviour of Q_{lat} is similar to that

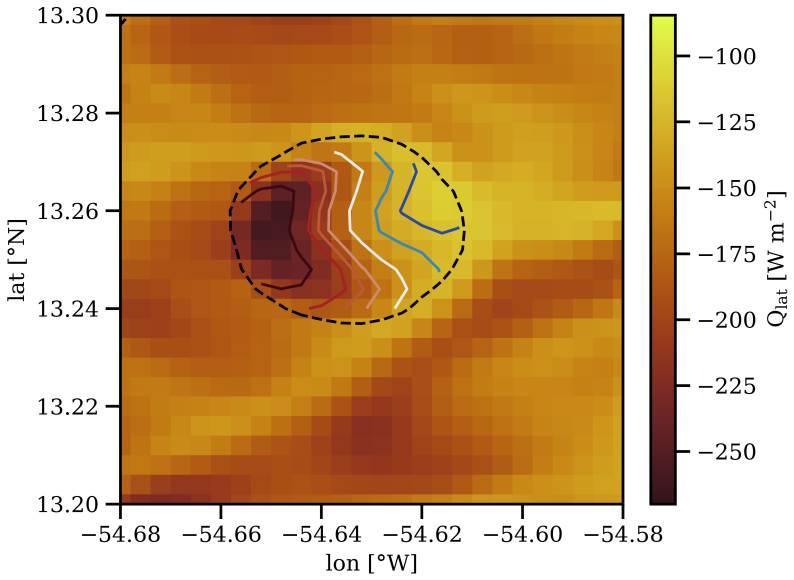

Figure 5. Enlarged view of the latent heat flux from Fig. 4c. The black dashed line marks the outer edge of a cold pool based on the definition in (9). The contour lines show U'_{cp} as in Fig. 3c with red indicating $U'_{cp} > 0$ and blue $U'_{cp} < 0$.

of Q_{ns}, which are both most negative (largest cooling rates) on the leading edges of the cold pools, where cold-pool wind bursts and trade winds align. In these regions, we have $U'_{cp} > 0$, which is reflected in a larger heat loss according to (5). This is evident more clearly from Fig. 5, which shows an enlarged view of a selected cold pool from Fig. 4c, overlaid with the contours of the wind anomaly U'_{cp}. This figure also shows that on the trailing sides of the cold pools, where wind bursts oppose the trade winds, we find $U'_{cp} < 0$ and thus a reduction of the cooling rate. The net effect of these opposing trends inside cold pools is unclear and will be investigated in more detail in the next section.

The long-wave heat flux (Fig. 4d) has the second largest contribution to the total surface heat flux with approx. 35%. The loss of long-wave heat from the ocean is reduced underneath cloud cover, which is shown by the bright yellow pattern in Fig. 4d. Cloud cover mostly coincides with the presence of cold pools, but is not strictly limited to it, as also seen by the presence of high clouds in the time series analysis that follows this section.

Lastly, the sensible heat flux Q_{sen} (Fig. 4b) has the smallest contribution to total Q_{ns} (approx. 5%). The strongest sensible heat loss with the largest negative values is inside cold pool areas. Over the entire model run, the mean atmosphere temperature T_a is approx. 1°C colder than the SST. The drop in air temperature within cold pools therefore leads to a larger T_a−SST difference and increases the sensible heat loss. Largest losses coincide here with the presence of precipitation, often found at the center of the cold pools.

3.2 Diurnal Variability and Net Impact of Cold Pools

To understand the mechanisms determining the temporal variability of the heat fluxes, in the following we analyze the non-solar surface heat flux components within and outside cold pools over the entire model run. We only include the central area of high resolution (marked in Fig. 3 and 4 by the gray square) in this analysis to exclude bound-

ary effects and under-resolved cold pools in the surrounding halo region with gradually expanding grid spacing. Furthermore, we exclude the first 24 hours, i.e. one diurnal cycle, of spin-up time from our analysis.

Fig. 6 shows the mean fluxes over different areas of the central model area. From the first two panels, it becomes clear that the mean $\langle Q_{\mathrm{ns}} \rangle$ is dominated by changes in mean wind speed over the 8 day model run. Throughout the simulation period, SST shows a clear diurnal signal that is indicative for the prevalence of DWLs even during periods with strong winds > 8 m s^{-1} observed in the second half of the simulation period. DWL amplitudes range from 0.1 to 0.4°C and match well with the DWL scaling relations recently derived by Schmitt et al. (2024) (red crosses in Fig. 6a). This scaling, based on Price et al. (1986), calculates DWL depth, bulk temperature and bulk velocity for two points in time, midday and the diurnal maximum, across a large physical parameter space, taking surface fluxes, latitude, waves and water type into consideration. In this simulation, the diurnal maximum occurs between 14:00 and 14:30 local time, which is 2.5 to 3 h after the solar maximum, about half an hour earlier than the predicted timing in Schmitt et al. (2024). The difference could be due to variations in the wind speed, which were not taken into account in the idealized model of Schmitt et al. (2024).

As mentioned earlier, the mean atmosphere temperature T_a is approx. 1°C colder than the SST. For this reason, an increase in the SST due to diurnal warming increases the $T_a - \mathrm{SST}$ difference and is therefore expected to increase the heat loss due to the latent and sensible heat flux components of the total surface flux. However, we observe the opposite instead. This peculiar behavior is explained by the reduction in mean wind speed by 2-3 m s^{-1} during daytime (Fig. 6a), which over-compensates the effect of increased SST according to the transfer functions in (3) and (5). A decrease in wind speed during daytime is a common feature in the trade wind zone and has also been observed during the EUREC^{4}A campaign (Savazzi et al., 2022). The mechanism behind it is not fully understood, but is believed to arise either because of pressure variations, solar atmospheric tides (Ueyama & Deser, 2008), or a stronger organization of the inner tropical convergence zone at nighttime, resulting in stronger trade winds (Ruppert & Hohenegger, 2018). As a result, we can not clearly distinguish the influence of DWLs and the associated diurnal increase in SST on the heat fluxes our simulations.

To systematically investigate the effect of the wind burst triggered by the cold pools on the non-solar heat flux Q_{ns}, we first distinguish between cold pool areas with $U'_{\mathrm{cp}} > 0$ (wind bursts aligned with trade winds) and areas with $U'_{\mathrm{cp}} < 0$ (wind bursts opposing trade winds). Fig. 6b shows that the alignment of wind bursts with the trade wind has a strong effect on Q_{ns}, with an averaged difference of approximately 40 W m^{-2} between cold-pool regions aligned with and opposing the trade winds, respectively. This difference is typically larger than the averaged sensible heat flux shown in Fig. 6c.

However, when averaging over all cold pool areas (blue line in Fig. 6b), the oceanic heat loss due to non-solar fluxes is generally smaller compared to the areas outside of cold pools (green line) by on average 30 W m^{-2}. This is in contrast to Brilouet et al. (2023), who find no clear impact on Q_{ns} for their entire cold pool population or, when looking at only active cold pools, an increase in heat loss of approximately 30 W m^{-2}. In the following, we analyze the reasons for this unexpected decrease we observe by inspecting the different flux components.

The average Q_{lat} in Fig. 6d behaves similarly to the total surface flux, with a clear increase in heat loss in the areas where $U_{\mathrm{cp}} > 0$, However, when averaging over all cold pool areas, there is either no difference to the outside area, or a significant reduction. When averaged over the entire time series, the difference between the blue and the green lines, representing the reduction of oceanic heat loss by Q_{lat} in the presence of cold pools, is 15 W m^{-2}. This reduction is explained by the higher air humidity q_a within the cold pools that decreases evaporation and therefore, according to (5), the magnitude of Q_{lat}.

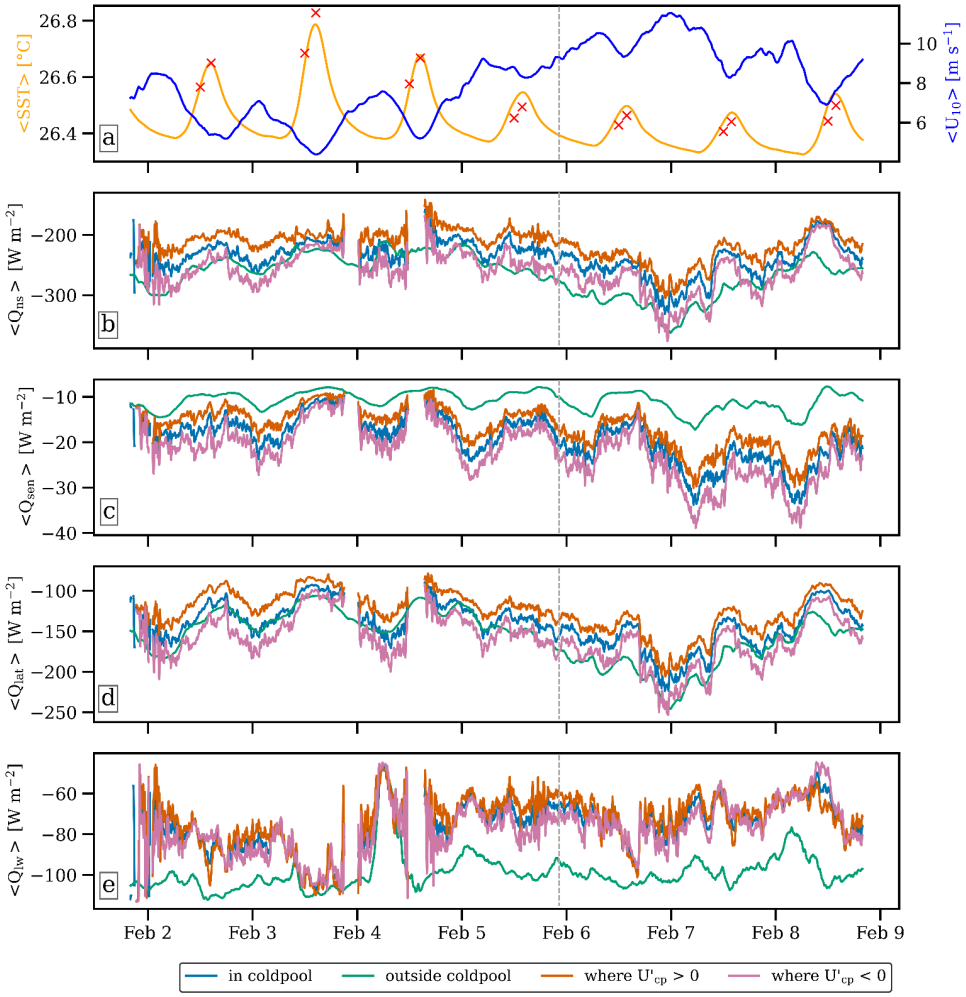

Figure 6. Time series of (a) mean wind and mean SST with scaling estimates from Schmitt et al. (2024) as red crosses, (b) mean non-solar surface heat flux Q_{ns}, (c) mean sensible heat flux Q_{sen}, (d) mean latent heat flux Q_{lat} and (e) mean net long-wave radiation Q_{lw}. Colors in panels (b)-(e) are the means within the cold pools (blue), over the area outside of the cold pools (green), over the area within the cold pools where $U'_{\mathrm{cp}} > 0$ (orange), and over the area within the cold pools where $U'_{\mathrm{cp}} < 0$ (pink). The vertical gray dashed line marks the time point shown in Figs. 3 and 4.

Moreover, in our simulations, the mean wind, which increases heat loss, is higher outside of the cold pool areas because of slackening winds in the wake of a cold pool. This finding is supported by the climatology of trade wind cold pools presented in Vogel et al. (2021), who also note the occurrence of pronounced negative values of the wind speed anomaly after the passage of a cold pool.

Cooling due to the sensible heat flux Q_{sen} (Fig. 6c) is clearly increased within cold pools by an average of 9 W m^{-2} compared to the ambient regions. Here as well, the strongest heat loss is on the leading edge where $U_{\mathrm{cp}} > 0$. In contrast, there is a strong reduction of surface cooling by the net long-wave heat flux Q_{lw} inside cold-pool areas (Fig. 6e) because of the effects of cloud cover and humidity on T_{rad}. The average reduction over all days, i.e. the difference between the green and blue line in panel (e), is 24 W m^{-2}, which cancels out the 9 W m^{-2} heat loss increase of Q_{sen} and leaves a total average oceanic heat loss reduction of 15 W m^{-2} in the presence of cold pools for Q_{lw}+Q_{sen}. As a side note, the overlap of all averages between 4-5 February in Fig. 6e is explained by the presence of high clouds that block nearly the entire model area, independently of the 10-m winds and cold pools regions. This shows that Q_{lw} is not only influenced by cold pools, but also by more complex atmospheric patterns at high altitudes.

Overall, we conclude that the presence of cold pools results in a net reduction of ocean surface cooling associated with the non-solar heat flux Q_{ns}. Three different effects contribute to this surprising behavior: (i) areas with cold pools are characterized by higher humidity, reducing that latent heat loss shown in Fig. 4c and Fig. 6d; (ii) areas with cold pools also have higher cloud cover, increasing atmospheric long-wave back radiation, and therefore reducing the net long-wave heat loss to the ocean as shown in Fig. 4d and Fig. 6e; and (iii) the cold pool areas are typically characterized by lower mean wind speeds in our study, thus reducing the latent heat loss (Fig. 4c and Fig. 6d). The increase in sensible heat loss in the presence of cold pools and the increase on the leading edges due to positive wind anomalies is hereby negligible. In additions to changes in the non-solar heat fluxes, we also observe a reduction in the surface short wave radiation in areas with cold pools by on average 25% due to cloud shading.

4 Impact on Ocean Surface Layer Processes

In addition to changing both the solar and non-solar fluxes at the air-sea interface, the presence of diurnal heating, rain and cold pools can also impact small-scale processes in the ocean surface layer. While the influence of stabilizing DWLs and RLs on vertical processes has been observed and modelled quite extensively (Shackelford et al., 2022; Moulin et al., 2018; Brilouet et al., 2023), the three-dimensional structures and processes that affect mixing and dispersion in the ocean surface layer, requiring high-resolution models and atmospheric forcing fields, has received much less attention. To address this gap, in the following, we will analyze the impact of small-scale atmospheric forcing on transport and mixing in the ocean surface layer.

4.1 Variability of Mixing Coefficients

The example shown in Fig. 7a,b again highlights the extreme small-scale variability in wind forcing and the effect that precipitation has on the surface salinity, where multiple small RLs of varying intensity form. Having investigated the effect that this variability has on the surface fluxes in the previous section, we will now focus on the impact of this forcing on small-scale processes in the ocean surface layer. Fig. 7c shows that wind burst leave a clear imprint on the near-surface horizontal subgrid diffusivity K_{sg} that, according to (1), can be traced back to burst-induced shear in the near-surface currents. Similarly, also the near-surface vertical diffusivity ν_t is increased in areas with high K_{sg} due to an increase in vertical shear instability underneath wind bursts (see Fig. 7d). This increased vertical mixing takes place at the outer edges of the cold pools, while, at the

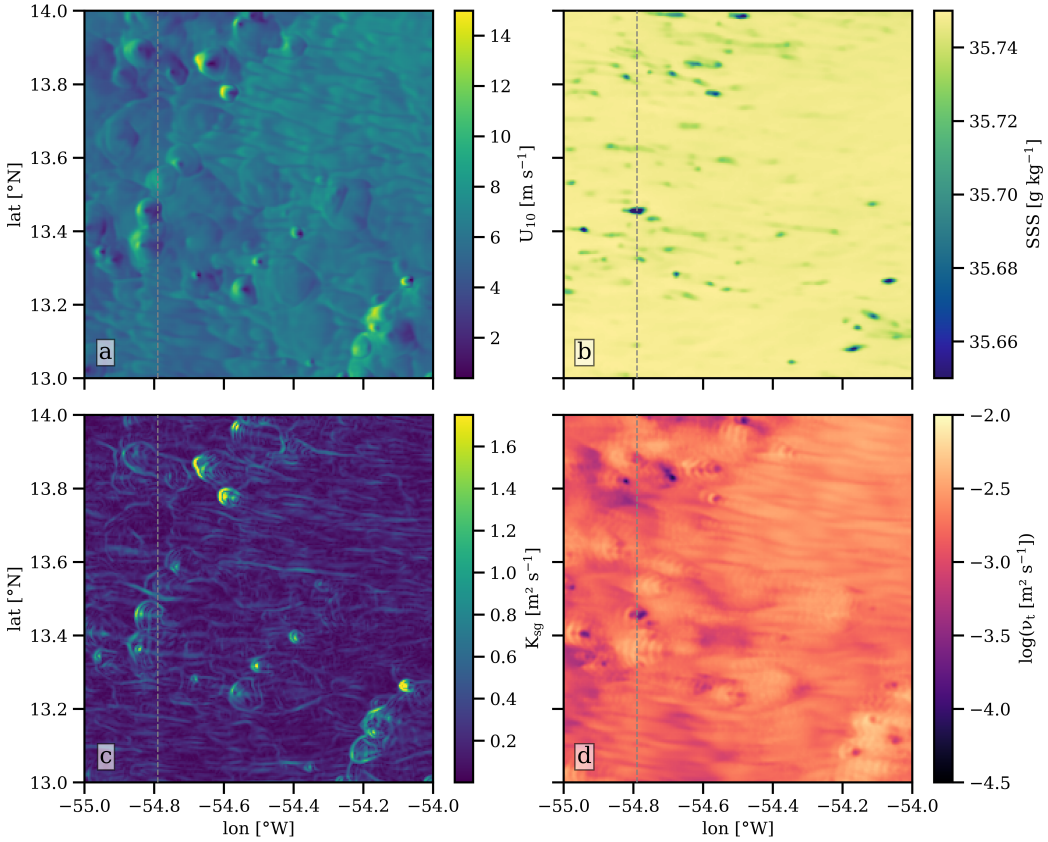

Figure 7. The high-resolution model domain on 2 February, 12:30 local time with (a) wind speed, (b) sea surface salinity, (c) surface horizontal subgrid diffusivity, (d) vertical turbulent diffusivity at $z = -1$ m. Dashed gray lines mark the cross section shown in Fig. 8.

same time, near-surface stratification induced by RLs in the center of the cold pools reduces ν_t. The overall impact of these partly competing effects on horizontal and vertical mixing and dispersion is unclear and will therefore be the focus of the following investigations.

The small-scale atmospheric forcing also leads to an unexpected lateral variability in DWL temperature and thickness distribution, as evident in Fig. 8a that shows a meridional cross-section (indicated by the dashed line in Fig. 7) across our study area. The small-scale variability in the atmospheric forcing is reflected in an extreme variability of the DWL thicknesses from 3 m to 10 m, approximately, and a factor two variability in DWL bulk temperatures. In view of the excellent agreement between regionally averaged DWL bulk parameters and those predicted by available DWL bulk parameterizations (see Fig. 6a), this is a surprising finding, suggesting a limited local applicability of these parameterizations in regions with a strong variability in the atmospheric forcing. The small-scale variability in DWL properties is also directly mirrored in a variability of the horizontal and vertical mixing coefficients (Fig. 8c,d), with possible consequences for ecosystem processes. The impact of the stronger RLs on the mixing coefficients can be clearly discerned (Fig. 8b,d) but, due to the weakness of the precipitation events in our study, only has a small and transient effect in the uppermost part of the surface layer.

It is worth noting that any low-pass filtered surface forcing, which would resemble the typical atmospheric forcing fields used in regional or high-resolution global modeling studies, would not capture the lateral variability discussed above. To investigate the overall impact of the small-scale variability in the surface-layer properties and processes on mixing and dispersion, we conducted several tracer release experiments that will be described in the following.

4.2 Tracer Experiments

Four tracer patches with an initial size of 3.56 km x 3.56 km in the horizontal were released in the surface layer at different locations of the model domain (dark blue squares in Fig. 1b) at the start of the simulation to gain information about the spatial variability of tracer dispersion. Initial tracer concentrations inside these patches were set to $c_0 = 1$ in the upper 30 m of the water column, slightly shallower than the initial mixed layer depth (see Fig. 2). All tracers were vertically mixed over the entire mixed layer depth within the first hour after initialization due to strong nighttime convection, suggesting that their subsequent evolution represents the surface-layer bulk dispersion characteristics. The horizontal scale of the initial tracer patches was chosen to represent a grid size typical for regional and high-resolution global models. Our goal here is to use our ultra high-resolution simulations to gain insights into ocean processes that would be "subgrid" in such coarser-resolution models in terms of both atmospheric forcing fields and ocean surface-layer processes.

Fig. 9a shows an example of the temporal evolution of the (normalized) vertically integrated tracer concentrations $C = \int c\mathrm{d}z / \int c_0 \mathrm{d}z$ for one of the tracer patches over the simulation period of 8 days (all four tracer patches behaved similarly during this period). Here, for greater clarity, the shape of the evolving tracer cloud is approximated by elliptical fits (details below). Despite prevailing winds from easterly and north-easterly directions during the simulation period, we find that all tracer patches were advected north-west, clearly indicating the relevance of Ekman effects. The total advected distance was 47.3 km when averaged over all tracer patches, corresponding to an average advection speed of 0.073 m s^{-1}. The mean advective tracer transport was super-imposed by inertial oscillations with a period $T_f \approx 50$ h and inertial displacements of 2-3 km. Most importantly, however, all tracer patches experienced a strongly anisotropic spreading in the horizontal with the largest spreading rates found along a direction oriented approximately 15-25 degrees to the right of the mean wind direction. In the following, we will

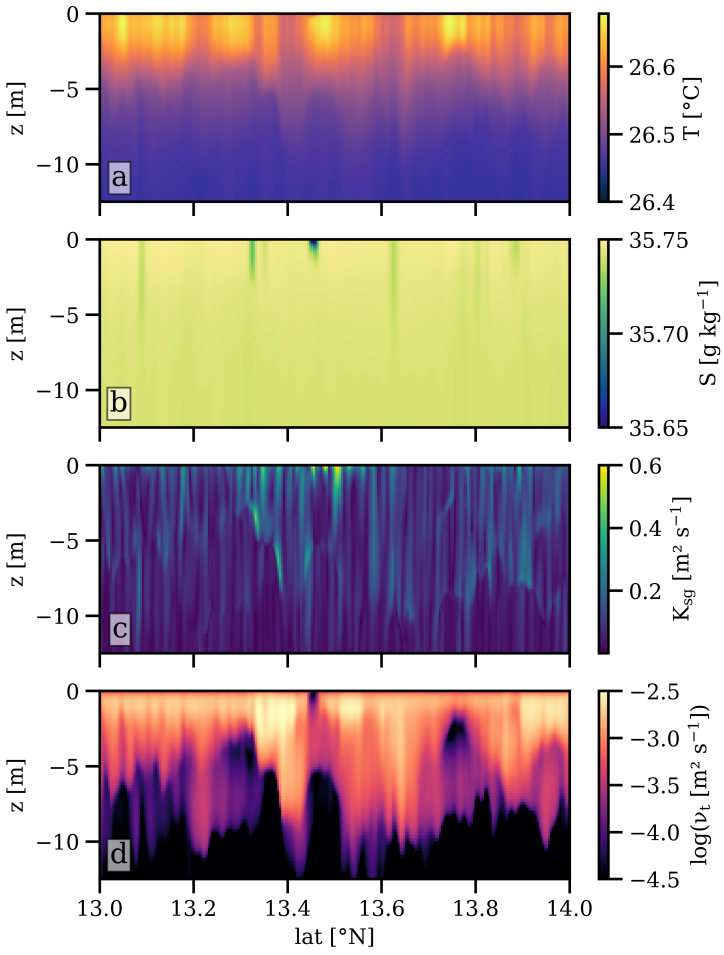

Figure 8. Cross section along 54.8°W with (a) temperature, (b) salinity, (c) horizontal subgrid diffusivity, (d) vertical turbulent diffusivity.

analyze the reasons for this anisotropic spreading and estimate the corresponding horizontal diffusivities.

Our analysis will be based on the equation for two-dimensional anisotropic diffusion of the (normalized) vertically-integrated tracer concentration,

$$\frac{\partial C}{\partial t} - \frac{\partial}{\partial \hat{x}}\left[K_{\hat{x}}\frac{\partial C}{\partial \hat{x}}\right] - \frac{\partial}{\partial \hat{y}}\left[K_{\hat{y}}\frac{\partial C}{\partial \hat{y}}\right] = 0\ , \tag{11}$$

where $K_{\hat{x}}$ and $K_{\hat{y}}$ are the spatially constant diffusivities in the time-dependent directions of $\hat{x}$ and $\hat{y}$ (that are generally different from the zonal and meridional directions x and y). Assuming that the normalized tracer concentration in each patch has a total mass M and a Dirac delta distribution at time $t = 0$ (our initial tracer distributions are only an approximation to this), the diffusion equation in (11) has a known solution of the form

$$C = \frac{M}{2\pi\sigma_{\hat{x}}\sigma_{\hat{y}}}\exp\left(-\frac{\hat{x}^2}{2\sigma_{\hat{x}}^2} - \frac{\hat{y}^2}{2\sigma_{\hat{y}}^2}\right)\ , \tag{12}$$

corresponding in shape to an anisotropic Gaussian distribution in $\hat{x}$ and $\hat{y}$ with variances $\sigma_{\hat{x}}^2 = 2K_{\hat{x}}t$ and $\sigma_{\hat{y}}^2 = 2K_{\hat{y}}t$, respectively. From these relations, it is clear that the diffusivities can be computed from the observed spreading rates according to

$$K_{\hat{x},\hat{y}} = \frac{1}{2}\frac{\partial \sigma_{\hat{x},\hat{y}}^2}{\partial t}\ . \tag{13}$$

To obtain estimates for the variances $\sigma_{\hat{x}}^2$ and $\sigma_{\hat{y}}^2$ (and thus the diffusivities $K_{\hat{x}}$ and $K_{\hat{y}}$), we fitted a 2D Gaussian distribution to the (normalized) depth-integrated tracer concentration C for each time step. The fitting algorithm uses a non-linear least-squares approach, which provides estimates for $\sigma_{\hat{x}}$ and $\sigma_{\hat{y}}$, the positions of the centers of the tracer patches (reflecting bulk advection), and the rotation angles of the ellipses' major axes.

The time evolution of the fitted 2-σ confidence ellipses for Tracer 1 (marked with "1" in Fig. 1b) is shown in Fig. 9a as an example for all tracers. Since the tracer is released as a square patch initially, the Gaussian distribution fit starts off as a circle with equal standard deviations $\sigma_{\hat{x}} = \sigma_{\hat{y}}$. Within the next days, however, the ellipses start to stretch and rotate out of the wind direction, while the entire tracer patch is advected north-west. Over the 8 days of the model run, Fig. 9b indicates very little growth in the $\hat{y}$-direction when compared to the strong spreading observed along the major $\hat{x}$-axis. The growth of $\sigma_{\hat{x}}$ occurs intermittently with the largest spreading rates observed each day during the afternoon and evening hours, followed by a nighttime plateau with strongly reduced (and sometimes even slightly negative) spreading rates.

To investigate this peculiar spreading behavior in more detail, we focus on the tracer distributions during two selected points in time on 2 February, on which the diurnal variability of tracer spreading was particularly pronounced: (i) in the afternoon at 16:00, when the tracer spreading was strongest and (ii) at midnight, when the tracer spreading had stopped and the nighttime plateau in the spreading curves was reached. These two points in time are marked in Fig. 9b.

Fig. 10a,b shows the surface tracer concentrations, c_s, at these two points in time. Also shown are, for comparison, the Gaussian fits to the tracer clouds at the surface and at $z = -30$ m. At 16:00, the Gaussian ellipses indicate a strong relative displacement by approximately 2.4 km between the tracer patches at the surface and at 30 m depth, respectively, along the ellipse's major axis. The reasons for this displacement become clearer from Fig. 10c, showing the vertical distributions of the tracer concentrations and current velocities interpolated onto the major axes from Fig. 10a. Fig. 10c shows a clear signature of the diurnal jet in the upper approximately 10 m, indicating the trapping of momentum inside the DWL that is still fully developed at 16:00 (see SST anomalies

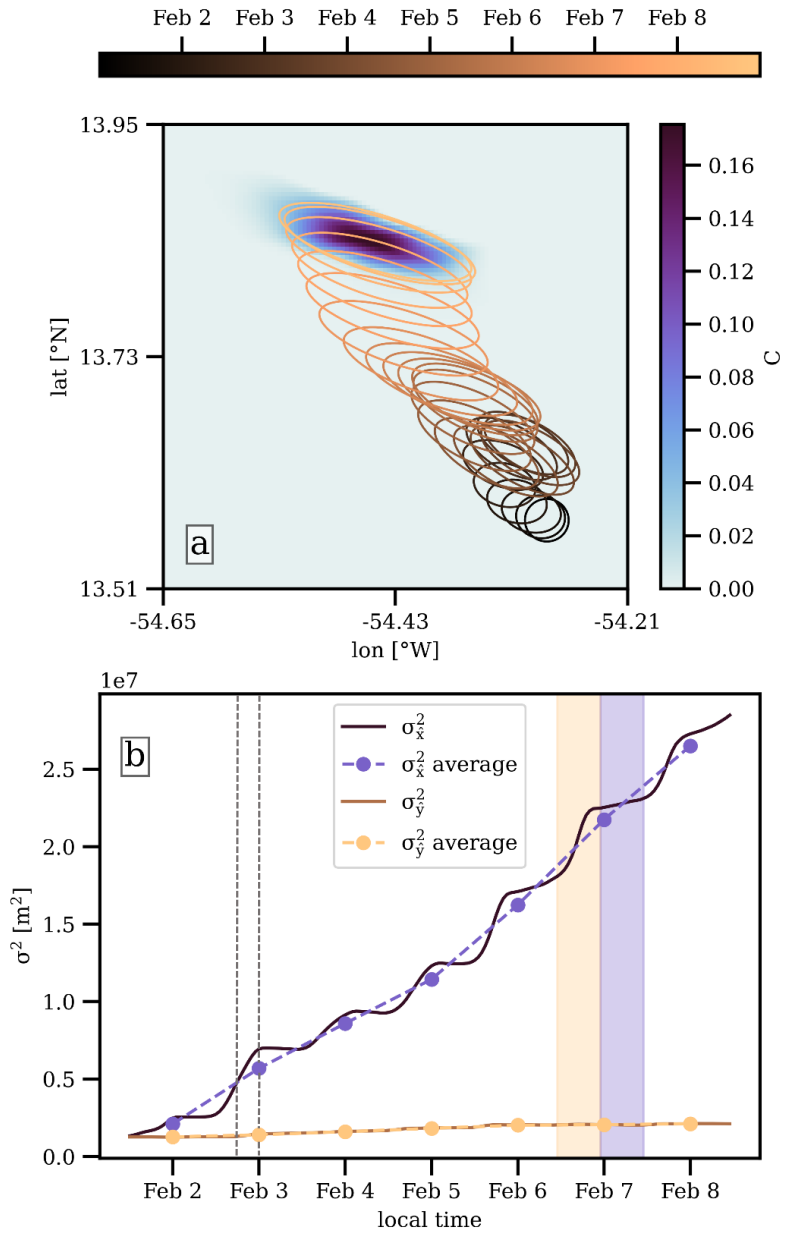

Figure 9. Evolution of Tracer 1 (see Fig. 1b) with (a) depth integrated normalized concentration on 8 February, 12:00 local time and evolution of fitted 2-σ tracer isocontours according to (12) over the entire time range, (b) time series of variances in major ($\hat{x}$) and minor ($\hat{y}$) axes directions with 24 h averages marked. Gray vertical lines mark the selected time points in Fig. 10, yellow and blue areas mark daytime and nighttime spreading periods discussed in the text.

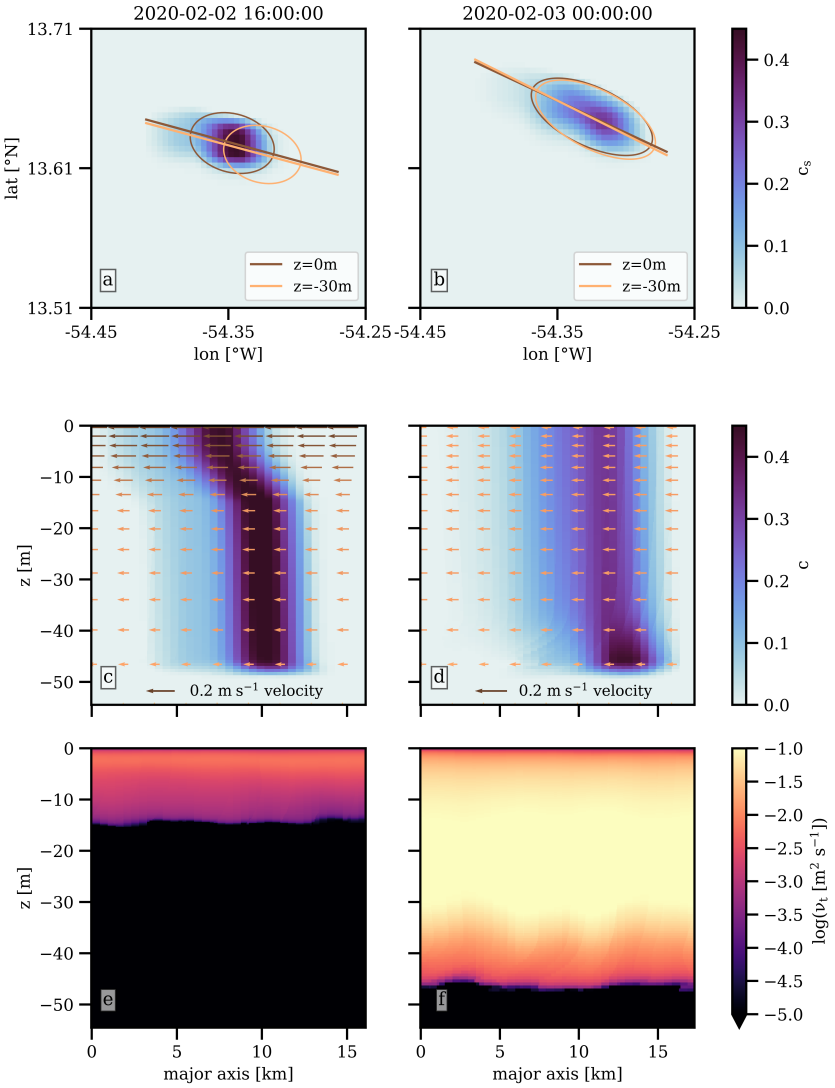

Figure 10. Afternoon and night snapshots of (a,b) surface tracer concentrations and Gaussian fits at two depths; (c,d) tracer concentrations and (e,f) vertical diffusivities along the major axes of the tracer distributions. Arrows in (c,d) show the velocity field.

in Fig. 6a). In our simulations, the diurnal jet forms at approximately 10:00 local time, and reaches its maximum velocity roughly 6 hours later, at around 16:00. The observed horizontal displacement of surface tracers by 2.4 km after 6 hours requires an average bulk velocity of 0.11 m s^{-1} relative to the underlying waters, which is consistent with the velocities shown in Fig. 10c. At the same time, vertical mixing is confined to the DWL (Fig. 10e), suggesting a decoupling of the laterally advected tracer inside the DWL from the underlying waters.

While the tracer distributions at any given depth level are hardly distorted, this differential advection process is clearly reflected in a stretching of the vertically integrated tracer patch in the direction of the diurnal jet, or, mathematically, in an increase in $\sigma_{\hat{x}}$, as observed in Fig. 9b. In the evening hours, the radiative buoyancy forcing ceases, and eventually nighttime convection starts to support wind-driven near-surface turbulence, and thus entrainment and DWL deepening (see Schmitt et al., 2024). As the vertical diffusivity increases (Fig. 10f), the DWL expands downward and the tracer is homogenized across the entire surface layer. Vertical mixing, however, does not change the horizontal distribution of the vertically integrated tracer concentrations, which explains the nighttime plateau in the horizontal spreading rates found in Fig. 9b.

In addition to this stretching of the tracer patch, Fig. 9a,b also shows a rotation of the major axis of the tracer patch to the right of the mean wind direction (average winds during the lifetime of the DWL on this day were almost perfectly from East). As shown by the following simple computation, this angle reflects the Ekman-induced veering of the diurnal jet out of the wind direction. It is easy to show (see, e.g., Hughes et al., 2020) that the transports into the wind direction, $\mathcal{U}$, and to the right to of the wind, $\mathcal{V}$, are given as

$$\mathcal{U} = \frac{\tau^w}{\rho_0 f}\sin(ft) \qquad \text{and} \qquad \mathcal{V} = \frac{\tau^w}{\rho_0 f}\left[\cos(ft) - 1\right] \ , \tag{14}$$

where τ^w is the wind stress and ρ_0 a constant reference density. Integrating the transports in (14) in time yields an expression for the angle ϕ between the wind stress and the direction in which the tracer has been displaced by the diurnal jet,

$$\tan\phi = \frac{\int_0^{\hat{t}} \mathcal{V}\mathrm{d}t}{\int_0^{\hat{t}} \mathcal{U}\mathrm{d}t} = \frac{\sin(f\hat{t}) - f\hat{t}}{\cos(f\hat{t}) - 1} \ , \tag{15}$$

where $\hat{t}$ is the time that has passed since the formation of the jet. The expression in (15) predicts $\phi = 13$ degrees for $\hat{t} = 6$ hours. The observed angle at which the near-surface tracer cloud was displaced between the formation of the diurnal jet at 10:00 and 16:00 (Fig. 10a) was 14.8 degrees, in fair agreement with the prediction. Eq. (15) predicts a nearly linear increase of ϕ with time, suggesting an increasing veering of the ellipse's major axes out of the wind direction also at later times. This is consistent with increased rotation angle visible at midnight (Fig. 10b) after the DWL has ceased to exist.

Overall, the above results show that horizontal tracer spreading is largely a result of a DWL-induced shear-dispersion mechanism, combining differential tracer advection due to the presence of DWLs during daytime with nighttime vertical mixing. To quantify this process, we applied a discretized version of (13) based on the 24-h averaged variances shown in Fig. 9b. The results, averaged over all four tracer patches, are compiled in Tab. 1, showing that $K_{\hat{x}}$ is $\mathcal{O}(10)$ m^2 s^{-1}, i.e. 10-30 times larger than $K_{\hat{y}}$, emphasizing the strongly anisotropic nature of DWL-induced tracer dispersion.

There is also a significant increase in $\sigma^2_{\hat{x}}$ during nighttime on 6-8 February when wind speeds exceeded 8 m s^{-1} (see Fig. 9b). This nighttime spreading is obviously not DWL-induced and can be traced back Ekman-driven shear-dispersion in the unstratified near-surface region. We computed a diffusivity of $K_{\hat{x}} = 7.3$ m^2 s^{-1} based on the increase of $\sigma_{\hat{x}}$ from 6 February 23:00 to 7 February 11:00 (blue area in Fig. 9), when Ekman-driven shear dispersion was particularly pronounced. This value is almost an order of

Table 1. 24-hour averaged horizontal diffusivities, averaged over all 4 tracers patches shown in Fig. 1b.

	$K_{\hat{x}}$ [m^2 s^{-1}]	$K_{\hat{y}}$ [m^2 s^{-1}]
Day 1	18.0	0.85
Day 2	17.66	0.81
Day 3	16.47	1.53
Day 4	28.71	1.4
Day 5	29.53	0.5
Day 6	23.68	0.23

magnitude smaller than the DWL-induced $K_{\hat{x}} = 55.6$ m^2 s^{-1} for the previous day (yellow area, 11:00-23:00 local time), underlining the relevance of DWLs for lateral dispersion in the surface layer.

For a simple parameterization of the diffusivities caused by the diurnal jet over a period of 24 h, we suggest

$$K_{\hat{x}} = \frac{1}{2}\frac{\partial \sigma^2}{\partial t} = \frac{1}{2}\frac{\mathrm{d}(l/2)^2}{\mathrm{d}t} = \frac{1}{8}\frac{(l+\Delta l)^2 - l^2}{\Delta t} = \frac{1}{8}\frac{\Delta l(2l+\Delta l)}{\Delta t} \approx \frac{l}{4}\frac{\Delta l}{\Delta t}\,, \tag{16}$$

where l is the length of the major axis and Δl the increase of l caused by the diurnal jet transport over $\Delta t = 24$ h (in the last step, we assumed $\Delta l/l \ll 1$). Δl can computed if the representative jet bulk velocity $\overline{v}$ and duration $\hat{t}$ are known. For example, $\overline{v} = 0.05$ m s^{-1} and $\hat{t} = 12$ h with an initial $l = 4$ km (similar to Day 2 shown in Fig. 10) gives $K_{\hat{x}} = 25$ m^2 s^{-1} which is close to the fitted $K_{\hat{x}} = 18.0$ m^2 s^{-1} in Tab. 1. If the bulk velocity is unknown, it can be approximated using the DWL bulk scaling in Schmitt et al. (2024) that incorporates the surface buoyancy forcing, latitude and water clarity. While this simply analysis provides a robust order-of-magnitude estimate of the tracer spreading rates along the main axis, the minor-axis spreading rates are more difficult to quantify. As small-scale processes not associated with the diurnal jet do not have a significant impact on tracer spreading, as shown in the following, it is likely that tracer spreading in this direction is associated with the veering of the diurnal jet out of the wind direction after DWL formation.

In order to quantify the impact of the small-scale atmospheric variability (especially regarding the effect of cold pools and associated wind bursts and RLs) on horizontal tracer dispersion, we conducted another short-term tracer release on 8 February between 08:00 and 20:00 local time. This period was characterized by an unusual cold pool distribution, which turned out to be ideal for this purpose. From midday to late evening, all cold pools remained confined to the northern half of the model domain while the southern part of the domain was cloud- and cold pool-free (see Fig. 1). One tracer was therefore released in the northern part of the domain where it experienced several cold pool and wind burst crossings, while, for comparison, the other tracer was released in the southern part where it was not influenced by any cold pools (see the light blue squares in Fig. 1b).

Despite these different settings, there was no visible difference in tracer patch evolution, and calculated 12-hour average horizontal diffusivities based on the fitted normal distributions (not shown) resulted in very similar values. We found the explanation for this in the horizontal resolution of our model and the time scales of the relevant processes. Fig. 11 shows two snapshots of the northern tracer patch and the surface velocities 10 minutes apart during the crossing of a cold pool. While the wind bursts associated with the cold pool showed a clear imprint on the surface velocities, the lifetime of these velocity anomalies, corresponding to the duration of the cold-pool crossing, was too short to have a significant effect. On average, the burst-induced velocities of $\mathcal{O}(0.1)$ m s^{-1}

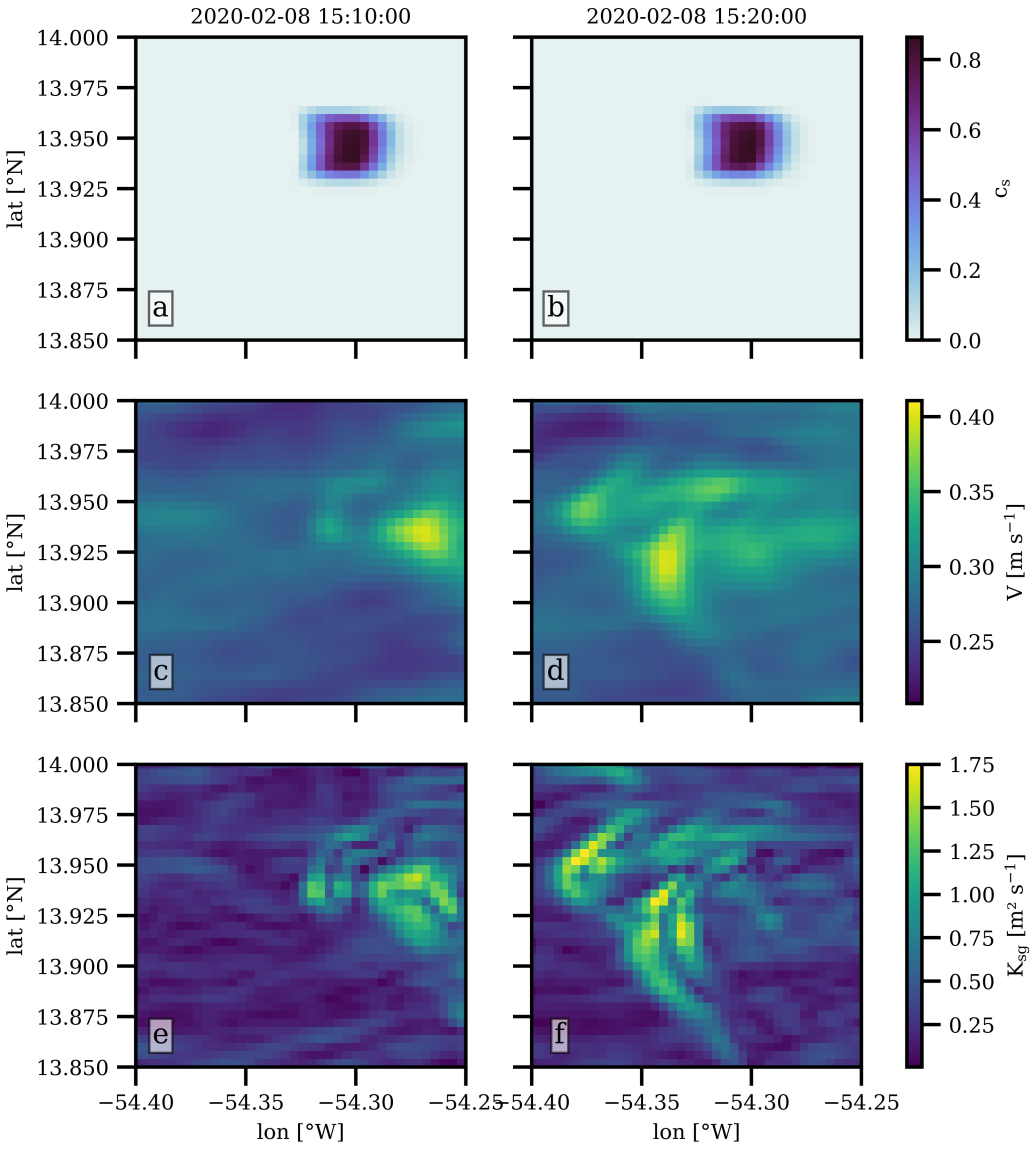

Figure 11. Two snap shots 10 minutes apart of (a,b) surface tracer concentration, (c,d) surface velocity, and (e,f) subgrid diffusivity.

only persisted for 10-15 minutes at the location of the tracer patch, corresponding to an advective length scale of approximately 0.1 m s^{-1} $\times$ 15 $*$ 60 s= 90 m, which is not resolved in this model configuration. Beyond their potential direct advective impact, burst-induced velocity anomalies also induce small-scale horizontal strain, which, according to (1), will be mirrored in an increased subgrid-scale dispersion rate. The increase in K_{sg} at the surface due to the cold pool crossing is again very pronounced (Fig. 11e,f), but of a smaller magnitude than the DWL-induced diffusivities derived earlier (Tab. 1). We conclude that tracer dispersion is only marginally influenced by cold pools.

5 Discussion and Conclusions

Based on a high-resolution regional ocean model for the tropical north-east Atlantic Ocean, we investigated the ocean surface layer's response to ultra high-resolution atmospheric forcing fields from LES, explicitly resolving atmospheric convection, cold pools and associated local rain patches, wind bursts, and cloud shading effects. These LES accompanied a large-scale field campaign in the study area (Bony et al., 2017) and provide a realistic, high-resolution representation of the key atmospheric processes in this region (Schulz & Stevens, 2023).

From these simulations we found an overall reduction of the oceanic heat loss underneath cold pools by 30 W m^{-2}, which is explained by the higher air humidity, reducing the latent heat loss, a reduction in mean winds induced by a cold-pool blocking effect, and stronger long-wave back radiation from increased cloud cover. Our result contrasts a recent publication by Brilouet et al. (2023), who find no clear influence of cold pools on their surface fluxes, or, in the case of active cold pools surrounded by wind bursts, an increase in heat loss by 30 W m^{-2}. We suspect that these different findings can be explained by the magnitude of the background wind field, which is one of the main drivers of the latent and sensible heat fluxes. Simulations in Brilouet et al. (2023) were located in the tropical Indian Ocean with mean background winds of approximately 1-2 m s^{-1}, significantly smaller than typical wind speed anomalies induced by cold pools. Their cold-pool wind bursts therefore had a stronger relative impact compared to our study with 5-11 m s^{-1} background trade winds. This suggests that the influence of cold pools on the surface heat fluxes is not universal, and may differ regionally, depending on background wind conditions.

The radiative and atmospheric forcing in our simulation became most clearly visible in the evolution of DWLs in the upper few meters of the surface layer, similar to many other studies of the tropical ocean. Previous investigations in other tropical regions like the Indian Ocean suggested that the increased atmosphere-ocean temperature contrast induced by the presence of DWLs increases the ocean heat loss to the atmosphere (Matthews et al., 2014; Brilouet et al., 2021). While this effect seems obvious from the flux parameterizations summarized in section 2.3, we did, however, not see a clear signature of it in our simulations. A more detailed analysis showed that the evolution of DWLs in our simulations co-occured with a slight reduction of the trade winds during daytime (Fig. 6a), which over-compensated the impact of the DWLs on the heat flux (Fig. 6b). The underlying mechanisms for this reduction in wind speeds are not fully understood at the moment but the phenomenon is widely observed in the trade wind zone (Savazzi et al., 2022). This suggests that the impact of DWLs on the air-sea fluxes may be overestimated in studies ignoring this effect.

While the impact of DWLs on the air-sea fluxes turned out to be not significant in our simulations, we found that the small-scale variability in the atmospheric forcing (cold pools, wind bursts, rain patches) induces a strong lateral variability in DWL properties, most notably a factor-3 variability in DWL thicknesses and a factor-2 variability in DWL temperature anomalies. This lateral variability is also seen in the vertical diffusivities with possible ecosystem implications.

Additional simulations focusing on the lateral dispersion of km-scale tracer patches in the surface layer showed that the small-scale atmospheric variability only had a negligible effect on the tracer spreading rates. These simulations, however, also revealed a new shear-dispersion mechanism with an advective component associated with the diurnal jet and a mixing component associated with nighttime convection. This mechanism, which is likely a subgrid-scale process even in regional and high-resolution global simulations, results in an extreme anisotropy of horizontal tracer spreading, determined by the direction of the diurnal jet, with net horizontal diffusivities of 16-30 m^2 s^{-1} along the major axis. For comparison, diffusivities associated with baroclinic mixed layer in-

stabilities in the vicinity of submesoscale surface layer fronts are in the range 1-100 $m^2\ s^{-1}$ according to Fox-Kemper et al. (2008), which is of the same magnitude. Tracer spreading due to classical Ekman-induced shear dispersion at nighttime is almost an order of magnitude weaker than DWL-induced shear dispersion. The increased horizontal transport and mixing in the presence of a DWL, which is not resolved in most regional model studies and has not received much attention yet, also has implications for the transport of particles like e.g. micro plastics and other marine debris (van Sebille et al., 2020).

This study solely focused on the response of the ocean surface layer to prescribed atmospheric forcing. While this approach has highlighted a number of new processes associated with the small-scale atmospheric variability that is not resolved in typical forcing fields used in ocean modeling, it does not account for potential feedbacks between the ocean and the atmosphere. Future studies with focus on atmosphere-ocean interactions will require a coupled model system, e.g. Bauer et al. (2021) and Brilouet et al. (2023).

6 Open Research

The LES simulation output that accompanies the EUREC^{4}A campaign is freely available and can be easily accessed via the EUREC^{4}A-Intake catalog via doi: 10.5281/zenodo.8422322 as described at `howto.eurec4a.eu` (EUREC4A community, 2023). The GETM source code used for this work is archived at doi: 10.5281/zenodo.12805570 (Klingbeil, 2024). The Global Ocean Forecasting System (GOFS) 3.1 41-layer HYCOM + NCODA Global 1/12° Analysis output is publicly available at `http://hycom.org` (HYCOM Consortium, 2024). Funding for the development of HYCOM has been provided by the National Ocean Partnership Program and the Office of Naval Research. Data assimilative products using HYCOM are funded by the U.S. Navy. Analysis and plotting scripts are archived at doi: 10.5281/zenodo.13323002 (Schmitt, 2024). For the fitting in Section 4, the scipy.optimize.curve_fit function created by the SciPy community was used.

Acknowledgments

This paper is a contribution to the project L4 (Energy-Consistent Ocean-Atmosphere Coupling) of the Collaborative Research Centre TRR 181 "Energy Transfers in Atmosphere and Ocean", funded by the German Research Foundation (DFG) under grant 274762653 to L. Umlauf.

References

Bauer, T. P., Holtermann, P., Heinold, B., Radtke, H., Knoth, O., & Klingbeil, K. (2021). ICONGETM v1.0 – flexible NUOPC-driven two-way coupling via ESMF exchange grids between the unstructured-grid atmosphere model ICON and the structured-grid coastal ocean model GETM. *Geoscientific Model Development*, *14*(8), 4843–4863. doi: 10.5194/gmd-14-4843-2021

Bony, S., Stevens, B., Ament, F., Bigorre, S., Chazette, P., Crewell, S., ... Wirth, M. (2017). EUREC4A: A Field Campaign to Elucidate the Couplings Between Clouds, Convection and Circulation. *Surveys in Geophysics*, *38*(6), 1529–1568. doi: 10.1007/s10712-017-9428-0

Brilouet, P.-E., Redelsperger, J.-L., Bouin, M.-N., Couvreux, F., & Lebeaupin Brossier, C. (2021). A case-study of the coupled ocean–atmosphere response to an oceanic diurnal warm layer. *Quarterly Journal of the Royal Meteorological Society*, *147*(736), 2008–2032. doi: 10.1002/qj.4007

Brilouet, P.-E., Redelsperger, J.-L., Bouin, M.-N., Couvreux, F., & Villefranque, N. (2023). A numerical study of ocean surface-layer response to atmospheric shallow convection: Impact of cloud shading, rain, and cold pools. *Quarterly*

Journal of the Royal Meteorological Society, *n/a*(n/a). doi: 10.1002/qj.4651

Burchard, H., & Bolding, K. (2002). *GETM: A General Estuarine Transport Model; Scientific Documentation* (Nos. EUR 20253 EN, JRC23237). European Commission, Joint Research Centre, Institute for Environment and Sustainability. Retrieved from `https://publications.jrc.ec.europa.eu/repository/handle/JRC23237`

Canuto, V. M., Howard, A., Cheng, Y., & Dubovikov, M. S. (2001). Ocean Turbulence. Part I: One-Point Closure Model—Momentum and Heat Vertical Diffusivities. *Journal of Physical Oceanography*, *31*(6), 1413–1426. doi: 10.1175/1520-0485(2001)031⟨1413:OTPIOP⟩2.0.CO;2

Dipankar, A., Stevens, B., Heinze, R., Moseley, C., Zängl, G., Giorgetta, M., & Brdar, S. (2015). Large eddy simulation using the general circulation model icon. *Journal of Advances in Modeling Earth Systems*, *7*(3), 963-986. Retrieved from `https://agupubs.onlinelibrary.wiley.com/doi/abs/10.1002/2015MS000431` doi: https://doi.org/10.1002/2015MS000431

Drushka, K., Gille, S. T., & Sprintall, J. (2014). The diurnal salinity cycle in the tropics. *Journal of Geophysical Research: Oceans*, *119*(9), 5874–5890. doi: 10.1002/2014JC009924

EUREC4A community. (2023). *Eurec4a* [dataset]. Zenodo. Retrieved from `https://doi.org/10.5281/zenodo.8422322` doi: 10.5281/zenodo.8422322

Fairall, C. W., Bradley, E. F., Godfrey, J. S., Wick, G. A., Edson, J. B., & Young, G. S. (1996). Cool-skin and warm-layer effects on sea surface temperature. *Journal of Geophysical Research: Oceans*, *101*(C1), 1295–1308. doi: 10.1029/95JC03190

Fairall, C. W., Bradley, E. F., Hare, J. E., Grachev, A. A., & Edson, J. B. (2003). Bulk Parameterization of Air–Sea Fluxes: Updates and Verification for the COARE Algorithm. *Journal of Climate*, *16*(4), 571–591. doi: 10.1175/1520-0442(2003)016⟨0571:BPOASF⟩2.0.CO;2

Fox-Kemper, B., Ferrari, R., & Hallberg, R. (2008). Parameterization of Mixed Layer Eddies. Part I: Theory and Diagnosis. *Journal of Physical Oceanography*, *38*(6), 1145–1165. doi: 10.1175/2007JPO3792.1

Heinze, R., Dipankar, A., Henken, C. C., Moseley, C., Sourdeval, O., Trömel, S., ... Quaas, J. (2017). Large-eddy simulations over germany using icon: a comprehensive evaluation. *Quarterly Journal of the Royal Meteorological Society*, *143*(702), 69-100. Retrieved from `https://rmets.onlinelibrary.wiley.com/doi/abs/10.1002/qj.2947` doi: https://doi.org/10.1002/qj.2947

Holt, J. T., & James, I. D. (2006). An assessment of the fine-scale eddies in a high-resolution model of the shelf seas west of Great Britain. *Ocean Modelling*, *13*(3), 271–291. doi: 10.1016/j.ocemod.2006.02.005

Hughes, K. G., Moum, J. N., & Shroyer, E. L. (2020). Evolution of the Velocity Structure in the Diurnal Warm Layer. *Journal of Physical Oceanography*, *50*(3), 615–631. doi: 10.1175/JPO-D-19-0207.1

Hughes, K. G., Moum, J. N., Shroyer, E. L., & Smyth, W. D. (2021). Stratified Shear Instabilities in Diurnal Warm Layers. *Journal of Physical Oceanography*, *51*(8), 2583–2598. doi: 10.1175/JPO-D-20-0300.1

HYCOM Consortium. (2024). *Hycom + ncoda global 1/12° analysis* [dataset]. Retrieved from `https://www.hycom.org/dataserver/gofs-3pt1/analysis`

Josey, S. A., Pascal, R. W., Taylor, P. K., & Yelland, M. J. (2003). A new formula for determining the atmospheric longwave flux at the ocean surface at mid-high latitudes. *Journal of Geophysical Research: Oceans*, *108*(C4). doi: https://doi.org/10.1029/2002JC001418

Kara, A. B., Hurlburt, H. E., & Wallcraft, A. J. (2005). Stability-Dependent Exchange Coefficients for Air–Sea Fluxes. *Journal of Atmospheric and Oceanic Technology*, *22*(7), 1080–1094. doi: 10.1175/JTECH1747.1

Klingbeil, K. (2024). *Schmitt-EUREC4A Ocean SML GETM code* [Software]. Zen-

odo. Retrieved from https://doi.org/10.5281/zenodo.12805570 doi: 10.5281/zenodo.12805570

Klingbeil, K., Lemarié, F., Debreu, L., & Burchard, H. (2018). The numerics of hydrostatic structured-grid coastal ocean models: state of the art and future perspectives. *Ocean Modelling*, *125*, 80–105. doi: 10.1016/j.ocemod.2018.01.007

Lee, E., & Hong, S.-Y. (2019). Impact of the Sea Surface Salinity on Simulated Precipitation in a Global Numerical Weather Prediction Model. *Journal of Geophysical Research: Atmospheres*, *124*(2), 719–730. doi: 10.1029/2018JD029591

Matthews, A. J., Baranowski, D. B., Heywood, K. J., Flatau, P. J., & Schmidtko, S. (2014). The Surface Diurnal Warm Layer in the Indian Ocean during CINDY/DYNAMO. *Journal of Climate*, *27*(24), 9101–9122. doi: 10.1175/JCLI-D-14-00222.1

Moulin, A. J., Moum, J. N., & Shroyer, E. L. (2018). Evolution of Turbulence in the Diurnal Warm Layer. *Journal of Physical Oceanography*, *48*(2), 383–396. doi: 10.1175/JPO-D-17-0170.1

Paulson, C. A., & Simpson, J. J. (1977). Irradiance measurements in the upper ocean. *Journal of Physical Oceanography*, *7*(6), 952 - 956. Retrieved from https://journals.ametsoc.org/view/journals/phoc/7/6/1520-0485_1977_007_0952_imituo_2_0_co_2.xml doi: 10.1175/1520-0485(1977)007⟨0952:IMITUO⟩2.0.CO;2

Pitarch, J., Bellacicco, M., Marullo, S., & van der Woerd, H. J. (2021). Global maps of forel–ule index, hue angle and secchi disk depth derived from 21 years of monthly esa ocean colour climate change initiative data. *Earth System Science Data*, *13*(2), 481–490. Retrieved from https://essd.copernicus.org/articles/13/481/2021/ doi: 10.5194/essd-13-481-2021

Price, J. F., Weller, R. A., & Pinkel, R. (1986). Diurnal cycling: Observations and models of the upper ocean response to diurnal heating, cooling, and wind mixing. *Journal of Geophysical Research: Oceans*, *91*(C7), 8411–8427. doi: 10.1029/JC091iC07p08411

Renault, L., & Marchesiello, P. (2022). Ocean tides can drag the atmosphere and cause tidal winds over broad continental shelves. *Communications Earth & Environment*, *3*(1), 1–7. doi: 10.1038/s43247-022-00403-y

Rosati, A., & Miyakoda, K. (1988). A general circulation model for upper ocean simulation. *Journal of Physical Oceanography*, *18*(11), 1601 - 1626. doi: 10.1175/1520-0485(1988)018⟨1601:AGCMFU⟩2.0.CO;2

Ruppert, J. H., & Hohenegger, C. (2018). Diurnal Circulation Adjustment and Organized Deep Convection. *Journal of Climate*, *31*(12), 4899–4916. doi: 10.1175/JCLI-D-17-0693.1

Savazzi, A. C. M., Nuijens, L., Sandu, I., George, G., & Bechtold, P. (2022). The representation of the trade winds in ECMWF forecasts and reanalyses during EUREC^{4}A. *Atmospheric Chemistry and Physics*, *22*(19), 13049–13066. doi: 10.5194/acp-22-13049-2022

Schmitt, M. (2024). *Scripts for 'Surface Mixed Layer Response to Rain, Wind bursts and Diurnal Heating'* [Software]. Zenodo. Retrieved from https://doi.org/10.5281/zenodo.13323002 doi: 10.5281/zenodo.13323002

Schmitt, M., Pham, H. T., Sarkar, S., Klingbeil, K., & Umlauf, L. (2024). Diurnal Warm Layers in the Ocean: Energetics, Nondimensional Scaling, and Parameterization. *Journal of Physical Oceanography*, *54*(4), 1037–1055. doi: 10.1175/JPO-D-23-0129.1

Schulz, H., & Stevens, B. (2023). Evaluating large-domain, hecto-meter, large-eddy simulations of trade-wind clouds using eurec4a data. *Journal of Advances in Modeling Earth Systems*, *15*(10), e2023MS003648. doi: https://doi.org/10.1029/2023MS003648

Shackelford, K., DeMott, C. A., van Leeuwen, P. J., Thompson, E., & Hagos, S.

(2022). Rain-Induced Stratification of the Equatorial Indian Ocean and Its Potential Feedback to the Atmosphere. *Journal of Geophysical Research: Oceans*, *127*(3), e2021JC018025. doi: 10.1029/2021JC018025

Shcherbina, A., D'Asaro, E., & Harcourt, R. (2019, June). Rain and Sun Create Slippery Layers in the Eastern Pacific Fresh Pool. *Oceanography*, *32*(2), 98–107. doi: 10.5670/oceanog.2019.217

Shevchenko, R., Hohenegger, C., & Schmitt, M. (2023). Impact of Diurnal Warm Layers on Atmospheric Convection. *Journal of Geophysical Research: Atmospheres*, *128*(14), e2022JD038473. doi: 10.1029/2022JD038473

Stevens, B., Bony, S., Farrell, D., Ament, F., Blyth, A., Fairall, C., ... Zöger, M. (2021). Eurec^{4}a. *Earth System Science Data*, *13*(8), 4067–4119. Retrieved from `https://essd.copernicus.org/articles/13/4067/2021/` doi: 10.5194/essd-13-4067-2021

ten Doeschate, A., Sutherland, G., Bellenger, H., Landwehr, S., Esters, L., & Ward, B. (2019). Upper Ocean Response to Rain Observed From a Vertical Profiler. *Journal of Geophysical Research: Oceans*, *124*(6), 3664–3681. doi: 10.1029/2018JC014060

Ueyama, R., & Deser, C. (2008). A Climatology of Diurnal and Semidiurnal Surface Wind Variations over the Tropical Pacific Ocean Based on the Tropical Atmosphere Ocean Moored Buoy Array. *Journal of Climate*, *21*(4), 593–607. doi: 10.1175/JCLI1666.1

Umlauf, L., & Burchard, H. (2005). Second-order turbulence closure models for geophysical boundary layers. A review of recent work. *Continental Shelf Research*, *25*(7), 795–827. doi: 10.1016/j.csr.2004.08.004

Umlauf, L., Burchard, H., & Bolding, K. (2005). GOTM - Scientic Documentation : Version 3.2. , *63*, 279. doi: 10.12754/MSR-2005-0063

van Sebille, E., Aliani, S., Law, K. L., Maximenko, N., Alsina, J. M., Bagaev, A., ... Wichmann, D. (2020). The physical oceanography of the transport of floating marine debris. *Environmental Research Letters*, *15*(2), 023003. doi: 10.1088/1748-9326/ab6d7d

Vogel, R., Konow, H., Schulz, H., & Zuidema, P. (2021). A climatology of trade-wind cumulus cold pools and their link to mesoscale cloud organization. *Atmospheric Chemistry and Physics*, *21*(21), 16609–16630. doi: 10.5194/acp-21-16609-2021

JGR Atmospheres

RESEARCH ARTICLE
10.1029/2022JD038473

Impact of Diurnal Warm Layers on Atmospheric Convection

Radomyra Shevchenko[1], Cathy Hohenegger[1], and Mira Schmitt[2]

[1]Max Planck Institute for Meteorology, Hamburg, Germany, [2]Leibniz Institute for Baltic Sea Research, Warnemünde, Germany

Key Points:

- diurnal warm layers (DWLs) increase atmospheric moisture
- The increase of cloud cover (CC) following the formation of a DWL is immediate and only lasts for several hours
- The magnitude of the CC increase is small and has no discernible influence on the global mean

Correspondence to:
R. Shevchenko,
radomyra.shevchenko@mpimet.mpg.de

Citation:
Shevchenko, R., Hohenegger, C., & Schmitt, M. (2023). Impact of diurnal warm layers on atmospheric convection. *Journal of Geophysical Research: Atmospheres*, *128*, e2022JD038473. https://doi.org/10.1029/2022JD038473

Received 31 DEC 2022
Accepted 26 JUN 2023

Abstract This manuscript presents a study of oceanic diurnal warm layers (DWLs) in kilometer-scale global coupled simulations and their impact on atmospheric convection in the tropics. With the implementation of thin vertical levels in the ocean, DWLs are directly resolved, and sea surface temperature (SST) fluctuations of up to several Kelvin appear in regions with low wind and high solar radiation. The increase of SST during the day causes an abrupt afternoon increase of atmospheric moisture due to enhanced latent heat flux (LHF), followed by an increase in cloud cover (CC) and cloud liquid water (CLW). However, although the diurnal SST amplitude is even exaggerated in comparison to reanalysis, this effect only lasts for 5–6 hr and leads to an absolute difference of 1% for CC and 0.01 kg m^{-2} for CLW. This can be explained by the fact that the low wind over the SST anomalies dampens their potential effect on the LHF and hence clouds. All in all, the impact of DWLs on convective CC is found to be negligible in the tropical mean.

Plain Language Summary The diurnal fluctuations of sea surface temperature (SST) have been extensively studied for the last decades, but the assessment of the importance of this phenomenon for atmospheric convection on the global scale has come within reach only very recently, thanks to the development of simulations with a horizontal resolution of O(1 km). In this manuscript we show that we can indeed observe an impact of SST fluctuations on moisture in the atmosphere. However, the impact on the amount of clouds in the tropics is found to be short-lived and its magnitude negligible on average.

1. Introduction

Diurnal sea surface temperature (SST) anomalies and their interplay with the atmosphere and in particular with the diurnal cycle of convection have been an object of study for many decades. In this study, we investigate this connection for the first time using simulations that can explicitly resolve both the diurnal temperature variations in the ocean and convection in the atmosphere on a global scale.

Diurnal variations in SST have already been described in Sverdrup et al. (1942). Since then, there have been numerous studies describing the physics and the conditions of appearance of diurnal SST variations, the seminal work by Price et al. (1986) being the first detailed description of this phenomenon. Under low-wind conditions and with sufficient insolation, a stable near-surface layer forms during the day in the upper layers of the ocean (until the depth of O(10 m)) that leads to a surface warming of up to 5 K (see Wick and Castro (2020)). In the absence of solar radiation during the night, the stratification dissolves as vertical turbulent mixing takes overhand, until a homogeneous mixed layer is restored. The physics of this phenomenon is described in detail in a monograph by Soloviev and Lukas (2013). This stratified, warm layer is known as diurnal warm layer (DWL) and it is ubiquitous in all latitudes, causing SST fluctuations of 0.2 K or more in the entire Northern hemisphere and beyond during boreal summer (see Gentemann et al. (2003)). A comprehensive discussion of its definition and properties can be found in a review by Kawai and Wada (2007). In particular, the authors of the review point out that the presence of DWLs in observations as well as in single column simulations leads to stronger latent and sensible heat fluxes. As surface fluxes connect the surface to the atmospheric boundary layer and since changes in boundary layer properties affect the development of convection, the question of the impacts of DWLs on atmospheric convection arises.

Investigating this question in models requires both fine enough vertical resolution in the ocean, to resolve DWLs, and fine enough horizontal grid spacing in the atmosphere, to resolve atmospheric convection. With the development of deca- to kilometer scale simulations in a coupled configuration (Hohenegger et al. (2023)) such investigations are becoming possible. Prominent among the newest studies are the papers by Voldoire et al. (2022) and Brilouet et al. (2021). In Voldoire et al. (2022), a single column coupled model has been considered, while

in Brilouet et al. (2021), a one column ocean model has been coupled to an atmospheric large-eddy simulation model integrated over a limited area. Both experiments are based on or validated with the data from the Dynamics of the Madden Julian Oscillation (DYNAMO) campaign, during which diurnal SST differences of several Kelvin were observed. Voldoire et al. (2022) showed that the impact of DWLs on the boundary layer depth, atmospheric moisture and precipitation seems to be small. In contrast, de Szoeke et al. (2021) argued that in the observations from the DYNAMO data set, convection is enhanced on days with large SST differences. Finally, Voldoire et al. (2022) conjectured that a single column model cannot capture horizontal interactions that might lead to a larger impact.

To the authors' knowledge, there is yet no study extending the question of interactions between DWLs and atmospheric convection to a realistic, global framework with resolved convection. And yet, atmospheric convection plays a key role in the energy and water cycle in the tropics, therefore describing the driving mechanisms of convection and assessing their importance is crucial.

The present study aims at closing this gap and at analyzing the impact of DWLs on atmospheric convection in a global, coupled ICON simulation with 5 km horizontal resolution and decimeter grid spacing in the first oceanic layers. This allows us to resolve DWL and convection, to assess their interactions, also by resolving horizontal gradients, and to analyze the global impacts of DWLs. We are particularly interested in understanding whether the presence of DWLs enhances CC in a time frame of several days and if so, whether this happens through a direct moistening by the latent heat flux (LHF) or by enhancing spatial gradient in SST and mesoscale circulations. Moreover, the global nature of our simulation allows to zoom in on different areas and encompass other meteorological and sea conditions than the ones of the DYNAMO campaign.

The manuscript is structured as follows. In Section 2 we describe the setup of the experiments, and in Section 3 we analyze the representation and properties of DWLs in global ICON simulations. In Section 4 we quantify the effect of DWLs on surface fluxes, atmospheric moisture and clouds, and finally in Section 5 we present the conclusions of our work.

2. Experimental Setup

To study the effect of DWLs, we conduct global coupled simulations with the ICON model in its Sapphire configuration. The Sapphire configuration targets simulations with a horizontal grid spacing finer than 10 km. For our simulations, we use a setup similar to the simulation called G_AO_5 km in Hohenegger et al. (2023), with small deviations that will be described below. The model is fully coupled, and at the horizontal resolution of approximately 5 km it is at the boundary of resolving convection. Although the cloud amount associated with shallow convection is expected to be overestimated (see Vial et al. (2019) and Hohenegger et al. (2020)), it has been demonstrated in Vial et al. (2019) that both amplitude and shape of the diurnal cloud cycle remain similar for horizontal resolutions varying between 150 m and 2.5 km in ICON simulations. This setup allows us to directly assess how an SST anomaly influences convection, to study possible interactions between clouds and DWLs in a highly realistic context, and to analyze global implications of including DWLs into models.

The main prerequisite for resolving DWLs in ocean simulations is high vertical resolution of the upper oceanic layers (cf. Brilouet et al. (2021)). The introduction of the z^* ocean coordinate into the ICON model (detailed in Singh and Korn (in preparation)) allows running global experiments with an unprecedented vertical resolution. For the purposes of this article, we conducted two simulations. One has 128 ocean vertical levels, starting at 2 m at the surface and gradually growing with depth, which is also the setup in G_AO_5 km in Hohenegger et al. (2023). This simulation plays the role of the reference simulation. The other has 139 ocean vertical levels, starting with 0.5 m and gradually increasing and blending into the reference setup from 45.4 m depth (see Figure A1 in Appendix A). To determine layer thicknesses necessary for resolving DWLs, while keeping the total number of layers as low as possible, we ran test simulations with the one dimensional ocean model GOTM (Umlauf et al. (2005)). The vertical grid that we chose is sufficiently coarse to obtain a numerically stable global run and produces DWLs whose temperature field is indistinguishable in its depth, magnitude and overall vertical structure from a run with a 10 cm uniform grid (compare Figure A2 in Appendix A and Figure 1). We run both simulations for 30 days starting 21 January 2020 and with the coupling and radiation time steps of 12 min, the atmosphere time step of 30 s, and the ocean time step of 80 s. Both simulations have identical initial conditions, whereby the

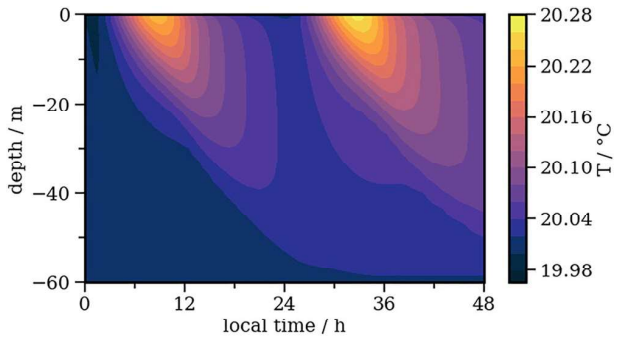

Figure 1. 48 hr simulation of diurnal warm layers in GOTM with 139 ocean vertical levels (see Figure A1 for the detailed vertical resolution), as will be used in ICON, for an idealized heat flux with a maximal radiation of 600 W m^{-2}, a constant wind speed of 8 m s^{-1}, and a time step of 80 s.

generation of the initial ocean state is described in Hohenegger et al. (2023). We call the runs with 128 and 139 ocean levels $S_{control}$ and S_{+DWL} respectively.

3. Representation of Diurnal Warm Layers

In this section we describe the features of DWLs as represented in our simulations and compare them to known properties derived from measurements, reanalysis, and limited-area decameter-scale simulations. As our main focus is on tropical convection, we concentrate our analysis on the tropics which we define here as the area comprised between 40°N and 40°S.

3.1. Occurrence and Magnitude

First we diagnose DWLs and assess their occurrence and magnitude. Rigorously speaking, DWLs are defined via vertical temperature gradients (see e.g., Matthews et al. (2014)), as they represent a temperature anomaly sitting on top of the ocean mixed layer. Instead of the temperature gradient, the diurnal SST amplitude (DSA) is often used as a proxy (e.g., in Voldoire et al. (2022)), because, as mentioned in Bellenger and Duvel (2009), in the tropics one can assume that horizontal advection happens at longer time scales, and the temperature changes in the upper ocean can be attributed to DWLs. We also adopt this approach, formally defining DWLs as places with DSA larger than 0.1 K, which corresponds to non-zero depth of a DWL in Matthews et al. (2014). Care is required when following this approach, as SST in our model is defined as the temperature in the uppermost layer. In S_{+DWL} it is the average temperature over 0.5 m and in $S_{control}$ the average temperature over 2 m. Since in this study our main interest is the response of the atmosphere, and since this is the temperature that the atmosphere sees, we do not correct for this difference in our analysis.

In our simulations, DWLs are ubiquitous: Even spots with DSA of over 1.5 K cover 5% of the tropical ocean area. Comparing DWLs in our simulations and in ERA5 reanalysis, we can see in Figure 2 that for the last 10 days of January the spatial distribution of DWLs is in moderately good agreement with each other, with a correlation coefficient of 0.51. The areas with large DSA are well represented by both simulations, but in the less active areas DWLs seem to appear more often in our simulations than in ERA5, creating a higher average. The major hot spots of DWLs are in the Indian ocean south of the equator, along the western coasts of America and Africa, and in the southern part of the Pacific, both in our simulations and in ERA5. Similar areas are also identified in the January climatology map of Bellenger and Duvel (2009). The discrepancy between the DSA pattern in simulations and ERA5 might be due to the divergence in atmospheric conditions over 10 days as well as to local biases in near-surface winds (not shown). A striking feature of our simulation is that, while for $S_{control}$ the DSA field appears nearly homogeneous and the extremes are underestimated compared to ERA5, as expected from the use of thick ocean vertical layers, the amplitudes in S_{+DWL} are much larger than in the reanalysis, with values twice as high. Our values are in contrast with observations as summarized in Kawai and Wada (2007), where the average DSA values during the boreal winter rarely surpass 1 K. Since Kawai and Wada (2007) employed the skin temperature to diagnose DWL, we can conclude that DSA is overestimated in S_{+DWL}. This is confirmed by further observations. The PIRATA buoys located at 0°N10°W and 0°N0°E at 1 m depth have each measured DSA of under 0.7 K in the same period, and the average DSA measured during the EUREC^{4}A field campaign in the area 56.5°W−59°W and 12°N−14.5°N is about 0.15 K, while in S_{+DWL} the values at these locations are 1.8 and 0.71 K respectively. A possible cause for the overestimation is insufficient vertical mixing in the upper layers of the ocean. As this study concentrates on the atmospheric effect of the DWLs, this problem does not jeopardize the analysis, and if anything indicates that the simulated effects will be too strong.

Another important feature is that in S_{+DWL}, DWLs tend to avoid areas with high CC: on a given day, 24% of cells over the ocean have a CC of 0.9 or higher, while for cells where DWLs develop this number reduces to 13%. However, there are also many areas with a low CC and yet no significant DWLs, as shown in Figure 3. For instance, out of all areas with CC below 0.3 on a given day, only 9% developed DWLs with DSA of 1.5 K or higher. This is a consequence of a property well documented in observational studies. Indeed, as explained in Soloviev and Lukas (2013), shortwave radiation and surface wind are the two principal driving factors of DWLs, where high shortwave radiation and low wind speed favor the appearance of DWLs. The previously mentioned

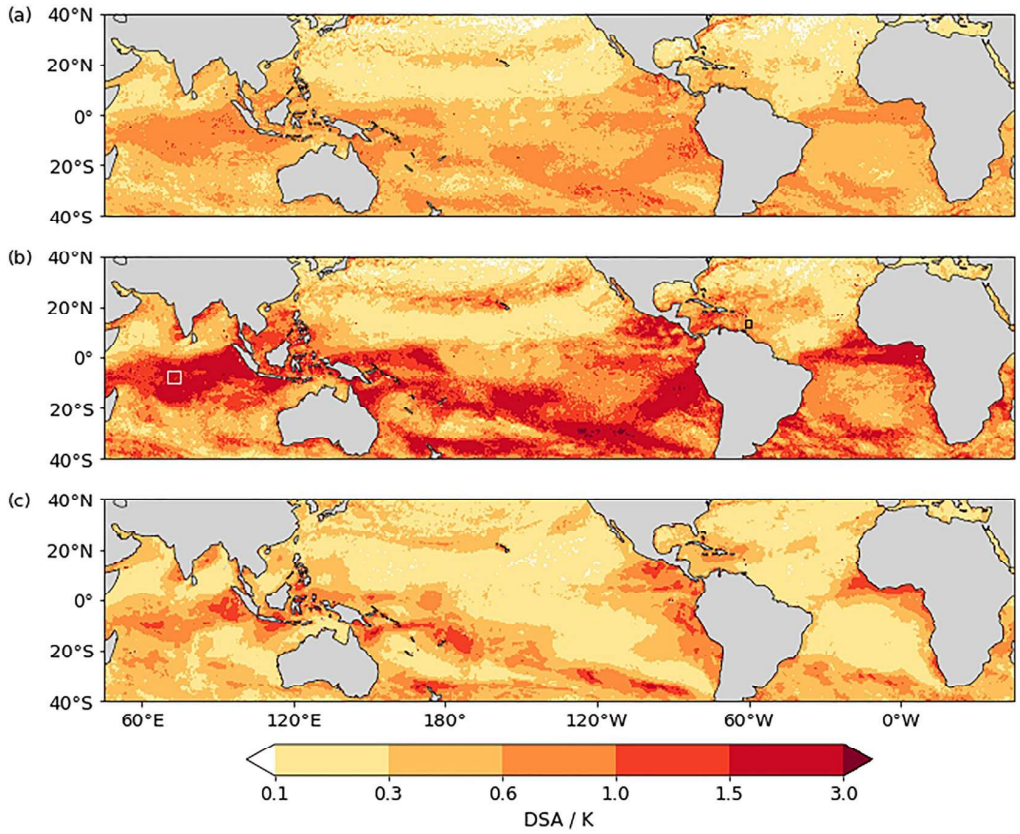

Figure 2. Magnitude of the diurnal SST amplitude (max−min), averaged between 22 and 30 January 2020 in (a) $S_{control}$, (b) S_{+DWL}, and (c) ERA5. The white rectangle in (b) designates an area in the Indian ocean that is analyzed in Section 3.1, and the black rectangle designates the EUREC^{4}A campaign area.

areas with low CC but no DWL correspond to high-wind zones. The relationship of DWLs with downward shortwave radiation and near-surface wind speed will be further explored in Section 3.2.

As to the horizontal extent of DWLs as simulated by S_{+DWL}, there are two observations to be made. As shown in Figure 4a, there are many small clusters of DWLs, but the total area they cover is practically negligible: although 177 clusters out of 799 are of size ≤625 km^2, the total area covered by them amounts to only 0.3% of the entire area covered by DWLs. On the opposite end of the histogram in Figure 4a, one can see that there are a few clusters of size 10^6 km^2. They form predominantly in the high DSA areas from Figure 2 (not shown).

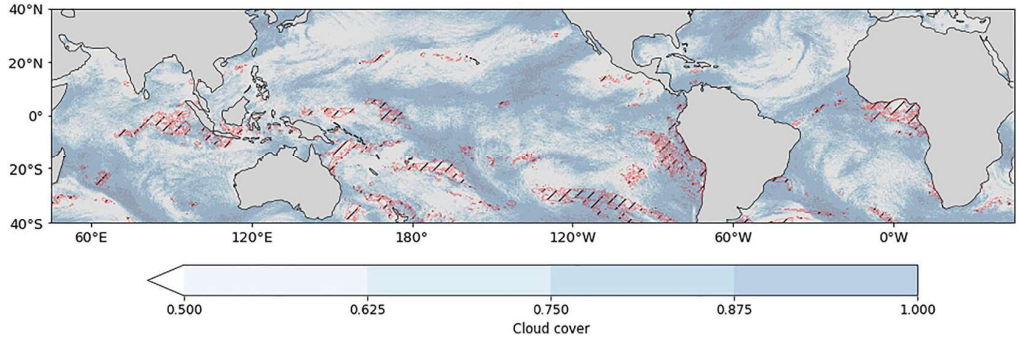

Figure 3. Cloud cover on a particular day (23 January 2020) in S_{+DWL}. Red shaded areas correspond to diurnal warm layer regions with DSA of over 1.5 K.

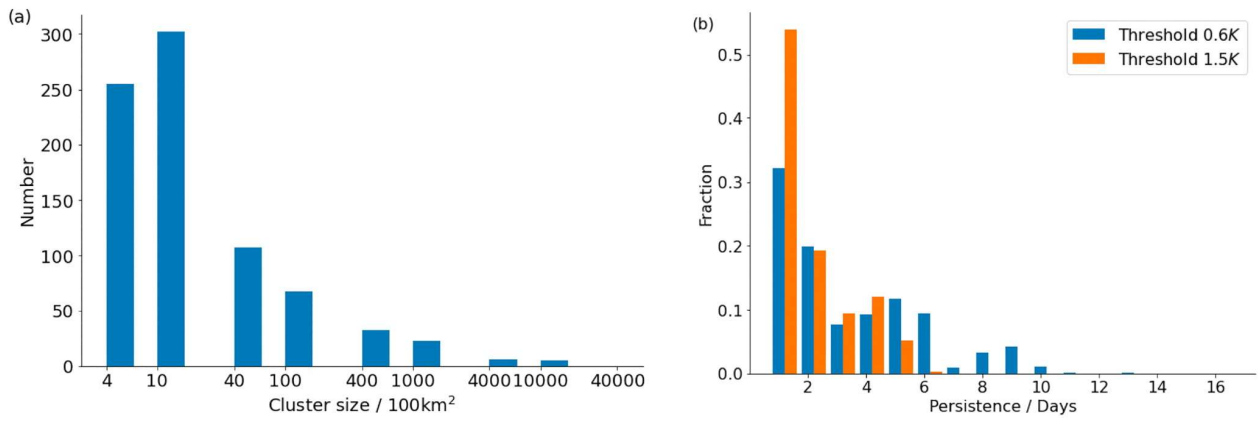

Figure 4. Diurnal warm layer (DWL) statistics for S_{+DWL}: (a) clusters of DWLs to the threshold of 1.5 K on a particular day (23 January 2020) ordered in a histogram of cluster sizes, (b) normalized histogram of DWL episode lengths to different thresholds for the box 70°E–75°E and 5°S–10°S (see white box in Figure 2) over a period of 30 days.

Moreover, for each particular grid cell, the DWLs do not seem to be persistent: for instance, in a region with very high DSA in the Indian ocean (between 70°E–75°E and 5°S–10°S, see the white square in Figure 2b) during a period of 30 days no episode of DSA >0.6 K lasted longer than 10 days, and 80% of all episodes lasted 5 days or less (see Figure 4b). Expectedly, the persistence time becomes shorter if a higher threshold for DSA is considered. This result is similar to the findings in the ERA40 forced simulation in Bellenger and Duvel (2009), where they showed that the DWL episode duration decays faster than exponentially. The lack of persistence applies even to large clusters that can completely change their location from 1 day to the next (not shown).

3.2. Structure of DWLs and Preconditions for Their Formation

For a deeper understanding of how the known properties of DWLs are captured by S_{+DWL} we focus on a study of this phenomenon in the tropical northern Atlantic region off the coast of Barbados, more precisely in the box 56.5°W–59°W and 12°N–14.5°N corresponding to the region of the EUREC^{4}A field campaign (Stevens et al. (2021)).

First, we examine the vertical structure of a DWL produced in the simulation S_{+DWL}. As shown in the anomaly profile (Figure 5), the incoming heat quickly accumulates in the upper layers during the day, as the warming of the upper layers creates a stable stratification if the mixing is slow, which is the case under low wind conditions. During the night, the DWL slowly dissipates until a single mixed layer is restored. As mentioned before, in this region, the heat anomalies are overestimated: a typical DSA in glider observations is approximately 0.15 K (see Hohenegger et al. (2023), Figure 11c), while in S_{+DWL} in a calm period it is around 0.3 K. The time of the maximum and minimum is captured accurately compared to these observations (between 14 and 17 hr LT and between 5 and 8 hr LT respectively).

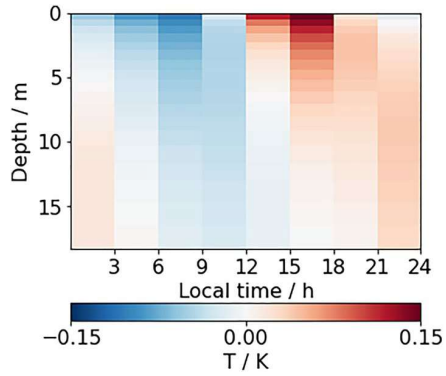

Figure 5. Sea water temperature (3 hr mean output) averaged over 3 days over the box 56.5°W–59°W and 12°N–14.5°N, time anomaly.

Another analysis demonstrates that the dependency of DSA on insolation and surface wind observed, among others, in satellite measurements in Gentemann et al. (2003), are reproduced in ICON simulations as expected, namely higher DSA correlates with lower winds and higher downward shortwave radiation at the surface. The scatterplot in Figure 6a shows a relationship similar to the formula

$$\mathrm{DSA} \sim \begin{cases} U^{-3} \text{ for } U < 4\text{-}5\,\mathrm{m\,s^{-1}}, \\ U^{-1} \text{ for } U > 4\text{-}5\,\mathrm{m\,s^{-1}}, \end{cases}$$

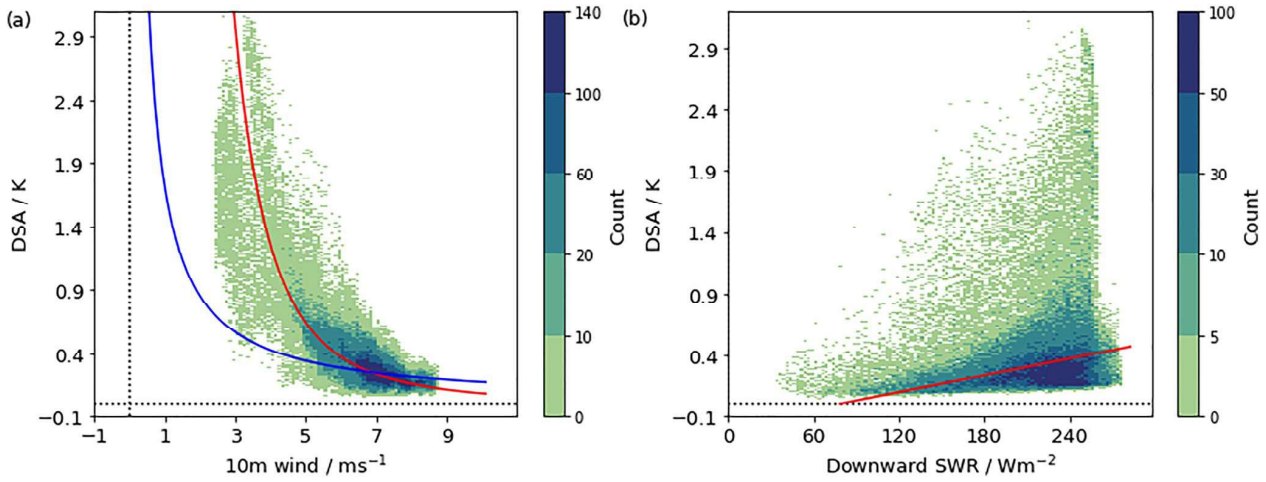

Figure 6. 2D histograms of sea surface temperature amplitude and (a) 10 m wind speed as well as (b) shortwave radiation over the box 56.5°W to 59°W and 12°N to 14.5°N in S_{+DWL}. The blue and red lines in (a) indicate the interpolation of U^{-1} and U^{-3} to higher and lower wind speeds respectively. The red line in (b) is the linear regression fit between the variables.

suggested in Soloviev and Lukas (2013) for 10 m wind speed U, although the threshold appears to be located at 6–7 m s^{-1} rather than at 4–5 m s^{-1}. Also the linear dependence on shortwave radiation described in Matthews et al. (2014) seems to be confirmed in S_{+DWL} (Figure 6b). In particular, the slope of the linear regression between DSA and surface downward shortwave radiation in ICON is 0.0023 K W^{-1} m^2, which is indeed close to the slope of 0.0021 K W^{-1} m^2 found in Matthews et al. (2014). The large scattering of points in Figure 6b is caused by the joint influence of wind speed and radiation on DWLs.

4. Effect of DWLs on Convection

The previous section shows that DWLs are frequent in the tropics, they cover large areas and persist over several days. We can therefore hypothesize that they might have an effect on atmospheric convection, either by creating horizontal air temperature gradients, or by enhancing the moistening of the overlying air. Moreover, as DSA in S_{+DWL} is overestimated, the effect of DWLs is expected to be too strong.

To assess the impact of DWLs on convective clouds, we need to compare the values of relevant variables in places where DWLs develop to places where they do not develop. A clean way to accomplish this without having to account for other sources of variability is to compare the differences between these values in S_{+DWL} and $S_{control}$ at places where DWLs of a certain magnitude are present in S_{+DWL}. A key point in this analysis is to only include the first 4 days after the start of the simulation into the investigation to ensure that the two simulations remain close and do not diverge due to the chaotic nature of the atmosphere. Figure 7 shows that both simulations indeed remain highly correlated during the first several days, and this correlation is well above a simple measure of persistence, computed here as 1-day lag correlation in $S_{control}$.

To conduct our analysis, we proceed as follows. As we are interested in the temporal evolution of the effects of DWLs, we move the entire output to local time. The analysis then starts at a given point on the first full day, making sure that at every grid cell a spin up period of at least 12 hr can be discarded. The ocean is then subdivided into 0.25° × 0.25° disjoint squares, and for each square the hourly maximal SST difference between S_{+DWL} and $S_{control}$ during a day, denoted by ΔSST, is computed. Based on this first day of the analysis that we also call the detection day, two groups can be formed: one called the "no DWL difference" group, where ΔSST stays below 0.1 K, and another one where ΔSST lies between certain thresholds T_1 and T_2, which we call the "DWL difference between T_1 and T_2" group. Note that the plot of ΔSST yields a map very similar to Figure 2b (Figure B1 in Appendix B), and thus can be used as a proxy for identifying DWL areas. We use this proxy from now on to cover a larger variety of cases and to obtain a cleaner comparison.

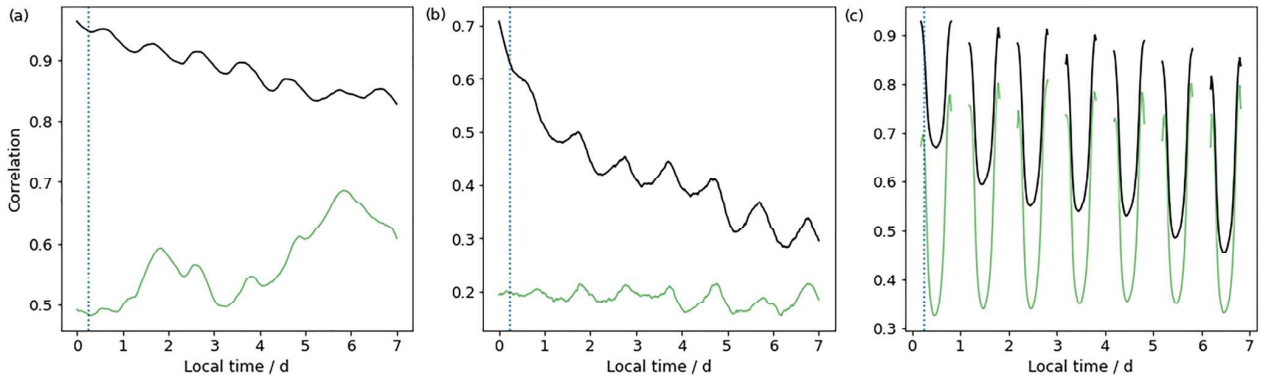

Figure 7. Temporal evolution of the global correlation between $S_{control}$ and S_{+DWL} (black line) and of $S_{control}$ with itself shifted by 24 hr (green line) for (a) near-surface wind, (b) cloud cover, and (c) incoming shortwave radiation at the surface. The vertical line at 6 hr LT designates the approximate beginning of the formation of diurnal warm layers.

The subsequent analysis consists in comparing the two groups to each other, focusing on the time series of the differences in relevant variables over the days 1–3, with day 1 being the detection day, see Figure 8 for an example of the differences in SST. Statistically, it is supported by *t*-tests for equality of means for independent samples with different variances. We consider groups with T_1 and T_2 increasing in steps of 0.1 K, every $T_2 - T_1 = 0.1$ K group having at least 1,695 cells, a sufficient number to ensure the robustness of the results. The size of the squares is chosen in accordance to the cluster sizes discussed in Section 3.1 (see Figure 4), as a mesoscale analysis is sufficient to capture a possible effect of DWLs, and also because the temperature and moisture changes produced by one isolated output cell are not expected to have a large effect and would be quickly mixed in the atmosphere. Moreover, we make the assumption that the effects in cloudiness are localized. Indeed, the impact of DWLs on CC via moistening is a local effect, and the mesoscale circulation created by SST gradients would also result in cloud formation over DWLs. With this assumption, the samples can be treated as independent. We analyze the results over 3 days, because we want to study the overall duration of the atmospheric reaction in the areas where there were DWLs and catch possible reinforcement phenomena under realistic persistence conditions of DWLs. To avoid capturing temporally correlated events, we also refrain from treating the output shifted by a day or more as additional samples.

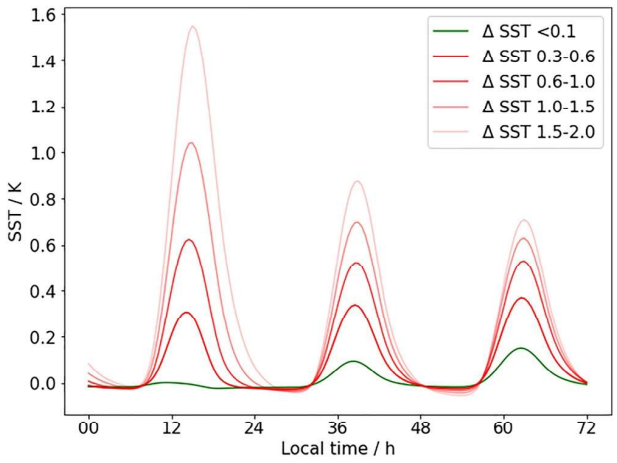

Figure 8. Time series of S_{+DWL}-$S_{control}$ for different ΔSST.

4.1. Impact on Latent Heat Flux and Related Quantities

First we investigate whether higher ΔSST leads to more moisture in the air over DWL areas. This will help understand whether cloud formation may be impacted over DWLs. In particular, we are going to concentrate on differences in LHF and column water vapor path (WVP) to measure the effects on evaporation and column moistening respectively, as shown in Figure 9.

The first observation concerning the plots (a, b) in Figure 9 is that the differences between S_{+DWL} and $S_{control}$ in the "no DWL difference" group after the detection day revolve around zero, as expected and further justifying our approach. This is not the case for the "DWL" groups. Differences are clearly appearing and are of larger magnitude, the stronger the DWL is.

The LHF is increased when DWLs are present, with a peak around noon on every day, as expected from the diurnal cycle in SST. WVP is always higher over DWLs. The difference decreases in the morning hours of the detection day and increases rapidly thereafter. The dip could be caused either by a dip in LHF, by an increase of precipitation or by a weakening in convergence of moisture. As LHF is increased and there is no excessive rain over DWLs (not shown), the dip must be due to weaker convergence, which might be caused by a weakening of surface wind required for DWL formation. The increase of

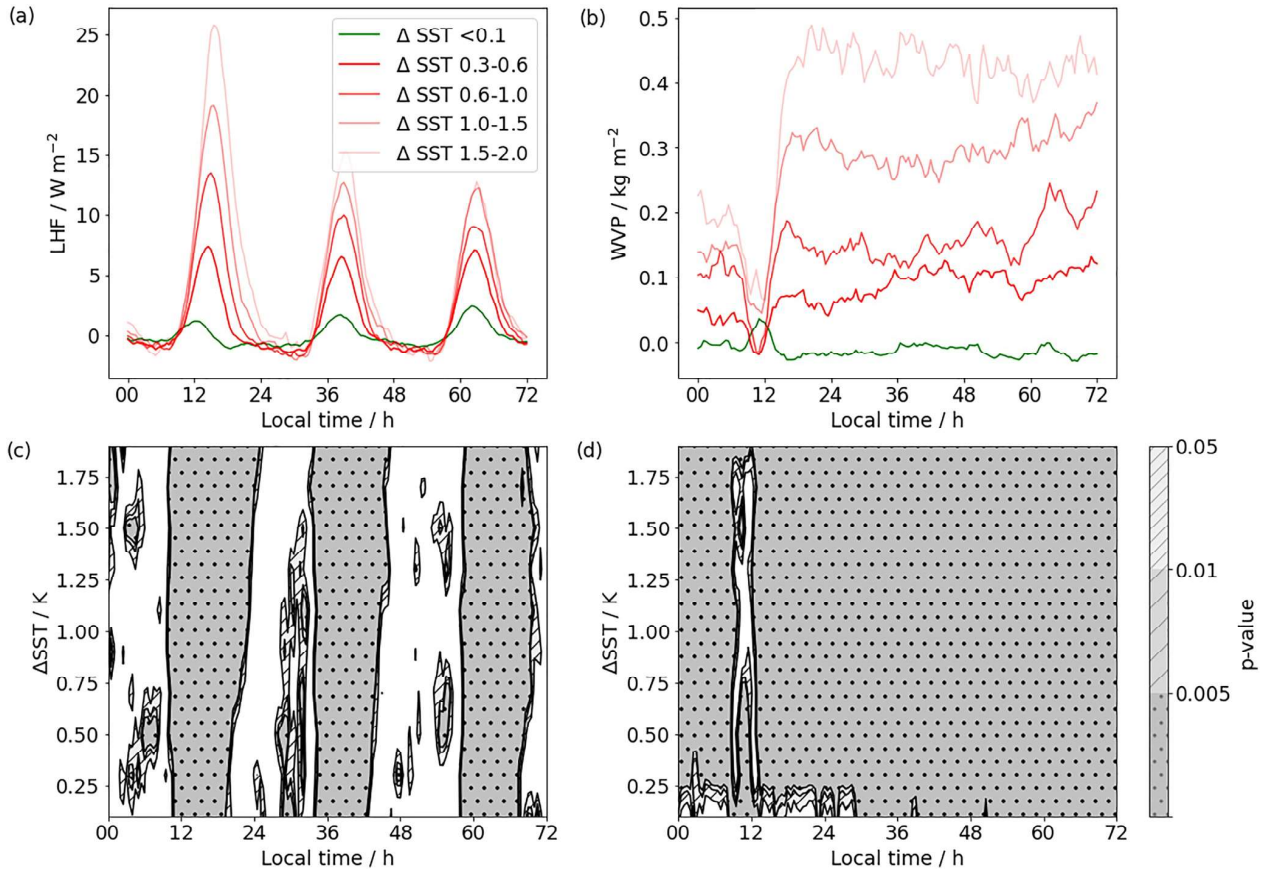

Figure 9. Time series of S_{+DWL}-$S_{control}$ and *t*-test significance levels in bins of 0.1 K for latent heat flux (a, c) and water vapor path (b, d). On panel c and d, white means not significant.

WVP after 12 hr LT reflects the increase in moisture due to increased LHF. One can trace the propagation of the moisture response to DWLs in Figure 9, since the onset and duration times of the effects are different: while LHF reacts immediately and is tied directly to differences in temperature (see Figure 8), the effect on WVP is delayed by several hours and persists over the following days without losing its magnitude.

Figures 9c and 9d confirms that the differences observed visually are highly significant even on the third day and even for small ΔSST with p-values smaller than 0.005, except for the nighttime values of LHF. However, an important point is that the absolute differences are rather small, especially for smaller ΔSST: For instance, for ΔSST between 0.6 and 1.0 K, the maximum difference of LHF is below 15 W m^{-2} and WVP is below 0.2 kg m^{-2}. One can compare these values with global averages of the two quantities over the ocean, which are ca. 130 W m^{-2} for LHF and ca. 34.6 kg m^{-2} for WVP. The order of magnitude of LHF changes is similar to that found in the single column configuration in Voldoire et al. (2022).

In Acquistapace et al. (2022), the authors described an observational case study in the EUREC^{4}A region that compares the atmospheric response to a mesoscale cold patch with 1 K difference to other parts of the ocean in this region. Although this difference in SST is comparable to the differences caused by DWLs, the impact on the LHF in this study is much higher than the values shown in Figure 9a and has on average 70 W m^{-2} higher values in the subcloud layer over the warmer area. The difference between the two studies could come from the different height use to compute the LHF, at the surface versus in the subcloud in Acquistapace et al. (2022). This is nevertheless unlikely as LHF only slightly increases with height (see Siebesma et al. (2003)). The other explanation could be the wind. The principal difference between DWLs and an SST anomaly of a different origin is that the appearance of DWLs requires windstill conditions, and this has an influence on LHF, as it scales linearly with wind. Indeed, the winds in Acquistapace et al. (2022) are about 10 m s^{-1}, while in our case, winds in

the 1 K difference group are on average 2.75 m s^{-1}. Given that in the 1 K difference group the LHF difference is 18 W m^{-2} (see Figures 8 and 9), a three times higher wind would have given values similar to Acquistapace et al. (2022). We can conclude from this simplified calculation that the wind is an important inhibition mechanism for the possible effect of SST anomalies caused by DWLs on the atmosphere.

4.2. Impact on Cloudiness

The variables we consider for analyzing the impact of DWLs on clouds are total CC and cloud liquid water (CLW) path (CLW). In our configuration of the ICON model, the CC values are binary, so the values over 0.25° boxes represent the fraction of the gridpoints in that box covered by clouds.

The responses of CC and CLW shown in Figure 10 are very similar to each other. The "no DWL difference" time series is fluctuating around zero after the detection day, but on the detection day itself there is a peak at midday. In contrast, the DWLs regions exhibit dips at the same time, and the magnitude of these dips is positively correlated with the ΔSST amplitude (see Figures 10a and 10b and Figures 10e and 10f). This illustrates the prerequisite for DWLs to exist mentioned in Section 3.1: The appearance of DWLs is generally favored by a lower cloud amount. Subsequently we can observe the cloud response to the formation of DWLs on the detection day: after about 12 hr LT, the difference between S_{+DWL} and $S_{control}$ in both CC and CLW over DWLs starts to grow, and by 15 hr LT the peak of discrepancy is reached. This growth is statistically significant starting from an SST amplitude of 0.3 K, and the effect persists longer for higher values of ΔSST, namely until 20 hr LT for ΔSST of 1.5–2.0 K and until 18 hr LT for ΔSST of 0.3–1.0 K for CC. Moreover, the effect seems to last longer for CLW, although the values of both variables fall back below the zero line already during the night. In total, the increase of cloud following the formation of a DWL lasts up to 5–6 hr.

A behavior similar to the first day, that is, less CC and CLW in S_{+DWL} compared to $S_{control}$ in the morning and rise of these quantities in S_{+DWL} in the afternoon, can be observed also on the second and third day after the detection day (Figures 10a and 10b), however, the deviation is barely significant: most of the time, the p-value is above 0.05, especially for higher values of ΔSST (Figures 10c and 10d). This means that the increase of the quantities is often not homogeneous enough to be interpreted as systematic (see Figures 10c and 10d). A crucial factor here is the absolute magnitude of the differences: In extreme cases, for ΔSST between 1.5 and 2.0 K, the deviation of CC reaches 0.03 and that of CLW 0.02 kg m^{-2} on the detection day. On the following day the corresponding maximal values fall to 0.01 and 0.01 kg m^{-2}, while the averages are 0.001 and 0.002 kg m^{-2} respectively (see Figures 10a and 10b). We can compare those to the average values of CC and CLW over DWLs, 0.65 for CC and 0.11 kg m^{-2} for CLW. The average increase in CLW is about 1% and the increase in CC is about 0.2% on the day following even very large ΔSST. We can therefore conclude that the effect on the cloud water content is higher than the contribution of DWLs to CC change, but the effects are very small.

The morning/midday dip of CC and CLW over DWLs even overcompensates the subsequent rise of these quantities. Figure 11 shows mean CC differences between S_{+DWL} and $S_{control}$ as a function of ΔSST on the detection day. For ΔSST above 0.1 K the simulation S_{+DWL} has lower values of CC than $S_{control}$, and only for ΔSST below 0.1 K the reverse is true, such that on average, S_{+DWL} has slightly less cloud than $S_{control}$. The effect of DWLs appears to be dominated by the variability of the model. All in all, we can conclude that DWLs do not increase the global mean of CC or CLW path.

We continue the analysis by looking at deep and shallower clouds separately, as one might expect to see more effects associated with one type of clouds. We differentiate between deep and shallow clouds by taking the outgoing longwave radiation at the top of the atmosphere of 240 W m^{-2} as a threshold. This value is mentioned in Fu et al. (1990) as the threshold often used to identify deep convection. The figures for shallower clouds are very similar to Figure 10 (not shown), which can be explained by the fact that most DWLs are found outside of deep convective regions, see Figure 2b or Figure B1. The deviation for CLW in deep clouds is somewhat larger, up to 0.03 kg m^{-2} on the detection day. As shown in Figure 12a for CC, the effects, despite being a bit larger, remain very small and do not exhibit systematic significance (Figure 12c). Considering precipitation as an additional possibility to see an impact of DWLs (Figures 12b and 12d), we see that there is no sufficient evidence to attribute the fluctuations of precipitation, even for higher values of ΔSST, to anything more than chance.

The global results obtained in this section for the CC, CLW, and precipitation seem robust with respect to the chosen large-scale area. In particular, excluding the subtropics has no effect on the amplitudes or the temporal

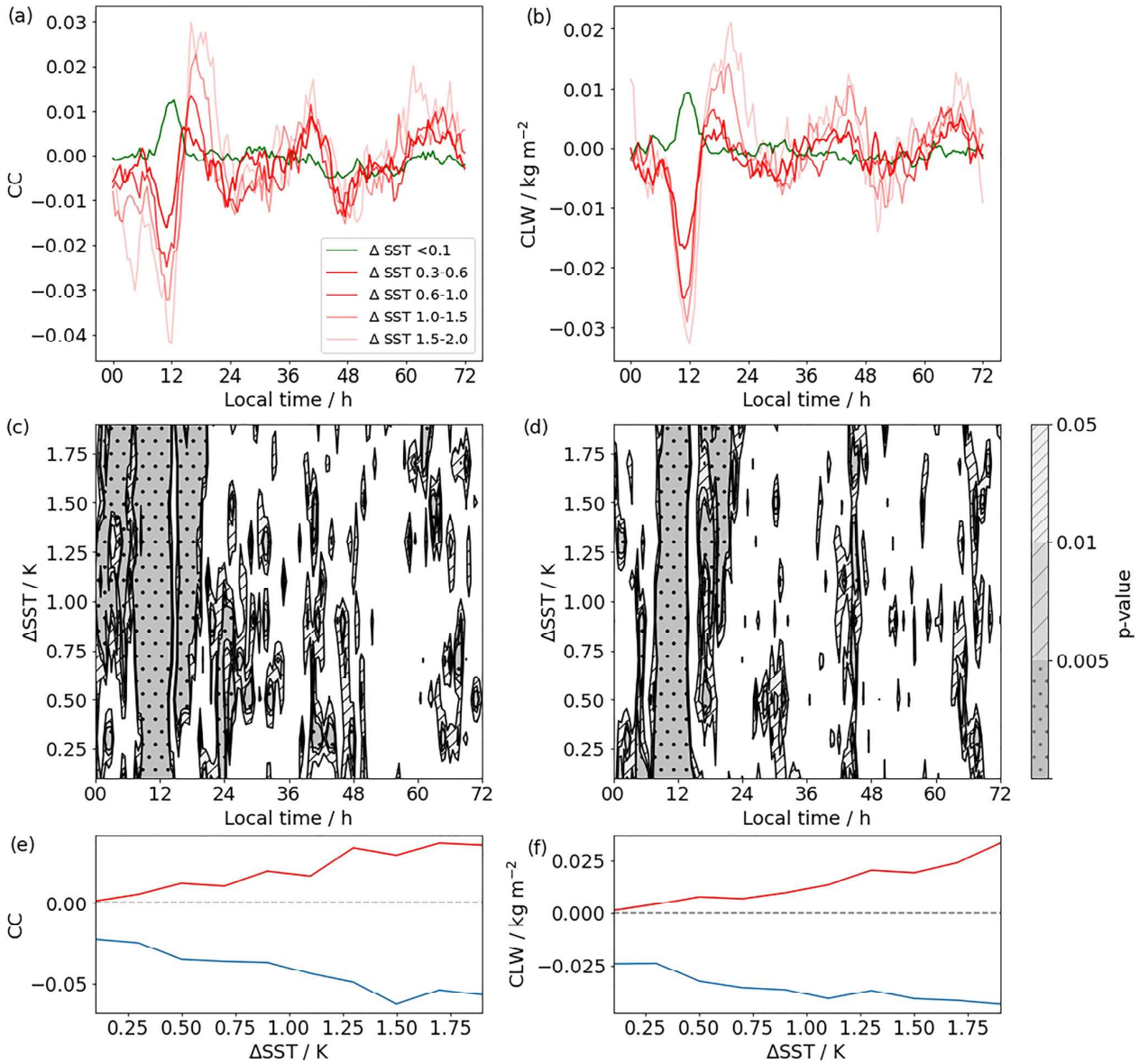

Figure 10. Time series of S_{+DWL}-$S_{control}$, *t*-test significance levels in bins of 0.1 K, and maximal (red) and minimal (blue) value of the deviation on the detection day for cloud cover (a, c, e) and cloud liquid water (b, d, f).

behavior of these quantities. Moreover, the results remain quantitatively unchanged if the simulations are compared after additional 24 hr of spinup (not shown).

The last question that we want to investigate is to what extent the presence of DWLs might affect the diurnal cycle of convection. We focus on the example of the EUREC^{4}A field campaign, which took place in the northern tropical Atlantic. For this region the diurnal cycle of shallow convection has been studied in great detail in Vial et al. (2019). In particular, it has been shown there that, in observations as well as in large-eddy simulations (LES), the CC peaks during the day, which might make it more susceptible to SST in comparison to other regions. In our case, both S_{+DWL} and $S_{control}$ overestimate the CC found in observations by a factor of 2, as was expected from the resolution sensitivity study in Vial et al. (2019), but capture perfectly the time structure as well as the amplitude of the cycle: minimum between 12 and 15 LT, maximum at 2 LT, amplitude of about 0.1 (Figure 13), in good agreement with observations in Vial et al. (2019). The increase in CC resulting from the appearance

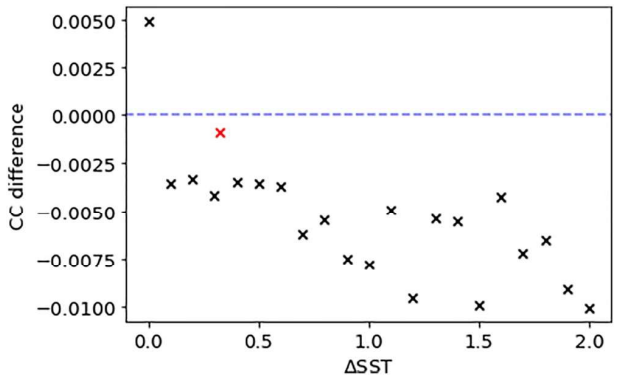

Figure 11. Diurnal mean cloud cover (CC) differences (S_{+DWL}-$S_{control}$) as a function of ΔSST (black crosses). The red cross is the average CC difference against the average ΔSST.

of DWLs occurs in the late-afternoon. If anything, CC slightly decreases at other times. Both effects taken together tend to slightly reduce the diurnal amplitude. The fact that DWLs only have a small influence on the diurnal cycle of CC is consistent with the study in Vial et al. (2019) that reproduced the main features of the cycle in LES despite using an SST with no diurnal cycle.

5. Discussion and Conclusions

By introducing thin vertical levels into the global coupled ICON model, we could directly resolve DWLs and assess their impact on the atmosphere. The simulations employed a grid spacing of 5 km, both in the atmosphere and ocean, so that ocean mesoscale eddies and atmospheric convection can be resolved explicitly. The DWLs produced by the simulation reproduce the physical features known from observations and limited area decameter simulations, but the magnitude of the diurnal SST fluctuations is exaggerated in comparison to reanalysis, by about a factor of two.

The increase in the amplitude of the diurnal cycle of SST in regions with DWLs leads to a corresponding increase in LHF and WVP. The effects are significant, even on days 2 and 3 following the detection of a DWL, but the values are small: 7 W m^{-2} difference in LHF and 0.1 kg m^{-2} difference in WVP for a SST difference of 0.6 K. In the late-afternoon of the detection day, CC and CLW content also increase, but the effects are small and lose statistical significance within 5–6 hr of appearance. What is however significant is a decrease in CC and liquid water content on the day of detection, around noon. This expresses the fact that DWLs favorably form in areas of

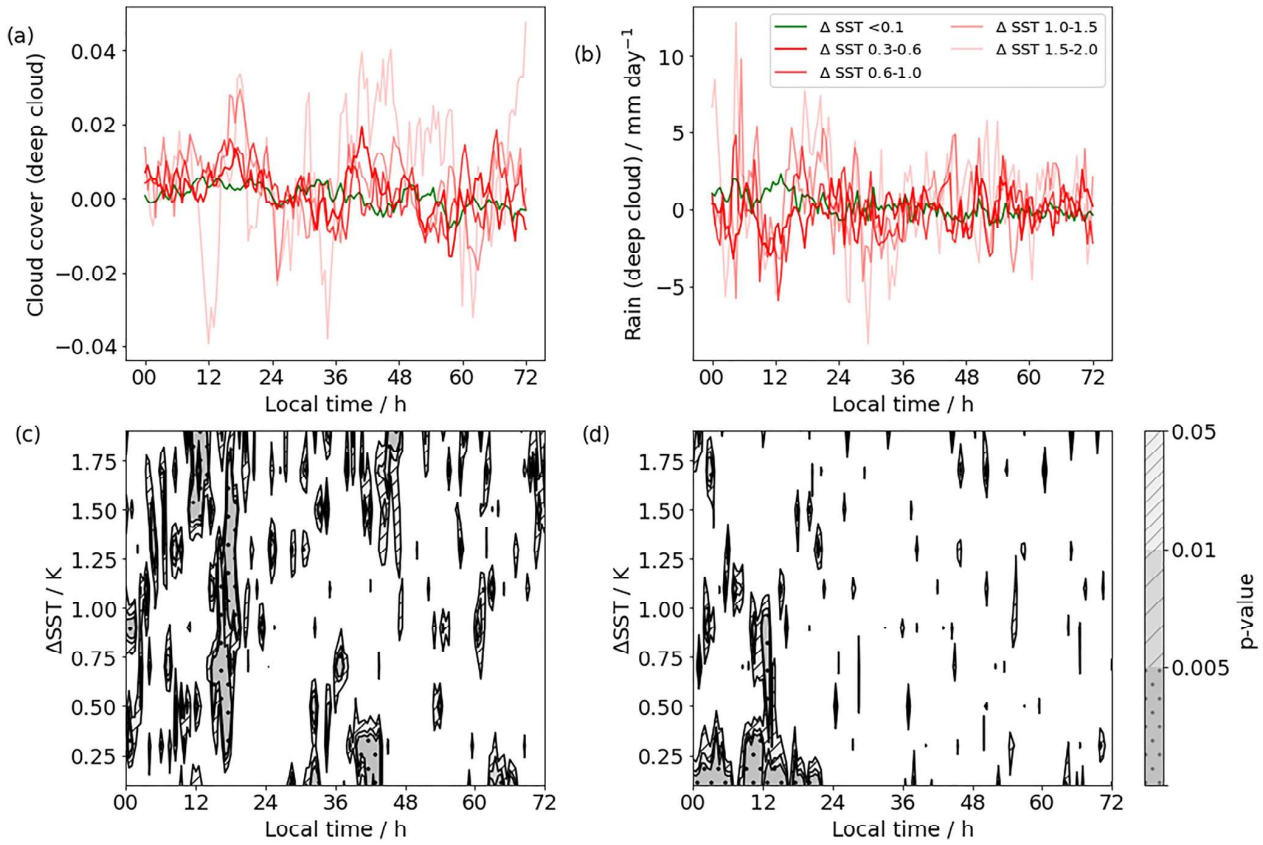

Figure 12. As Figure 9, but for cloud cover (a, c) and precipitation (b, d) associated with deep convection.

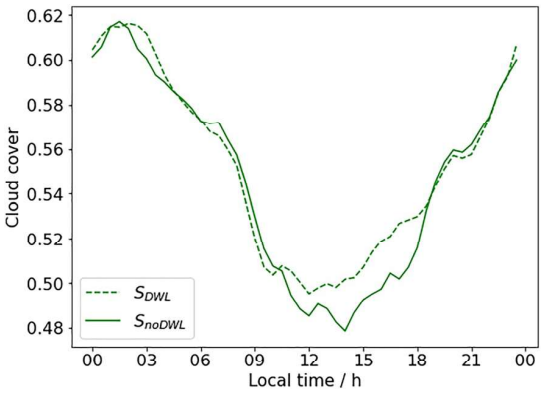

Figure 13. Diurnal cloud cover cycle in the box 56.5°W to 59°W and 12°N to 14.5°N, composite over 30 days.

low CC, and hence high insolation. This effect compensates the subsequent increase. All in all, resolving DWLs does not affect the mean CC over tropical oceans.

The amplitude of the observed differences in LHF is similar to findings in Voldoire et al. (2022), and the impact on CC shows that convection over DWLs is enhanced, as it is claimed in the observation study of de Szoeke et al. (2021). Moreover, the small influence of DWLs on the CC diurnal cycle in the tropical Atlantic supports the results in Vial et al. (2019). A surprising finding of our study is that the impact of DWLs on convection remains small even for a strongly enhanced diurnal SST amplitude over this particular region as well as globally. A possible reason for this is that DWLs develop in windstill areas, and their impact on the LHF therefore remains small, in contrast to the observational study in Acquistapace et al. (2022) showing a large atmospheric effect of a 1 K SST anomaly under high wind (10 m s^{-1}). In view of this crucial difference, we conclude that it is important to resolve (sub)mesoscale oceanic structures such as eddies that result in large SST anomalies even under strong wind conditions.

We finish the discussion by focusing on the implications and limitations of our study. In the subtropics, the resolution of 5 km can strongly distort the representation of shallow convection. Although the similar behavior between the different resolution simulations in Vial et al. (2019) is encouraging, we cannot exclude at the outset that our results may be biased by a poor representation of shallow convection. Still, we could also not find any significant effect of DWL on deep convection, which suffers less from the limitation in grid spacing.

Regarding the question of the importance of DWLs in models, one needs to differentiate between the local and the overall impact. In our exemplary study in the northern tropical Atlantic, the presence of DWLs can reduce the amplitude of the diurnal cycle of the CC by up to 10% (see Figure 13). In some specific cases with extraordinarily high DSA, DWLs might indeed play a role. However, this remains a rare and local phenomenon.

The analysis in this manuscript only concerns short-term effects of DWLs. However, it is known that the mean SST increases in DWL areas (Bellenger and Duvel (2009)). Therefore, inclusion of DWLs will have a long-term influence on the energy budget that is not treated here, but at least for short-term effects, our study demonstrates that DWLs do not have a global and significant impact.

Appendix A: Vertical Resolution of the Simulations

Figure A1 demonstrates the difference in vertical resolutions between S_{+DWL} and $S_{control}$.

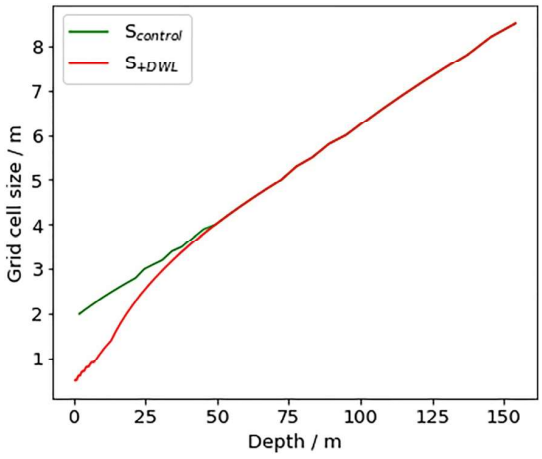

Figure A1. Layer thicknesses for S_{+DWL} and $S_{control}$ for the upper 150 m.

Figure A2 shows vertical temperature profiles for a GOTM run with 0.1 m uniform vertical resolution.

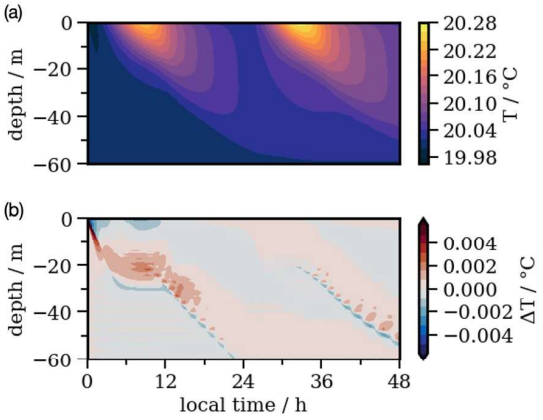

Figure A2. (a) As in Figure 1, but with uniform 0.1 m thick vertical layers. (b) Difference between the temperature profiles in Figure 1 and (a).

Appendix B: Average ΔSST as Proxy for DSA

Figure B1 shows the field of ΔSST on the detection day.

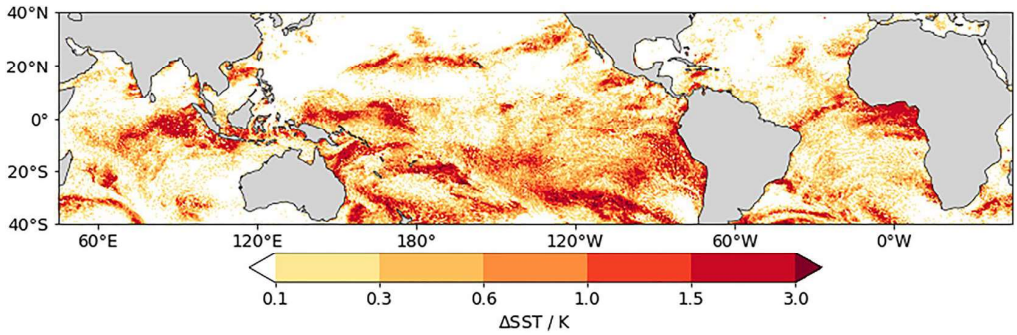

Figure B1. ΔSST on detection day.

Data Availability Statement

Detailed information concerning the ICON model is contained in the publication Hohenegger et al. (2023). The ocean model GOTM is documented in Umlauf et al. (2005) and can be installed from https://gotm.net. The ERA5 data set used in this study has been provided by the Climate Data Store. The versions of ICON and GOTM used to produce the output, the run scripts, as well as the code that produces the figures can be found in https://hdl.handle.net/21.11116/0000-000C-1447-E.

Acknowledgments
This work used resources of the Deutsches Klimarechenzentrum (DKRZ) granted by its Scientific Steering Committee (WLA) under project ID bm1253. This paper is a contribution to the project L4 ("Energy-Consistent Ocean-Atmosphere Coupling") of the collaborative research centre TRR 181 "Energy Transfers in Atmosphere and Ocean" funded by the Deutsche Forschungsgemeinschaft (DFG, German Research Foundation)—Project-ID 274762653. Open Access funding enabled and organized by Projekt DEAL.

References

Acquistapace, C., Meroni, A. N., Labbri, G., Lange, D., Späth, F., Abbas, S., & Bellenger, H. (2022). Fast atmospheric response to a cold oceanic mesoscale patch in the north-western tropical Atlantic. *Journal of Geophysical Research: Atmospheres*, *127*(21), e2022JD036799. https://doi.org/10.1029/2022JD036799

Bellenger, H., & Duvel, J.-P. (2009). An analysis of tropical ocean diurnal warm layers. *Journal of Climate*, *22*(13), 3629–3646. https://doi.org/10.1175/2008JCLI2598.1

Brilouet, P.-E., Redelsperger, J.-L., Bouin, M.-N., Couvreux, F., & Lebeaupin Brossier, C. (2021). A case-study of the coupled ocean–atmosphere response to an oceanic diurnal warm layer. *Quarterly Journal of the Royal Meteorological Society*, *147*(736), 2008–2032. https://doi.org/10.1002/qj.4007

de Szoeke, S. P., Marke, T., & Brewer, W. A. (2021). Diurnal Ocean surface warming drives convective turbulence and clouds in the atmosphere. *Geophysical Research Letters*, *48*(4), e2020GL091299. https://doi.org/10.1029/2020GL091299

Fu, R., Genio, A. D. D., & Rossow, W. B. (1990). Behavior of deep convective clouds in the tropical Pacific deduced from ISCCP radiances. *Journal of Climate*, *3*(10), 1129–1152. https://doi.org/10.1175/1520-0442(1990)003<1129:bodcci>2.0.co;2

Gentemann, C. L., Donlon, C. J., Stuart-Menteth, A., & Wentz, F. J. (2003). Diurnal signals in satellite sea surface temperature measurements. *Geophysical Research Letters*, *30*(3), 1140. https://doi.org/10.1029/2002GL016291

Hohenegger, C., Korn, P., Linardakis, L., Redler, R., Schnur, R., Adamidis, P., et al. (2023). ICON-Sapphire: Simulating the components of the Earth system and their interactions at kilometer and subkilometer scales. *Geoscientific Model Development*, *16*(2), 779–811. https://doi.org/10.5194/gmd-16-779-2023

Hohenegger, C., Kornblueh, L., Klocke, D., Becker, T., Cioni, G., Engels, J. F., et al. (2020). Climate statistics in global simulations of the atmosphere, from 80 to 2.5 km grid spacing. *Journal of the Meteorological Society of Japan. Ser. II*, *98*(1), 73–91. https://doi.org/10.2151/jmsj.2020-005

Kawai, Y., & Wada, A. (2007). Diurnal sea surface temperature variation and its impact on the atmosphere and ocean: A review. *Journal of Oceanography*, *63*(5), 721–744. https://doi.org/10.1007/s10872-007-0063-0

Matthews, A. J., Baranowski, D. B., Heywood, K. J., Flatau, P. J., & Schmidtko, S. (2014). The surface diurnal warm layer in the Indian Ocean during Cindy/dynamo. *Journal of Climate*, *27*(24), 9101–9122. https://doi.org/10.1175/JCLI-D-14-00222.1

Price, J. F., Weller, R. A., & Pinkel, R. (1986). Diurnal cycling: Observations and models of the upper ocean response to diurnal heating, cooling, and wind mixing. *Journal of Geophysical Research*, *91*(C7), 8411–8427. https://doi.org/10.1029/JC091iC07p08411

Siebesma, A. P., Bretherton, C. S., Brown, A., Chlond, A., Cuxart, J., Duynkerke, P. G., et al. (2003). A large eddy simulation intercomparison study of shallow cumulus convection. *Journal of the Atmospheric Sciences*, *60*(10), 1201–1219. https://doi.org/10.1175/1520-0469(2003)60<1201:alesis>2.0.co;2

Soloviev, A., & Lukas, R. (2013). *The near-surface layer of the ocean: Structure, dynamics and applications*. Springer Netherlands.

Stevens, B., Bony, S., Farrell, D., Ament, F., Blyth, A., Fairall, C., et al. (2021). EUREC^{4}A. *Earth System Science Data*, *13*(8), 4067–4119. https://doi.org/10.5194/essd-13-4067-2021

Sverdrup, H., Johnson, M., & Fleming, R. (1942). *The oceans, their physics, chemistry, and general biology*. Prentice-Hall.

Umlauf, L., Bolding, K., & Burchard, H. (2005). *GOTM—Scientific documentation. Version 3.2* (Vol. 63). Leibniz-Institute for Baltic Sea Research.

Vial, J., Vogel, R., Bony, S., Stevens, B., Winker, D. M., Cai, X., et al. (2019). A new look at the daily cycle of trade wind cumuli. *Journal of Advances in Modeling Earth Systems*, *11*(10), 3148–3166. https://doi.org/10.1029/2019MS001746

Voldoire, A., Roehrig, R., Giordani, H., Waldman, R., Zhang, Y., Xie, S., & Bouin, M.-N. (2022). Assessment of the sea surface temperature diurnal cycle in CNRM-CM6-1 based on its 1D coupled configuration. *Geoscientific Model Development*, *15*(8), 3347–3370. https://doi.org/10.5194/gmd-15-3347-2022

Wick, G. A., & Castro, S. L. (2020). Assessment of extreme diurnal warming in operational geosynchronous satellite sea surface temperature products. *Remote Sensing*, *12*(22), 3771. https://doi.org/10.3390/rs12223771